
DNA Origami Structures for Applications in Single Molecule Spectroscopy and Nanomedicine

Verena Johanna Schüller

Dissertation

durchgeführt an der Fakultät für Physik
der Ludwig–Maximilians–Universität
München

vorgelegt von

Verena Johanna Schüller
aus München

München, den 26.03.2013

Erstgutachter: Prof. Dr. Tim Liedl

Zweitgutachter: Prof. Dr. Philip Tinnefeld

Tag der mündlichen Prüfung: 14.05.2013

Nevertheless, biology is no longer the only branch of science where DNA is finding a significant role: It is now possible to exploit DNA complementarity to control the structure of matter.

Nadrian C. Seeman (2010)[1]

Contents

1	Introduction to Structural DNA Nanotechnology	1
1.1	Deoxyribonucleic Acid	1
1.1.1	Structure	2
1.1.2	Base Pairing and Base Stacking	2
1.1.3	Chemical and Physical Properties	3
1.2	Structural DNA Nanotechnology	6
1.2.1	DNA as Building Material	6
1.2.2	The DNA Origami Method	9
2	Single-Molecule FRET Ruler Based on Rigid DNA Origami Blocks	15
2.1	Single-Molecule FRET Measured by ALEX	15
2.2	FRET Ruler: Polyproline and Double-Stranded DNA	18
2.3	FRET Ruler: Rigid DNA Origami Structure	21
2.4	MgCl ₂ Dependent E-Value Shift in FRET Measurements on DNA Origami Structures	24
2.4.1	Interhelical Gaps in DNA Origami Structures	24
2.4.2	Structure of DNA Origami Rectangle	25
2.4.3	MgCl ₂ Dependence of DNA Origami Rectangle Structure	26
2.5	Associated Publication P1	32
3	Cellular Immunostimulation by CpG-Sequence-Coated DNA Origami Structures	41
3.1	Immunostimulation Measured by ELISA and Flow Cytometry	41
3.2	DNA Carrier Systems for Nanomedicine	43

3.3	Immunostimulation via CpG ODN Delivered by DNA Nanostructures	45
3.4	Associated Publication P2	48
4	Design and Analysis of Specific DNA Origami Structures	57
4.1	Tetrahedral DNA Origami Structure	57
4.2	M1.4 Based DNA Origami Structures	58
4.3	Associated Publication P3	60
4.4	Associated Publication P4	70
A	Appendix	79
	Supporting Information for Associated Publication P1	80
	Supporting Information for Associated Publication P2	90
	Supporting Information for Associated Publication P3	102
	Supporting Information for Associated Publication P4	108

List of Figures

1.1	Structure of DNA.	3
1.2	Sticky-end hybridization.	6
1.3	Self-assembly of DNA molecules.	8
1.4	DNA origami structures.	10
1.5	Design and analysis of a rectangular DNA origami structure.	12
2.1	FRET measured by ALEX.	16
2.2	FRET Ruler double-stranded DNA.	20
2.3	Size determination of DNA origami FRET Ruler.	22
2.4	Accurate Distance Determination on DNA origami FRET Ruler.	23
2.5	DNA origami rectangle for interhelical gap studies.	25
2.6	FRET measurements on DNA origami sample at increasing MgCl ₂ concentrations.	28
2.7	AFM and TEM analysis of DNA origami rectangle at increasing MgCl ₂ concentrations.	30
3.1	Methods to quantify immune stimulation of cells.	42
3.2	Stability of compact DNA origami structure and loose DNA ravel.	44
3.3	Immunostimulation by CpG Oligodeoxynucleotides delivered by DNA nanostructures.	46
4.1	Tetrahedral DNA origami structure.	58
4.2	M1.3 based DNA origami structures.	59

Zusammenfassung

Desoxyribonukleinsäure (DNA) ist vor allem als Träger der genetischen Erbinformation bekannt. Doch ihre einzigartige Struktur vereint darüber hinaus die Eigenschaften Programmierbarkeit, selektive Hybridisierung und Adressierbarkeit mit Biokompatibilität und Stabilität. Mit diesen Voraussetzungen ist DNA prädestiniert unter einem neuen Gesichtspunkt betrachtet zu werden: als molekularer Baustein für Objekte im Nanometerbereich. DNA Nanotechnologie nutzt gerade diesen Aspekt, um intelligente Materialien zu entwickeln, die in unterschiedlichsten Forschungsbereichen Verwendung finden. Eine vielversprechende Methode zur Herstellung von Nanopartikeln ist die DNA Origami-Technik. Sie basiert auf einem Selbstorganisationsprozess, in dem ein DNA Einzelstrang durch hunderte komplementäre Oligonukleotide in eine bestimmte Form gefaltet wird. In dieser Dissertation werden DNA Nanostrukturen vorgestellt, die für Anwendungen in Bereichen der Einzelmolekülspektroskopie sowie der Nanomedizin entwickelt wurden.

Der Fluoreszenz Resonanz Energie Transfers (FRET) zwischen zwei Chromophoren ist stark abhängig von der Distanz zwischen den Farbstoffen. Für den experimentellen Nachweis dieser Distanzabhängigkeit wurden in der Vergangenheit verschiedene Moleküle als Abstandshalter für Donor-Akzeptor Paare verwendet, darunter das Polypeptid Polyprolin sowie doppelsträngige DNA. In dieser Arbeit wird die Entwicklung einer neuen DNA Origami-Plattform zur exakten Positionierung von FRET Paaren in definierten Abständen für Einzelmolekül Messungen beschrieben. Die Vorteile gegenüber den vorherigen Systemen bestehen zum einen in der langen Persistenzlänge der starren Struktur und zum anderen in einer vereinfachten Distanzabschätzung der Fluorophore. Auf diese Weise konnte der farbstoffspezifische Förster-radius R_0 für das in der Forschung häufig verwendete FRET Paar Cy3/Cy5 auf 5.3 nm bestimmt werden. In einem weiteren Schritt wurde das hohe räumliche Auflösungsvermögen von Einzelmolekül FRET Messungen genutzt, um strukturelle Veränderungen von zweidimensionalen DNA Origami-Konstrukten in Bezug auf variierende Salzkonzentrationen zu untersuchen. Es wurde beobachtet, dass mit wachsender Magnesiumionen-Konzentration die FRET Effizienz zwischen Farbstoffen, die auf parallelen Helices einer DNA Origami-Struktur fixiert waren, stieg. Dies könnte auf einen verminderten Helix-zu-Helix Abstand schließen lassen. Allerdings wird vermutet, dass photophysikalische Effekte auf die fluoreszenten Farbstoffe verursacht durch die Magnesiumionen mit dieser Reaktion interferieren.

Die Eigenschaft der Biokompatibilität von DNA als körpereigener Baustein verspricht den Einsatz von DNA Origami-Partikeln als pharmakologische Trägersysteme im Bereich der Nanomedizin. Im zweiten Teil dieser Dissertation wird eine DNA Origami-Struktur vorgestellt, die für die Anwendung speziell in der Immuntherapie entwickelt wurde. Das röhrenähnliche DNA Konstrukt diente hierbei als Trägersystem für immunogene Cytosin-Phosphat-Guanin Oligonukleotide (CpG ODN), die nach ihrer Aufnahme in Säugetierzellen eine Immunantwort auslösten. Die spezifische CpG Sequenz ist im Genom von Wirbeltieren seltener vertreten als im mikrobiellen Genom. Sie wird durch den endosomalen Toll-like Rezeptor 9 (TLR9) erkannt, was zur Segregation von Zytokinen wie Interleukin 6 (IL-6) sowie der Expression transmembraner Proteine wie C-Typ Lektin (CD69) und damit zu einer Aktivierung des Immunsystems führt. Im Vergleich zu freien CpG ODN, lösten CpG ODN gebunden an die

DNA Origami-Struktur eine signifikant gesteigerte Produktion von IL-6 und CD69 in frisch isolierten Milzzellen der Maus aus. Dabei konnte nachgewiesen werden, dass die Zellviabilität über mehrere Stunden hinweg unbeeinflusst blieb.

Abstract

The unique nature of DNA combines programmability and selective hybridization with biocompatibility and physical stability. These are optimal prerequisites to consider DNA not only as a carrier of genetic information but also as a molecular building material. DNA nanotechnology exploits this outstanding molecule to develop intelligent structures on the nanometer scale for applications in numerous research areas. The established DNA origami method uses a virus-based single DNA strand that is folded into desired shapes and patterns by hundreds of short oligonucleotides. In this dissertation, DNA nanostructures that are based on the DNA origami technique and their applications in single-molecule FRET spectroscopy and nanomedicine are presented.

In the past, the distance dependence of fluorescence resonance energy transfer (FRET) was characterized by using several molecules such as the polypeptide polyproline or double-stranded DNA as spacer for donor and acceptor dyes. In this work, the DNA origami technique was applied to create a rigid DNA nanostructure that was used as a reliable FRET ruler in single-molecule spectroscopy. The DNA origami FRET ruler overcame drawbacks from previous systems by its long persistence length, the precise positioning of fluorophores and consequentially the direct distance determination. In contrast, the translation of the base-pair separation into physical distance between donor and acceptor on the double-stranded DNA FRET ruler required a multiparametric fit with the knowledge of the Förster radius of the specific dye pair. Alternating laser excitation for single-molecule spectroscopy allowed measurements of the distance dependent FRET efficiencies on both DNA ruler constructs. The origami-based FRET ruler directly yielded a Förster radius R_0 of 5.3 nm for the FRET pair Cy3/Cy5. The high spatial resolution of the single-molecule FRET measurements were proven to investigate structural changes within a two-dimensional DNA origami object in the presence of magnesium ions. The FRET efficiency values increased dependent on increasing MgCl_2 concentrations for FRET pairs attached to parallel helices within the DNA origami structure. This observation could be attributed to the screened electrostatic repulsion between the negatively charged backbones of the DNA helices, which caused changes in the interhelical distances, but also could have arisen from photophysical effects of the salt ions on the fluorescence dyes possibly interfering with this reaction.

The biocompatibility of DNA origami nanostructures qualifies them for applications in drug-delivery, targeted nanomedicine and immunotherapy. A DNA origami carrier system for delivering immunostimulating nucleic acids to cells was designed to trigger an artificial immune response. The tube-like DNA origami structure was decorated with unmethylated cytosine-phosphate-guanine oligodeoxynucleotides (CpG ODN). The highly specific CpG sequence, which is more abundant in the genome of microbes than in vertebrates, can be recognized after uptake by cells of the mammalian immune system via the endosomal Toll-like receptor 9 (TLR9). This leads to the secretion of pro-inflammatory cytokines like interleukin-6 (IL-6) and the surface expression of transmembrane proteins like C-type lectin CD69, which are known markers for an activated immune system. Conjugating CpG ODNs to the DNA origami carrier provoked a significantly enhanced IL-6 and CD69 expression in freshly isolated spleen cells compared to free CpG ODNs. The finding that splenic cells from TLR9 deficient mice

did not show any difference between CpG ODN-functionalized and undecorated DNA origami tubes confirmed that the increased immune stimulation was TLR9 receptor mediated. The uptake efficiency of the DNA origami structures was completely unaffected by the CpG-ODN functionalization, while the uptake of free CpG ODNs was considerably lower. After transfection with DNA origami structures, the viability of the cells was stable over several hours, which confirmed that the DNA origami nanostructure represented a biocompatible and efficient carrier system for immune active CpG ODNs, with potential stimulus-like capability.

1 Introduction to Structural DNA Nanotechnology

Nanotechnology is the engineering of materials, pharmaceuticals and functional devices on the atomic and molecular level. Defining nanotechnology by size encompasses diverse areas in science such as molecular biology, surface chemistry and semiconductor physics. Material on the nanometer scale can be found in a broad range of applications in medicine, electronics and energy production. There are mainly two approaches to create nanomaterials. Top-down approaches use large technical devices such as electron beam microscopes to direct the fabrication of smaller objects. In contrast, bottom-up approaches seek to arrange single components into more complex structures by molecular recognition in self-assembling processes. Several systems exemplified by carbon nanotubes, quantum dots and gold nanoparticles are built by self-organization of subunits. Exploiting the specificity of Watson-Crick base pairing, nucleic acids are used as building material in structural DNA nanotechnology. This will be discussed in the next paragraphs by introducing the structure and properties of deoxyribonucleic acid and its applications.

1.1 Deoxyribonucleic Acid

Deoxyribonucleic Acid (DNA) is the central molecule in the conservation of genetic information by encoding the genetic functions. First isolated by the swiss physician Friedrich Miescher in 1869, the role of DNA as the carrier of genetic information was identified by the classic experiments of Oswald Avery and co-workers in 1944 and was confirmed eight years later in the Hershey-Chase experiment [2–4]. The elucidation of the correct double helix model of the DNA structure by James Watson and Francis Crick in 1953 was a milestone in the the history of DNA discovery. It was based on the X-ray fiber diffraction patterns generated by Rosalind Franklin, Maurice Wilkins and co-workers as well as on the chemical prediction that the DNA bases are complementary paired by Erwin Chargaff (see figure 1.1 A and B) [5–7]. In 1962, Watson, Crick and Wilkins received the Nobel Prize in Physiology or Medicine for this discovery. The biological function follows directly from the biomolecular structure: the semiconservative replication mechanism proposed by Watson and Crick was experimentally confirmed by Matthew Meselson and Franklin Stahl in 1958 [8, 9]. Over twenty years later, Nadrian Seeman was a pioneer considering DNA not only to be a carrier of biological information but to exploit DNA as a structural building material [10]. Since that proposal, DNA nanotechnology uses the unique complementary recognition properties of DNA to create self-

assembling DNA constructs that are used nowadays in numerous areas from life science to nanotechnology.

1.1.1 Structure

The polymeric structure of DNA consists of up to millions of repeating units called nucleotides. As proposed by Watson and Crick, two complementary DNA chains hybridize to form a right handed double helix structure with a center-to-center distance of 0.34 nm between two following nucleotides and a helical pitch of 10.5 nucleotides [11]. The diameter of the DNA double helix is 2 nm. Double-stranded DNA in this conformation which is the most common one under physiological conditions, is called B-form DNA. Depending on the base sequence and the environmental conditions like pH value, DNA can be present in various other forms such as in right handed A-form or in left handed Z-form DNA [2, 12]. A DNA nucleotide is composed of the sugar 2-deoxyribose, a phosphate group and one of the four bases adenine (A), cytosine (C), guanine (G), and thymine (T). Alternating phosphate and sugar residues form the phosphate-deoxyribose backbone of the DNA strand at which phosphodiester binds covalently to the 3'-hydroxyl group and the 5'-phosphate of two adjacent pentose sugars. These asymmetric bonds lead to a chemical polarity of each polynucleotide strand with a terminal phosphate group at the 5' end and a terminal hydroxyl group at the 3' end of the DNA strand. The two polar polynucleotide chains in the double helix structure of DNA pair antiparallely and hybridize via hydrogen bonds between the bases that point to the inner side of the double helix. The four different bases that exist in naturally occurring DNA are essentially planar and have limited conformations. The purines adenine and guanine are two-ring bases of fused five- and six-membered heterocyclic rings, while thymine and cytosine are pyrimidines consisting of one six-membered ring [2, 13].

1.1.2 Base Pairing and Base Stacking

The favored base pairing in a double helix is the Watson-Crick base pairing at which the purine A hybridizes with the pyrimidine T and the purine G binds to the pyrimidine C. These two types of base pairs differ in the number of hydrogen bonds that are formed between the bases. AT-pairs are connected by two hydrogen bonds while CG-pairs form three hydrogen bonds between their bases, thus this pair binds slightly stronger (see figure 1.1 C). Compared to covalent binding energies of more than 100 kJ/mol, with an energy of 5 – 30 kJ/mol the molecular force of the hydrogen bonds per base pair are relatively weak. However, the double helix structure of the DNA is stabilized by the additive forces of the hydrogen bonds of numerous bases. The complementary base pairing enables an energetically favorable packing of the base pairs at the inner side of the double helix. This geometry allows a regular helical structure for any nucleotide sequences with an essentially constant distance between the C₁' atoms of sugars on opposite strands for both AT- and GC-base pairs (see figure 1.1 C). The asymmetric arrangement of the DNA stands with respect to each other leads to the appearance of two grooves of different sizes of the double helix: a major groove with a width of 2.2 nm and a minor groove with a width of 1.2 nm (see figure 1.1 B). These grooves are caused by the fact that the glycosidic bonds of a base pair are not diametric. The minor groove is located on that side of the base pair where the sugars are bound [2, 13].

The second stabilizing interaction between nucleotides in a DNA double helix besides base pairing is base stacking. In aqueous solution, single nucleotides favor stacking caused by

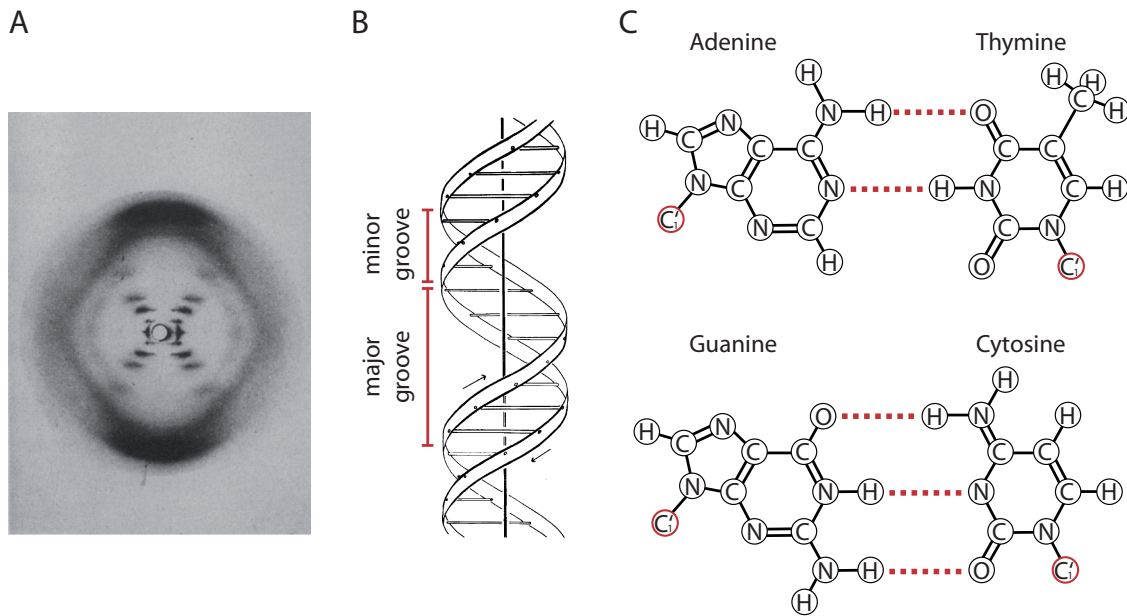


Figure 1.1: Structure of DNA. **A** X-ray fiber diffraction pattern of B-form DNA from Franklin and Gosling. Reprinted by permission from Macmillan Publishers Ltd: Nature ref. [6], copyright 1953 **B** Scheme of double helix structure of B-form DNA from Watson and Crick with major and minor grooves. The ribbons represent the two phosphate-deoxyribose backbones while the horizontal rods illustrate the base pairs. Reprinted by permission from Macmillan Publishers Ltd: Nature ref. [5], copyright 1953. **C** Watson-Crick base pairs shown with two hydrogen bonds (dashed lines) between A and T and three hydrogen bonds between G and C. The distance between the C_1' atoms of the sugars on opposite strands is constant for both AT- and GC-base pairs.

overlapping delocalized π -electron systems instead of forming base-base hydrogen bonds. In other solutions such as chloroform, which is a nonaqueous solvent, base pairs are formed. All of the intermolecular interactions between the bases and the solvent determine the Gibbs free energy of the stacked and paired bases in solution, whereupon base stacking accounts mainly for the stability. Both base stacking and base pairing interactions are responsible for the formation of the double helix structure of the DNA [2, 14, 15].

1.1.3 Chemical and Physical Properties

The backbone of a DNA strand is highly negatively charged because of deprotonation of each phosphate group at pH values higher than 1. Salt in the surrounding solution prevents double-stranded DNA from denaturation due to electrostatic repulsion of the two negatively charged DNA strands. The Debye-Hückel theory can be a first approach to describe the distribution of ions around the DNA strand. In this model, the double helix is reduced to be a continuously charged polymer that is surrounded by two layers of ions. The counterions of the electrolytic solution condense to the DNA backbone within a distance called Bjerrum length l_B . At this distance the electrostatic interaction between two ions is comparable in magnitude to the thermal energy scale $k_B T$ with $k_B =$ Boltzmann constant and $T =$ temperature. For double-stranded DNA in water at 25°C $l_B = 0.714$ nm [16]. Cations and Anions build the second shell

of loosely bound ions. Due to the fact that there exist three hydrogen bonds between CG base pairs compared to two between AT base pairs, double-stranded DNA with a higher percentage of CG pairs is more stable than with a lower CG content [17]. Further factors that influence the stability of double-stranded DNA are the base sequence because of sequence specific base stacking and the total length of the DNA strand. The melting temperature of a specific DNA strand gives information about its stability. When a double-stranded DNA molecule is heated in solution, the absorbance at 260 nm increases about 40 % because of single strand formation. This effect which is called melting hypochromicity is due to the dissociation of the hydrogen bonds between the Watson-Crick base pairs. The hydrogen bonds in double-stranded DNA limit the resonance of the aromatic rings and therefore the absorbance. A typical absorbance versus temperature curve, a so-called melting curve, for double-stranded DNA is S-shaped due to the sharp phase change from double to single strands. The temperature at the midpoint of the absorbance transition is the melting temperature T_m . At this temperature T_m 50 % of the DNA strands exist in a double-stranded DNA configuration. An equation for the calculation of T_m in $^{\circ}C$ that includes the nearest neighbor thermodynamic parameters for Watson-Crick base pairs is given by

$$T_m[^{\circ}C] = \frac{\Delta H^{\circ} \cdot 1000}{\Delta S^{\circ} + R \cdot \ln(C_T/4)} - 273.15, \quad (1.1)$$

with ΔH° = changing enthalpy in kcal/mol, ΔS° = changing entropy, R = gas constant 1.9872 cal/(K·mol), and C_T = total molar strand concentration [18]. Since T_m is a parameter for the stability of DNA, it is dependent on both the base sequence and the solvent. Single strand melting curves give information about the thermodynamics and cooperativeness of base stacking. With increasing temperature the absorbance increases slightly due to decreasing stacking which is dependent on the enthalpy of stacking. In melting curves of duplex DNA, in addition to base stacking, base pairing influences the shape of the transition from which the base composition heterogeneity can be determined [2].

Single stranded DNA can be described by one of the simplest models of an ideal polymer: the freely jointed chain (FJC) model [19]. In this model, the DNA strand is considered as a flexible polymer consisting of n bond vectors \vec{r}_i ($1 \leq i \leq n$) with a constant length l connecting $n + 1$ points A_i . The angle between two bond vectors \vec{r}_i and \vec{r}_j is indicated by θ_{ij} . Under the assumption of an ideal chain there are no interactions between two farther points even if they can share the same space at the same time. The end-to-end vector \vec{R}_n can be written as

$$\vec{R}_n = \sum_{i=1}^n \vec{r}_i. \quad (1.2)$$

If there is no restriction in the bond vector orientations, the average end-to-end vector is $\vec{R}_n = 0$. In contrast, the mean-square end-to-end distance $\langle R^2 \rangle$ is

$$\langle R^2 \rangle = \sum_{i=1}^n \sum_{j=1}^n \langle \vec{r}_i \cdot \vec{r}_j \rangle = l^2 \sum_{i=1}^n \sum_{j=1}^n \langle \cos \theta_{ij} \rangle. \quad (1.3)$$

In the FJC model, there are no correlations between the directions of different bond vectors and therefore $\langle \cos \theta_{ij} \rangle = 0$ for $i \neq j$. In the equation for the mean-square end-to-end distance,

only terms for $i = j$ remain. In this case $\theta = 0$ and $\cos \theta_{ij} = 1$ which results in

$$\langle R^2 \rangle = l^2 n \quad (1.4)$$

for the mean square end-to-end distance of a single stranded DNA assuming the FJC model. The mechanical properties of a double-stranded DNA molecule can be described by the worm-like chain model (WLC) or Kratky-Porod model which is a good model for very stiff polymers. As the FJC model, the WLC model is an ideal chain model, where the interactions between monomers separated by a long distance are ignored. It is a special case of the freely rotating chain model, where all bond lengths and bond angles of the monomers are constant, while all torsion angles are equally likely. The mean-square end-to-end distance $\langle R^2 \rangle$ of the polymer is then given by

$$\langle R^2 \rangle = nl^2 \cdot \frac{1 + \cos \theta}{1 - \cos \theta} \quad (1.5)$$

with the number of bonds in the chain backbone n , the length of each backbone bond l and the bond angle θ . The maximal end-to-end distance of the chain is called contour length:

$$R_{max} = nl \cdot \cos \left(\frac{\theta}{2} \right). \quad (1.6)$$

For stiff polymers like a double-stranded DNA, the values of the bond angle θ are very small ($\theta \ll 1$) and therefore $\cos \theta$ can be expanded to $\cos \theta \cong 1 - \frac{\theta^2}{2}$. For the persistence segment s_p of the chain which is the scale at which local correlations between bond vectors decay and for the persistence length l_p which is the length of the persistence segment, we get

$$\langle s_p \rangle = -\frac{1}{\ln(\cos \theta)} \cong \frac{2}{\theta^2}. \quad (1.7)$$

$$\langle l_p \rangle = s_p l = l \frac{2}{\theta^2}. \quad (1.8)$$

The persistence length of double-stranded DNA is $l_p \approx 53 \text{ nm}$ [20]. A further characteristic parameter is the Kuhn length b of a polymer which is the effective bond length of an equivalent chain with the same $R_{max} = Nb$ and the same $\langle R^2 \rangle = Nb^2$ as the actual polymer. In the WLC model, b becomes twice the persistence length:

$$b \cong 2l_p. \quad (1.9)$$

Thus in a double-stranded DNA the Kuhn length is $b \approx 106 \text{ nm}$ [20]. The mean-square end-to-end distance in the WLC model can be written as

$$\langle R^2 \rangle = 2l_p R_{max} - 2l_p^2 \left(1 - \exp \left(-\frac{R_{max}}{l_p} \right) \right). \quad (1.10)$$

For chains that are much longer than their persistence length, $\langle R^2 \rangle$ becomes $\langle R^2 \rangle \cong bR_{max}$ and for chains that are much shorter than their persistence length, $\langle R^2 \rangle \cong R_{max}^2$ [19, 21].

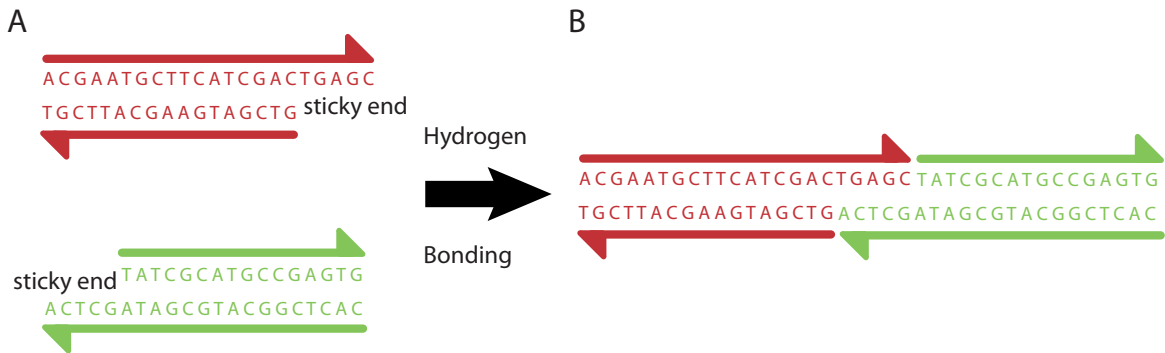


Figure 1.2: Sticky-end hybridization. Two double-stranded DNA strands (red and green) with single stranded overhangs that are complementary to each other, cohere in solution via hydrogen bonding to one double-stranded DNA molecule.

1.2 Structural DNA Nanotechnology

1.2.1 DNA as Building Material

Since Watson and Crick resolved the structure of DNA in the 1950s, nucleic acid was finally known as the carrier of genetic information. Three decades later, Nadrian Seeman was a pioneer in thinking about DNA in a non-biological context, using DNA as a molecular building material. This was the beginning of the fast expanding field of structural DNA nanotechnology. The DNA molecule is a perfect material that combines many important prerequisites for the use in nanotechnology: size, stiffness of double strands, selective hybridization, stability of branched molecules, programmability, and convenient synthetic producibility [1, 22]. Furthermore, the biocompatibility of DNA constructs plays a crucial role for medical applications [23].

Size and Stiffness

As described in the previous chapter, the DNA molecule possesses with its diameter of 2 nm and its helical pitch of 3.5 nm the adequate size and with a persistence length of 53 nm for double-stranded DNA the required stiffness for constructs in the small nanometer range [13, 20]. By connecting multiple DNA strands, rigid DNA structures with dimensions of several hundred nanometers up to 3D crystalline lattices can be built [24–30].

Hybridization

The highly selective hybridization of two complementary DNA strands is indispensable for the self-assembly process in structural DNA nanotechnology. In principle, every base can hybridize with all the other bases, but the energetically favored constellation is the Watson-Crick base pairing of A with T and G with C which is the driving force for bottom-up self-assembly into the programmed structure. Two double-stranded DNA molecules can be combined along their helical axis by using so-called 'sticky ends'. This has been used for over 40 years in *in vitro* genetic engineering: the single stranded overhang of a double-stranded DNA molecule coheres with the complementary single stranded overhang of a second DNA molecule via hydrogen bonding between the sticky ends [31, 32] (see figure 1.2). The intermolecular association process and the crystal structure of the resulting double-stranded DNA complex is

completely predictable and specific for the DNA molecule. In contrast to other intermolecular affinities like antibody - antigen complexes, the relative three-dimensional orientation of each cohered DNA pair is known a priori without crystalline analysis which is necessary for other molecules. Furthermore, the number of possible sticky end sequences is 4^n for n single stranded bases at the sticky ends. This leads to a high diversity of possible sequences that can be programmed.

Stability of Branched DNA

Since the cohesion of two sticky ends of DNA molecules results in a longer but linear one dimensional line, a second important prerequisite for using DNA in structural nanotechnology is needed: stability of branched DNA. To create DNA constructs in multiple dimensions, programmed branched DNA molecules must self-assemble via hybridization into lattices and compact structures. In 1964, Robin Holliday described a motif of branched DNA in nature in his article about *a mechanism for gene conversion in fungi* [33]. A four-armed branched junction, called Holliday junction, occurs in the process of genetic recombination, when homologous chromosome pairs exchange adjacent sequences by crossing over each other to pass genetic diversity onto the next generation. In a Holliday junction, four DNA strands are linked together to form four double helical arms flanking a branch point (see figure 1.3 A). Due to sequence symmetry of homologous chromosomes in the process of recombination, the branch point of the four arm junction of biologically derived branched DNA can migrate throughout the molecule [34]. This movement is called branch migration. To avoid the dynamic process of branch migration in static DNA constructs, synthetic DNA nanotechnology has the advantage that the sequences can be designed to be asymmetric in the vicinity of the branch point. Furthermore, the synthesis of oligonucleotides allows for the construction of DNA complexes with three-armed or multi-armed branched junctions [10, 35]. If connecting multiple Holliday Junctions via sticky ends, the extension to an infinite lattice in two and three dimensions can be created (see figure 1.3 A) [10, 36].

Programmability and Convenient Synthetic Producibility

The programmability of DNA sequences is one of the major advantages of structural DNA nanotechnology. This allows the design and the synthesis of DNA molecules of arbitrary sequences that cohere into determined structures [37]. The possibility to synthesize convenient oligonucleotides of almost every sequence is just restricted by the length of the DNA strands. Because of the error rate per synthesized nucleotide, affordable synthetic producibility is given for oligonucleotides with up to 60 nucleotides. However, even longer DNA strands can be commercially synthesized, although with decreasing yield and higher costs. Until today the field of DNA nanotechnology has extended from controlling the formation of DNA complexes of arbitrary shapes to the functionalization of such DNA structures by modified oligonucleotides, e.g. via biotinylated, fluorescently labeled or amino modified oligonucleotides which are commercially available. These options support the fast growth of the field [38–40].

The first artificial DNA structure in DNA nanotechnology that combined the above mentioned prerequisites was a cube-like construct that the group of Nadrian Seeman developed in 1991[41]. This branched structure consisted of six single strands which each hybridized to four neighbors, thereby forming double-stranded edges (see figure 1.3 B). The same group also assembled a truncated octahedron with each edge again corresponding to two turns of double-stranded DNA [42]. Since then, several polyhedra like DNA buckyballs and many kinds of deltahedra like tetrahedra, octahedra, and icosahedra have been developed [24, 43–45]. The combination of right handed B-DNA junctions with left handed Z-DNA junctions enabled the

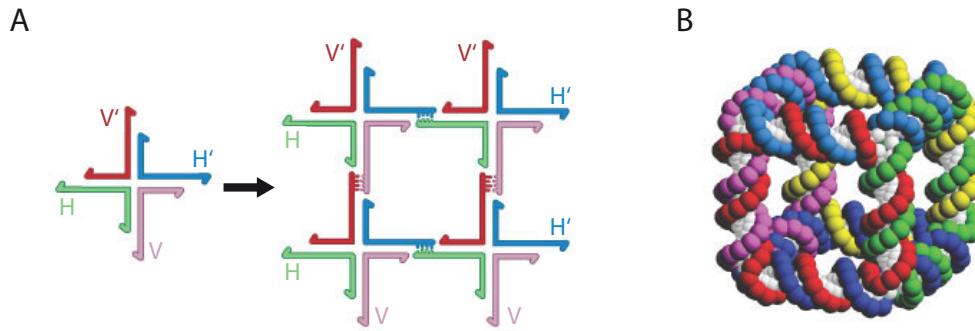


Figure 1.3: Self-assembly of DNA molecules. **A** Formation of a 2D crystal by hybridization of Holliday junction forming DNA molecules via sticky-end overhangs. **B** Self-assembly of six single DNA strands to the first artificial DNA structure created by Seeman in 1991. Reprinted by permission from Macmillan Publishers Ltd: Nature ref. [22], copyright 2003.

construction of Borromean rings from DNA [46]. The design of motifs that are less floppy than these individual branched junctions was the initial step towards stable two-dimensional arrays. The DNA double crossover (DX) molecule is characterized by the crossover of a DNA strand that exchanges between two strands of opposite polarity [47, 48]. This enabled robust connections between several DNA helices. Compared to a linear duplex DNA, the persistence length of the DX molecule doubles [49]. A modification of the DX motif is the DX+J motif with an extra domain perpendicular to the plane. This enables the creation of patterns which can be visualized by atomic force microscopy. One more modification is the three-domain DNA triple crossover (TX) complex that connects three DNA helix axes by one strand in one plane [50]. Using rigid DX or TX tiles, regular two-dimensional arrays could be created by sticky-ended cohesion of several molecules [36, 50, 51]. Alternating combinations of DX and DX+J tiles formed regular stripe-like patterns. The extension of two-dimensional to three-dimensional lattices was done by crystallization of tensegrity triangles [52, 53]. Associated with sticky ends, these tensegrity triangles self-assembled into three-dimensional crystals in the macroscopic range. This was the first step towards the original intention to use DNA constructs as a scaffold for the organization of biological macromolecules for X-ray crystallographic structure analysis. Although this specific goal has not been reached yet, DNA nanotechnology is used in many different fields to arrange other species of molecules with high spatial accuracy. The DNA origami technique that Paul Rothemund invented as a very robust method for DNA self-assembly plays a crucial role in this development and will be addressed in detail in the next paragraph [54]. Another technique uses single stranded DNA tiles and blocks that self-assemble into arbitrary two and three-dimensional shapes [55–57]. Proteins are often in the focus of interest when DNA arrays and DNA origami structures are used as templates to arrange and observe molecules and their interactions [58–64]. In recent years, the use of DNA constructs for the precise organization of metallic nanoparticles for applications in nanophotonics and nanoelectronics emerged [65–71]. Also, DNA structures can be labeled with fluorophores to record dynamic processes by fluorescence resonance energy transfer (FRET) spectroscopy [39]. In single-molecule spectroscopy and super-resolution microscopy, DNA origami constructs are often used as templates to arrange fluorescent dyes with nanometer precision in distinct distances [40, 72–76]. During the last years, the relevance of structural DNA nanotechnology for nanomedicine developed rapidly. It has been shown

that DNA structures can act as promising carriers for biomedical applications like the delivery of drugs, antibodies or in immune therapy [38, 77–85]. Apart from complex DNA structures which serve as templates and scaffolds, there exist DNA devices that undergo specific structural transitions due to their sequence dependence. Devices like molecular tweezers, DNA walkers and molecular DNA circuits are often driven by processes such as branch migration and strand displacement using the toehold principle [86–89].

1.2.2 The DNA Origami Method

In 2006, Paul Rothemund's publication about a new technique called 'DNA origami' revolutionized the field of structural DNA nanotechnology by increasing the complexity and size of self-assembled DNA structures [54]. The term 'origami' comes from the Japanese words 'ori = folding' and 'kami = paper' and describes the traditional Japanese art of paper folding. Analogous to a sheet of paper being folded into an object, the original DNA origami method uses the 7249 nt single stranded viral DNA derived from the bacteriophage M13 as a scaffold strand that is folded into shape by hundreds of shorter oligonucleotides, so-called 'staple strands'. The idea of using a scaffold strand and short helper strands had already been reported by Hao Yan and William Shih, but the impact of Rothemund's technique resulted from the surface area of roughly 100 nm in diameter that is highly addressable with a spatial resolution of 6 nm and from the simplicity of the method, resulting in high yields of up to 90 % [45, 90]. Unlike for single stranded DNA assemblies, the stoichiometry and the purity of the individual oligonucleotides is not crucial. In his publication Rothemund presented diverse two-dimensional DNA structures of arbitrary shapes such as squares, stars and disks that self-assembled in a one-pot reaction (see figure 1.4 A). He also showed the markability by extending distinct staple strands by dumbbell shaped hairpins protruding at predetermined positions on the surface of a structure which created complex patterns such as words and images that could be visualized by atomic force microscopy (AFM). Furthermore, the formation of larger assemblies by multimerization of single DNA origami constructs was reported.

In 2009, after a period of three years where DNA origami structures in two dimensions had been developed by several groups [65, 94], Douglas and co-workers extended the technique to build three-dimensional objects by stacking sheets of parallel helices (see figure 1.4 B)[24]. Each inner helix is connected to three neighbors by crossovers of the staple strands in distances of multiples of seven nucleobases. This leads to angles of 240° , 120° and 0° between the crossovers when assuming that one helical turn of 360° of B-form DNA consists of 10.5 bases. The alignment of the helices results in a honeycomb lattice. It was also a group around Douglas that developed the software caDNAno, a graphical interface-based computer-aided design program that allows for the design process and staple strand sequence generation for DNA origami objects in an user-friendly way [95]. The helices can also be arranged in a square lattice to form three-dimensional shapes in which one helix is connected to four neighbors [96]. In this formation, the crossovers are separated by multiples of eight bases which causes a general twist in the structure that can be corrected by manually inserted deletions. A further concept to build structures of three-dimensional shapes is to connect flat DNA origami sheets at their edges. Andersen et al. demonstrated this principle by constructing a DNA origami box with a controllable lid (see figure 1.4 D)[39]. In contrast to the use of a single stranded scaffold for DNA origami assembly, the group of Shih demonstrated the assembly of two different structures from a double-stranded scaffold source in a one-pot an-

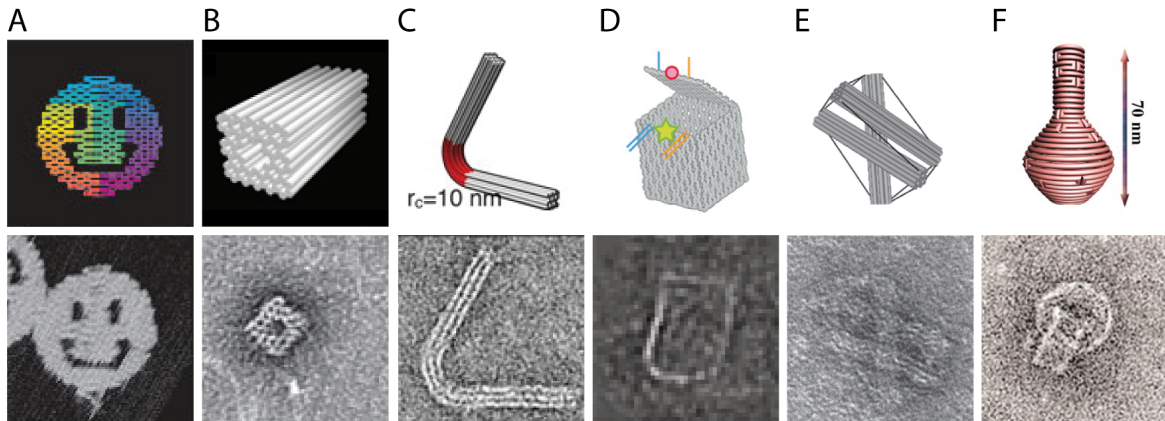


Figure 1.4: DNA origami structures. Top: Schemes of structure designs. Bottom: Resulting structures as imaged by AFM (A) and TEM (B-F). The sizes of the structures are 30 nm - 100 nm. **A** One of the first examples of the DNA origami method developed by Rothemund: disk with three holes. Reprinted by permission from Macmillan Publishers Ltd: Nature ref. [54], copyright 2006. **B** Three-dimensional structure by Shih and co-workers. Reprinted by permission from Macmillan Publishers Ltd: Nature ref. [24], copyright 2009. **C** Curved structure by Dietz et al.. From ref. [91]. Reprinted with permission from AAAS. **D** DNA box with controllable lid by Andersen et al.. Reprinted by permission from Macmillan Publishers Ltd: nature ref. [39], copyright 2009. **E** Tensegrity design by Liedl et al.. Reprinted by permission from Macmillan Publishers Ltd: Nature Nanotechnology ref. [92], copyright 2010. **F** Nanoflask by Yan and co-workers. From ref. [93]. Reprinted with permission from AAAS.

nealing reaction [97]. The development of targeted insertions and deletions of base pairs into DNA origami structures enabled the formation of twisted and curved objects with a minimal radius of curvature of 6 nm (see figure 1.4 C)[91]. Recently, the group of Yan demonstrated the self-assembly of DNA origami structures with complex high curvatures in three dimensions by designing objects like a nanoflask (see figure 1.4 F)[93]. A different tool for building three-dimensional DNA origami structures was presented in 2010, when Liedl and co-workers reported the assembly of so called DNA tensegrity structures which use single stranded parts of the scaffold as entropic springs connecting rigid DNA origami beams under tension (see figure 1.4 E)[92]. Several groups showed that the DNA origami technique can also be used to create larger two-dimensional DNA arrays. Different approaches have been reported: a jigsaw puzzle design [26], DNA origami tiles ordered by preformed scaffold frames [29], a symmetric cross-like assembly [98], super-sized DNA origami sheets using a longer scaffold [28] and crystallization of DNA origami sheets with loop arrangements [30].

The achievement to be able to control various DNA origami objects of almost arbitrary shapes in two and three dimensions paved the way to proceed from structural to functional investigations. The increasing accessibility of the DNA origami technique for interested nanotechnology groups supported the fast growth of the scientific community developing DNA origami structures for several applications. One of the first applications used a flat DNA origami structure as a molecular sensor. The attachment of biologically relevant RNA targets to staple strand extensions led to protrusions detectable by AFM [99]. The ability to place molecules on an origami structure at predicted positions was exploited to investigate the distance dependence

of aptamer-protein binding [61]. Moreover, the spatial resolution of DNA origami surfaces was used for super resolution microscopy and single-molecule spectroscopy of fluorescent dyes that had been attached at distinct positions [40, 72–74, 76]. In chapter 3, a more detailed discussion on this can be found. Also, the conjugation of various kinds of nanoparticles by chemical modifications was shown by several groups. The high addressability of DNA origami objects was exploited to attach objects like silver nanoparticles, gold nanoparticles, carbon nanotubes and quantum dots [65, 66, 71, 100, 101]. Furthermore, the total metallization of DNA origami structures could be shown by using methods like gold enhancement or chemical crosslinking reagents [70, 102]. More recently, the development of DNA origami structures for biomedical applications came into focus. In *in vitro* as well as in *in vivo* studies it could be shown that DNA origami constructs represent efficient carrier systems for immunostimulants, cancer therapeutics and antibodies [80, 82, 84, 85]. In chapter 3 one of the first publications in this field is described in detail. The invention of high-speed AFM enabled the monitoring of molecular dynamics on DNA origami platforms such as the conformational switching of a G-quadruplex structure, the reversible hybridization of photoresponsive oligonucleotides or the site-selective targeting of specific locations in a DNA origami frame via zinc-finger protein adaptors [64, 103, 104]. Several groups have reported on the programmed motion of so-called 'molecular DNA walkers' or 'spiders' on one dimensional tracks made from DNA origami tiles. These objects show enzyme driven movement or can pick up cargos [105–107].

The working flow from design to millions of equal copies of a DNA origami structure includes the following steps: 1. determination of target shape by approximation with cylindrical model where cylinders represent double-stranded DNA, 2. routing of scaffold strand through structure and sequence determination of staple strands, 3. scaffold strand preparation and staple strand synthesis, 4. annealing process of staple and scaffold strands in salt-containing aqueous buffer, 5. purification and analysis of folded DNA origami structures by filtration, gel electrophoresis, transmission electron microscopy (TEM) or AFM [54, 108].

The first step in structural DNA origami design is to define the exact functions for the intended application that the structure should fulfill while considering the minimal complexity. This potentially increases the yield and decreases the annealing times. DNA origami constructs can consist of a single layer as well as of multiple layers. In multilayer DNA origami structures the helices are arranged on a honeycomb lattice, square lattice, closed-packed hexagonal lattice or on a combination thereof [24, 96, 109]. The helices can be curved, twisted and rolled up [91, 93]. In tensegrity structures the helices are under tension and pressure [92]. Using the software caDNAno, the target shape is approximated by selecting a scaffold strand routing that passes between neighboring helices along antiparallel crossovers at defined positions (see figure 1.5 A, B)[95]. In a next step, the program assigns staple strand paths that are complementary to the scaffold path. The staple strand paths are broken by hand into shorter segments that are 21 nt to 50 nt long. Oligonucleotides of this lengths are synthesizable in an adequate manner, taking costs into account. Staple strands shorter than 18 nt do not bind stably at room temperature. The distances of the staple strand crossovers vary, depending on factors like size, shape and function of the desired structure. To prevent stacking effects between individual DNA origami structures, many designs have unpaired scaffold strand loops at the end of the helices. The sequence of each single staple strand is then generated depending on the desired variants of the M13mp18 scaffold strand. To predict the three-dimensional structure of a designed object, the computational framework CanDo can be used that models base pairs as two-node beam finite elements representing an elastic rod [108]. The staple

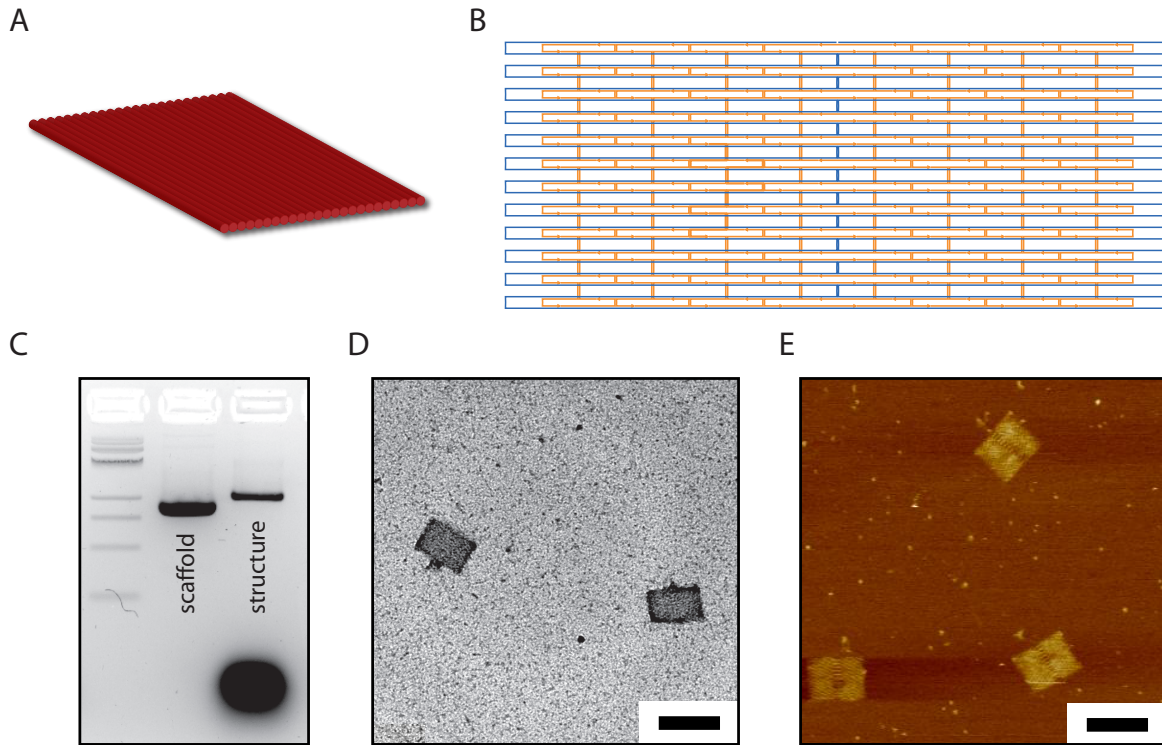


Figure 1.5: Design and analysis of a rectangular DNA origami structure. **A** Scheme of a DNA origami structure consisting of 24 DNA helices arranged in a square lattice. **B** Design of the DNA structure using the *caDNAno* software. The scaffold strand is shown in blue, the staple strands in orange. **C** Gel analysis of the DNA origami structure. Left to right: 2-log 1 kb DNA ladder, m13mp18 scaffold strand, assembled DNA origami structure with the 10x excess of staple strands in the fastest band. **D** Electron micrograph of DNA origami structure. **E** AFM image of DNA origami structure. Scale bars: 100 nm.

oligonucleotides as well as the single stranded, M13mp18-derived scaffold DNA can be purchased from various vendors. The different versions of the scaffold strand can also be prepared by growing and collecting phages with subsequent purification of the genomic DNA. For the annealing process, it is crucial to choose appropriate salt concentrations. During the annealing procedure, the desired Watson-Crick base pairs are formed only if this minimizes the free energy of the system. Due to electrostatic repulsion of the negatively charged DNA strands in the structure, this is highly dependent on the salt concentration of the folding buffer. In a common assembly solution, the scaffold strands are mixed with a staple strand excess of about 5 to 10 fold in pH-stabilizing buffer containing magnesium chloride (MgCl_2) [54]. It has been shown that instead of divalent magnesium ions also monovalent sodium ions can be added [110]. In a next step, the mixture is heated up to approximately 80°C to denature potential secondary structures of the single DNA strands before the solution is cooled down to room temperature over the course of a few hours or even days. This thermal annealing time depends on the complexity of the DNA origami structure: while monolayer objects can assemble within one hour, multilayer and tensegrity constructs need several days for folding [24, 92]. Beside the conventional thermal annealing, isothermal assembly using chemical dena-

turing agents was demonstrated [111]. In a recent study the rapid folding of multilayer DNA origami objects at constant temperature has been reported [112]. After the annealing process, the self-assembled DNA origami structures can be purified by various methods, separating excess staple strands, mis-folded and aggregated objects. Filters with distinct pore sizes can be used to remove unbound staple strands. However, one should take into account that this filtering technique is only suitable for structures folded with high yield because no selection of degraded material can be done. Analysis with subsequent purification of well-folded DNA origami objects can be achieved by agarose gel electrophoresis (see figure 1.5 C). The applied voltage causes migration of the negatively charged DNA structures and excess staple strands, depending on their length and compactness. Aggregates, multimers as well as defective structures migrate at lower speed than faultless, monomeric DNA origami constructs. The later can be found in the fastest band of the gel after staining if the well-defined line built by the excess staple strands is not considered. The intensity distribution of the bands gives information about the yield after the annealing process. The desired band can be excised and the DNA objects be recovered by centrifugation through a filter from the excised gel slice [24]. A more gentle method for sensitive structures is their extraction from the gel by cutting an elution well in front of the band of interest which is filled with a viscous sucrose solution. After applying voltage again, the DNA origami objects migrate into the sucrose solution from which they can be collected [113]. Beside purification via gel electrophoresis, rate-zonal centrifugation is a further purification technique that recovers DNA origami products without residual agarose gel fibers [114].

Purified DNA origami objects are characterized by AFM or TEM imaging. Further techniques that prevent labile DNA objects from potentially disruptive sample fixation are dynamic light scattering (DLS) and small-angle X-ray scattering (SAXS). The hydrodynamic radius estimated by DLS as well as the scattering data can be compared to values obtained by atomic model calculations [39].

Transmission Electron Microscopy

A commonly used method to visualize single DNA origami objects which are about 100 nm in size is TEM (see figure 1.5 D). Due to the resolution limit proposed by Ernst Abbe, light microscopy is not suitable because the minimal distance d between two resolvable objects is restricted to

$$d = \frac{1.22\lambda}{2NA} \quad (1.11)$$

with λ = wavelength and NA = numeric aperture. The wavelength of visible light is in the range of 400 nm - 700 nm which results in an approximated resolution limit of about 200 nm. For that reason, electron microscopy represents an appropriate technique for imaging DNA origami. According to Louis de Broglie, the material wavelength of an electron λ_e is dependent on its kinetic energy E :

$$\lambda_e \approx \frac{h}{\sqrt{2m_0E(1 + \frac{E}{2m_0c^2})}} \quad (1.12)$$

with h = Planck constant, m_0 = electron rest mass, c = speed of light. The acceleration of an electron by an applied voltage U of about 80 - 100 kV which is a common voltage used in TEM imaging for biological samples, shows a kinetic energy $E = e \cdot U$ and therefore results in a wavelength of about 4 pm. Even higher voltages can be applied for less sensitive sam-

ples. From this, the approximated theoretical resolution in vacuum is 2 pm which can not be reached in electron microscopes due to intrinsic imperfections of the electron lens system that lead to spherical and chromatic aberrations. At present, the best resolution achieved by using a highly coherent focused electron probe in an aberration-corrected TEM is 50 pm [115]. The beam of electrons is emitted from a filament by thermionic emission into vacuum to prevent uncontrolled deflection of electrons by molecules. A condenser lens forms the beam, while the objective lens focuses the beam that comes through the sample, before a projector lens expands the beam onto a phosphor screen or charge-coupled device (CCD) camera after reducing the electron intensity by translating it via a scintillator into light. The beam electrons are diffracted by the atoms of the specimen due to Rutherford scattering and thus contain the atomic information about the sample. The scattering effect is proportional to the square of the atomic number. This is the reason for the negative staining of DNA origami samples with heavy ions such as uranyl acetate which increase the contrast. The disadvantage of negative staining TEM imaging is the dehydration of the samples which might cause some structural changes in the DNA origami objects. To circumvent this problem for accurate structure determination in a pseudoatomic model, cryo-electron microscopy can be used [116]. For this purpose, the DNA origami sample is plungefrozen in liquid ethane to prevent water crystallization and to preserve the structure in a frozen-hydrated state.

Atomic Force Microscopy

The second imaging method for the visualization of DNA structures is AFM which is a scanning probe microscopy technique (see figure 1.5 E)[117]. The resolution of AFM is like for TEM in the subnanometer regime. The basic working principle of an AFM is to scan the surface of the sample by a tip that has a curvature radius in the nanometer range. The AFM image in figure 1.5 E is taken by using a tip with a radius of curvature of 2 nm - 3 nm. The tip is attached to a flexible cantilever reflecting a laser beam dependent on the cantilever deflection while scanning the surface. The position of the reflected laser beam is detected on two or four closely spaced photodiodes and then translated into an image. In most scanning modes, a feedback mechanism maintains the distance between tip and sample which is mounted on a piezoelectric element at a constant level to prevent damage. Depending on the constitution of the specimen, distinct imaging modes can be chosen: contact mode, non-contact mode and intermittent contact mode. For DNA origami structures as well as for most biological samples, the intermittent mode is used. Therefore, the negatively charged DNA origami structures are immobilized onto a also negatively charged mica surface by using positively charged magnesium ions as screening intermediate layer. In intermittent mode, the cantilever is externally excited to oscillate during scanning the surface with a frequency close to its resonance frequency and with an amplitude of about 100 nm - 200 nm. When the tip approaches the sample, force interactions like Van der Waals forces, dipole-dipole interactions and electrostatic forces occur. Thereby the amplitude of the cantilever oscillation is damped and thus serves as feedback mechanism to adjust the distance between sample and tip by maintaining the set oscillation amplitude. The information about the damping of the cantilever oscillation is used to create a height profile of the scanned area and thus an image can be generated.

2 Single-Molecule FRET Ruler Based on Rigid DNA Origami Blocks

Theodor Förster's ground-breaking theory of fluorescence resonance energy transfer (FRET) was published in the 1940s. Since then, FRET measurements have been used as a powerful tool in several scientific fields such as life sciences, drug development and medicine and the continued growth of new applications in these areas can be expected. In the past, the inverse sixth power distance dependence of FRET was experimentally confirmed by using a donor dye and an acceptor dye separated on several spacer molecules such as polyproline or double-stranded DNA. In the first part of this chapter a three-dimensional rigid DNA origami structure is introduced that serves as a reliable FRET ruler on the single-molecule level. In the second part, structural changes within a two-dimensional DNA origami object in the presence of magnesium ions are investigated by using the high spatial resolution of single-molecule FRET measurements.

2.1 Single-Molecule FRET Measured by ALEX

Single-molecule fluorescence studies enable the investigation of individual subpopulations without time or ensemble averaging. In contrast, ensemble measurements require e.g. synchronization of the molecules to get an information about event developments over time [118]. FRET measurements on the single-molecule level allow the determination of the efficiency of the energy transfer between each single FRET pair per particle. By positioning two suitable chromophores within a short distance of 15 nm, FRET can be observed after excitation by light with a distinct wavelength. Described by the theory of Theodor Förster, a so-called donor dye in its electronic excited state transfers the excitation energy non-radiatively to an acceptor dye via induced dipole-dipole coupling [119]. Hereupon, the acceptor molecule releases the energy by emitting a photon. In general, the energy and therefore the wavelength of the emitted photon of the acceptor dye is red-shifted compared to the excitation wavelength of the donor dye. For the non-radiative FRET, the emission spectrum of the donor molecule has to overlap with the absorption spectrum of the acceptor molecule (see figure 2.1 A). Beside FRET between two different types of donor and acceptor fluorophores, in many biological systems two or more chromophores of the same type can transfer energy without a red-shift from excitation to emission wavelength. One example is the absorption of photons by photosynthetic pigments in light-harvesting complexes (LHC) that are located around the reaction center of a photosystem in specific cells. The excitation energy is transferred by FRET within

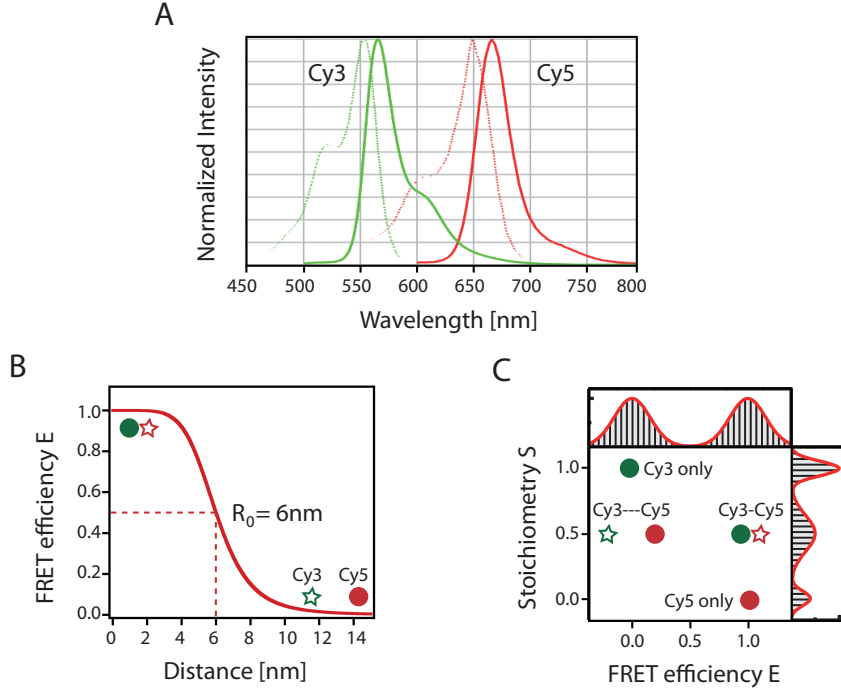


Figure 2.1: FRET measured by ALEX. **A** Absorption (dashed lines) and emission (solid lines) spectra of donor Cy3 (green) and acceptor Cy5 (red). The emission spectrum of Cy3 overlaps with the absorption spectrum of Cy5 while both emission spectra are well separated. **B** The FRET efficiency E is highly dependent on the distance between donor Cy3 (green) and acceptor Cy5 (red). At distance $R_0 = 6$ nm, half of the energy is transferred from the donor to the acceptor molecule ($E = 0.5$). **C** E - S histogram for four different labeled populations: donor Cy3 (green) only ($E = 1$, $S = 0$), acceptor Cy5 (red) only ($E = 0$, $S = 1$), Cy3-Cy5 FRET pair separated by a long distance ($E = 0$, $S = 0.5$) and Cy3-Cy5 FRET pair separated by a short distance ($E = 1$, $S = 0.5$).

picoseconds from one pigment molecule to a neighboring molecule toward the reaction center. The FRET efficiency E is defined as the fraction of energy transfer events occurring per donor excitation event and is dependent on the distance R between the molecules (see figure 2.1 B). If $E = 1$, the donor dye always relaxes to its ground state by FRET without photon emission, while for $E = 0$ no energy transfer occurs. E can be written as

$$E = \frac{1}{1 + \left(\frac{R}{R_0}\right)^6}. \quad (2.1)$$

The Förster radius R_0 describes the characteristic distance between a distinct FRET pair at which 50% of the excitation energy is transferred to the acceptor ($E = 0.5$). A typical Förster radius value for a classical FRET pair like Cy3/Cy5 is approximately 6 nm. A quantum mechanical derivation of R_0 is given by:

$$R_0^6 = \frac{9 \cdot \Phi_D \cdot \ln 10 \cdot \kappa^2 \cdot J}{128 \cdot \pi^5 \cdot n^4 \cdot N_A} \quad (2.2)$$

with Φ_D = quantum yield of the donor molecule in absence of the acceptor molecule, n = refractive index of the medium, N_A = Avogadro's number, J = spectral overlap integral of the donor emission spectrum and the acceptor absorbance spectrum and κ^2 = dipole orientation factor which indicates the relative orientation of the donor dipole moment to the acceptor dipole moment. For dye molecules that rotate freely and are isotropically oriented during the lifetimes of their excited states, $\kappa^2 = 2/3$. In most cases this value can be used as a good approximation [120]. Due to the fact that the FRET efficiency E falls with the sixth power of R , FRET measurements are a highly sensitive spectroscopic technique to measure distances in the range of 1 nm - 10 nm. A small distance change around R_0 causes a maximal change in the E -values. The choice of the FRET pair dyes depends on their spectral and photophysical properties like photostability with little intensity fluctuations, high extinction coefficients and high quantum yields that lie in the same range for both dyes. In publication P1, the established FRET pair Cy3/Cy5 is used, with Cy3 as the donor dye with a maximum absorption wavelength at $\lambda_{max}^{ab} = 550$ nm and a maximum emission wavelength of $\lambda_{max}^{em} = 570$ nm and Cy5 as the acceptor dye with $\lambda_{max}^{ab} = 649$ nm and $\lambda_{max}^{em} = 670$ nm (see figure 2.1 A). Both dyes are photostable in oxygen free environments and the Cy3 emission spectrum shows a significant overlap with the Cy5 absorption spectrum, while the emission spectra are well separated by approximately 100 nm. Anti-correlated intensity changes are guaranteed by a quantum yield that is in the same range for Cy3 and Cy5 [121]. Further, the dyes are commercially available in amine reactive forms, which enables the labeling of various molecules. In particular, DNA strands can be internally labeled with Cy3 and Cy5 by synthesis of oligonucleotides with amine-modified thymines. These modified oligonucleotides can be used in DNA origami structures as staple strands. The stability of fluorescent dyes like Cy5 can be greatly enhanced if an oxygen scavenger system like glucose is used together with glucose oxidase and catalase [122]. A further improvement can be reached by addition of reducing agents like Trolox [123]. In publication P1, ascorbic acid and *N,N*-methylviologen are used to prevent fluorescence fluctuations and bleaching according to a reducing and oxidizing scheme that depletes electron triplet states which compete with radiative electron transitions [124].

The apparent FRET efficiency E_{app} can be determined experimentally by measuring ratiometrically the emission intensities of the donor I_D^D and the acceptor I_D^A during donor excitation [125]

$$E_{app} = \frac{I_D^A}{I_D^A + I_D^D}. \quad (2.3)$$

The notation I_X^Y gives the amount of sensitized photons detected in the channel of dye Y while excitation with the laser for dye X. In contrast to E , E_{app} does not include any correction terms depending on background, crosstalk such as leakage and direct excitation, different quantum yields or collection efficiencies of donor and acceptor dyes. The detection of the donor emission in the channel of the acceptor dye emission is termed leakage $le = I_D^A/I_D^D$ and typically accounts for about 10% and 15%. It can be determined via detecting the emission of molecules that are only labeled with a donor dye in the acceptor dye channel. In addition to leakage, the direct excitation $dx = I_D^A/I_A^A$ of the acceptor by the laser that is designed to excite the donor has to be taken into account. The crosstalk corrected value I_{FRET} can then be written as [126]

$$I_{FRET} = I_D^A - le \cdot I_D^D - dx \cdot I_A^A. \quad (2.4)$$

Including the crosstalk between the dyes, E_{app} can be evaluated into E^*

$$E^* = \frac{I_D^A - le \cdot I_D^D - dx \cdot I_A^A}{I_D^A - le \cdot I_D^D - dx \cdot I_A^A + I_D^D} = \frac{I_{FRET}}{I_{FRET} + I_D^D}. \quad (2.5)$$

The detection correction factor $\gamma = \frac{\eta_A}{\eta_D} \cdot \frac{\Phi_A}{\Phi_D}$ represents the relative quantum yields Φ and collection efficiencies η of donor and acceptor and can be estimated from photobleaching events or stoichiometric values of high FRET and low FRET samples determined by alternating laser excitation (ALEX) measurements [121, 126]. Resulting from all correction terms, E is finally given by

$$E = \frac{E^*}{\gamma + E^*(1 - \gamma)}. \quad (2.6)$$

Alternating Laser Excitation

In 2004, Kapanidis, Weiss and co-workers introduced an improved technique for FRET measurements that uses alternating laser excitation (ALEX) for fluorescence-aided molecule sorting and single-molecule analysis of structures and interactions [127]. While diffusing through a confocal detection volume, a single molecule labeled with a FRET pair is excited alternate by both the acceptor excitation wavelength and the donor excitation wavelength. In addition to the FRET efficiency E , the direct excitation of the acceptor dye provides information about the stoichiometric ratio S between the molecules labeled only with a donor dye, only with an acceptor dye or labeled with both. S is defined as

$$S = \frac{I_{FRET} + I_D^D}{I_{FRET} + I_D^D + I_A^A}. \quad (2.7)$$

For donor-only species, $S = 1$ because $I_A^A = 0$, while for acceptor-only species $S = 0$ due to $I_{FRET} = 0$ and $I_D^D = 0$. In contrast, a S -value of 50 % characterizes a molecule that is labeled by exactly one acceptor and one donor dyes. Deviations from this theoretical value of $S = 0.5$ can depend on different photophysical properties of the dyes and variations in their detection efficiencies. Further, S can demonstrate changes in the local environment by reacting sensitive to changes in the brightness of the dye molecules. The representation of E and S -values in a 2D histogram allows the quantitation of sorted molecules together with distance information (see figure 2.1 C). In publication P1, E-S histograms are used to retrieve information about the fraction of the population of DNA origami constructs labeled with both FRET molecules compared to populations with either donor or acceptor molecules only.

2.2 FRET Ruler: Polyproline and Double-Stranded DNA

To prove the Förster theory experimentally, the dependence of the FRET efficiency on the distance was initially measured by several groups while calculating the Förster radius R_0 by equation (2.2). For verification of the R^{-6} -dependence, a molecular spacer was needed on which the fluorophores can be attached in a tunable distance in the Ångström range. In turn, such a FRET ruler can be employed as a tool for the quantification of photophysical or instrumental influences on FRET measurements or, as in publication P1 can be used for the direct determination of the Förster radius R_0 by fitting the FRET curve to experimental

data. Several molecules have been tested to serve as an appropriate spacer between the donor and acceptor dye. Poly-L-proline as well as double-stranded DNA molecules played a crucial role in this process.

Poly-L-Proline Ruler

In 1967, Stryer and Haugland reported that under suitable conditions FRET can be a 'spectroscopic ruler' at distances between 10 Å and 60 Å and confirmed the R^{-6} -dependence of the energy transfer proposed by Förster [128]. In their experimental study oligomers of poly-L-proline were labeled with an α -naphthyl donor group at the carboxyl end of the polypeptide and a dansyl acceptor group at the amino end. Proline is a non-essential heterocyclic α -amino acid that can be polymerized by peptide bonds to form a polyproline helix. The polypeptide used in Stryer's and Haugland's experiments consisted of $n = 5$ to $n = 12$ proline residues that resulted in assumed polymer lengths of 12 Å to 46 Å. The proline helix can be left-handed (poly-Pro II) or right-handed (poly-Pro I) due to *trans* isomers (poly-Pro II) respectively *cis* (poly-Pro I) isomers of their peptide bonds. Due to steric hindrance most amino acids prefer the *trans* peptide bond conformation, but the structure of proline also stabilizes the *cis* form, so both Poly-Pro II helix and poly-Pro I helix can be found under biologically relevant conditions, while the poly-Pro I conformation is rarer than the poly-Pro II. Catalyzed by prolyl isomerase enzymes, *cis-trans* interconversions can occur. Stryer supposed that the oligomers used in the measurements are in the poly-L-proline II *trans* helical conformation and calculated the distances from molecular models assuming a rigid rod for the spacer. Schimmel et al. also characterized polyproline as the stiffest homooligopeptide [129]. The ensemble measurements of Stryer on the FRET efficiencies were done on a recording spectrofluorimeter. The function is given by $E = (R_0/r)^j / [(R_0/r)^j + 1]$ with the fitting parameters j and R_0 . The obtained value for j was 5.9 ± 0.3 which is in perfect agreement with the R^{-6} -dependence of the Förster theory. The Förster radius instead showed a divergence between the observed value of $R_0 = 2.7$ nm and the value $R_0 = 3.5$ nm calculated by equation (2.2), where κ^2 is assumed to be $2/3$ due to measured randomized angular relationships between donor and acceptor during excitation lifetimes.

Over three decades later, Schuler and co-workers revisited polyproline as an appropriate spacer for FRET measurements [130]. In their study, they used longer polypeptides than Stryer consisting of $n = 6$ to $n = 40$ proline residues labeled with Alexa Fluor 488 as donor dye and Alexa Fluor 594 as acceptor dye. Their experimentally observed FRET efficiency values E were higher for long polymers while the efficiencies for short polyprolines seemed to be lower than expected. The low E -values can be explained by $\kappa^2 < 2/3$ due to incomplete orientational averaging during the donor lifetime. Furthermore the size of the fluorophores can not be supposed to be small compared to intermolecular separation resulting in a revision of the point-dipole approximation. The high E -values for calculated long distances indicate that the estimation of polyproline as a rod-like spacer is not given. Instead, due to Langevin molecular dynamics simulations on end-to-end distance distributions, the polymer has to be treated as a semi-flexible chain similar to a worm-like chain with a persistence length of $l_p = 4.4 \pm 0.9$ nm [130]. By using combined single-molecule fluorescence intensity and lifetime measurements, Best and co-workers investigated the effect of flexibility and *cis* residues of polyproline [131]. The simulated l_p value for a poly-Pro II consisting exclusively of *trans* prolines was estimated to be 9 nm - 13 nm which is longer than the experimentally obtained value. This indicated the existence of internal *cis* prolines that occur in about 30% of the molecules in water according to nuclear magnetic resonance measurements and results in higher mean FRET efficiencies

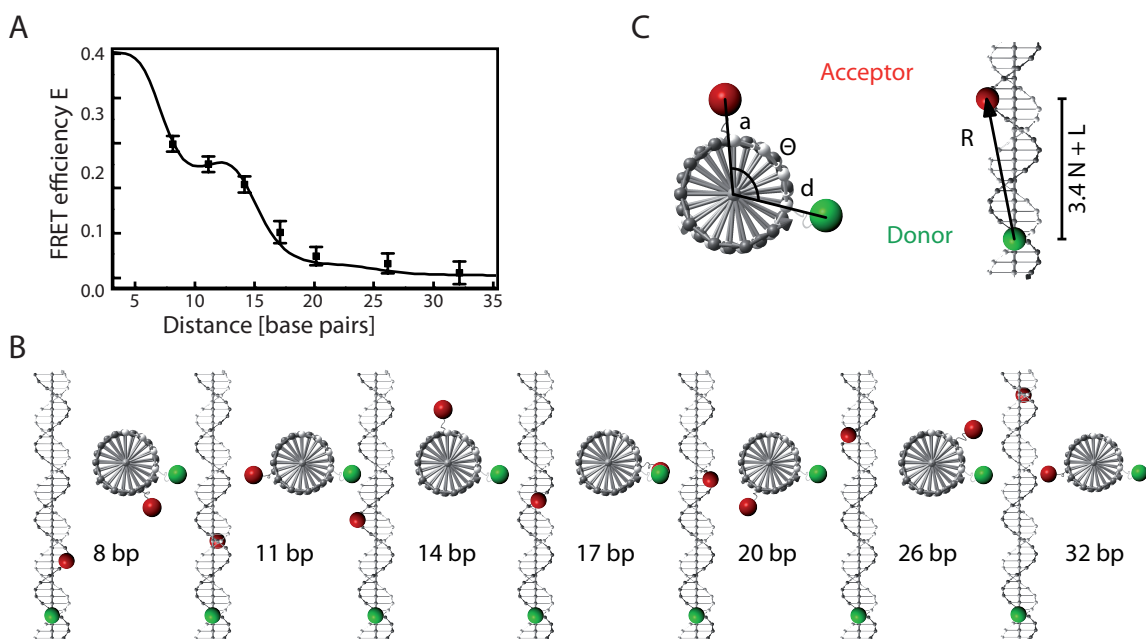


Figure 2.2: FRET Ruler double-stranded DNA. **A** The helical geometry of double-stranded DNA can be observed by measuring the FRET efficiency E dependent on the base pair separation $N = 8$ to $N = 32$ bp. The fit is based on the cylindrical model of double-stranded DNA shown in **C** with the fitting parameters L , $d = a$ and ϕ . R_0 is set to 5.4 nm for the FRET pair Cy3 and Cy5. **B** Schematic representation of side (left) and front (right) view of the base pair separation on double-stranded DNA for $N = 8$ to $N = 32$ bp. **C** Cylindrical model for helical geometry of double-stranded DNA. $|\vec{R}| = R$ is the distance between donor and acceptor dyes, L is the offset of the molecular centers of the dyes in relation to the base plane, d and a are the perpendicular distances of the dyes to the helical axis and ϕ is the cylindrical angle between the dyes.

due to kinks in the polyproline polymer. This finding was confirmed by Doose et al. who probed the structure and dynamics of polyproline via fluorescence quenching by photoinduced electron transfer [132]. In conclusion, these studies showed the unfeasibility of poly-L-proline as a stiff ruler for accurate distance determination.

Double-Stranded DNA Ruler

It has been shown in several studies that measuring FRET is an appropriate technique to investigate nucleic acid structures. The conformation of a Holliday junction in solution was determined to be a right-handed cross of antiparallel molecules by measuring the relative distances between the ends of a four-way DNA junction [133]. The persistence length l_p is about 50 nm for duplex B-form DNA [134] as well as the addressability by fluorophores at varying distances relevant for FRET characterizes the molecule as a rigid regular spacer with a linear geometry to separate donor and acceptor dyes at distinct positions [118, 120, 126, 135, 136]. In 1993, Clegg and co-workers used FRET ensemble measurements to observe the helical geometry of a double-stranded DNA in solution. The donor molecule fluorescein and the acceptor molecule rhodamine were covalently attached to both 5' termini of DNA double helices of several lengths. The number of base pairs and therefore the distance between donor

and acceptor dye varied from eight to 20 bp. The dependence of distance R on the base pair separation due to the helical structure of the DNA molecule is highly non-linear (see figure 2.2 A). The arrangement of the fluorophores nearly perpendicular to the helix axis leads to a maximal dye displacement at a base pair separation of about 11 bp because the dyes point into opposite directions (see figure 2.2 B). While the distance increases rapidly between 5 bp to 10 bp separation, this slope in displacement decreases between 10 bp to 15 bp. To transform the base pair separation into R a simplified schematic model which represents the cylindrical properties of a DNA helix in B-form was developed (see figure 2.2 C). In this model, vector \vec{R} points from the center of the donor dye to the center of the acceptor dye while the distance is given by the length of the vector $|\vec{R}| = R$. R is dependent on five parameters: the number of separating base pairs N , the perpendicular distances of the donor dye d and the acceptor dye a from the helical axis, the offset of the dye plane corresponding to the plane of bases L and the polar angle between the dyes ϕ . The distance is then given by

$$R = \sqrt{(3.4 \cdot N + L)^2 + (d \cdot \sin \theta)^2 + (a - d \cdot \cos \theta)^2} \quad \text{with} \quad \theta = N \cdot \frac{360}{10.5} + \phi. \quad (2.8)$$

In publication P1, the fraction in the term for θ is modified by $\frac{360}{10.5}$ corresponding to a helical pitch of 10.5 bases per turn. Furthermore, the assumption that the fluorophores Cy3 and Cy5 have a linker length in the same order of magnitude leads to the simplification of $a = d$. While N is *a priori* known, the values for a , b , L and ϕ can be determined by fitting the FRET curve by equation (2.1) after measuring the FRET efficiencies E dependent on base pair separation N . Thereby R is substituted by equation (2.8). Due to the large number of fitting parameters, the Förster radius R_0 has to be determined via equation (2.2).

Although Clegg et al. showed that their experimental data are consistent with the R^{-6} -dependence of the FRET efficiencies E , the helical structure of double-stranded DNA prohibits the direct determination of the Förster radius R_0 by fitting the FRET curve without estimation of Φ_D , n , J and κ^2 .

2.3 FRET Ruler: Rigid DNA Origami Structure

The development of the DNA origami technique described in chapter 1 enables the self-assembly of highly addressable DNA origami structures that can be used as breadboards to attach molecules at distinct positions. In publication P1, a DNA origami block consisting of three DNA double-helix layers was designed to serve as a rigid spacer for donor and acceptor dyes for FRET measurements (see figure 2.3 A). The FRET pair fluorophores Cy3 and Cy5 are attached to an internal thymine base of a staple strand via a six carbon linker and point nearly perpendicular out of the DNA origami plane. To achieve a totally flat plane, the DNA origami structure is arranged in a twist corrected square lattice of 14 x 3 helices. The theoretical dimensions of the structure are 57 nm x 28 nm x 6 nm assuming an dehydrated diameter of double-stranded DNA of 2 nm and a base to base distance of 0.34 nm. These values were proven by TEM imaging of annealed and purified DNA origami FRET blocks shown in figure 2.3 B. Integrated intensity profiles of each DNA object reproduced the parallel alignment of the 14 helices and were used for proper width determination (see figure 2.3 C). The histograms in figure 2.3 D represent the measured length and width distributions of the dried DNA origami structures on TEM grids. The ascertained mean values 58.4 ± 1.6 nm x 29.5 ± 1.4 nm at a thickness of 7 nm are in good agreement with the expected values taking into

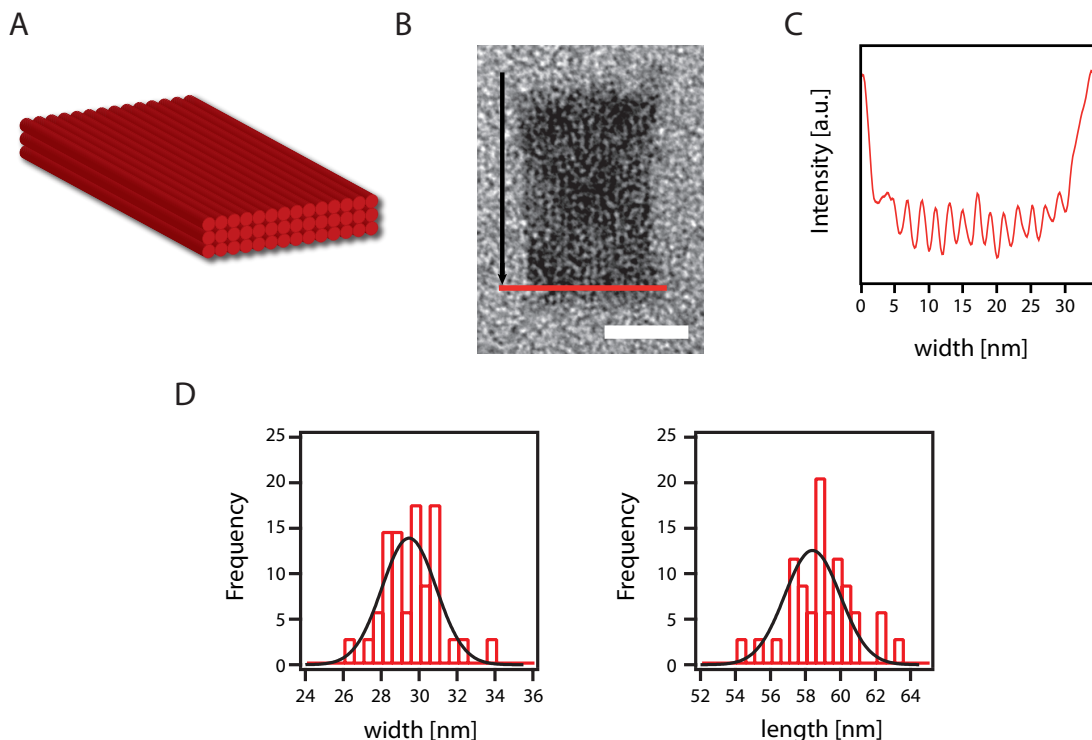


Figure 2.3: Size determination of DNA origami FRET Ruler. **A** Scheme of the DNA origami structure consisting of three layers of 14 parallel helices. **B** TEM micrograph of a typical DNA origami FRET ruler. Scale bar: 20 nm. **C** Integrated-intensity profile of a line orthogonal to the longitudinal axis (red line in B) of the DNA origami structure. **D** Histograms with gaussian fits of the measured width and length distributions of the DNA origami FRET ruler on TEM micrographs. The mean values are 58.4 ± 1.6 nm (length) and 29.5 ± 1.4 nm (width).

account that due to electrostatic repulsion an interhelical gap could occur which is discussed in detail in the following section. Comparable DNA origami objects imaged by cryo-electron microscopy (cryo-EM) that enables the conservation of the hydrated structure predicted an effective helix midpoint to midpoint distance of 2.6 nm for double-stranded DNA which is a combination of the hydrated helix diameter and the interhelical gap.

The advantage of this DNA origami ruler over polyproline and double-stranded DNA is given by the ability of an exact distance determination between donor and acceptor dye by calculation without the need of a multiparametric fit to estimate the linker lengths, the offset of the dye molecules relative to the base plane L and the polar angle between the dyes ϕ . Compared to the arrangement on a double-stranded DNA ruler the exact linker length a plays a negligible role on the static distance between donor and acceptor. While the linker lengths of dyes that are attached on opposite sides of a DNA double strand add up and thus contribute strongly to the dye separation, the linker lengths of donor and acceptor cancel out when they point into the same direction (see figure 2.4 A). The underlying calculation for the exact distance determination of the fluorophores on the DNA origami ruler is the Pythagorean theorem $R = \sqrt{x^2 + y^2}$. $x = b \cdot 0.34$ nm gives the displacement along the helix axis with the number of base separation b , while $y = h \cdot 2.6$ nm + $y_1 + y_2$ defines the separation perpendicular

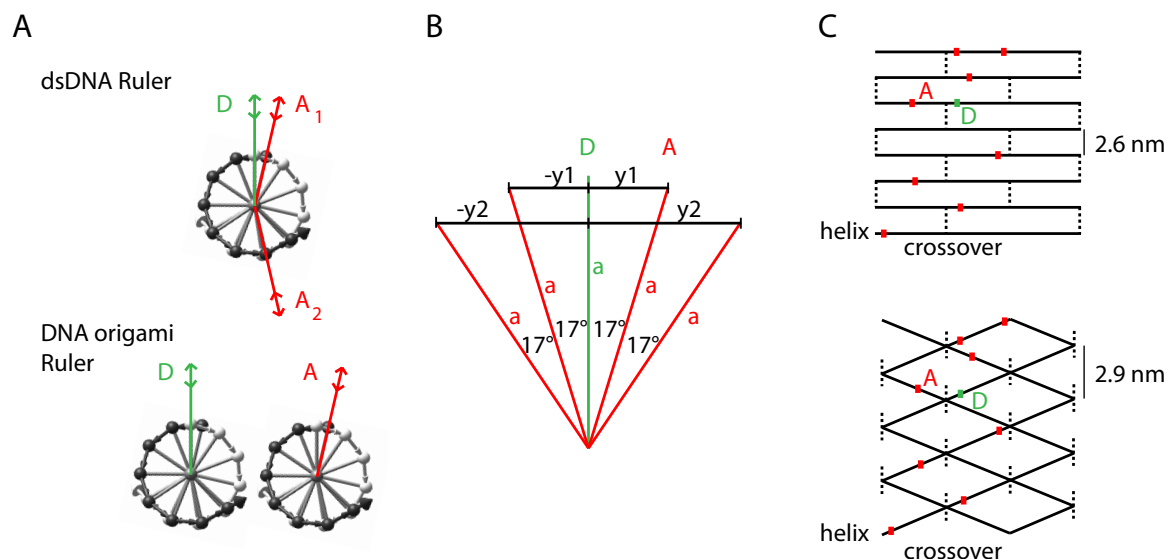


Figure 2.4: Accurate Distance Determination. **A** Influence of the linker length on the distance. Top: On a double-stranded DNA ruler, the influence of the linker length depends on the position of donor and acceptor. If donor D points into the same direction as acceptor A_1 , the influence of the linker length is canceled out while for an acceptor A_2 that points into the opposite direction, the linker length contributes largely to the distance. Bottom: On a DNA origami Ruler all linkers point nearly in the same direction which results in a negligible influence of the linker length on the distance. Reprinted with permission from the supporting information of ref. [73]. Copyright 2011 WILEY-VCH. **B** View along the direction of the helix axis of a DNA origami ruler to illustrate the correction on the orientation of the acceptor dyes A in relation to the donor dye D . A separation of 10 or 11 bases (20 or 22 bases, respectively) between donor and acceptor dye leads to a tilt of 17° (34°) and therefore to a shift of $\pm y_1$ ($\pm y_2$) in the distance calculation for the y -value. **C** The interhelical distance of 2.6 nm shown at top has to be corrected to values dependent on the dye positions in relation to the crossovers (bottom).

to the helix axis with the number of helices between donor and acceptor h . The correction factor y_1 represents the possible tilt of the acceptor dye orientation in respect to the donor dye orientation. The inhomogeneous inter helical gaps due to electrostatic repulsion are considered by y_2 . The tilt correction depends on the base separation b : for $b = 10$ or $b = 11$, the angle between acceptor and donor fluorophores is 17° , while for $b = 20$ or $b = 22$ the acceptor dye is tilted by 34° in relation to the donor dye (see figure 2.4 B). The second correction takes the inter helical spacing into account which is discussed in detail in the next paragraph. Instead of supposing completely parallel helices with a constant center to center distance of 2.6 nm (see figure 2.4 C, top), at scaffold crossovers between neighboring helices the helix to helix distance is assumed to be 2.3 nm. The interhelical gap is highest in the middle of two crossovers and therefore the distance is set to 2.9 nm (see figure 2.4 C, bottom). Taking these corrections into account, R can be calculated for each donor - acceptor separation. Supposing that the exact helix to helix distance is known, the direct determination of the Förster radius R_0 should be possible for any donor-acceptor pair by fitting the FRET curve without the knowledge of parameters like the donor quantum yield Φ_D or the orientation factor κ^2 which require complex measurements besides the FRET measurements.

2.4 MgCl₂ Dependent E-Value Shift in FRET Measurements on DNA Origami Structures

2.4.1 Interhelical Gaps in DNA Origami Structures

As mentioned in the previous paragraph, the assumption of close parallel double helices with a midpoint distance between two neighboring helices of 2 nm in DNA nanostructures cannot be confirmed by AFM, cryo electron microscopy (cryo-EM) and TEM imaging. In contrast, Rothemund observed interhelical gaps of 1 nm - 2 nm in his DNA origami structures imaged by AFM on mica in buffer solutions [54]. Therefore the width measured perpendicular to the helices of a DNA origami object differs from the simplified estimation of $H \times 2$ nm when H is the number of parallel helices. Averaged cryo-EM and TEM images over multiple DNA origami particles showed helix-gaps as well [96]. In a high resolution study on the structure of a three-dimensional DNA origami object based on cryo-EM imaging together with the generation of a pseudoatomic model, the distance of midpoints of neighboring helices varies between 1.85 nm and 3.6 nm depending on the pattern of crossovers that connects parallel helices via Holliday junctions [116]. While at crossover points the helices show close proximity, the DNA double strands tend to diverge with increasing distance. This results in a diamond-shaped lattice of double helices. The observed conformations of Holliday junctions within a DNA origami arrangement are different from such of free four way junctions that form an angle of 60° between two arms in the presence of Mg^{2+} -ions [116, 133]. The detailed geometry of the Holliday junctions occurring in DNA origami structures as well as the mechanics of DNA bending may affect the exact arrangement of the helices. Furthermore, a crucial factor that induces the formation of interhelical gaps may be the electrostatic repulsion between neighboring DNA backbones that bear one negative charge per phosphate group [54]. A coarse-grained description of double-stranded DNA at the individual base-pair level that includes the electrostatic interaction between several helices can reproduce mechanical and elastic properties of DNA origami structures [137]. In this model it is necessary to include the factor of electrostatic repulsion to represent the perforated structure of two-dimensional DNA origami objects imaged by AFM. Therefore, a 'stack of plates' (SOP) model for double-stranded DNA is extended for interactions between adjacent DNA strands integrating an excluded volume and a factor for the interhelical electrostatic interactions. Multivalent ions like Mg^{2+} play a crucial role in the self assembling process of DNA origami structures, thus counterions have to be taken into consideration for the model. While molecular dynamics simulations show the condensation of parallel DNA double strands in the presence of Mg^{2+} due to bridging two phosphates with one ion, helices incorporated into DNA origami structures behave differently. This can be explained by the crossovers that hinder the free orientation of the DNA strands relatively to each other. In the model, these electrostatic characteristics are taken into account by a negative charge at each phosphate location and a description of the counterion effect by a Debye type screening. This leads to a complete description of the characteristic interhelical gap pattern observed in DNA origami structures by the model [137]. In this paragraph, ALEX measurements in solution are used to report the shift in FRET efficiency between donor acceptor pairs attached to parallel helices of a planar DNA origami rectangle as a function of the salt concentration which might indicate a change in the helix to helix distance within a DNA origami object.

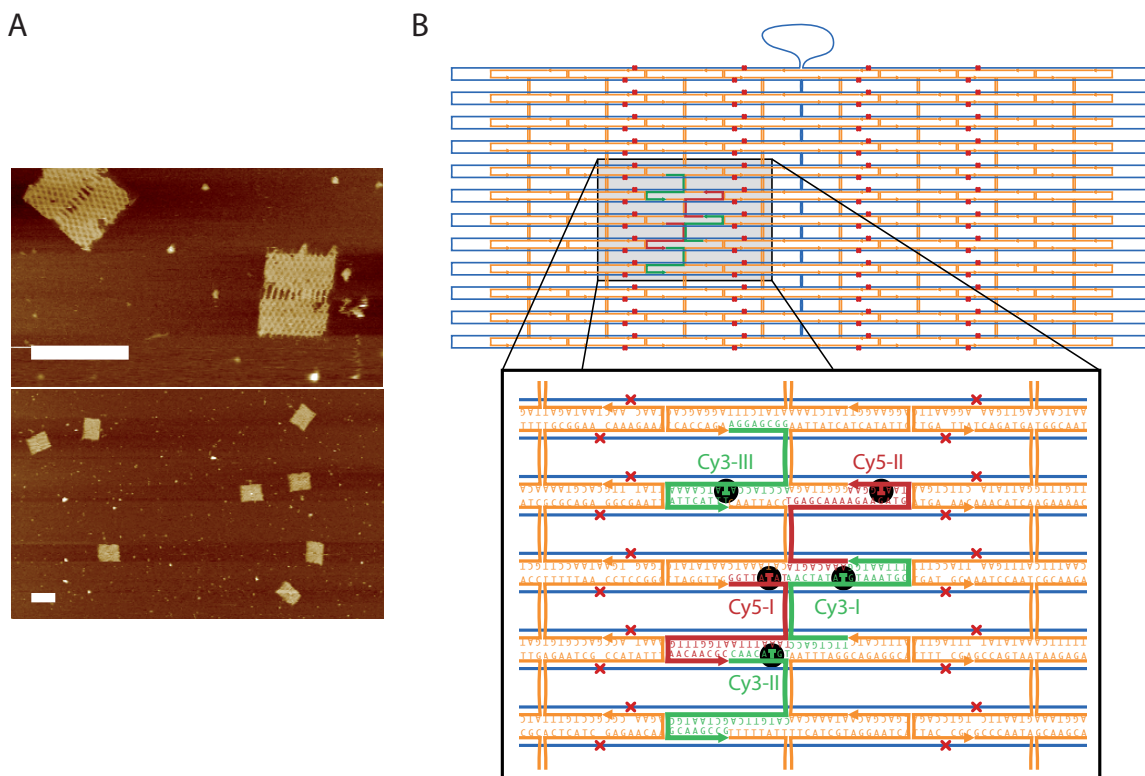


Figure 2.5: DNA origami rectangle for interhelical gap studies. **A** AFM images of DNA origami structures on mica. Ruptures of the structure are due to a high drive amplitude of the cantilever to visualize the interhelical gaps (top). Scale bars: 100 nm. **B** caDNAno aided design of the twist corrected DNA structure with scaffold strand pathway (blue), unmodified staple strands (orange), fluorescently labeled staple strands (green and red) and base deletions (red crosses). The detailed view (bottom) shows the position of the Cy3 or Alexa Fluor 488 dye (green) or the Cy5 dye (red) modified thymine bases of the staples strands.

2.4.2 Structure of DNA Origami Rectangle

To investigate the dependence of interhelical gaps on the salt concentration of the surrounding solution, a rectangular monolayer structure combined with a high folding yield was chosen that is close to an DNA origami structure originating from Rothmund [54]. The scaffold and staple path design was generated using the caDNAno software tool [95]. The DNA origami rectangle consists of 24 parallel helices arranged in a square lattice formation. As scaffold strand the 7,249 nt containing M13mp18-based single strand is used which is folded into shape by 192 oligonucleotides with an average length of 32 nt per staple strand. For self-assembly of the DNA origami structure in a one-pot reaction, a solution containing 10 nM of scaffold strands, 100 nM of each unmodified staple strand, 200 nM of each fluorescently modified staple strand as well as 10 mM Tris-HCl, 1 mM EDTA (pH 8.0 at 20°C) and a salt concentration of 12 mM MgCl₂ was rapidly heated to 95°C followed by slow cooling to 20°C during a linear thermal-annealing ramp within one hour. Each double helix of the folded structure consists of 256 bp which results in a length of 87 nm, if a spacing of 0.34 nm between two neighboring

bases is assumed. The width of the DNA origami rectangle is dependent on the helix to helix distance which is in the focus of this section. The underlying pattern of crossovers and the central seam are clearly visible in the AFM images presented in figure 2.5 A. In contrast to Rothmund’s structure, the outermost rows of staple strands were removed to leave loops of 32 unpaired scaffold bases between each two adjacent helices to avoid unwanted multimerization and the scaffold was permuted with a 73 nt hairpin segment. As described in detail in publication P1 for the DNA origami FRET ruler, a slight twist correction was done for the DNA origami rectangle by one base pair deletion within 64 bases in the caDNAno design to approach a standard B-DNA twist of 10.5 bp per turn instead of the program generated twist of 16 bp per 1.5 turns (see figure 2.5 B, top). For the FRET measurements by ALEX under distinct salt concentrations, three positions for donor dyes and two positions for acceptor dyes were chosen on the DNA origami rectangle (see figure 2.5 B, bottom). As for the DNA origami FRET ruler in publication P1, the well-studied Cy3 and Cy5 FRET pair is attached via a six-carbon linker to internal thymine bases whose backbones point all to the same surface side of the structure. Furthermore, an Alexa Fluor 488 dye is used as an alternative donor molecule. As shown in 2.5 B (bottom), several combinations of donor-acceptor arrangements for interhelical gap studies are programmed and listed in table 2.1.

Denotation	Donor	Acceptor	Separation in nucleotides and helices
0H-I	Cy3-I	Cy5-I	10 nt separation on same helix
0H-II	Cy3-III	Cy5-II	21 nt separation on same helix
2H	Cy3-II	Cy5-I	1 nt and 2 helices separation
3H-I	Cy3-III	Cy5-I	6 nt and 3 helices separation
3H-II	Cy3-I	Cy5-II	5 nt and 3 helices separation

Table 2.1: Denotation of combinations for donor-acceptor arrangements on DNA origami rectangle.

2.4.3 MgCl₂ Dependence of DNA Origami Rectangle Structure

Due to the strong distance dependence of the FRET efficiency between donor and acceptor dyes, ALEX measurements on the single-molecule level are expected to be an appropriate tool for the quantification of the interhelical gap size at different salt concentrations. In contrast to AFM and TEM imaging, ALEX measurements on DNA origami particles can be done while the objects diffuse freely in solution. Thus, surface interactions that might interfere with the interhelical gaps between the negatively charged helices can be excluded.

Experimental Section

The single-molecule fluorescence measurements were carried out on the custom-built confocal microscope described in the experimental section of publication P1. Due to faster diffusion times of the DNA origami rectangles as compared to the DNA origami FRET block, the light intensities were changed to 20 μ W at 533 nm for Cy3 and at 640 nm for Cy5. For Alexa Fluor 488 and Cy5 labeled DNA origami rectangles, the laser power was set to 20 μ W at 495 nm for Alexa Fluor 488 and 18 μ W at 640 nm for Cy5 and the dual-band dichroic beam splitter *Dual Line z 488/647* (AHF Analysetechnik, Germany) was used. Spectral filtering of the

emission beams for the Cy3/Cy5 dye pair is done by the combination of the filters *Brightline HC 582/75* and *Brightline HC 685/40* and for the Alexa Fluor 488/Cy5 pair by the filters *Brightline Exciter 531/40* and *Razoredge Long Pass 647* (all filters: AHF Analysetechnik, Germany). In the data evaluation for the ALEX measurements, the parameters in the Seidel burst search algorithm were adapted to the DNA origami rectangle (T = 0.5 ms, M = 30, L = 50). The sample preparation for the fluorescence measurements of the DNA origami rectangles was carried out as for the DNA origami FRET blocks. To remove the excess staple strands, Amicon Ultra-0.5mL Centrifugal Filters (100,000 MWCO) were used. The Tris-HCl/EDTA (TE) buffer that was added during the filtration steps contained 12 mM MgCl₂. The experiments were done at room temperature (22°C) in standard phosphate buffered saline (PBS) or TE buffer without adding an enzymatic oxygen-scavenging system. As in publication P1, ascorbic acid and methylviologen were used for blinking and bleaching reduction according to the ROXS scheme [124]. To the small sample volume of 50 μ l (\approx 200 pM of DNA origami rectangles), MgCl₂ was added according to the concentration conditions between 0 mM and 100 mM. The sample chamber was passivated by BSA to prevent DNA accumulation at the surface. For AFM imaging, 50 μ l (\approx 2 nM of DNA origami rectangles) of filtered samples in TE buffer containing 12 mM, 50 mM or 100 mM MgCl₂ were deposited on mica. After 10 min of incubation, the TE buffer was removed and the surface was washed twice before 50 μ l MgCl₂ containing TE buffer was added for imaging. The DNA origami samples were imaged in tapping mode on a Multimode III AFM with an J-scanner (Veeco Instruments) with SNL-10 sharp nitride cantilevers (Veeco Probes). For TEM imaging, the exchange of the annealing buffer with TE buffer containing 25 mM MgCl₂ was done during the purification steps with Amicon Ultra-0.5mL Centrifugal Filters (100,000 MWCO). Imaging and processing was performed as described in reference [110].

MgCl ₂ [mM]	0	5	10	30	50	70	100
FRET efficiency E^* (dx/le corr.)	-0.01	0.03	0.06	0.12	0.14	0.16	0.16
Distance R^* [nm] ($R_0 = 5.3$ nm)	inf	9.2	8.4	7.4	7.1	7.0	7.0
Interhelical gap G^* [nm] (y_1 corr.)	inf	0.8	0.5	0.2	0.1	0.0	0.0

Table 2.2: DNA origami samples 3H-I with FRET pair Cy3/Cy5 were measured in PBS buffer at increasing MgCl₂ concentrations. FRET efficiencies E^* were corrected for direct excitation ($dx = 0.089$) and leakage ($le = 0.090$). Distances R^* were obtained from E^* -values and Förster radius $R_0 = 5.3$ nm using equation (2.11). Interhelical gaps G^* were calculated from R^* -values under consideration of the angle correction factor ($y_1 = 0.6$ nm) using equation (2.12).

Results and Discussion

To investigate the interhelical gap dependence on different salt concentrations by FRET, several donor - acceptor positions on the DNA origami rectangle were chosen (see table 2.1). Two different FRET pairs were used to determine dye dependent effects: Cy3 - Cy5 and Alexa Fluor 488 - Cy5. The FRET efficiencies between donor and acceptor were measured in PBS and TE buffer under the influence of increasing MgCl₂ and NaCl concentrations. The results of the FRET measurements by ALEX were discussed in detail on sample 3H-I with the donor - acceptor pair Cy3 - Cy5. The described E_{app} -value shift was caused by varying addition of MgCl₂ to the 3H-I sample in standard PBS buffer which contained 137 mM NaCl. Two typical two-dimensional E_{app} - S_{app} histograms of double labeled DNA origami objects

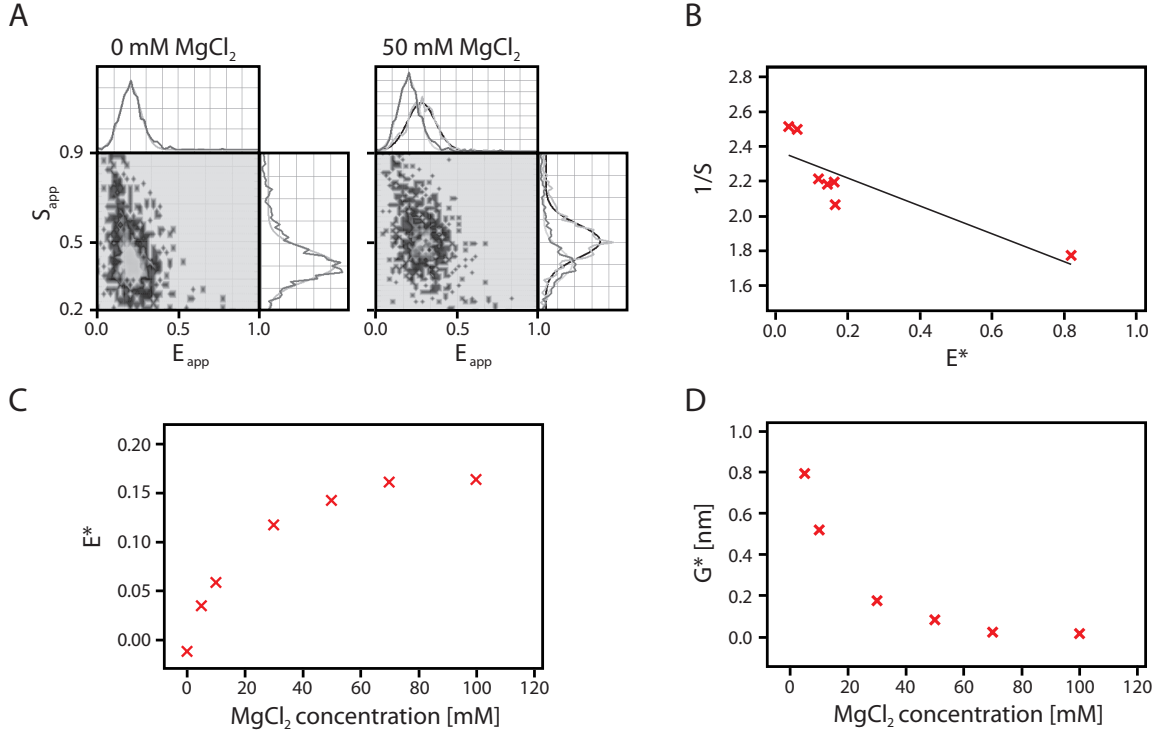


Figure 2.6: DNA origami sample 3H – I with FRET pair Cy3/Cy5 measured in PBS buffer at increasing $MgCl_2$ concentrations. **A** Two-dimensional E_{app} - S_{app} histograms of sample 3H – I measured at 0 mM (left) and 50 mM $MgCl_2$ (right). In the histograms for 50 mM $MgCl_2$, also the E_{app} and S_{app} distributions for 0 mM $MgCl_2$ are shown to visualize the shift after salt addition. **B** $1/S$ versus E^* for low FRET sample 3H – I at several $MgCl_2$ concentrations and one high FRET sample 0H – I to report the γ correction factor. The slope Σ of the linear fit $1/S = \Sigma \cdot E^* + \Omega$ is -0.80 and the intercept Ω is 2.38 . **C** Leakage l_e and direct excitation dx corrected FRET efficiencies E^* versus $MgCl_2$ concentrations. **D** Calculated interhelical gap G^* dependence on $MgCl_2$ concentrations, assuming no photophysical effects on the dyes.

($0.2 < S < 0.9$) without $MgCl_2$ (left) and after addition of 50 mM $MgCl_2$ (right) are shown in figure 2.6 A. The shift to a higher mean FRET efficiency E_{app} after the addition of salt can be clearly seen when comparing the E_{app} -histograms of both in figure 2.6 A (right). To obtain E^* , the E_{app} -values were corrected for leakage ($l_e = 0.090$) and direct excitation ($dx = 0.089$) by equation (2.5). For the determination of the γ -factor, $1/S_{app}$ was plotted against different low FRET E^* values of sample 3H-II at increasing $MgCl_2$ and the high FRET E^* value of sample 0H-I (see figure 2.6 B). The linear relation between E^* and $1/S$ is [126]

$$1/S = \Omega + \Sigma \cdot E^*. \quad (2.9)$$

The best linear fit yielded an intercept $\Omega = 2.38$ and a slope $\Sigma = -0.80$. The γ -factor was determined by

$$\gamma = \frac{\Omega - 1}{\Omega + \Sigma - 1} = 2.38. \quad (2.10)$$

The obviously non-linear distribution of the E^* - $1/S$ -values as well as this high value for the

γ -factor argue against the determination of E by using equation (2.6). This result may indicate photophysical effects of MgCl₂ on the fluorophores attached to the DNA origami structure that interfere with the effect on the interhelical gaps. In figure 2.6 C, the E^* -values for MgCl₂ concentrations between 0 mM and 100 mM were plotted. The slightly negative E^* -value at 0 mM concentration could be due to a overcorrection of leakage or direct excitation. After a strong increase of E^* between 0 mM and 50 mM, saturation occurs at MgCl₂ concentrations around 60 mM. Neglecting the fact that the shift of the FRET efficiency with increasing salt concentrations could be overlaid by several effects beside an absolute distance shift, E^* was translated into an approximated distance R^* by equation

$$R^* = R_0 \left(\frac{1}{E^*} - 1 \right)^{1/6}, \quad (2.11)$$

with a Förster Radius $R_0 = 5.3$ nm as had been determined for the FRET pair Cy3/Cy5 in publication P1. The calculated R^* -values are listed in table 2.2. From these approximated distances R^* , a first approach for the change of the mean interhelical gap G^* depending on MgCl₂ concentrations between donor and acceptor was calculated via

$$G^* = \frac{\sqrt{(R^*)^2 - (N \cdot 0.34 \text{ nm})^2} - (H \cdot 2 \text{ nm} + y_1)}{H}. \quad (2.12)$$

For DNA origami sample 3H-I, the number of separating bases between donor and acceptor is $N = 6$ and the number of helices between the dyes is $H = 3$. The angle correction factor is $y_1 = 0.6$ nm (see figure 2.4 B). The obtained mean interhelical gap G^* between donor and acceptor on 3H-I at a concentration of 5 mM would have a size of 0.8 nm (see figure 2.6 D). At MgCl₂ concentrations higher than 50 mM, G^* converges to 0 nm. This would indicate close parallel double helices within a DNA origami structure at relatively high salt concentrations. If taking into account the positions of the dyes relatively to the next crossover, these values would be in the expected range (see figure 2.5 B).

Furthermore, the addition of NaCl instead of MgCl₂ to sample 3H-I in PBS caused an increase of E_{app} as well. At a concentration of 100 mM NaCl, saturation occurred. Both MgCl₂ and NaCl addition to sample 3H-I in TE buffer caused similar increase in the FRET efficiencies as in PBS. E_{app} of sample 3H-I in TE without salt was lower than in PBS due to the 137 mM NaCl already present in standard PBS buffer.

Qualitatively, FRET measurements between Cy3 and Cy5 dyes on the DNA origami samples 3H-II, 0H-I and 0H-II in PBS after MgCl₂ addition showed the anticipated tendency of the E_{app} shift. E_{app} of sample 3H-II increased with increasing salt concentrations, while E_{app} of samples 0H-I and 0H-II on which the dyes are attached on the same helix, decreased due to assumed reduced bending of the DNA double strands within a DNA origami structure at high MgCl₂ concentrations. For sample 2H, the E_{app} -value remained constant after salt addition, which could be a further indication that factors like the exact DNA origami environment influence the FRET between the dyes.

Using the FRET pair Alexa Fluor 488 and Cy5 on the samples 3H-I, 0H-I and 0H-II, the results of the measurement with Cy3/Cy5 could be repeated. In contrast, sample 3H-II showed no shift in E_{app} after the addition of even high MgCl₂ concentrations. Furthermore, the FRET efficiency between donor and acceptor on sample 2H decreased with increasing salt concentration, which confirms the assumption of interfering effects mentioned before.

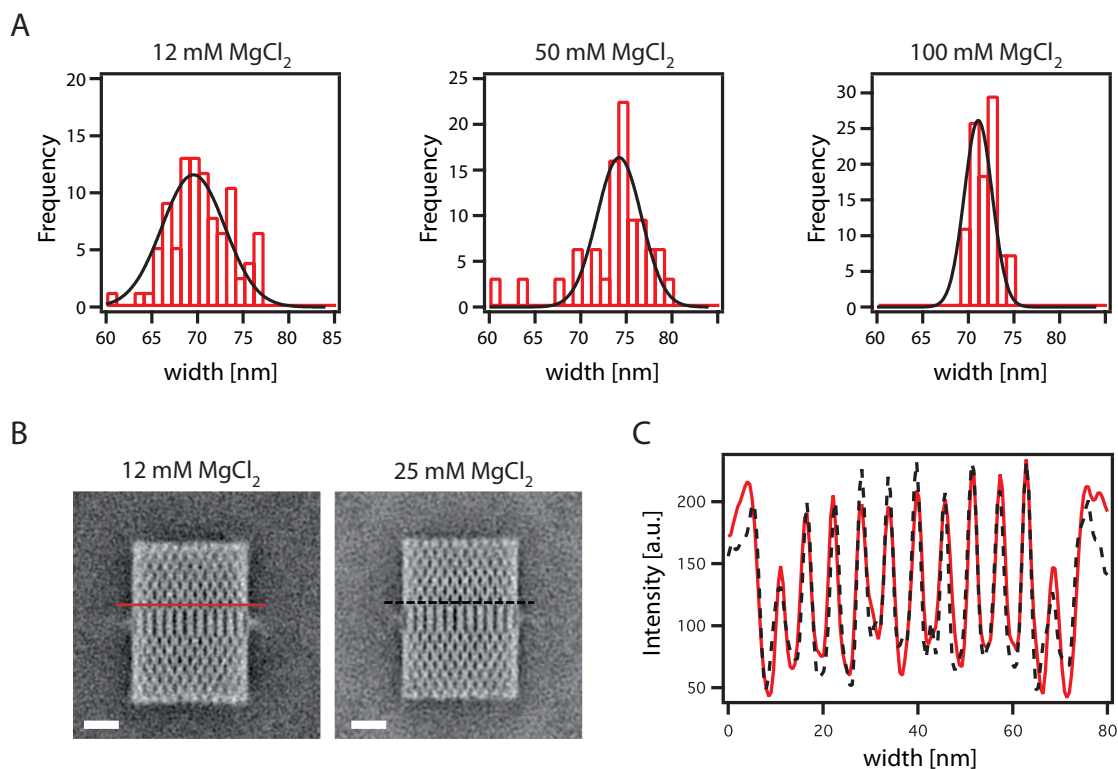


Figure 2.7: AFM and TEM analysis of DNA origami rectangle at increasing $MgCl_2$ concentrations. **A** Width distributions of DNA origami rectangles at 12 mM (left), 50 mM (center) or 100 mM (right) $MgCl_2$ measured by AFM imaging. The mean values of the gaussian fits are 69.5 ± 3.4 nm (12 mM), 74.2 ± 2.4 nm (50 mM) and 71.2 ± 1.5 nm (100 mM). **B** Average negative-stain TEM micrographs of objects were obtained by imaging structures after incubation in TE buffer containing 12 mM (left, sum of 255 particles) or 25 mM (right, sum of 195 particles) $MgCl_2$. Scale bars: 20 nm. **C** Intensity profiles of lines orthogonal to the longitudinal axis of the objects shown on the TEM micrographs in B. Red line indicates profile for 12 mM $MgCl_2$ and black dashed line for 25 mM $MgCl_2$.

Additionally to single-molecule FRET measurements, the interhelical gap size of the DNA origami rectangle was investigated by using AFM and TEM imaging. The DNA origami structures were imaged by AFM in TE buffer containing 12 mM, 50 mM or 100 mM $MgCl_2$. As shown in figure 2.7 A left, the mean width of the DNA origami rectangles on mica in solution containing 12 mM $MgCl_2$ was measured to be 69.5 ± 3.4 nm by fitting the size distribution with a Gaussian fit. This results in an interhelical gap of 0.9 ± 0.2 nm, if a diameter of 2 nm for double-stranded DNA is assumed. This is in the range of Rothmund's measured values of 0.9 nm - 1.2 nm for the gaps in his DNA origami rectangle which has the same crossover distance of 16 nt. By increasing the $MgCl_2$ concentration of the buffer to 50 mM, the measured mean width of the DNA origami rectangle was 74.2 ± 2.4 nm (see figure 2.7 A center). This would indicate an interhelical gap of 1.1 ± 0.1 nm which is a slightly larger value than obtained for structures in 12 mM $MgCl_2$ containing buffer. At a very high $MgCl_2$ concentration of 100 mM, the mean width was 71.2 ± 1.5 nm which results in a gap size of

1.0 ± 0.1 nm (see figure 2.7 A right). These determined values for the width of the DNA origami rectangle under increasing salt concentrations were all in the same range with respect to their margins of error. The large standard deviations of the width values might be due to difficulties in AFM imaging. This includes the influence of the orientation of the object in respect to the scanning direction which seemed to have an impact on the structure width. Further factors could be slight drift or cantilever specific imprecisions. To compare the mean widths of the DNA origami structures in the presence of 12 mM and 25 mM MgCl₂ by TEM imaging, micrographs were prepared by classifying and averaging individual particle views (see figure 2.7 B). In figure 2.7 C, the intensity profiles of lines orthogonal to the longitudinal axis of the objects on the average TEM micrographs are shown. These profiles of DNA origami rectangles after being in buffers containing 12 mM versus 25 mM MgCl₂ were highly similar and agreed both in width which was determined to be 66.9 nm. The results show that neither AFM nor TEM imaging of the objects could reveal a significant structural dependence on the salt concentration.

Conclusion

In summary, the non-linear $1/S$ -value shift with increasing E^* -values in single-molecule FRET measurements as well as the unexpected qualitative E_{app} shifts of some samples lead to the following assumption. The shift of the FRET efficiency after MgCl₂ addition could be caused by several factors like photophysical effects that interfere with the influence of the salt ions on the interhelical gaps between the negatively charged double helices. These factors might be specific for fluorophores on DNA origami structures because FRET measurements on double-stranded DNA showed no salt dependence. If for example the free rotation of either dye is constrained by interactions between the fluorophore and the DNA origami structure, the dipole orientation factor κ^2 could not be assumed to be $2/3$ anymore. Furthermore, lifetime measurements of the fluorophores on the DNA origami rectangle under distinct MgCl₂ concentrations showed no deterministic influence. As long as these interfering factors are not quantitatively determined, the FRET efficiencies E can not be translated into absolute distances R between the donor and acceptor which prevents the exact determination of the interhelical gap dependence from the salt concentration. AFM as well as TEM imaging of DNA origami structures at varying MgCl₂ concentrations showed no significant differences in the interhelical gaps. This might indicate strong interactions between the DNA origami structures and the surfaces to which the objects were attached. Concluding, the exact influence of the salt concentration on the structure of DNA origami objects remains to be determined by further techniques.

2.5 Associated Publication P1

Single-Molecule FRET Ruler Based on Rigid DNA Origami Blocks

By

Ingo H. Stein, Verena Schüller, Philip Böhm, Philip Tinnefeld and Tim Liedl

published in

ChemPhysChem 2011, 12, 689–695

Reprinted with permission from ref. [73]. Copyright 2011 WILEY-VCH.

DOI: 10.1002/cphc.201000781

Single-Molecule FRET Ruler Based on Rigid DNA Origami Blocks

Ingo H. Stein,^[a] Verena Schüller,^[b] Philip Böhm,^[b] Philip Tinnefeld,^{*[a, c, d]} and Tim Liedl^{*[b, c]}

Fluorescence resonance energy transfer (FRET) has become a work-horse for distance measurements on the nanometer scale and between single molecules. Recent model systems for the FRET distance dependence such as polyprolines and dsDNA suffered from limited persistence lengths and sample heterogeneity. We designed a series of rigid DNA origami blocks where each block is labeled with one donor and one acceptor at distances ranging between 2.5 and 14 nm. Since all dyes are attached in one plane to the top surface of the origami block, static effects of linker lengths cancel out in contrast to com-

monly used dsDNA. We used single-molecule spectroscopy to compare the origami-based ruler to dsDNA and found that the origami blocks directly yield the expected distance dependence of energy transfer since the influence of the linkers on the donor–acceptor distance is significantly reduced. Based on a simple geometric model for the inter-dye distances on the origami block, the Förster radius R_0 could directly be determined from the distance dependence of energy transfer yielding $R_0 = 5.3 \pm 0.3$ nm for the Cy3–Cy5 pair.

1. Introduction

The length scale below 10 nm is of profound interest for macromolecular and biomolecular interactions and structures and is accessible under biological conditions by fluorescence resonance energy transfer (FRET).^[1] The use of FRET for studying biomolecular complexes began with the presentation of FRET as a spectroscopic ruler using a donor–acceptor labeled polyproline.^[2] This study also experimentally demonstrated the theoretically predicted distance dependence of the energy transfer efficiency although measured FRET efficiencies were generally higher than expected.^[2] Since this work, a number of approaches have been pursued to further elaborate defined donor–acceptor distances. A defined FRET ruler would be a valuable tool to estimate the accuracy of FRET-assisted distance measurements,^[3] and to quantify the influence of photophysical and photochemical effects, structural flexibility and molecular heterogeneity as well as instrumental factors. Another important issue to be evaluated is the length of the linkers that are needed to attach fluorophores to the molecules of interest. With the spreading of FRET for imaging and in single-molecule spectroscopy, the interest to achieve accurate FRET measurements has further increased.

So far, the polypeptide polyproline and oligonucleotides were used to validate Förster theory and as references in biomolecular FRET studies.^[3–9] Stiff organic compounds such as oligomers of *para*-phenyleneethynylene have also been suggested as FRET rulers. Such (bio-)polymers, however, exhibit a limited persistence length of ≈ 5 –50 nm. Polyprolines had been used recently to revisit the original spectroscopic ruler and a strong deviation to expected FRET values was in particular found for larger distances.^[8] This discrepancy could recently be ascribed to *cis*–*trans* isomerization of individual proline residues leading to a deviation from the expected stiff structure.^[3,9,10] FRET as well as intramolecular quenching experi-

ments revealed that a significant fraction of polyproline residues adopted a conformation that involved much shorter distances between donor and acceptor under relevant conditions. Due to the simplicity to produce donor- and acceptor-labeled double-stranded (ds) DNA, oligonucleotides have been used most frequently and FRET was used to illustrate the helical structure of DNA.^[4–7,11–14]

On the other hand, changing the distances between donor and acceptor along DNA base-pair by base-pair does not only yield a stepwise distance change of 0.34 nm per base, but additionally goes along with a distance modulation due to the helical pitch of dsDNA, which has a diameter of ≈ 2 nm and a native twist of 10.5 bp per 360°. A geometric model is fre-

[a] I. H. Stein,^{*} Prof. Dr. P. Tinnefeld
Angewandte Physik–Biophysik
Ludwig-Maximilians-Universität
Amalienstraße 54, 80799 Munich (Germany)
Fax: (+49) 89 2180 2050
E-mail: p.tinnefeld@tu-braunschweig.de

[b] V. Schüller,^{*} P. Böhm, Prof. Dr. T. Liedl
Physik weicher Materie und Biophysik
Ludwig-Maximilians-Universität
Geschwister-Scholl-Platz 1, 80539 Munich (Germany)
Fax: (+49) 89 2180 3182
E-mail: Tim.Liedl@lmu.de

[c] Prof. Dr. P. Tinnefeld, Prof. Dr. T. Liedl
Center for NanoScience
Ludwig-Maximilians-Universität
Schellingstr. 4, 80799 Munich (Germany)

[d] Prof. Dr. P. Tinnefeld
Physical and Theoretical Chemistry–NanoBioScience
TU Braunschweig, Hans-Sommer-Str. 10, 38106 Braunschweig (Germany)

[*] These authors contributed equally to this work.

Supporting information for this article is available on the WWW under <http://dx.doi.org/10.1002/cphc.201000781>.

quently used to account for this increased complexity.^[11,12] The model however, implies several fit parameters to the data and especially the role of the linkers that connect the DNA base with the dye induces considerable uncertainty because the influence of the linker length varies strongly dependent on the basepair distance between donor and acceptor. For a donor-acceptor separation of for example, 7 bps on opposite strands, the linkers should be almost parallel and on the same side of the DNA helix and their lengths (but not their dynamics) should cancel out. On the other hand, for one or twelve base pairs separation, corresponding roughly to a full turn, the dyes are on the opposite side of the DNA cylinder and the relatively undefined linker lengths largely contribute to the donor-acceptor distance (see Figure S1 in the Supporting Information). Further issues with dsDNA are the varying materials located between donor and acceptor, the anisotropic dipole-dipole orientation of molecules attached to the surface of a cylinder and the fraying and breathing of an isolated DNA double strand at a finite temperature.

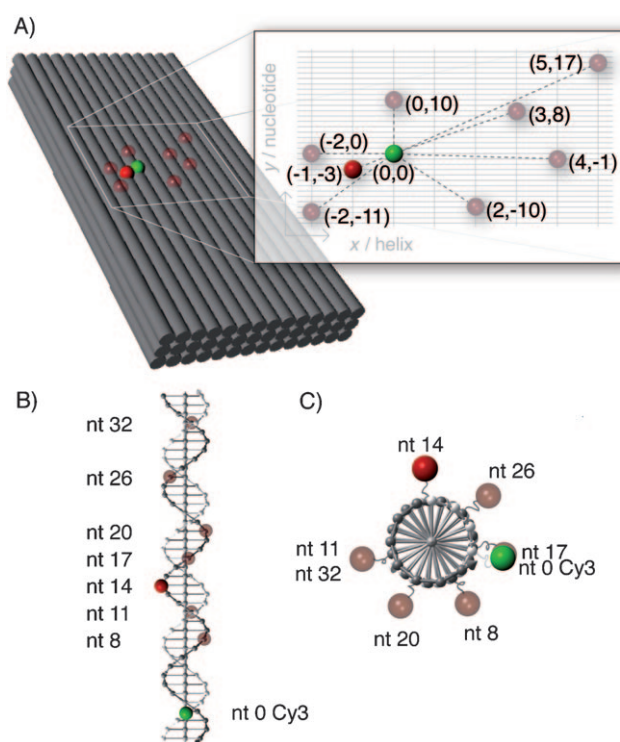
DNA has long been used as a building material for nano-scale structures.^[15] Herein, we introduce rigid three-dimensional DNA origami blocks as stiff FRET rulers. For DNA origami, a 8 kb-long single-stranded DNA "scaffold" is folded into shape by hundreds of short "staple" oligonucleotides.^[16] This allows for the construction of arbitrarily-formed DNA objects with tunable mechanical properties.^[16–20] Each position of such an object can be addressed individually, since each of the staple strands can be functionalized with (bio)chemical groups or fluorescent dyes.^[21–24, 25]

We attached Cy3-donor and Cy5-acceptor dyes to the surface of an origami structure so that linkers always point in the same direction, minimizing their static influence on FRET efficiencies (Figure S1, Supporting Information). We varied the distances between the dyes and studied energy transfer efficiencies using single-molecule spectroscopy with alternating laser excitation of diffusing molecules. We compared the distance dependence of the energy transfer efficiency on the origami structure to a common double-stranded DNA FRET ruler.

2. Results and Discussion

2.1. DNA Origami Design

Using the software caDNAo,^[17] we designed a rigid DNA origami block, which serves as a "breadboard" for the arrangement of fluorescent dyes in a single plane on top of the DNA object (Scheme 1 A). To achieve a high density of potential fluorophore sites, we chose a tightly packed square arrangement of 3×14 double helices. As scaffold-folding strand we used a 8064 nucleotide (nt) M13mp18-



Scheme 1. Positions of the donor (green) and the acceptors (red) on the DNA FRET block and on a DNA double strand. The donor fluorophore was present in all assembled structures while only one of the acceptor dye positions was occupied in each sample.

based single strand, that is arranged by 165 oligonucleotides into a plane of parallel helices that fold up to multiple layers. Each helix has a length of 168 basepairs. At the ends of the objects loops of unpaired bases (16–32 nt) are formed between each two adjacent helices (Figure S2, Supporting Information). The objects were annealed in a one-pot-reaction (Experimental Section) and analyzed with gel electrophoresis and transmission electron microscopy (TEM) (Figure 1). The measured lateral dimensions of the blocks after staining with

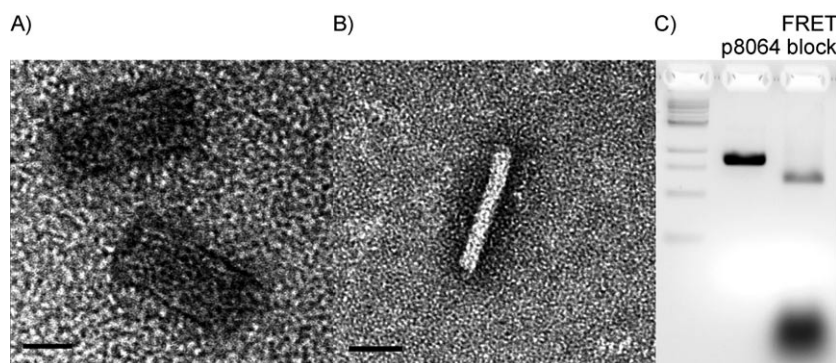


Figure 1. Electron micrograph of the DNA origami FRET blocks stained with uranyl acetate. A) Flat-lying objects. B) Standing DNA origami FRET block. The thickness of three helices is clearly visible. C) Gel analysis of assembled objects. Left to right: 2-log DNA ladder, p8064 scaffold, FRET block. The band containing the structure has been extracted and investigated with TEM. Scale bars: 20 nm.

uranyl acetate and drying are 58 nm × 30 nm, the thickness is 7 nm. These values are close to the expected values of 57 nm × 28 nm × 6 nm, if an unhydrated diameter of double-helical DNA of 2.0 nm and a spacing of 0.34 nm between two neighboring bases is assumed. However, Cryo-EM measurements of comparable objects in frozen solvent revealed an average effective diameter of 2.6 nm (± 0.3 nm) for dsDNA in a square-lattice arrangement.^[26] Under buffer conditions, the effective diameter is the summation of a helical diameter of 2.1 nm and an interhelical gap produced by electrostatic repulsion on the order of 0.5 nm.

The square lattice arrangement is achieved by implementing crossovers from one helix to one of its neighboring helices every eight basepairs. At a native twist of 10.5 bp per 360°,^[27] eight base-pair steps along the axis of a dsDNA would correspond to a helical twist of 274.3° between two crossovers or, if a perfect square arrangement is assumed, to 10.67 bp/360° and therefore to an underwinding of the helices. To overcome the resulting global twist of the structure, we introduced targeted deletions by removing single base-pairs every 64 bp from each helix. This restores the regular 10.5 bp per 360° throughout the structure. TEM images of the corrected DNA origami FRET blocks revealed no detectable global twist (Figure 1 B).

For the donor, we chose a designated position close to the center on the “top” surface of the origami block and eight sites in close proximity in the same plane for the acceptor dyes. As donors and acceptors, we chose the well-studied Cy3 and Cy5 dyes attached to an internal thymine base via a six-carbon linker. The thymine bases were chosen such, that the dye molecules all protrude almost perpendicular out of the plane of the origami block. Thus, all dyes had approximately the same orientation—though still free to rotate and wiggle at the end of their linkers (that we refer to as dynamic heterogeneity)—and had no DNA molecule located in the direct path between them.

2.2. Double-Stranded DNA Design

For comparison, we also studied the same donor–acceptor pair with a system, where a single DNA double-helix is used as spacer between the fluorophores. The Cy3 donor was attached to a thymine close to the 5′ end of a 39 nt long oligonucleotide (Experimental Section). Each of seven complementary strands carried a Cy5 acceptor at a distance of 8, 11, 14, 17, 20, 26, and 32 base pairs from the donor (Scheme 1 B,C).

2.3. Distance Dependence of Energy Transfer

We used single-molecule fluorescence spectroscopy with alternating laser excitation (ALEX)^[28] on diffusing molecules to investigate the distance dependence of FRET in our dsDNA and FRET blocks. ALEX was used to separate intact doubly-labeled populations from donor-only and acceptor-only populations and to determine correction factors (see the Experimental Section for details). Solution measurements were performed at a concentration of ≈ 0.1 nM such that the fluorescence bursts of

diffusing molecules could be well identified by a burst search algorithm. Three consecutive measurements were taken for each sample (10 min each for the seven dsDNA samples and 15 min each for the eight FRET blocks) to obtain a total average number of bursts of 5000 (dsDNA) and 3000 (origami block) for each sample. Lower-burst yields of FRET blocks are due to their slower diffusion time. The energy transfer efficiencies E for each burst were calculated from the photon counts as described in detail in the Experimental Section. The energy transfer efficiency E for each sample as plotted in Figures 2

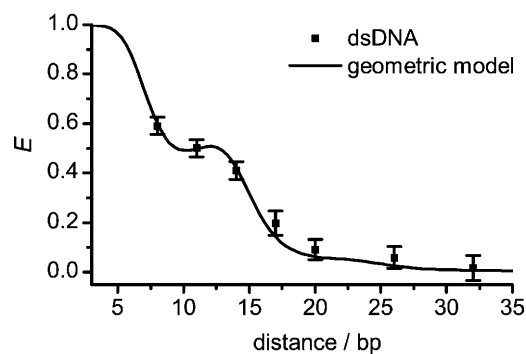


Figure 2. FRET efficiencies of dsDNA samples as a function of donor–acceptor separation in base-pairs. The solid line is a fit to the data according to a geometric model of dsDNA as described in the text.

and 3 were determined by applying a Gaussian fit to the histogram of E values of the selected doubly-labeled population. The statistical error was determined from three separate measurements taking into account the uncertainty of the corrections for direct excitation and leakage.

The shape and width of the energy transfer and stoichiometry histograms of the DNA origami samples are similar to the corresponding histograms of the dsDNA samples (Figure S3, Supporting Information). Besides small donor-only and acceptor-only populations, a single homogenous FRET population is observed, indicating that correctly folded structures were obtained quantitatively without a detectable fraction of misfolded origami structures.

To compare the two systems, we used molecular models for the dsDNA as well as for the origami structures. For dsDNA we adopted the model of Clegg et al.^[11] used for mapping the helical structure of double-stranded DNA via FRET. Instead of ten basepairs per helical turn of the double strand as observed in the solid state, we adjusted the value in the model to 10.5 turns—the same value we used for the origami structures—which is appropriate for dsDNA in solution.^[27] The model takes into account the rotation of the dyes around the helical axis and their linker lengths. All in all, four parameters were introduced in the model: a and d , as helix radius plus individual linker lengths to donor and acceptor dyes, a displacement L along the helical axis and an angle θ_0 between the dyes for zero basepair separation. In the case of Cy3 and Cy5 as donor and acceptor pair it seems reasonable to assume equal lengths a and d , due to the similar structure and properties of the two

cyanine dyes and their identical linker length of six carbon atoms. To account for these geometrical constraints we used Equation (1):^[11]

$$R = \sqrt{(0.34\text{nm}\Delta n + L)^2 + 2a^2 - 2a^2 \cos\left(\frac{360^\circ}{10.5}\Delta n + \theta_0\right)} \quad (1)$$

The above equation together with the Förster equation [Eq. (5) with $R_0=5.4$ nm for the Cy3–Cy5 dye pair^[29,30]] was fitted to the data using the Levenberg–Marquardt least-squares algorithm and is shown in Figure 2. The following fit parameters were obtained: $a=18\pm 1$ Å, $L=9\pm 1$ Å, $\theta_0=243^\circ\pm 9^\circ$. As a result of the geometrical fit of the dsDNA data, the separations in basepairs were converted to absolute distances in nm. The corrected distance dependence of the energy transfer efficiency is shown in Figure 3.

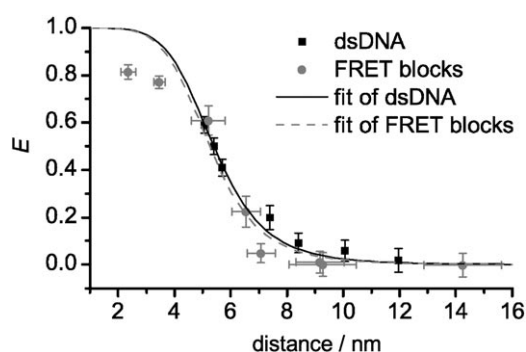


Figure 3. FRET efficiencies of dsDNA (black) and FRET block samples (grey) as a function of distance. The distances for dsDNA were calculated from the basepair separation according to the geometrical model with the prior obtained fit parameters. The FRET block data was fitted to the Förster equation [Eq. (5)] yielding $R_0=5.3\pm 0.3$ nm.

Figure 3 also contains a distance-corrected plot of the origami block, which was modelled incorporating two significant corrections: 1) The position of the labeled thymine bases could not always be chosen such that each base is exactly pointing along the normal of the plane formed by the 14 parallel helices. In fact, most of the labeled bases were tilted either 17° clockwise (cw) or counter clockwise (ccw) away from this normal when the line of sight follows the axis of the respective helix. For example, an acceptor located two helices away and 10 bases downstream from the donor is tilted 17° ccw with respect to the donor, which is oriented in the plane normal. The projected shift was added (or subtracted) in the model, assuming a distance of the dye to the helix center of 2 nm. 2) Since the helices are connected through crossovers only every 31 bases, the gap between two double strands is not constant along their axis. Analyzing the cryo-electron-microscopy data of Ke et al.,^[26] we estimate a minimal center-to-center distance of 2.3 nm at the crossovers sites and a maximum distance of 2.9 nm in the central position between two crossovers (Table S4, Supporting Information). These minimum and maximum values were also used for the error estimation in the dis-

tance calculation for each origami sample. The individual widths of the error bars in Figure 3 are due to different numbers of helices that are crossed between donor and acceptor. In between the extremes we interpolate the distances between neighboring helices. Based on the models used to derive the interchromophore distances, the FRET efficiency graphs are in good agreement with the values expected from Förster theory for both the dsDNA as well as for the FRET blocks (Figure 3). We ascribe deviations for the shortest distances of the FRET blocks to decreased orientational averaging at small distances due to fast energy transfer as has been suggested for polyprolines and to photophysical effects due to direct chromophore interactions.^[8,12] The fit for the FRET block directly yields a Förster radius of 5.3 nm for the Cy3–Cy5 pair.

The key difference between the two discussed molecular FRET rulers is that for dsDNA a complex geometrical model with several fit parameters had to be used to translate the basepair distance into physical distance. The parameters a and L are not experimentally accessible. It was not possible to achieve an adequate fit of the data in Figure 2 with reasonable assumptions for these parameters. Specifically, the presented fit required three variable parameters and a fixed Förster radius R_0 . Varying R_0 as a fourth fit parameter, for example, yields: $a=20\pm 1$ Å, $L=31\pm 5$ Å, $\theta_0=227^\circ\pm 7^\circ$, $R_0=7.5\pm 0.4$ nm. Although the linker length a and the angle θ_0 adopt reasonable values, the displacement L along the helical axis as well as the Förster radius R_0 deviate strongly from expected values.

In contrast, our model of the origami samples directly provides interchromophore distances that allow a fit to the Förster equation yielding a reasonable R_0 value. Importantly, all assumptions of the origami structure that are the basis for the distance determination are principally accessible by other experimental methods. The inaccessible linker lengths between the DNA and the fluorophores essentially cancel out for the FRET blocks. For an interhelix spacing of 2.6 nm for example, the fitted R_0 varies by less than 0.06 nm if the dye distance to the helix center is changed from 1.7 nm to 2.3 nm. This comparison shows that the origami FRET rulers directly exhibit a distance dependence that closely resembles the predicted behavior by the Förster model.

It is worth mentioning that the presence of magnesium ions during our measurements generally increases FRET efficiencies for the FRET blocks whereas FRET values are independent of magnesium for the dsDNA (Figure S5, Supporting Information). This can be attributed to the fact that electrostatic repulsion between the negatively charged backbones of adjacent helices are screened more effectively by divalent ions which leads to smaller interhelical gaps. A thorough analysis of the influence of changing mono- and divalent ion concentrations on DNA origami geometry is currently underway. This will also reveal whether remaining deviations of energy transfer efficiencies are related to the limited structural model of the origami block and the uncertainty of the dye positions or whether for example, linker dynamics and photophysical effects are more significant.

3. Conclusions

Rigid DNA origami blocks prove to be a suitable FRET ruler with distinct advantages compared to double-stranded DNA or polyprolines. Compared to dsDNA, the influence of the linker is minimized and no multiparametric fit is required to translate the basepair separation into physical distance. By placing all dyes in a single plane on one side of the origami block, the inter-dye distance is known a priori and, importantly, the linker influence is reduced. Our data of eight origami blocks directly reveal the distance dependence of Förster theory and yield a reasonable R_0 value of 5.3 ± 0.3 nm well in accordance with literature values that vary between 5.4 and 6.0 nm.^[14,29,30] The variation is related to the environmentally sensitive quantum yield of Cy3.^[31] It will be a matter of future studies whether remaining fit uncertainties are related to the accuracy of our structural origami model or to uncertainties in the measurements related for example, to the linker dynamics. The high resolution of the method certainly shows that single-molecule FRET is well-suited to study structural and dynamic aspects in DNA origami and related nanostructures. FRET probes at sensitive positions could be used, for example, to characterize folding of highly complex three-dimensional origami constructs. Compared to AFM or TEM imaging, single-molecule FRET provides improved local resolution and the relatively non-invasive measurements are carried out in solution.

Experimental Section

Preparation of dsDNA Samples: HPLC-purified oligonucleotides were purchased from IBA GmbH (Göttingen, Germany). Sequences used to spatially separate the FRET pair: donor strand: 5'-ATC T_{Cy3}CA CGA TTA AGA TGA GTA TAA GAA ATA GGA GCA ACA-3'-Biotin, acceptor strands: 5'-TGT T_{Cy5}GC TCC T_{Cy5}AT TTC T_{Cy5}TA T_{Cy5}AC T_{Cy5}CA T_{Cy5}CT T_{Cy5}AA TCG TGA GAT-3'. The donor fluorophore (T_{Cy3}) is fixed on the fourth base of the donor strand while the acceptor positions (T_{Cy5}) on the acceptor strands vary from 8 nucleotides (nt) to 32 nt between donor and acceptor. In total, seven 39-basepair (bp) dsDNAs with distinct distances between donor and acceptor were tested. The DNA duplexes were formed with a molar ratio of 1:1 between each two strands at a concentration of 10 μ M per oligonucleotide. Hybridization was achieved by cooling from 95 °C down to 20 °C in the course of two hours.

Preparation of DNA Origami FRET Block: The unmodified and HPSF® purified staple strands were purchased from Eurofins MWG Operon (Ebersberg, Germany) (see the Supporting Information, Tables S6 and S7 for sequences). The following fluorescently labeled and HPLC purified sequences were acquired from IBA GmbH (Göttingen, Germany): donor strand: 5'-AAT GCG CGA GTT ACA AAT CCT GAT AAA CAT AGT AGG T_{Cy3}CT GTA AAT AAG-3', acceptor strands: 2.4 nm: 5'-AGA GTC CAC ACA GAC AAT CCA GAA AAT CAA TAT ATC TTT AGA ATT AT_{Cy5}C-3', 3.5 nm: 5'-ACA AAG TTA GTC CTG AGC GCC CAA GCG TTA TAT AAG GCG TAG AGA CT_{Cy5}A-3', 5.2 nm: 5'-AGA GTC CAC ACA GAC AAT CCA GAA AAT CAA TAT ATC TTT AGA AT_{Cy5}T ATC-3', 6.5 nm: 5'-AAT AAA CAT TT_{Cy5}T AGC GAA ATC AGA AAA AAC AGG AAA CCG ATA ATA ACG-3', 7.1 nm: 5'-TGC CTG AGA T_{Cy5}CT AAA ATC TGG TCA TCA ATA TAA ATC GCG CTA TTC ATT-3', 9.2 nm: 5'-GCC AGA ATA AAA GAA CAA AAG GGC ATT AGA CGT TGT_{Cy5} TTA AGA CTT GCG-3', 9.3 nm: 5'-AAT AGA TAA CCA

GAA GGG AAG CGC GAC ATT CAT TAT_{Cy5} CAC CCA TAG CCC-3', 14.2 nm: 5'-CGT ACT CAC AT_{Cy5}C GGC AGG AAC CGC CCA AAG ACT GGC ATG AAT AGC CGA-3'. A solution containing scaffold strand (10 nm, p8064, M13mp18 phage-based), unmodified staple strands (100 nm each), fluorescently modified staple strands (500 nm each), Tris-HCl (10 mM)+EDTA (1 mM, pH 8.0 at 20 °C), MgCl₂ (18 mM), was heated to 80 °C for 5 min., cooled to 60 °C over the course of 80 min., and cooled further down to 24 °C in 21.6 h.

Gel Electrophoresis: 2% Agarose in Tris borate (45 mM)+EDTA (1 mM, pH 8.2 at 20 °C) was heated to boiling and cooled to 60 °C. MgCl₂ (11 mM) were added and filled into the gel cask for solidification. Both scaffold strands (10 μ L of 20 nm, p8064, M13 mp18 phage-based) and initially annealed DNA origami structures (20 μ L of 10 nm) were each mixed with 6 \times Agarose Gel Loading Buffer (30% glycerol weight-to-volume in water, 0.025% xylene cyanol, 0.025% bromophenol blue). Gel pockets were filled with 2-Log DNA ladder, scaffold strands (2×10^{-13} mol) and origami structures (2×10^{-13} mol). To protect structures from denaturation, the gel cask was cooled in an ice-water bath. After running for 3 h at 70 V, the gel was stained with Ethidium Bromide (0.5 μ g mL⁻¹) and imaged. The origami structure band was extracted from the gel and run through spin columns (Freeze'n Squeeze Spin Columns, Biorad) at 5000 \times g. The samples were then imaged using a JEM-1011 transmission electron microscope (JEOL) after negative staining with uranyl acetate for 8 s.

Purification of DNA Origami FRET Blocks for Fluorescence Measurements: To remove the excess staple strands, the samples were purified using Amicon Ultra-0.5 mL Centrifugal Filters (100,000 MWCO) 4 \times at 14000 \times g for 5 min. Between each centrifugal step 450 μ L of buffer (TE with 18 mM MgCl₂) were added. After the last step, the filter was turned upside down and spun once more at 1000 \times g for 3 min to recover the samples.

Conditions for Single-Molecule Fluorescence Measurements: The single-molecule fluorescence measurements were carried out at room temperature (22 °C) in standard phosphate buffered saline (PBS) with oxygen removal using an enzymatic oxygen-scavenging system [PBS, pH 7.4, containing 10% (w/v) glucose and 12.5% (v/v) glycerine, glucose oxidase (50 μ g mL⁻¹), catalase (100–200 μ g mL⁻¹), and tris(2-carboxyethyl)phosphine hydrochloride (TCEP) (0.1 mM)]. Additionally, ascorbic acid (1 mM) and *N,N*-methylviologen (1 mM) were added to reduce blinking and bleaching according to the ROXS scheme.^[32] (For the measurements with magnesium 18 mM magnesium were added.) The solution based measurements were performed on glass slides, which were prepared with perforated adhesive silicone sheets (Grace Bio-Labs, OR) to enable small sample volumes of 50 μ L. To prevent DNA accumulation at the surface these custom sample chambers were incubated with BSA (1 mg mL⁻¹ BSA in PBS) prior to the measurement.

Single-Molecule Fluorescence Spectroscopy: To study fluorescence and energy transfer on the level of single molecules, a custom-built confocal microscope was used as described in ref. [33]. The setup allowed alternating laser excitation of donor and acceptor fluorophores on diffusing molecules with separate donor and acceptor detection. Therefore the laser beam of a pulsed supercontinuum source (Koheras SuperK Extreme, NKT Photonics, Denmark) was coupled into a single-mode fiber and alternated on microsecond time scales by use of an acousto-optical tunable filter (AOTFnc-VIS, AA optoelectronic). Two excitation wavelengths were chosen: 533 nm (spectral width of 2 nm, excitation of Cy3) and 640 nm (spectral width of 2 nm, excitation of Cy5). The spatially filtered beam entered an inverse microscope and was coupled into a

water-immersion objective (60X, NA 1.20, UPlanSApo 60XW, Olympus) by a dual-band dichroic beam splitter for solution measurements (Dualband z532/633, AHF Analysentechnik, Germany). The light intensities were 120 μW at 533 nm for the donor Cy3 and 60 μW at 640 nm for the acceptor Cy5 for the measurements of the dsDNA samples and 15 μW (533 nm) and 10 μW at 640 nm for measurements of the origami samples. The laser alternation period between the two laser beams was fixed at 50 μs . The resulting fluorescence was collected by the same objective, focused onto a 50 μm pinhole, and split spectrally at 640 nm by a dichroic beam splitter (640DCXR, AHF Analysentechnik, Germany). Two avalanche photodiodes (SPCM-AQR-14, PerkinElmer) detected the donor and acceptor fluorescence with appropriate spectral filtering (Brightline HC582/75 and Razoredge Long Pass 647, AHF Analysentechnik, Germany). The detector signal was registered and evaluated using custom made LabVIEW software.

Data Evaluation for ALEX Measurements: In solution measurements, fluorescence bursts from single molecules diffusing through the laser focus were identified by the Seidel burst search algorithm applied to the sum of donor and acceptor photons (parameters used for origami block: $T=5$ ms, $M=60$, $L=100$, for dsDNA: $T=500$ μs , $M=40$, $L=60$).^[34] Molecules are alternately excited and the fluorescence of donor and acceptor is separately detected. This defines three different photon counts: donor emission due to donor excitation F_D^D , acceptor emission due to acceptor excitation F_A^A and acceptor emission due to donor excitation F_D^A . F_D^A is sometimes referred to as the FRET channel. Using these values the stoichiometry parameter S and the proximity ratio E^* are defined [see Eqs. (2) and (3)], where S describes the ratio between donor and acceptor dyes of the sample and E^* stands for the proximity ratio between the dyes in terms of energy-transfer efficiency:^[28]

$$E^* = \frac{F^{\text{FRET}}}{F^{\text{FRET}} + F_D^D} \quad (2)$$

$$S = \frac{F^{\text{FRET}} + F_D^D}{F^{\text{FRET}} + F_D^D + F_A^A} \quad (3)$$

where $F^{\text{FRET}} = F_D^A - leF_D^D - dxF_A^A$.

The above equations include two additional terms apart from the photon counts, namely leakage le and direct excitation dx , which correct for crosstalk of the dyes. These parameters can be experimentally obtained by taking the ratio $le = F_D^A/F_D^D$ for a donor-only sample and $dx = F_D^A/F_A^A$ for an acceptor-only sample. Apart from the crosstalk correction, the detection correction factor γ is necessary to take into account differing detection efficiencies and quantum yields of the dyes. This enables the determination of an accurate E value that directly reports on the distance between the dyes [Eq. (4)]:

$$E = \frac{E^*}{\gamma + E^*(1 - \gamma)} \quad (4)$$

This accurate E value can then be used to calculate the distances according to the Förster equation [Eq. (5)]:

$$E = \frac{1}{1 + (R/R_0)^6} \quad (5)$$

For γ calculation the method employing low- and high-FRET samples was employed,^[6] that is, the measurements of the dsDNA as well as the origami samples could directly be used to calculate the corresponding γ values.

Acknowledgements

We thank Christian Steinhauer for valuable advice, Susanne Kempter and Robert Schreiber for assistance in sample preparation and Martina Bucher for assistance with the ALEX measurements. We gratefully acknowledge financial support by the DFG (TI 329/5-1 LI1743/2-1), the Volkswagen Foundation, the Nanosystems Initiative Munich, the Center for NanoScience and the Elite Network of Bavaria (International Doctorate Program NanoBio-Technology).

Keywords: DNA · FRET · nanotechnology · self-assembly · single-molecule studies

- [1] T. Förster, *Ann. Phys.* **1948**, 437, 55–75.
- [2] L. Stryer, R. P. Haugland, *Proc. Natl. Acad. Sci. USA* **1967**, 58, 719–726.
- [3] R. B. Best, K. A. Merchant, I. V. Gopich, B. Schuler, A. Bax, W. A. Eaton, *Proc. Natl. Acad. Sci. USA* **2007**, 104, 18964–18969.
- [4] M. Antonik, S. Felekyan, A. Gaiduk, C. A. M. Seidel, *J. Phys. Chem. B* **2006**, 110, 6970–6978.
- [5] A. A. Deniz, M. Dahan, J. R. Grunwell, T. Ha, A. E. Faulhaber, D. S. Chemla, S. Weiss, P. G. Schultz, *Proc. Natl. Acad. Sci. USA* **1999**, 96, 3670–3675.
- [6] N. K. Lee, A. N. Kapanidis, Y. Wang, X. Michalet, J. Mukhopadhyay, R. H. Ebricht, S. Weiss, *Biophys. J.* **2005**, 88, 2939–2953.
- [7] E. Nir, X. Michalet, K. M. Hamadani, T. A. Laurence, D. Neuhauser, Y. Kovchegov, S. Weiss, *J. Phys. Chem. B* **2006**, 110, 22103–22124.
- [8] B. Schuler, E. A. Lipman, P. J. Steinbach, M. Kumke, W. A. Eaton, *Proc. Natl. Acad. Sci. USA* **2005**, 102, 2754–2759.
- [9] L. P. Watkins, H. Chang, H. Yang, *J. Phys. Chem. A* **2006**, 110, 5191–5203.
- [10] S. Doose, H. Neuweiler, H. Barsch, M. Sauer, *Proc. Natl. Acad. Sci. USA* **2007**, 104, 17400–17405.
- [11] R. M. Clegg, A. I. Murchie, A. Zechel, D. M. Lilley, *Proc. Natl. Acad. Sci. USA* **1993**, 90, 2994–2998.
- [12] N. Di Fiori, A. Meller, *Biophys. J.* **2010**, 98, 2265–2272.
- [13] J. Vogelsang, S. Doose, M. Sauer, P. Tinnefeld, *Anal. Chem.* **2007**, 79, 7367–7375.
- [14] A. Dietrich, V. Buschmann, C. Muller, M. Sauer, *Rev. Mol. Biol.* **2002**, 82, 211–231.
- [15] N. C. Seeman, *Nature* **2003**, 421, 427–431.
- [16] P. W. Rothmund, *Nature* **2006**, 440, 297–302.
- [17] S. M. Douglas, H. Dietz, T. Liedl, B. Hogberg, F. Graf, W. M. Shih, *Nature* **2009**, 459, 414–418.
- [18] H. Dietz, S. M. Douglas, W. M. Shih, *Science* **2009**, 325, 725–730.
- [19] T. Liedl, B. Hogberg, J. Tytell, D. E. Ingber, W. M. Shih, *Nat. Nanotechnol.* **2010**, 5, 520–524.
- [20] E. S. Andersen, M. Dong, M. M. Nielsen, K. Jahn, R. Subramani, W. Mamdough, M. M. Golas, B. Sander, H. Stark, C. L. P. Oliveira, J. S. Pedersen, V. Birkedal, F. Besenbacher, K. V. Gothelf, J. Kjems, *Nature* **2009**, 459, 73–76.
- [21] Y. Ke, S. Lindsay, Y. Chang, Y. Liu, H. Yan, *Science* **2008**, 319, 180–183.
- [22] J. Sharma, R. Chhabra, C. S. Andersen, K. V. Gothelf, H. Yan, L. Yan, *J. Am. Chem. Soc.* **2008**, 130, 7820–7821.
- [23] S. Pal, Z. T. Deng, B. Q. Ding, H. Yan, Y. Liu, *Angew. Chem.* **2010**, 122, 2760–2764; *Angew. Chem. Int. Ed.* **2010**, 49, 2700–2704.
- [24] B. Ding, Z. Deng, H. Yan, S. Cabrini, R. N. Zuckermann, J. Bokor, *J. Am. Chem. Soc.* **2010**, 132, 3248–3249.
- [25] C. Steinhauer, R. Jungmann, T. L. Sobey, F. C. Simmel, P. Tinnefeld, *Angew. Chem.* **2009**, 121, 9030–9034; *Angew. Chem. Int. Ed.* **2009**, 48, 8870–8873.
- [26] Y. Ke, S. M. Douglas, M. Liu, J. Sharma, A. Cheng, A. Leung, Y. Liu, W. M. Shih, H. Yan, *J. Am. Chem. Soc.* **2009**, 131, 15903–15908.
- [27] M. Levitt, *Proc. Natl. Acad. Sci. USA* **1978**, 75, 640–644.
- [28] A. N. Kapanidis, N. K. Lee, T. A. Laurence, S. Doose, E. Margeat, S. Weiss, *Proc. Natl. Acad. Sci. USA* **2004**, 101, 8936–8941.
- [29] A. Iqbal, S. Arslan, B. Okumus, T. J. Wilson, G. Giraud, D. G. Norman, T. Ha, D. M. Lilley, *Proc. Natl. Acad. Sci. USA* **2008**, 105, 11176–11181.

- [30] S. Lee, J. Lee, S. Hohng, *PLoS One* **2010**, *5*, e12270.
- [31] M. E. Sanborn, B. K. Connolly, K. Gurunathan, M. Levitus, *J. Phys. Chem. B* **2007**, *111*, 11064–11074.
- [32] J. Vogelsang, R. Kasper, C. Steinhauer, B. Person, M. Heilemann, M. Sauer, P. Tinnefeld, *Angew. Chem.* **2008**, *120*, 5545–5550; *Angew. Chem. Int. Ed.* **2008**, *47*, 5465–5469.
- [33] J. Vogelsang, T. Cordes, P. Tinnefeld, *Photochem. Photobiol. Sci.* **2009**, *8*, 486.
- [34] C. Eggeling, S. Berger, L. Brand, J. R. Fries, J. Schaffer, A. Volkmer, C. A. M. Seidel, *J. Biotechnol.* **2001**, *86*, 163–180.

Received: September 22, 2010

Revised: January 7, 2011

Published online on February 9, 2011

3 Cellular Immunostimulation by CpG-Sequence-Coated DNA Origami Structures

3.1 Immunostimulation Measured by ELISA and Flow Cytometry

Enzyme-Linked Immunosorbent Assay (ELISA)

A standard method in immunology to detect and quantify substances like cytokines is the enzyme-linked immunosorbent assay (ELISA). This antibody based assay enables the quantitative analysis of antigens by using an enzymatic color change reaction. ELISA is the further development of formerly used radioimmunosorbent (RIST) techniques that have been the standard methods for quantitative antigen detection since the 1960s [138]. To overcome the hazardous usage of radioactively labeled antigens, the isotopes were substituted by suitable reporter enzymes such as alkaline phosphatase, horseradish peroxidase (HRP) or glucose oxidase since ELISA was developed in 1971 simultaneously by two Swedish groups [139, 140]. In publication P2, the so called 'sandwich-ELISA' method is used to quantify the amount of cytokines like interleukin 6 (IL-6) segregated by immune cells after transfection with immune stimulative oligonucleotides (see figure 3.1 A). Hereby, antigen specific monoclonal capture antibodies are immobilized on a plate. These capture antibodies bind to a distinct epitope of the cytokine antigens contained in the supernatant of the stimulated immune cells that is added to the plate. As second monoclonal antibody, a so-called detection antibody, which is biotinylated and conjugated to a streptavidin - HRP complex, binds hereupon to a further epitope of the antigen. The HRP enzyme catalyzes the added chromogenic substrate Tetramethylbenzidine (TMB) to the product TMB diimine in a two step e^- -oxidation process by reducing the oxidation agent hydrogen peroxide (H_2O_2) to water (H_2O). This reaction causes a significant color change of the solution due to the deep blue color of TMB diimine and is proportional to the amount of enzymes and therefore to the antigen concentration in the sample. Phosphoric acid stops the catalyzing reaction and provokes a further color change into yellow that can be detected on a plate reader by spectrometric estimation of the optical density (OD) of the solution at a wavelength of 450 nm. The OD of the sample gives accurate information about the amount of antigens and enables the quantitative determination of the cytokine concentration in the supernatant of the immune stimulated cells.

Fluorescence Based Flow Cytometry

Another technique used in publication P2 to quantify the effect of stimulative oligonucleotides

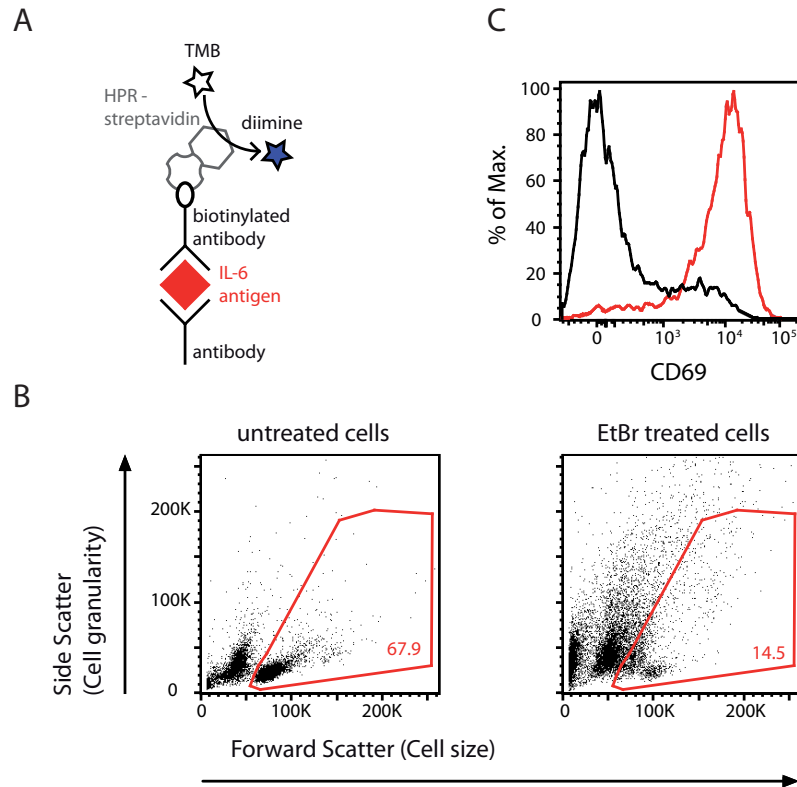


Figure 3.1: Methods to quantify grade of immune stimulation of cells. **A** 'sandwich-ELISA' from bottom to top: capture antibody immobilized on plate, antigen IL-6 (red), biotinylated detection antibody that is conjugated to streptavidin - HRP complex, TMB substrate that is catalyzed by HRP enzyme to product TMD diimine (blue), which causes color change reaction. **B** Two-dimensional forward versus side scatter dot plots showing morphology of splenocytes. Gates are set for viable cells. The number indicates the percentage of viable cells within the sample. Left: Untreated cells. Right: Cells treated with Ethidium bromide. **C** Histogram representing CD69 expression on B-cells after transfection with immune stimulative oligonucleotides (red) and without stimulation (black).

on immune cells is flow cytometry. This high-throughput analysis of cells and particles in a size range between 200 nm to 150 μ m enables the determination of size, structure and fluorescence intensity of thousands of particles within seconds. The fluorescence based flow cytometry was developed in 1968 by Dittrich and Godde after the introduction of a cell sorter by Fulwyler in 1965 [141, 142]. The basic principle of flow cytometry is the signal detection of single cells hydrodynamically focused to pass separately through a laser beam. Thereby the forward and side scattering of the laser beam as well as the intensity of the fluorescence emission of the labeled cell while crossing the beam is collected and analyzed. Forward scattering gives information about the volume of the particle passing the laser beam, while side scattering correlates with the granularity of the cell. The granularity depends on parameters like the shape of the nucleus, the composition of the cytoplasmatic vesicles and the membrane surface roughness. This scattering pattern is characteristic for each cell type and enables the identification of different cell types in one sample, such as granulocytes, macrophages, dendritic

cells and lymphocytes. Due to structural changes of apoptotic cells, also the viability can be detected by the scattering plots (see figure 3.1 B). Labeling of cells by fluorescent antibodies against cell surface antigens of the cluster of differentiation (CD) can be used to analyze the degree of immune activation of distinct cells. The data is represented in histograms or two-dimensional dot-plots that provide statistical information about the cell sample (see figure 3.1 C).

3.2 DNA Carrier Systems for Nanomedicine

The development of targeted and tailored drugs that specifically effect diseases of patients is the declared aim in pharmaceutical research. Over 100 years ago, the vision of the physician Paul Ehrlich, who is the inventor of chemotherapy and Nobel Prize laureate in Physiology or Medicine for his contribution to immunology was a 'magic bullet', an ideal therapeutic agent that selectively targets the pathogenic cells and acts toxic without any adverse reactions like cytotoxicity to healthy cells [143]. Structural DNA nanotechnology is one of the promising tools in the development of efficient delivery systems that combines many prerequisites such as size control, addressability, programmability, biocompatibility, stability, efficiency in targeting and/or uptake by cells and controlled release of drugs [23, 144]. Since size control, addressability and programmability of DNA nanostructures are discussed in chapter 1, in this caption the focus lays on parameters specific for DNA carrier systems used for medical applications: 1. stability under physiological conditions, 2. noncytotoxicity and 3. efficient delivery.

For *in vivo* applications, the stability of DNA constructs in the bloodstream for several hours is a crucial criterion for the efficiency of the carrier system. Double-stranded DNA is degraded by nucleases very fast, while assembled DNA based structures such as a compact DNA origami construct but also a DNA tetrahedron consisting of few oligonucleotides have shown longer resistance against degradation by diverse endo- and exonucleases using enzyme concentrations significantly higher than under physiological conditions [108, 145]. In publication P2 the stability of a hollow DNA origami tube was tested via incubation at 37°C for several hours in fetal bovine serum (FBS) containing buffer. FBS, a commonly used ingredient for cell culture medium, is a bovine derived blood serum with nuclease concentrations at physiological levels [80]. In contrast, a second DNA object with only a fraction of the staple molecules small enough to prevent full assembly into the designed compact structure was proven by gel electrophoresis analysis to be less stable under the same conditions (see figure 3.2 A and B). While the gel band of the DNA origami tube was still preserved after six hours of incubation, the gel band of the loose DNA object disappeared. This result was confirmed by uptake studies into cells four hours after pre-incubation of the structures in FCS medium (see figure 3.2 C and D). In the same way, small tetrahedral DNA structures were tested in FBS for the course of 24 hours and showed high resistance within the first four hours. But even after 24 hours a small fraction of the structures remained intact [79]. Mei et al. compared the stability of DNA origami structures of different shape, size and probes in lysate from various cell lines over the course of 12 hours. They demonstrated the superior structural integrity of all of these DNA origami constructs compared to individual DNA strands [146]. This promising stability characteristic of DNA structures might be further enhanced by external protection schemes that either cover the hole construct or concern the chemical structure of DNA. Rädler and co-

3. CELLULAR IMMUNOSTIMULATION BY CPG-SEQUENCE-COATED DNA ORIGAMI STRUCTURES

44

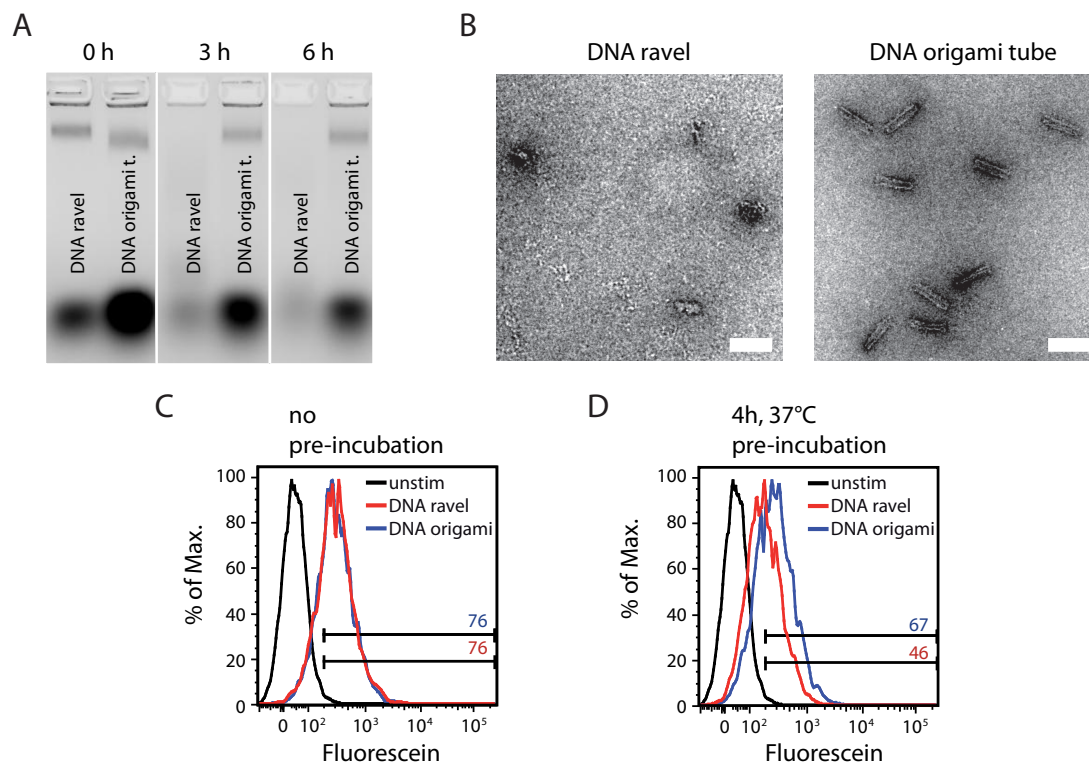


Figure 3.2: Stability of compact DNA origami structure and loose DNA ravel. **A** Gel analysis: DNA ravel (left lane) and DNA origami structure (right lane) 0h, 3h and 6h after pre-incubation in FBS containing buffer. No pre-incubation: prominent band for both DNA ravel and origami structures. 3hrs and 6hrs of incubation: band of DNA ravel disappeared while the preserved band of the DNA origami tube indicates intact structures. **B** Electron micrographs of DNA ravel (left) and DNA origami structure (right). Scale bars: 100 nm **C** Histograms show same fluorescence indicating identical uptake of DNA ravel and DNA origami structure without pre-incubation in FBS containing buffer. **D** Histograms show fluorescence shift indicating decreased uptake of DNA ravel compared to DNA origami structure after 4h of pre-incubation. Reprinted with permission from ref. [80]. Copyright 2011 American Chemical Society.

workers demonstrated the covering of double-stranded DNA by a closed shell of a lipid bilayer with an outer polyethylene glycol (PEG) shield and showed long resistance of the complex against enzymatic degradation [147]. Similar results were shown for lipid encapsulation of a DNA origami structures [23]. Direct PEGylation of DNA origami constructs was reported by Ke et al., although the effect on degradation prevention is not tested yet [148]. DNA strands with a phosphorothioate (PTO) modified backbone instead of the natural phosphodiester (PS) backbone are more resistant against degradation from nucleases. However, the PTO backbone may cause lower hybridization efficiency and therefore could provoke a premature dissociation. In publication P2, PTO modifications of single stranded DNA overhangs showed higher immune activation than unmodified DNA strands indicating a protective effect of the PTO backbone against nucleases in the endosomes.

While on the one hand the stability of the delivery system is a major prerequisite, on the other hand the non cytotoxicity and even more the residual-free degradation is essential for nanopar-

ticles to serve in medical applications without adverse effects. Like discussed in the previous part about prevention from fast degradation by nucleases of DNA nanostructures, nucleotide materials offer the advantage to be naturally degraded after a certain time within the human body. The challenge in developing DNA carrier systems is to stabilize the nanoparticles as long as they act on the cells but ensure the subsequent decomposition. Further, DNA is not inherently cytotoxic due to the fact that nucleic acids are a crucial native constituents of the cells. Several studies including publication P2 confirmed this assumption of biocompatibility even if effects on the immune system have to be taken into account when working with DNA nanostructures. While small DNA tetrahedra constructs triggered no characteristic signs of uncontrolled immune stimulation, the DNA origami tubes in publication P2 provoked an intermediate immune reaction due to the viral-based scaffold strand [79, 80]. However, in both *in vitro* studies the cell viability was unaffected by the DNA nanostructures more than 18 hours after transfection. First *in vivo* applications in mice of functionalized DNA tetrahedra caused neither toxic effects on the living organism nor unregulated detectable immune response [84]. So far, all these studies are promising indicators for the biocompatibility of DNA based nanostructures.

In recent years, DNA nanostructures emerged to be efficient carrier systems for various payloads that show good internalization characteristics into different kinds of cells like cancer and immune cells. In cancer therapy, anthracycline doxorubicin (Dox) is a well-known anti-cancer drug that intercalates DNA and subsequently activates apoptosis by inhibiting the process of replication. The efficient delivery of Dox may reduce adverse reactions due to lower dosages needed when the drug is highly concentrated on a carrier system. Two groups showed that DNA origami nanostructures can be used as effective carriers by loading high levels of Dox onto them, operating cytotoxic not only to regular breast cancer cells, but also to Dox-resistant cancer cells [85, 149]. Another promising agent in cancer therapy are small interfering RNAs (siRNAs) that suppress the expression of targeted genes in tumors. An *in vivo* study reported the successful targeted delivery of siRNAs into cells with subsequent gene silencing by attaching the siRNA molecules to DNA tetrahedral nanoparticles [150]. A next step towards highly directed delivery of drugs was the development of a logic-gated DNA origami 'nanorobot' that consists of two halves containing cell-signaling stimulating payloads. The controlled release of the payload by an aptamer-encoded logic gate was demonstrated in several *in vitro* studies [82].

The delivery of immune stimulating oligonucleotides by DNA carriers is discussed in detail in the next section and in publication P2.

3.3 Immunostimulation via CpG ODN Delivered by DNA Nanostructures

The advantages of using DNA nanostructures as carriers for immunoactive oligonucleotides instead of free DNA strands are the increased stability discussed in the previous section, the potential of targeted delivery via functionalization and high local and controllable surface density by precise spatial arrangements of the immune stimulating oligonucleotides on the DNA delivery system [79, 80, 84]. Immunoactive oligonucleotides are short DNA strands of specific sequences that act as artificial stimulants of the immune system by mimicking the DNA sequence pattern of pathogenic microbes. They are therefore a promising agent in vaccination strategies for the therapy of cancer, allergy and infectious diseases [151, 152].

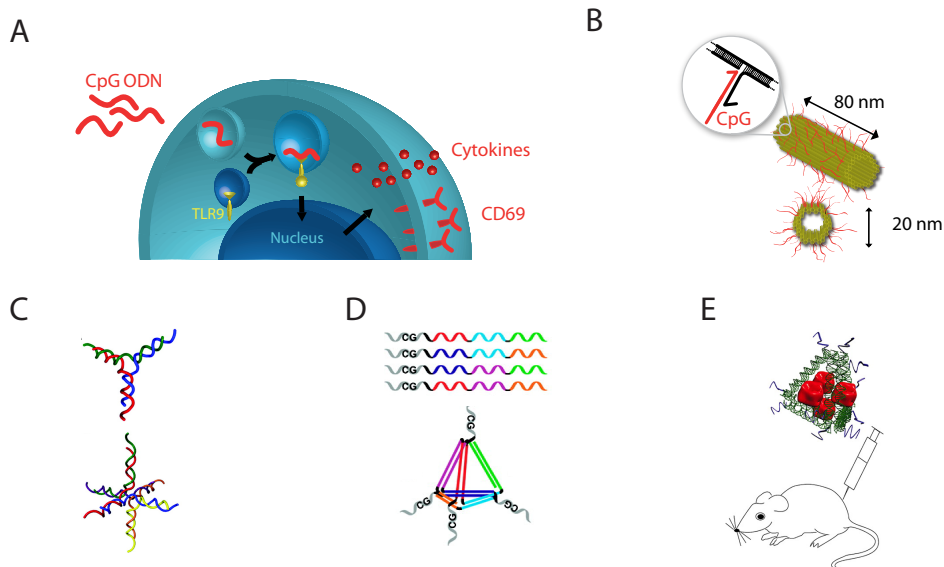


Figure 3.3: Immunostimulation by CpG Oligodeoxynucleotides delivered by DNA nanostructures. **A** CpG/TLR9-mediated pathway: CpG ODN uptake, TLR9 recognition, cytokine segregation and expression of surface molecules. **B** Hollow DNA origami tube-like structure of publication P2 decorated with 62 CpG ODNs. **C** Polypod-like DNA structures delivering three (top) and six (bottom) CpG ODNs per nanoparticle. Reprinted with permission from ref. [83]. Copyright 2012 American Chemical Society. **D** Tetrahedral DNA structure with four CpG ODNs. Reprinted with permission from ref. [79]. Copyright 2011 American Chemical Society. **E** In vivo immune activation in mice by CpG ODN containing DNA tetrahedron vaccine complexes consisting of CpG ODN adjuvant molecules (purple) and model antigen streptavidin (red). Reprinted with permission from ref. [84]. Copyright 2012 American Chemical Society.

The immune stimulating sequence of the oligonucleotide used in publication P2 is based on the finding by Krieg et al. in 1995. He reported that so-called 'CpG-motifs', which consist of unmethylated cytosine-phosphate-guanine dinucleotides integrated in some specific sequences, are responsible for previously described immune stimulating effects of bacterial DNA on distinct mammalian immune cells [153]. The fact that the genomes of vertebrates contain significantly less CpG motifs than the genomes of microbes supported the hypothesis of selective differentiation by the mammalian immune system between endogenous and invasive DNA from microorganisms like bacteria and viruses via specific DNA receptors [153, 154]. One such DNA receptor that mediates the activation of innate immunity is the endosomal Toll-like receptor 9 (TLR9), which recognizes unmethylated CpG sequences [155, 156]. As a consequence of TLR9 stimulation, proinflammatory cytokines, interferons and chemokines are secreted and particular transmembrane proteins are expressed (see figure 3.3 A) [157]. In publication P2, cytokines such as interleukin IL-6 in the supernatant of immune cells and the surface expression of the transmembrane C-type lectin CD69, an early marker of immune activation, are used as parameters to quantify the degree of external immune stimulation.

To enhance the delivery of CpG oligodeoxynucleotides (ODNs) into the endosomes of mammalian immune cells and thus initiate immune responses stronger than with free CpG ODNs, several groups have developed various DNA nanocarriers. In 2008, Takakura et al. developed

a Y-shaped DNA nanostructure consisting of three CpG motifs that provoked significantly higher amounts of IL-6 and tumor necrosis factor- α (TNF- α) in macrophage-like, TLR9-positive RAW263.7 cells than free CpG ODNs due to the increased cellular uptake of the DNA carrier system [77]. Further parameters like the increased local density within the endosome and the accessibility of the 5'-ends of the CpG motif can be crucial factors that influence this enhancement in immune stimulatory activity [78]. More complex DNA constructs like dendrimer-like and polypod-like structures that deliver higher amounts of CpG ODNs per particle showed further increased efficiency in immune stimulation in RAW264.7 cells (see figure 3.3 C)[78, 83]. In addition, three-dimensional tetrahedral DNA nanostructures were used as delivery system for up to four appending PTO modified CpG motifs, which induced cytokine segregation dependent on the number of CpG ODNs attached to the DNA tetrahedron (see figure 3.3 D)[79].

In publication P2, the local surface density could be raised to 62 CpG ODNs per carrier by attaching them onto a hollow DNA origami tube-like structure (see figure 3.3 B)[80]. The *ex vivo* immune activation by the DNA CpG origami complexes were characterized by IL-6 and IL-12 segregation and CD69 expression of freshly isolated spleen cells from mice. DNA origami bound CpG ODNs caused a significantly enhanced immune response compared to free CpG ODNs, especially when the CpG motifs were PTO modified. To exclude immune activation by the DNA origami structure itself, all parts of the system were tested separately. Even if a mediate immune response due to undecorated DNA origami structures was detected, CpG carrying complexes provoked considerably higher immune stimulation. DNA origami tubes with a control ODN sequence, where CpG was replaced by GpC and the test on TLR9 deficient mice cells further confirmed the assumed immune stimulation pathway.

Liu et al. were the first to demonstrate *in vivo* immune activation in mice after transfection with CpG ODN containing DNA tetrahedra (see figure 3.3 E)[84]. By functionalization of the CpG DNA tetrahedon complex with the model antigen streptavidin, a synthetic vaccine construct was generated that induced strong antibody responses.

To achieve the aim of developing powerful delivery systems like envisioned by Paul Ehrlich and in particular to design immunogenic vaccines, the close spatial arrangement of immune active substances like CpG ODNs to an antigen is crucial. DNA nanostructures can exactly meet this requirement.

3.4 Associated Publication P2

Cellular Immunostimulation by CpG-Sequence-Coated DNA Origami Structures

By

Verena J. Schüller, Simon Heidegger, Nadja Sandholzer, Philipp C. Nickels, Nina A.
Suhartha, Stefan Endres, Carole Bourquin and Tim Liedl

published in

ACS Nano 2011, 5, 9696–9702

Reprinted with permission from ref. [80]. Copyright 2011 American Chemical Society.

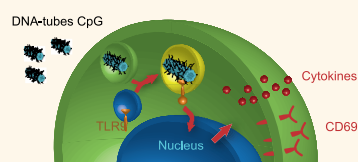
Cellular Immunostimulation by CpG-Sequence-Coated DNA Origami Structures

Verena J. Schüller,^{†,‡} Simon Heidegger,^{†,‡} Nadja Sandholzer,[‡] Philipp C. Nickels,[†] Nina A. Suhartha,[‡] Stefan Endres,[‡] Carole Bourquin,^{‡,§,*} and Tim Liedl^{†,*}

[†]Center for Nanoscience and Department of Physics, Ludwig-Maximilians-Universität, Geschwister-Scholl-Platz 1, 80539 München, Germany, [‡]Abteilung für Klinische Pharmakologie, Medizinische Klinik, Klinik der Universität München, Ziemssenstrasse 1, 80336 München, Germany, and [§]Chair of Pharmacology, Department of Medicine, University of Fribourg, Chemin du Musée 5, 1700 Fribourg, Switzerland. [‡]These authors contributed equally to this work.

Rapid development of the field of DNA nanotechnology, where DNA is used as a building material for nanoscale objects^{1,2} and functional devices,^{3,4} opens the route for the construction of carrier systems that can interact with cellular machinery on the molecular level. In particular, DNA assemblies based on the DNA origami method^{5–7} can exhibit shapes of high complexity presenting nanometer-precise arrangements of (biomolecular) components on their surfaces.^{8–11} This method uses a 7 to 8 kb long M13mp18 phage-derived DNA single strand that is folded into a desired shape by some 200 oligonucleotides. To be employable as a molecular carrier system in mammals, any DNA construct must meet three important criteria: (i) it needs to be stable in the extracellular space and in the cytoplasm of the cell long enough to fulfill its predefined task; (ii) no toxic side effects should occur; and (iii) the mammalian immune system should tolerate the nanoscopic carrier systems. So far, it has been shown that oligonucleotide-based tetrahedral cages are resistant to several endonucleases,¹² can enter mammalian cells, stay intact, once taken up, for at least 48 h,¹³ and can act as carriers of CpG oligonucleotides into macrophage-like RAW264.7 cells, as shown in a very recent study by Li *et al.*¹⁴ Also Nishikawa, Takakura, and co-workers have demonstrated earlier that Y-shaped and dendritic CpG-containing DNA structures are internalized efficiently by the same cell line and provoke enhanced immunostimulation responses.^{15,16} Furthermore, programmed RNA hairpins can sequence-selectively trigger apoptosis in cancer cells¹⁷ or act as color-coded labels in *in situ* experiments¹⁸ in a wide variety of cell types.

ABSTRACT To investigate the potential of DNA origami constructs as programmable and noncytotoxic immunostimulants, we tested the immune responses induced by hollow 30-helix DNA origami tubes covered



with up to 62 cytosine-phosphate-guanine (CpG) sequences in freshly isolated spleen cells. Unmethylated CpG sequences that are highly specific for bacterial DNA are recognized by a specialized receptor of the innate immune system localized in the endosome, the Toll-like receptor 9 (TLR9). When incubated with oligonucleotides containing CpGs, immune cells are stimulated through TLR9 to produce and secrete cytokine mediators such as interleukin-6 (IL-6) and interleukin-12p70 (IL-12p70), a process associated with the initiation of an immune response. In our studies, the DNA origami tube built from an 8634 nt long variant of the commonly used single-stranded DNA origami scaffold M13mp18 and 227 staple oligonucleotides decorated with 62 CpG-containing oligonucleotides triggered a strong immune response, characterized by cytokine production and immune cell activation, which was entirely dependent on TLR9 stimulation. Such decorated origami tubes also triggered higher immunostimulation than equal amounts of CpG oligonucleotides associated with a standard carrier system such as Lipofectamine. In the absence of CpG oligonucleotides, cytokine production induced by the origami tubes was low and was not related to TLR9 recognition. Fluorescent microscopy revealed localization of CpG-containing DNA origami structures in the endosome. The DNA constructs showed in contrast to Lipofectamine no detectable toxicity and did not affect the viability of splenocytes. We thus demonstrate that DNA origami constructs represent a delivery system for CpG oligonucleotides that is both efficient and nontoxic.

KEYWORDS: DNA origami · DNA nanotechnology · immunology · cytotoxicity · CpG

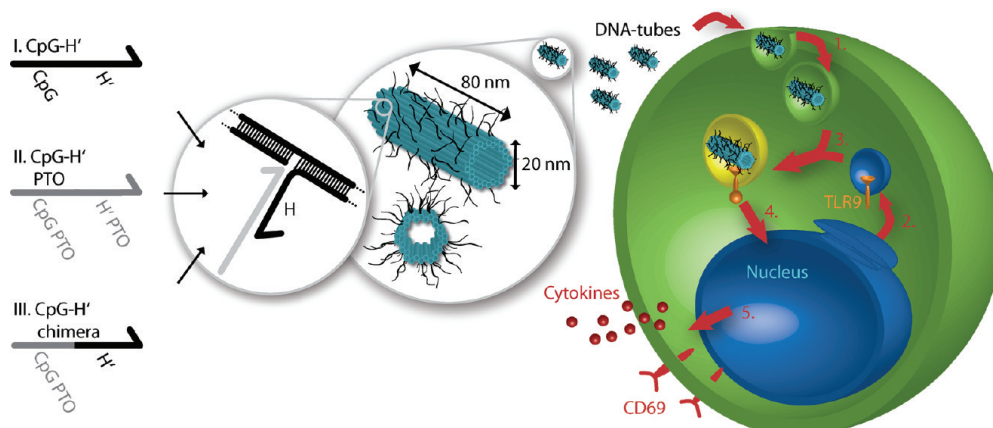
A further study tested the degradation of DNA origami structures exposed to multiple endonucleases, including DNase I, T7 endonuclease I, T7 exonuclease, *Escherichia coli* exonuclease I, Lambda exonuclease, and MseI restriction endonuclease and found high stabilities of the DNA constructs compared to duplex plasmid DNA.¹⁹ This is consistent with findings of Mei *et al.*, who demonstrated that DNA

* Address correspondence to carole.bourquin@unifr.ch, tim.liedl@lmu.de.

Received for review August 17, 2011 and accepted November 17, 2011.

Published online November 17, 2011 10.1021/nn203161y

© 2011 American Chemical Society



Scheme 1. Design of 30-helix DNA origami tube and endocytotic pathway. Left: Three different types of CpG-H's with (I) unmodified phosphate backbone, (II) phosphorothioate (PTO)-modified backbone, and (III) partly PTO-modified backbone. Middle: Computer model of front (bottom) and side (top) view of 30-helix tube. Blue cylinders indicate double helices; black lines indicate possible connection sites for CpG sequences. Right: (1) DNA origami tube internalized by endocytosis; (2) vesicle segregated by the Golgi apparatus containing the transmembrane Toll-like receptor 9 (TLR9); (3) fusion of endosome with DNA origami tube and TLR9 containing vesicle; (4) recognition of CpG sequence by TLR9 and starting signaling cascade; (5) expression of surface molecules and release of cytokines that stimulate the further immune response.

origami structures maintain their structural integrity when exposed to cell lysates of various cell lines.²⁰

In this study, we focused on the immunological response of mammalian primary splenic cells to DNA origami structures. Indeed, the mammalian immune system is poised to detect foreign DNA from invading viruses or bacteria through specific receptors that, upon recognition of their cognate DNA ligand, initiate a full-blown immune response. One such receptor is the endosomal Toll-like receptor 9 (TLR9), which recognizes unmethylated CpG sequences that are a hallmark of microbial DNA.²¹ Further immunological DNA receptors detect DNA structures from viruses in the cytosol, from which endogenous DNA is normally absent.²² Stimulation of these receptors following specific recognition of DNA leads to activation of innate immunity and, in particular, to the secretion of proinflammatory cytokine mediators such as the interleukins IL-6 and IL-12p70.^{23,24} For the implementation of DNA origami constructs as molecular delivery systems, it is therefore essential to fully understand their immunostimulatory potential in order to tightly control the initiation of immune responses according to the therapeutic goal.

RESULTS AND DISCUSSION

We designed a DNA origami construct to serve as an efficient biologically active carrier system for CpG sequences in order to stimulate immune responses in mammalian cells. For this purpose, we developed a hollow tube-shaped DNA origami structure consisting of 30 parallel double helices with maximized surface area for both 62 inner or 62 outer binding sites (handle sequences H) for cytosine-phosphate-guanine (CpG) + anchor sequences (CpG-H's). The CpG sequence used in all experiments is referred to as CpG

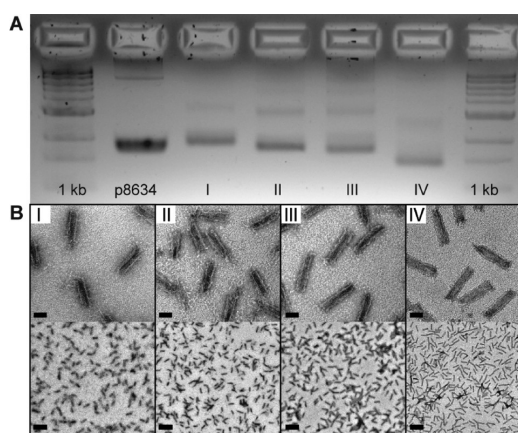


Figure 1. Characterization of DNA origami tubes. (A) Gel analysis of assembled DNA origami tubes after purification with AMICON spin filters. Left to right: 2-log 1 kb DNA ladder, p8634 scaffold, (I) tube CpG, (II) tube CpG PTO, (III) tube chimera, (IV) tube without CpG, 2-log 1 kb DNA ladder. (B) Electron micrograph of the DNA origami tubes I-IV. Scale bars: 30 nm (top), 200 nm (bottom).

1826, a well-characterized, highly active 20-mer oligonucleotide, which is specific for mouse TLR9.²⁵ Three different types of phosphate backbone for the CpG-H's were used in this study: (I) unmodified CpG-H' (tube CpG); (II) CpG-H' PTO with a phosphorothioate-modified backbone (tube CpG PTO); (III) CpG-H' chimera with PTO-modified CpG sequence and unmodified H' sequence (tube chimera) (see Materials and Methods). A plain tube without handles H for CpG-H's (tube w/o CpG) as well as tubes decorated with GpC-H's instead of CpG-H's served as controls. The DNA origami tubes were assembled from 227 oligonucleotides (staple strands) that fold an 8634 nucleotide (nt) M13mp18-based single strand (scaffold) into shape during a 2 h long annealing

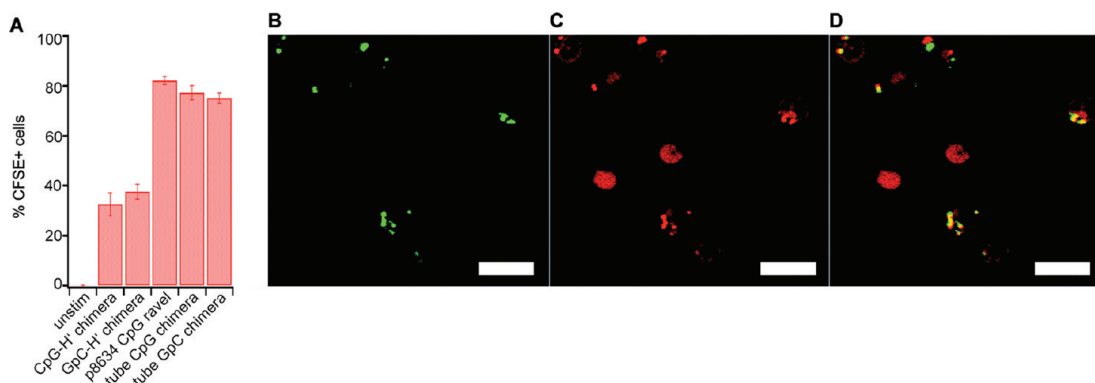


Figure 2. Uptake of CpG-covered DNA nanostructures by immune cells. (A) Uptake of fluorescently labeled CpG sequences coupled to different DNA nanostructures by splenic macrophages. The graph shows the percentage of cells that are positive for the fluorescent marker. Data show the mean value of triplicate samples \pm SE and are representative of two independent experiments. (B–D) Confocal micrographs of splenocytes showing intracellular colocalization of DNA origami CpG tubes and lysosomes 4 h after transfection. (B) Green: DNA origami tubes chimera III with FITC. (C) Red: LysoTracker (lysosomes). (D) Merge of A and B. Yellow: colocalized DNA origami CpG tubes in lysosomes. Due to diffusion of cells between time-delayed image capturing of A and B, some colocalized objects are shifted in C. Scale bars: 10 μ m.

procedure. The construct has a designed length of \sim 80 nm and a diameter of \sim 20 nm, if a spacing of 0.34 nm between two stacking bases and a center-to-center distance of 2.5 nm between two parallel helices is assumed.^{5,9} For each of the 62 inner and outer CpG binding sites, a particular staple strand is extended with a 18 nt long sequence H that is complementary to the anchor sequence H' of the CpG-H's (Scheme 1). Using the DNA origami tube as a defined carrier of 62 CpG-H's per structure enables a high local concentration of CpG sequences within the endosomes after internalization. The correct assembly of the DNA structures I–III and the plain tube (IV) was analyzed with gel electrophoresis (Figure 1A) and transmission electron microscopy (TEM) (Figure 1B). The prominent band for all DNA origami tubes as well as the decreased mobility of CpG-decorated tubes (I–III) compared to the tube without CpG (IV) indicates the efficient binding and assembly of the DNA origami tubes.

We first tested whether DNA origami tubes can serve as a delivery tool for immunostimulatory CpG oligonucleotides. Therefore, we analyzed the cellular uptake of fluorescently labeled CpG-H' strands coupled to different DNA nanostructures (Figure 2A). Freshly isolated mouse splenocytes were incubated with the DNA samples for 3 h, and uptake of fluorescein isothiocyanate (FITC)-coupled CpG-H' strands was analyzed by flow cytometry. Splenocytes consist of a pool of immune cell subsets, including antigen-presenting cells such as dendritic cells and macrophages that initiate and control immune responses, and immune effector cells such as B and T lymphocytes. The uptake of CpG-H' strands by macrophages was much more efficient when the CpG oligonucleotides were coupled to the DNA origami tubes or a ravel consisting only of the p8634 scaffold and the handle H'-containing staple strands (p8634 CpG ravel, TEM image in Supporting

Figure 6). We conclude that structures of larger size and higher compactness get incorporated more efficiently than individual or short DNA single strands. This effect was independent of the CpG motif as GpC-H' strands showed similar uptake characteristics. As the receptor that detects CpG sequences, TLR9, is located in the endosome, an endosomal uptake of the DNA origami tubes is a vital prerequisite for the efficient delivery of synthetic TLR9 ligands. Fluorescence microscopy confirmed the colocalization of CpG-decorated origami tubes labeled with FITC together with the endosomal marker LysoTracker, demonstrating that the DNA origami constructs indeed target CpG sequences to the endosome (Figure 2B–D).

To examine whether the DNA constructs induce an immune response, freshly isolated mouse splenocytes were incubated with the DNA samples for 18 h. The immunostimulatory activity of the DNA origami tubes and of all control samples was quantified by measuring the induced secretion of different proinflammatory cytokines such as IL-6 in culture supernatants of stimulated cells by enzyme-linked immunosorbent assay (ELISA). In addition, surface expression of the transmembrane C-type lectin CD69, an early marker of immune activation, was examined on different immune cell subsets by flow cytometry after staining of cell surface molecules by specific fluorochrome-coupled antibodies. The gating strategy for lymphocyte subsets can be found in Supporting Figure 1.

We tested the immunostimulatory activity of the individual components of the DNA constructs, that is, a mix of the 227 staple strands, the p8634 scaffold strand, and the tube without CpG (IV) and observed that the mix of staple strands did not induce detectable IL-6 production. The p8634 scaffold strands and DNA origami tubes without anchors for CpG-H's induced only low levels of IL-6 (Figure 3). Analysis of further proinflammatory cytokines showed that the release of

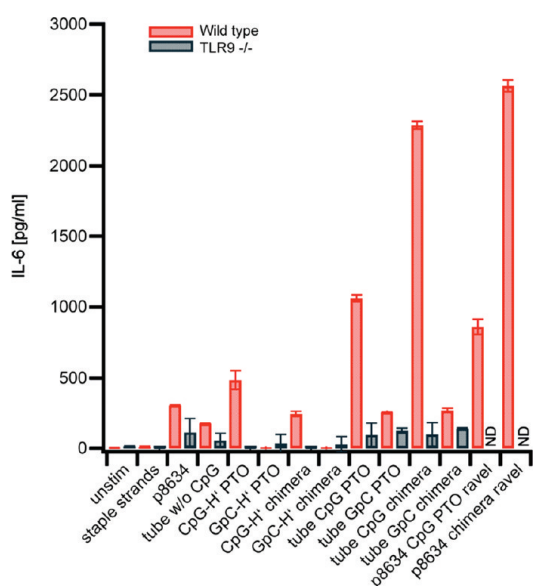


Figure 3. ELISA analysis of IL-6 levels after splenocytes were cultured in the presence of different DNA origami structures for 18 h; 50 μ L of 2.4 nM (DNA origami tubes, p8634, staple strands) or 50 μ L of 62 \times 2.4 nM (CpG-H' PTO, CpG-H' chimera) of sample was added per 400 000 cells in a well. In all experiments, the net CpG weight was 50 ng. Data show the mean value of triplicate samples \pm SE and are representative for two independent experiments.

IL-12p70 in response to the DNA origami tubes was similar to IL-6 (Supporting Figure 2) and that origami tubes did not induce detectable levels of interferon- α or IL-1 β (data not shown). Flow cytometry measurements of the early activation marker CD69 on the surface of dendritic cells, a cell type that plays a crucial role in the initiation of immune responses, confirmed these results (Figure 4A). The mix of staple strands did not upregulate CD69 expression, the scaffold strand p8634, as well as the tube without CpG-triggered intermediate cell activation in this cell type. B lymphocytes responded with high expression of CD69 in response to the unfolded p8634 scaffold, while the DNA origami tube induced only moderate CD69 upregulation (Figure 4B,C). The recognition of the DNA origami tube or its individual components was largely independent of TLR9, as cells from mice that are genetically deficient for this receptor (TLR9^{-/-}) were activated by these structures to an extent similar to wild-type cells (Figure 4). We thus show that even in the absence of immunostimulatory CpG oligonucleotides, DNA origami constructs can activate innate immunity *via* non-TLR9-mediated pathways, an effect that must be taken into consideration for future applications of DNA origami constructs as drug delivery vehicles.

Next, the ability of DNA origami tubes to act as an efficient nontoxic CpG sequence carrier to induce a potent immune response was tested. The immunostimulation through free CpG-H's, either with an entire phosphorothioate (PTO) or chimera backbone (Scheme 1), was compared to the immune activation caused

by these CpG-H's bound to the DNA origami tube (Figures 3 and 4). ELISA as well as flow cytometry analysis showed that splenocytes exposed to free CpG-H's produced moderate amounts of IL-6 and showed intermediate CD69 expression. In contrast, CpG-H'-decorated DNA origami tubes triggered high cytokine production and resulted in an up to 5-fold increase in CD69 expression on splenic dendritic cells. The CpG-induced immunostimulation was entirely dependent on TLR9 since the CpG-mediated increase in immune activation was lost in TLR9-deficient cells. In addition, CpG immune activation was highly sequence-specific, as DNA origami tubes bearing control oligonucleotides with an inverted GpC sequence did not stimulate stronger responses than origami tubes without CpG (Figures 3 and 4). Interestingly, no significant differences in cytokine secretion as well as cell activation was observed for DNA tubes carrying the CpG-H's on the inner surface or on the outer surface (Supporting Figure 3). This points toward the dissociation of the CpGs from the carrier tubes or toward a partial disassembly of the tubes within the endosome as the TLR9 receptors are embedded in the endosomal membranes and could not access the CpG sequences on the inner surface otherwise.

We further compared the efficacy of the DNA origami tubes for delivery of CpG oligonucleotides to that of the commonly used lipid transfection reagent Lipofectamine, which mediates intracellular delivery of oligonucleotides (Supporting Figure 4).²⁶ We show that the IL-6 production and CD69 expression on B cells induced by CpG-decorated origami tubes is superior to that induced by the same tubes complexed with Lipofectamine, demonstrating that DNA origami tubes represent an efficient delivery system for CpG oligonucleotides. The cellular viability of cells stimulated with DNA constructs was verified by flow cytometry analysis based on forward and side scattering: The proportion of live lymphocytes did not change following activation with CpG-decorated origami tubes in the absence of a transfection reagent. In contrast, cells incubated with the same tubes complexed with Lipofectamine showed a partly decreased viability (Supporting Figure 5).

Although the amount of CpGs used in all experiments was the same, immunostimulation was strongest when the CpG sequences were conjugated to the carrier tubes. Our experiments also demonstrate that the immune response initiated by the decorated origami tubes does not simply rely on the larger amount of delivered DNA: origami tubes that carry 62 non-stimulating GpC-H' sequences gave rise to activation levels comparable to tubes without any strands coupled to their anchors (Figures 3 and 4). The highest levels of IL-6 secretion and cell activation were observed for tubes decorated with the chimera CpG-H's and p8634 CpG ravel, which were not conjugated with

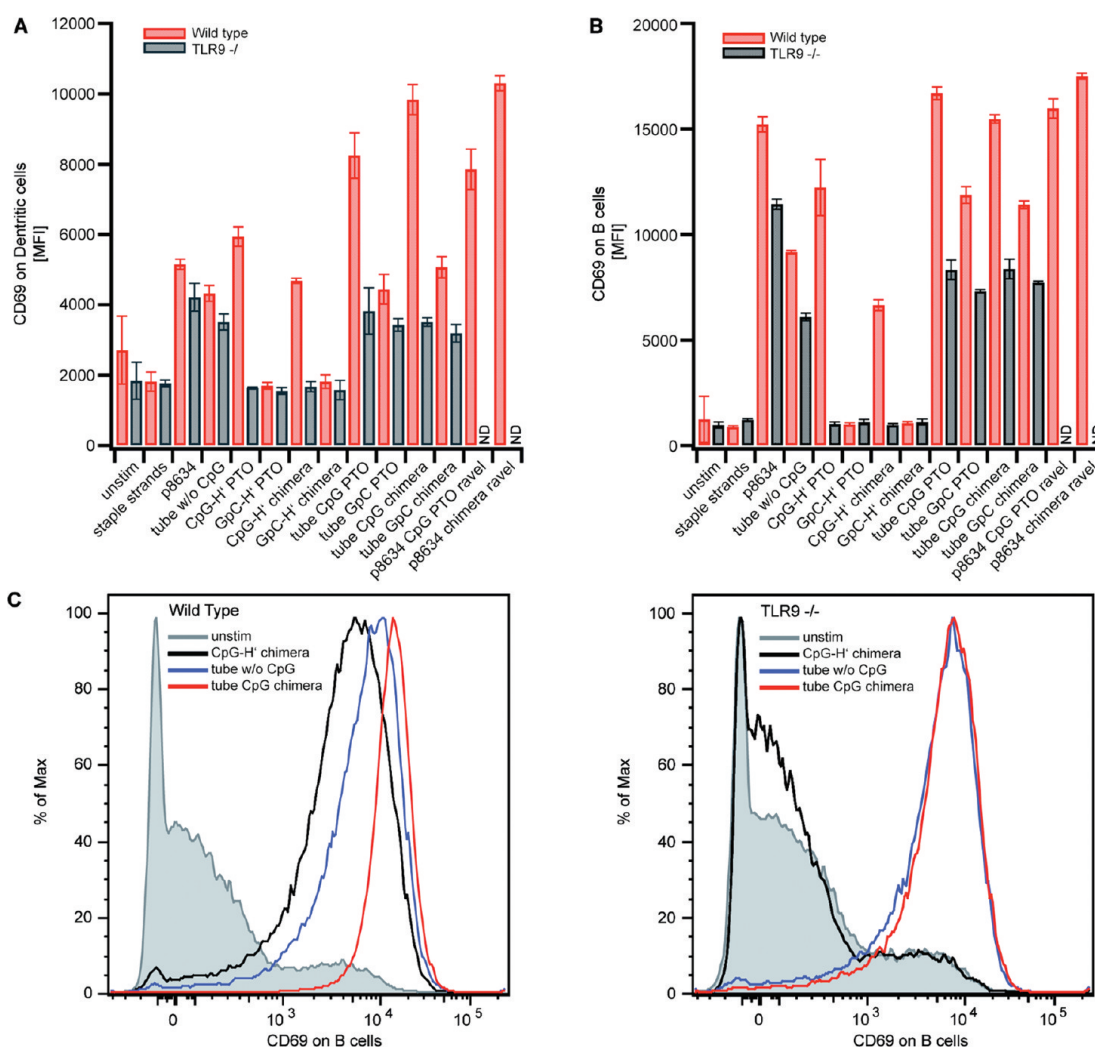


Figure 4. Flow cytometry analysis of immune cell activation after incubation with DNA origami tubes. Freshly isolated splenocytes from wild-type and TLR9-deficient mice were incubated with 50 μ L of 2.4 nM (DNA origami tubes, p8634, staple strands) or 50 μ L of 62×2.4 nM (CpG-H' PTO, CpG-H' chimera) for 18 h. Surface expression of the early activation marker CD69 was analyzed on (A) dendritic cells and (B) B lymphocytes. (C) Representative histograms show CD69 expression on B cells after splenocytes have been incubated for 18 h with the indicated DNA samples. Data show the mean value of triplicate samples \pm SE and are representative of at least two independent experiments. CD69 expression levels are presented as the mean fluorescence intensity (MFI) of the fluorochrome coupled to a specific anti-CD69 antibody.

a transfection agent (Figure 3). This can be explained by the discussed high internalization efficiency of compact and large objects in combination with a degradation-resistant PTO backbone of the conjugated CpGs (*cf.* Figure 2). The slightly less pronounced immune response of cells that were incubated with tubes that carry full PTO-modified CpG-H's may result from the lower hybridization efficiency of these DNA anchors to their handle sites. This could lead to an untimely dissociation of the CpGs from the carrying tube. Tubes that carry CpG-H's without any PTO modification also provoke lower immune activation than their chimera-decorated counterparts (Supporting Figure 4), an effect that may originate from the fast degradation of these oligonucleotides in the DNase-rich endosome. Importantly, even CpG oligonucleotides with an unmodified backbone lead to enhanced

immune responses when DNA origami tubes are used as carriers, suggesting that this delivery system protects the CpGs to some extent from degradation (Supporting Figure 4B).

We stated above that the elevated immunostimulatory activity of DNA origami structures may result from a more efficient cellular uptake of origami-bound CpG-H' over free CpG-H' which might be due to the folded origamis compactness and size. To test this hypothesis, we assembled constructs that consist of the p8634 scaffold strand and only the 62 staple stands that carry the CpG anchors (p8634 CpG ravel). These oligonucleotides are not able to fold the entire scaffold strand and thus form a ravel-like structure with moderate compactness (Supporting Figure 6A). However, CpG-decorated ravels showed similar uptake and activation characteristics as the decorated DNA origami tubes

(Figures 2–4). In contrast, samples that consisted only of the scaffold strand and an excess of CpG oligonucleotides were not able to assemble into any structure and showed low immunogenic potential similar to the scaffold strand alone (data not shown). Our results suggest that the immune-activating potential is not dependent on the three-dimensional (3D) shape but the construct's compactness, size, and stability. Importantly, DNA origami tubes proved to be more stable than DNA ravel when kept in fetal bovine serum (FBS)-containing medium at 37 °C for several hours (Supporting Figure 6B). Uptake studies confirmed this hypothesis by showing less internalization and immune stimulation of DNA ravel compared to origami structures after 4 h of preincubation of the structures in FBS before addition to cells (Supporting Figure 6C). This stability of the DNA origami structure can be an essential advantage that might play a key role in future *in vivo* applications. Further studies on the cell uptake of DNA constructs depending on their 3D shape will help to elucidate this phenomenon.

In conclusion, we describe a novel delivery system for immune-activating CpG oligonucleotides that targets

the endosome. This system is built from biomolecules—the origami tube solely consists of DNA—and is nontoxic. The unmodified DNA origami tubes as well as their individual building blocks trigger only non-TLR9-mediated immune responses in primary immune cells. If the same DNA tubes are decorated with CpG sequences, pronounced immunostimulation *via* the TLR9 is observed. Although the biological application of DNA nanostructures is a very young field of research and more studies on the cytotoxicity, the immunological behavior, and the general biocompatibility of DNA constructs must be executed, we believe that such objects can be used as intelligent drug carriers. In addition to being used as enclosing containers that potentially release their payload on demand,⁶ DNA architectures can also be modified with biologically active molecules on their surfaces to trigger cellular mechanisms such as immune responses as we have shown in this study. Since DNA oligonucleotides can be modified with a wide variety of biomolecules, this approach could be extended in combination with viral moieties to generate vaccines and adjuvants with nanometer precisely tailored surfaces.

MATERIALS AND METHODS

Design and Preparation of DNA Origami CpG Tube. DNA constructs were designed using the software caDNAo developed by Douglas *et al.*²⁷ We designed a hollow DNA origami tube with a length of 80 nm and a diameter of 20 nm which can be decorated with up to 62 cytosine-phosphate-guanine (CpG: TCC ATG ACG TTC CTG ACG TT) + anchor sequences (CpG-H's; H': AAG ATT ACG GTG AAG AGA) or guanine-phosphate-cytosine (GpC-H's: TCC ATG AGC TTC CTG AGC TT) + the same anchor sequences. Site-selective binding is achieved *via* the anchor parts H' of the CpG-H's that bind to complementary single-stranded DNA handles (H) protruding from the origami structures at defined positions. To achieve an untwisted well-formed DNA origami tube, we chose a honeycomb arrangement of double helices. We used an 8634 nucleotide (nt) M13mp18-based single strand as a scaffold to arrange 227 oligonucleotides (staple strands) into a tube-shaped DNA origami structure consisting of 30 parallel double helices. To prevent stacking effects of blunt dsDNA ends, we connected the ends of two collateral helices with loops of 24–52 unpaired bases. During this study, we used three different types of backbone for the CpG-H's (5'-TCC ATG ACG TTC CTG ACG TT AAG ATT ACG GTG AAG AGA-3') to functionalize the DNA origami tube: (I) DNA CpG-H's consisting of the 20 nt CpG sequence and the 18 nt anchor sequence; (II) CpG-H's with a phosphorothioate-modified backbone (PTO); (III) chimera CpG-H's with PTO-modified CpG sequence and unmodified H' sequence. Those nucleotides also had a fluorescein isothiocyanate (FITC) label on the 5'-end. As a reference, we also prepared a DNA origami tube without conjugated CpG-H's (sample IV in Figure 1). The staple strands and the unmodified CpG-H's were HPSF purified by the supplier, and the PTO-modified CpG-H's were HPLC purified by the supplier. All oligonucleotides were purchased from Eurofins MWG Operon (Ebersberg, Germany). For annealing of the complete constructs, 10 nM of scaffold strand (p8634, M13 mp18 phage-based), 100 nM of each unmodified staple strand, and 12.4 mM of CpG-H's were mixed in Tris-HCl (10 mM) + EDTA (1 mM, pH 8.0 at 20 °C) and 16 mM MgCl₂. This solution was heated to 80 °C for 5 min, cooled to 60 °C over the course of 80 min, and cooled further to 24 °C in 35 min.

Purification of DNA Origami CpG Tube. To remove the 10× excess of staple strands and 20× excess of unbound CpG-H's after the annealing process, the DNA origami samples were purified using Amicon Ultra-0.5 mL centrifugal filters (100 000 MWCO). Then, 100 μL of annealed DNA origami tubes and 400 μL of buffer (10 mM Tris-HCl + 1 mM EDTA, pH 8.0 at 20 °C + 16 mM MgCl₂) were filled into one filter and centrifuged four times at 14 000g for 5 min. Between every centrifugation step, the flow-through is removed and the filter is refilled with 500 μL of buffer. To recover the purified DNA origami samples, the filter was turned upside down and centrifuged once more at 1000g for 3 min. Overall, roughly 70% of the samples are lost during this purification procedure. We obtained ~20 μL of 14 nM decorated and undecorated origami samples from each filter.

Gel Electrophoresis and Transmission Electron Microscopy. For analysis of the DNA origami tubes, the samples were electrophoresed in an agarose gel; 2% agarose was dissolved in Tris borate (45 mM) + EDTA (1 mM, pH 8.2 at 20 °C) by heating to boiling. After cooling to 60 °C, MgCl₂ (11 mM) was added and filled into the gel cask for solidification. Twenty microliters of 2.4 nM filtered DNA origami tube samples I–IV was each mixed with 4 μL of 6× agarose gel loading buffer (30% glycerol weight-to-volume in water, 0.025% xylene cyanol, 0.025% bromophenol blue) before they were filled into the gel pockets. Additionally, 10 μL of 100 nM scaffold strands (p8634) mixed with 2 μL of 6× agarose gel loading buffer was filled next to the DNA origami tubes as well as a 1 kb 2-log DNA ladder. During running for 3 h at 60 V, the gel cask was cooled in an ice–water bath to prevent heat-induced denaturation of the DNA origami tubes. For imaging, the gel was stained with ethidium bromide (0.5 μg/mL) for 30 min. The filtered DNA origami tubes were further checked by electron microscopy using a JEM-1011 transmission electron microscope (JEOL). The DNA origami structures were adsorbed on plasma-exposed carbon-coated grids (spi Formvar, Cu) and then negatively stained with 1% uranyl acetate for 8 s.

Stimulation of Cells. Female C57BL/6 mice were purchased from Harlan-Winkelmann (Rossdorf, Germany). Mice were 6–10 weeks of age at the onset of experiments. Freshly isolated splenocytes were suspended in ammonium chloride buffer to lyse erythrocytes, washed with PBS, and seeded in a 96-well

plate (Falcon); 400 000 cells per well in culture medium (RPMI VLE, 10% FCS, 2 mmol/L L-glutamine, 100 μ g/mL streptomycin, and 1 IU/mL penicillin and 0.0001% β -mercaptoethanol). For stimulation, cells were incubated with different origami probes or oligonucleotides for 18 h at 37 °C in 10% CO₂. For the analysis of origami structure stability, the constructs were kept in serum-containing medium for 4 h at 37 °C prior to cell culture. Culture supernatants and cells were collected and analyzed by ELISA and flow cytometry.

Flow Cytometry and ELISA. Concentration of IL-6 and IL-12p70 in culture supernatants was determined by ELISA according to the manufacturer's instructions (Opteia, BD Biosciences). For flow cytometric analysis, cells were stained with fluorochrome-conjugated monoclonal antibodies (B220, CD3, CD11b, CD11c, CD69, CD80, F4/80, and isotype controls) from BioLegend. For uptake analysis, fluorescence intensity of fluorescein coupled to CpG-H' was determined by flow cytometry. Data were acquired on a FACSCalibur or a FACSCanto II (BD Biosciences) and analyzed using FlowJo software (Tree Star, Ashland, OR).

Confocal Microscopy. Splenocytes were incubated for 5 h with fluorescein-5'-tagged CpG oligonucleotides, washed, and resuspended in culture medium. Then, 75 nM LysoTracker (Invitrogen) and 3 μ g/mL Hoechst (Invitrogen) were used for lysosomal and nuclear staining. Stained cells were visualized using a confocal laser scanning microscope (TCS SP5II, Leica).

Acknowledgment. We thank J. O. Rädler for helpful discussions. This work was funded by the DFG cluster of excellence Nanosystems Initiative Munich (NIM), DFG LI1743/2-1, and the Bavarian Immunotherapy Network BayImmuNet (to C.B. and S.E.). N.S. and S.H. are supported by the Graduiertenkolleg 1202 of the German Research Foundation.

Supporting Information Available: Additional experimental data, the design and the sequences of the DNA origami construct. This material is available free of charge via the Internet at <http://pubs.acs.org>

REFERENCES AND NOTES

- Seeman, N. C. Nucleic-Acid Junctions and Lattices. *J. Theor. Biol.* **1982**, *99*, 237–247.
- Seeman, N. C. Nanomaterials Based on DNA. *Annu. Rev. Biochem.* **2010**, *79*, 65–88.
- Yurke, B.; Turberfield, A. J.; Mills, A. P.; Simmel, F. C.; Neumann, J. L. A DNA-Fueled Molecular Machine Made of DNA. *Nature* **2000**, *406*, 605–608.
- Liedl, T.; Sobey, T. L.; Simmel, F. C. DNA-Based Nanodevices. *Nano Today* **2007**, *2*, 36–41.
- Rothmund, P. W. K. Folding DNA To Create Nanoscale Shapes and Patterns. *Nature* **2006**, *440*, 297–302.
- Andersen, E. S.; Dong, M.; Nielsen, M. M.; Jahn, K.; Subramani, R.; Mamdouh, W.; Golas, M. M.; Sander, B.; Stark, H.; Oliveira, C. L. P.; Pedersen, J. S.; Birkedal, V.; Besenbacher, F.; Gothelf, K. V.; Kjems, J. Self-Assembly of a Nanoscale DNA Box with a Controllable Lid. *Nature* **2009**, *459*, 73.
- Douglas, S. M.; Dietz, H.; Liedl, T.; Högberg, B.; Graf, F.; Shih, W. M. Self-Assembly of DNA into Nanoscale Three-Dimensional Shapes. *Nature* **2009**, *459*, 414–418.
- Sharma, J.; Chhabra, R.; Andersen, C. S.; Gothelf, K. V.; Yan, H.; Yan, L. Toward Reliable Gold Nanoparticle Patterning on Self-Assembled DNA Nanoscaffold. *J. Am. Chem. Soc.* **2008**, *130*, 7820–7821.
- Stein, I.; Schüller, V.; Böhm, P.; Tinnefeld, P.; Liedl, T. Single-Molecule FRET Ruler Based on Rigid DNA Origami Blocks. *ChemPhysChem* **2011**, *12*, 689–695.
- Jahn, K.; Tørring, T.; Voigt, N. V.; Sørensen, R. S.; Kodal, A. L. B.; Andersen, E. S.; Gothelf, K. V.; Kjems, J. Functional Patterning of DNA Origami by Parallel Enzymatic Modification of Staple Strands. *Bioconjugate Chem.* **2011**, *22*, 819–823.
- Schreiber, R.; Kempter, S.; Holler, S.; Schüller, V.; Schiffels, D.; Simmel, S. S.; Nickels, P. C.; Liedl, T. DNA Origami-Templated Growth of Arbitrarily Shaped Metal Nanoparticles. *Small* **2011**, *7*, 1795–1799.
- Keum, J. W.; Bermudez, H. Enhanced Resistance of DNA Nanostructures. *Chem. Commun.* **2009**, *45*, 7036–7038.
- Walsh, A. S.; Yin, H.; Erben, C. M.; Wood, M. J. A.; Turberfield, A. J. DNA Cage Delivery to Mammalian Cells. *ACS Nano* **2011**, *5*, 5427–5432.
- Li, J.; Pei, H.; Zhu, B.; Le Liang, L.; Min Wei, M.; Yao He, Y.; Nan Chen, N.; Di Li, D.; Qing Huang, Q.; Fan, C. Self-Assembled Multivalent DNA Nanostructures for Noninvasive Intracellular Delivery of Immunostimulatory CpG Oligonucleotides. *ACS Nano* **2011**, DOI: 10.1021/nn202774x.
- Nishikawa, M.; Matono, M.; Rattanaki, S.; Matsuoka, N.; Takanura, Y. Enhanced Immunostimulatory Activity of Oligodeoxynucleotides by Y-Shape Formation. *Immunology* **2007**, *124*, 247–255.
- Ranakiat, S.; Nishikawa, S.; Funabashi, H.; Luo, D.; Takakura, Y. The Assembly of a Short Linear Natural Cytosine-Phosphate-Guanine DNA into Dendritic Structures and Its Effect on Immunostimulatory Activity. *Biomaterials* **2009**, *30*, 5701–5706.
- Venkataraman, S.; Dirks, R. M.; Ueda, C. T.; Pierce, N. A. Selective Cell Death Mediated by Small Conditional RNAs. *Proc. Natl. Acad. Sci. U.S.A.* **2011**, *107*, 16777–16782.
- Choi, H. M. T.; Chang, J. Y.; Trinh, L. A.; Padilla, J. E.; Frase, S. E.; Pierce, N. A. Programmable *In Situ* Amplification for Multiplexed Imaging of mRNA Expression. *Nat. Biotechnol.* **2010**, *28*, 1208–1212.
- Castro, C. E.; Kilcherr, F.; Kim, D. N.; Shiao, E. L.; Wauer, T.; Wortmann, P.; Bathe, M.; Dietz, H. A Primer to Scaffolded DNA Origami. *Nat. Methods* **2011**, *8*, 221–229.
- Mei, Q.; Wei, X.; Su, F.; Liu, Y.; Youngbull, C.; Johnson, R.; Lindsay, S.; Yan, H.; Meldrum, D. Stability of DNA Origami Nanoarrays in Cell Lysate. *Nano Lett.* **2011**, *11*, 1477–1482.
- Hemmi, H.; Takeuchi, O.; Kawai, T.; Kaisho, T.; Sato, S.; Sanjo, S.; Matsumoto, M.; Hoshino, K.; Wagner, H.; Takeda, K.; Akira, S. A Toll-like Receptor Recognizes Bacterial DNA. *Nature* **2000**, *408*, 740–745.
- Hornung, V.; Latz, E. Intracellular DNA Recognition. *Nat. Rev. Immunol.* **2010**, *10*, 123–130.
- Krieg, A. M.; Yi, A. K.; Matson, S.; Waldschmidt, T. J.; Bishop, G. A.; Teasdale, R.; Koretzky, G. A.; Klinman, D. M. CpG Motifs in Bacterial DNA Trigger Direct B-Cell Activation. *Nature* **1995**, *374*, 546–549.
- Krieg, A. M. CpG Motifs in Bacterial DNA and Their Immune Effects. *Annu. Rev. Immunol.* **2002**, *20*, 709–760.
- Ballas, Z. K.; Krieg, A. M.; Warren, T.; Rasmussen, W.; Davis, H. L.; Waldschmidt, M.; Weiner, G. J. Divergent Therapeutic and Immunologic Effects of Oligodeoxynucleotides with Distinct CpG Motifs. *J. Immunol.* **2001**, *167*, 4878–4886.
- Bourquin, C.; Wurzenberger, C.; Heidegger, S.; Fuchs, S.; Anz, D.; Weigel, S.; Sandholzer, N.; Winter, G.; Coester, C.; Endres, S. Deliver of Immunostimulatory RNA Oligonucleotides by Gelatin Nanoparticle Triggers an Efficient Antitumoral Response. *J. Immunother.* **2010**, *33*, 935–944.
- Douglas, S. M.; Marblestone, A. H.; Teerapittayanon, S.; Vazquez, A.; Church, G. M.; Shih, W. M. Rapid Prototyping of Three-Dimensional DNA-Origami Shapes with caDNA. *Nucleic Acids Res.* **2009**, *37*, 5001–5006.

4 Design and Analysis of Specific DNA Origami Structures

In publications P3 and publication P4, the development of DNA origami structures with specific requirements on morphology, dimensionality, cavity and size are shown. Publication P3 describes the design of a tetrahedral cage-like DNA origami structure that was analyzed by gel electrophoresis, TEM, AFM and the super resolution microscopy technique PAINT (*Points Accumulation for Imaging in Nanoscale Topography*). In publication P4, various small DNA origami constructs on the basis of a short 704 nt fragment 'M1.3' of the commonly used 7249 nt long M13mp18 scaffold were presented.

4.1 Tetrahedral DNA Origami Structure

Emerging three-dimensional super resolution microscopy techniques such as PAINT can profit from the development of three-dimensional DNA objects such as a tetrahedral DNA origami structure. Therefore a DNA tetrahedron with six struts consisting of so-called six-helix bundles (6HBs) with 227 nt in length was constructed using the software tool caDNAo [95] (see figure 4.1 A and B). Two helices of each 6HB are connected by single stranded parts of the circular 8634 nt scaffold to the two neighboring 6HB. The length of this single stranded hinge varied between 4 nt and 20 nt. Gel analysis showed faster migration and a slightly less defined band structure of tetrahedrons with longer single stranded sections between the struts. This could be explained by the enhanced flexibility of the structure while migrating through the agarose network, resulting in a broader distribution of migration speed (see figure 4.1 C). Annealing times of 18 h and 170 h showed no significant difference in yield that could be estimated via relative band intensities to about 20 %. A second light band of structures migrating more slowly might indicate aggregation to dimers. Even if the defined gel band argues for correct assembly of the structures, TEM analysis reported exclusively disrupted DNA tetrahedra which could be explained by the strong electrostatic interactions between the dried DNA constructs and the grid surface used for TEM imaging that has to be done in vacuum. Indirect verification of the initially precise folding of the DNA origami tetrahedron by TEM and AFM is described in detail in publication P3. The DNA origami structure was designed to have a defined orientation and height when fixed to a surface via biotin linkers. The binding sites for the attachment and detachment of fluorescently labeled PAINT strands were positioned at accurate distances in all three directions in space. The super resolution

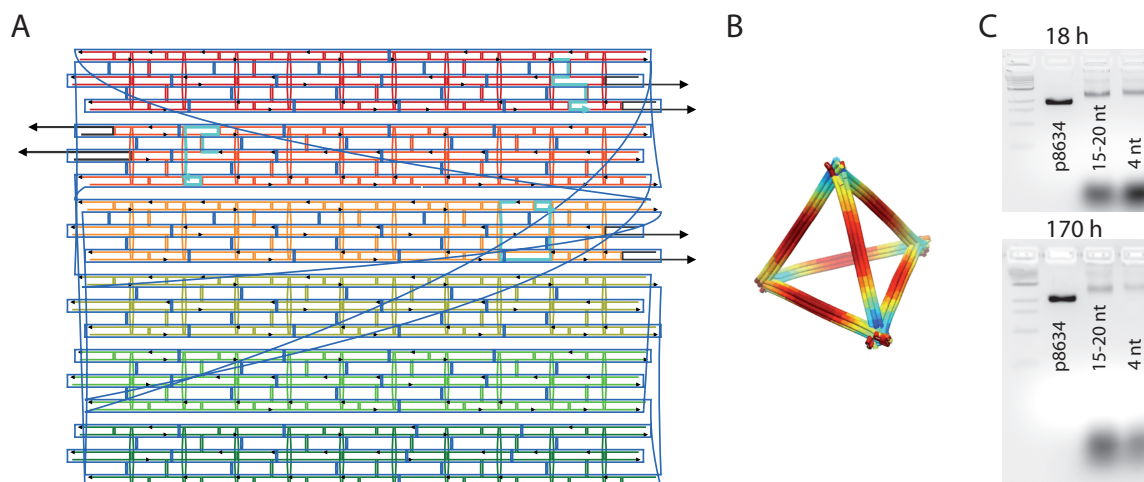


Figure 4.1: Tetrahedral DNA origami structure. **A** *caDNA* aided structure design with the scaffold strand path shown in blue and colored staple strands. Each 6HB for the six struts is illustrated in a different color. Staple strands with 3' handle extensions for biotin modified DNA strand attachment are indicated in black. Staple strands with 3' handle extensions for transient hybridization of complementary 8 nt PAINTE oligos are in light-blue. **B** Representation of DNA origami tetrahedron simulated by *CanDo* [108]. **C** 2% agarose gel analysis of tetrahedral DNA origami structure folded for 18 hours (top) and 170 hours (bottom). Gels run at 70 V for approximately 3 h. Left to right: 2-log 1 kb DNA ladder, p8634 scaffold, tetrahedra with a 4 nt single-stranded connection between adjacent struts, tetrahedra with 15 nt to 20 nt single-stranded connections.

microscopy method PAINTE which circumvents drying of the structure, could prove the defined assembly of the tetrahedron that is bound to a surface. Experiments on a newly developed 3D PAINTE setup are in progress.

4.2 M1.4 Based DNA Origami Structures

For many biological and chemical applications, relatively small DNA origami platforms in the size range of 10 nm - 30 nm have advantages over the commonly designed DNA origami structures that are folded into shape by approximately 200 synthetic staple strands. Even if just a small-sized defined area on a DNA origami surface is needed as workbench for the positioning of functionalized oligos, the majority of the frequently used M13mp18 scaffold strands have to be paired to staple strands to prevent interference of long single stranded scaffold loops with the structure functionalization. In publication P4 the restriction enzyme based preparation of a 704 nt fragment of the complete 7249 nt containing M13 was reported. The so-called 'M1.3' was tested as scaffold strand for various DNA origami structures consisting of only 15 to 25 staple strands. To demonstrate the potential of assembling comparable objects to M13 based constructs, five different kinds of DNA origami structures similar in shape to larger previously described M13 based versions were designed and analyzed by gel electrophoresis and TEM imaging. Two-dimensional monolayer objects, a triangle and a twist corrected frame (not

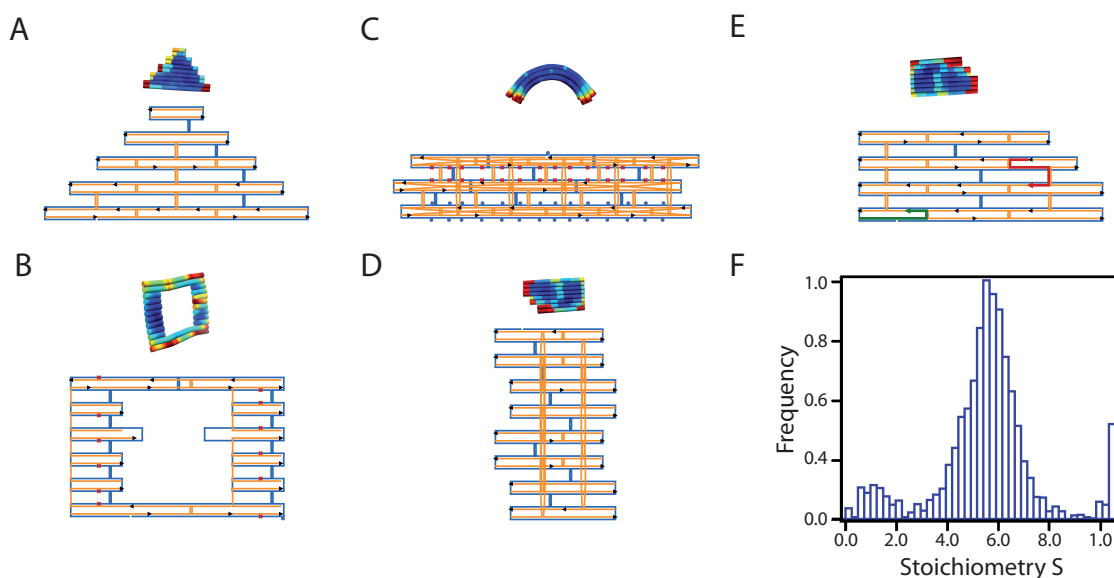


Figure 4.2: M1.3 based DNA origami structures. **A-E** Top (A-E): Schemes of the objects simulated by CanDo. Bottom (A-E): caDNAno aided structure designs with scaffold strand paths (blue) and staple strands (orange). **A** Monolayer triangle in square lattice arrangement. **B** Twist-corrected monolayer frame in square lattice arrangement. Deletions indicated by crosses (red). **C** Curved six helix bundle in honey comb arrangement with deletions (red crosses) and insertions (blue loops). **D** Three-dimensional multilayer cube. **E** Two-dimensional hand-like rectangle with two fluorescently labeled staple strands (Atto647N = green, Atto565 = red). **F** Stoichiometry histogram of structure shown in E. The major fraction of objects carries both dyes ($S = 0.5$). An absolute value for the ratio between completely labeled and singly labeled object can not be determined due to the burst search algorithm that detects doubly labeled structures preferentially over singly labeled structures.

shown in publication P4) were arranged in a square lattice (see figure 4.2 A and B). A curved six helix bundle in honey comb alignment contains deletions and insertions as indicated by crosses (red) and loops (blue) in figure 4.2 C. Furthermore, a compact three-dimensional multilayer cube with a side length of 14 nm was designed and assembled (see figure 4.2 D). To show the successful integration of fluorescently labeled staples, a hand-like rectangle was functionalized by an Atto565 dye (green) and an Atto647N dye (red) (see figure 4.2 E). The efficient binding of the fluorophores to the small DNA origami structure was measured by ALEX. The determination of the stoichiometry value S (see equation (3.7)) confirmed the availability of both fluorophores per structure ($S = 0.5$) for the majority of the objects even if an absolute value for the ration can not be given due to the burst search algorithm that detects doubly labeled structures preferentially over singly labeled structures (see figure 4.2 F).

4.3 Associated Publication P3

A Structurally Variable Hinged Tetrahedron Framework from DNA Origami

By

David M. Smith, Verena Schüller, Carsten Forthmann, Robert Schreiber, Philip Tinnefeld
and Tim Liedl

published in

Journal of Nucleic Acids 2011, vol. 2011, Article ID 360954, 9 pages, 2011.
doi:10.4061/2011/360954

Reprinted with permission from ref.[158]. Copyright 2011 David M. Smith et al.

Research Article

A Structurally Variable Hinged Tetrahedron Framework from DNA Origami

David M. Smith,^{1,2} Verena Schüller,¹ Carsten Forthmann,^{3,4} Robert Schreiber,¹
Philip Tinnefeld,^{2,4} and Tim Liedl^{1,2}

¹Physik Weicher Materie und Biophysik, Ludwig Maximilian University, 80539 Munich, Germany

²Center for NanoScience, Ludwig Maximilian University, 80799 Munich, Germany

³Angewandte Physik-Biophysik, Ludwig Maximilian University, 80539 Munich, Germany

⁴Physikalische und Theoretische Chemie-NanoBioScience, Braunschweig University of Technology, 38106 Braunschweig, Germany

Correspondence should be addressed to David M. Smith, david.smith@physik.uni-muenchen.de

Received 15 May 2011; Accepted 27 June 2011

Academic Editor: F. C. Simmel

Copyright © 2011 David M. Smith et al. This is an open access article distributed under the Creative Commons Attribution License, which permits unrestricted use, distribution, and reproduction in any medium, provided the original work is properly cited.

Nanometer-sized polyhedral wire-frame objects hold a wide range of potential applications both as structural scaffolds as well as a basis for synthetic nanocontainers. The utilization of DNA as basic building blocks for such structures allows the exploitation of bottom-up self-assembly in order to achieve molecular programmability through the pairing of complementary bases. In this work, we report on a hollow but rigid tetrahedron framework of 75 nm strut length constructed with the DNA origami method. Flexible hinges at each of their four joints provide a means for structural variability of the object. Through the opening of gaps along the struts, four variants can be created as confirmed by both gel electrophoresis and direct imaging techniques. The intrinsic site addressability provided by this technique allows the unique targeted attachment of dye and/or linker molecules at any point on the structure's surface, which we prove through the superresolution fluorescence microscopy technique DNA PAINT.

1. Introduction

The design and self-assembly of DNA strands into precisely defined objects on the nanometer scale has emerged as a promising technique in the field of nanotechnology. Stemming from the initial idea of generating periodic lattices from DNA [1], the concurrent exploitation of (i) complimentary base pairing between short strands, (ii) branch-like Holliday junctions, and (iii) the inherent helical twist of double-stranded DNA complexes has allowed for the assembly of small, identical motifs which constitute the repeating unit cells of periodic two-dimensional sheets or three-dimensional crystal structures extending nearly to the millimeter scale [2–5]. The development of techniques to build rigid, three-dimensional DNA-based structures is, however, an important aspect to the future utilization of this methodology in nanofabrication [6–11]. While many attempts to construct simple three-dimensional polyhedra have been fraught with problems of instability, unwanted by-products,

low-yield, or overly complex synthesis strategies, the recent utilization of hierarchical assembly schemes [12] and the DNA origami technique [13, 14] has provided a path towards the relatively simple generation of uniform populations.

The DNA origami technique is based on the use of a long, usually circular “scaffold” strand, which is folded and clamped into a desired shape by hybridization with hundreds of shorter “staple” oligonucleotides [13]. In contrast to earlier schemes for generating nanostructures from synthesized oligonucleotides, the utilization of a viral scaffold, which is typically the 7 kb circular single-stranded M13mp18 bacteriophage genome or alternatively PCR-templated products [15, 16], allows for the construction of far larger structures often extending to several hundreds of nanometers [17]. The heterogeneous sequence of the underlying scaffold strand forms the basis for the unique strength of this method, by which each staple strand has the potential to act as a “handle” for the placement of accessory molecules at virtually any site in the structure with nanometer precision

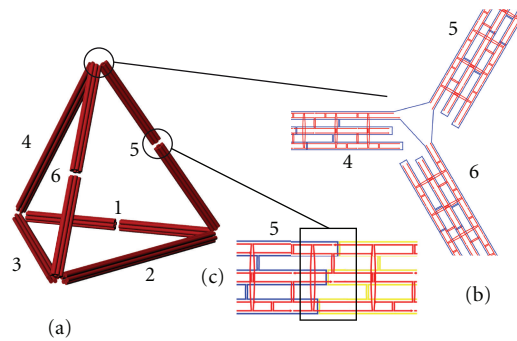


FIGURE 1: Schematic view of DNA origami tetrahedron. (a) In the three-dimensional representation, each double-helical section is represented by a single red cylinder. The six struts are labeled 1 through 6, and each consist of a bundle of six parallel connected double helices. (b) A two-dimensional diagram of the hinged vertex formed by struts 4, 5, and 6 shows the path of the m13MP18-based scaffold (blue) forming the single-stranded connections between bundles and the pattern of staple oligonucleotides (red) around the hinge. (c) Local structure of the scaffold path within strut 5 shows three closely aligned scaffold crossovers stabilized by short staple sections forming the weakened gap. The scaffold path on opposite sides of the gap is marked in either yellow or blue to emphasize the discontinuity.

[18, 19]. Through standard purification techniques, relatively uniform populations of folded structures of the desired conformation can be isolated. This method is suited not only for compact, structurally rigid objects, but also for those which incorporate single-stranded sections amongst rigidly extended helical bundles to generate objects displaying flexible hinges and inherent tensile strain [20].

Hollow, load-bearing frameworks represent one class of structures which holds a broad relevance in applied nanoscience as potential container systems. The use of programmed DNA self-assembly offers a highly suitable alternative pathway in their construction, as has been demonstrated in several recent studies. Two in particular have succeeded in generating highly uniform populations of rigid nanostructures. Small tetrahedral structures measuring less than 10 nanometers per strut have been rapidly assembled from four distinct oligonucleotides and have shown a significant mechanical stability, withstanding compression forces in excess of 100 pN before exhibiting buckling [10]. It was later demonstrated that a hierarchical self-assembly concept utilizing simple repeating motifs from a relatively small number of oligonucleotides [12] or DNA origami-based subunits [14] can be used to generate larger polyhedra suitable as containers or for the orientation of functional units in space with nanometer precision. While the above strategies based upon hybridization of shorter oligonucleotides produce high yields of correctly assembled products, the former is significantly size-limited based on its dependence on a simple annealing scheme, while the ability to selectively attach molecules at distinct points on the polyhedra constructed by hierarchical means suffers due to the redundancy of strands or units within the repeated motifs. The use of subunits constructed from DNA origami [14] can solve this issue of redundancy via a simple internal shifting of the scaffold strand; however, it does require the additional and often intricate control over correct three-dimensional orientation and self-assembly of the multiple segments. Consequently, the fabrication of enclosed hollow frames from a single DNA scaffold via the origami method,

as previously demonstrated in a spherical architecture [21], offers the potential for the straightforward generation of a wide variety of fully and uniquely addressable structures.

As shown in the present study, utilization of the DNA origami method to construct a rigid, enclosed tetrahedral framework, illustrated in Figure 1, provides the ability to generate structures reaching a size of 75 nanometers along each edge while retaining the full addressability afforded by the heterogeneous sequence of the scaffold strand. Single stranded “hinges” at each of the four vertices of the tetrahedron allow for a structural variability. By selective staple oligonucleotide omission, four unique two-dimensional structures varying in length and width between 75 nanometers and 300 nanometers are generated. Even though the full three-dimensional structure displays mechanical rupture likely due to electrostatic-mediated surface binding and flow-induced shearing, proper annealing can nevertheless be confirmed through gel electrophoresis and examination of the assorted open frames. Additionally, binding of fluorescent molecules at precisely determined points on the structure emphasizes its potential to act as a three-dimensional ruler for emerging superresolution microscopy methods such as DNA-PAINT and Blink [22–24].

2. Materials and Methods

2.1. Preparation of DNA Structures. Reverse-phase cartridge-purified unmodified staple oligonucleotides were shipped dry from Bioneer Corporation (Alameda, Calif, USA) and resuspended to a concentration of 100 μ M in H₂O. HPLC-purified dye- and biotin-modified oligonucleotides for PAINT analysis were purchased from IBA GmbH (Göttingen, Germany) at a concentration of 50 μ M in H₂O. The ATTO655-labeled oligonucleotide contained the sequence 5'-GGT GAA GA_{ATTO655}-3' and the biotin-modified strand 5'-GGT AGT AAT AGG AGA ATG_{bt}-3'. The 8634-nucleotide-long M13mp18-phage-based scaffold strand was prepared and isolated as previously described [14].

As a general annealing condition, 10 nM of scaffold strand and 100 nM of each staple were mixed in TE buffer (10 mM Tris-HCl + 1 mM EDTA, pH 8.0 at 20°C) containing 14 mM MgCl₂, heated to 80°C for 5 minutes, and quickly cooled to 60°C over 20 minutes, before being slowly cooled to 24°C in steps of 0.5°C over approximately 40 hours. When applicable for dye or biotin attachment, staple oligonucleotides with docking handle extensions replaced unextended staples in the solution and biotin- or dye-modified oligonucleotides were included at 500 nM per staple during annealing. For PAINT analysis, a total of six biotin attachment sites (two per vertex) and three ATTO655 sites (one per strut) were used to modify struts I, II, and III, as shown in Figure 4(a) and in the Supplementary Materials in Figure S1.

Gel electrophoresis was performed with an agarose concentration of either 2.0% (for band analysis) or 0.7% (for structure purification). Agarose was first heated to boiling temperature in 45 mM Tris borate + 1 mM EDTA (pH 8.2 at 20°C) then cooled to 60°C in an ice bath, at which point MgCl₂ was added to a final concentration of 11 mM, before being cooled to room temperature in a gel cask. For sample preparation, 5 μL of DNA origami structures were mixed with 3 μL of 6x agarose gel loading buffer (30% glycerol weight-to-volume in water, 0.025% xylene cyanol, 0.025% bromophenol blue) and brought to a total volume of 18 μL in H₂O, for roughly $5 \cdot 10^{-14}$ moles of structures per gel pocket. Similarly, bare scaffold strands were mixed with loading buffer and H₂O to give a total amount of $1 \cdot 10^{-13}$ moles per sample. The different gel pockets were filled with the origami and scaffold samples along with a 1 kb DNA ladder and run for approximately 3 hours at constant 70 V over a cathode-anode distance of 22 cm. The entire apparatus was cooled in an ice water bath while running to avoid unwanted structure denaturation. Afterwards, the gel was stained with an ethidium bromide solution at 0.5 μg/mL and imaged under 302 nm UV excitation. Following electrophoresis, the primary band was excised from the gel and centrifuged at 5000 ×g for 7 minutes in spin columns (Freeze'n Squeeze Spin Columns, Biorad) to isolate structures. Purified origami samples were usually estimated to contain approximately 1 nM of annealed structures.

2.2. Visualization of Structures (TEM and AFM)

TEM Imaging. Formvar-supported carbon coated TEM grids were purchased from Plano GmbH (Wetzlar, Germany). Grids were first hydrophilicized in a Diener Electronic Femto plasma cleaner. 2 μL of purified origami samples was added to the grids, and structures were allowed to bind for 60 seconds. Excess sample was then quickly removed from the grids by absorption with filter paper. Grids were quickly washed with 1% uranyl acetate in H₂O, then stained for 15 seconds with the same and allowed to dry completely. The samples were then imaged with a JEM-1011 transmission electron microscope (JEOL) operated at 100 kV.

AFM Imaging. For viewing with atomic force microscopy, 5 μL of purified origami sample placed onto a freshly cleaved

mica surface (Plano GmbH, Wetzlar, Germany) which had been attached by hot glue to a 15 mm metal specimen disc (Ted Pella, Inc., Redding, Calif, USA). Structures were allowed to bind for 60 seconds before being washed twice with 30 μL of TE buffer solution containing 12.5 mM MgCl₂ to remove unbound origami objects and other debris. Samples were imaged in Tapping Mode in the previously mentioned TE/Mg⁺⁺ buffer conditions using a NanoScope III Multimode AFM from Digital Instruments (Veeco Instruments Ltd., Plainview, Tex, USA) with a silicon-nitride tip with a spring constant of $k = 0.24$ N/m (Veeco).

2.3. Shape Analysis by DNA PAINT

Sample Preparation. Chambered Cover Glass Slides (LabTek, NUNC, Langensfeld, Germany) were prepared for Total Internal Reflection (TIR) Microscopy in the following manner: glass surfaces were first cleaned with 0.1 M HF for 30 seconds and washed with PBS. They were then passivated with a mixture of 5 mg/mL bovine serum albumin (BSA) and 1 mg/mL biotin-conjugated BSA for 16 hours. Following a second washing with PBS to remove unbound proteins, the surface was incubated for 15 minutes with 0.01 mg/mL streptavidin (IBA GmbH) then again washed with PBS to remove any excess, unbound streptavidin. 50 μL of the sample solution which contained 90% of a 1 M MgCl₂ buffer and 10% purified origami solution (for a final structure concentration of approximately 0.1 nM) was added to the chamber and allowed to bind to the surface. Binding was facilitated by biotin linkers on the origami structures, included at each vertex of the plane formed by struts I, II, and III. Chambers were again washed with PBS to remove unbound structures, and a 50 nM solution of ATTO655-labeled oligonucleotides (PAINT-DNA) in 500 mM NaCl was added.

Microscopy Setup. An inverted Olympus IX-71 in objective-type TIRF configuration outfitted with a UPlanSApo objective (100x, NA 1.40, oil immersion) was used for monitoring. Dyes were excited by a single-mode diode laser (XTL, Toptica Photonics, Grafelfing, Germany) operated at 100 mW with a wavelength of $\lambda = 650$ nm. Fluorescence was imaged on an EMCCD camera (Ixon DU-897, Andor Technologies, Belfast, Northern Ireland). Image size was 128 × 128 pixels, with each pixel representing a length of approximately 90 nm. Each acquired sequence of images contained approximately 2000 frames taken at a rate of 20 Hz.

3. Results and Discussion

3.1. Tetrahedron Design. The tetrahedral design was implemented using the caDNano [25] software package, which was developed to facilitate the layout of both three-dimensional and flat DNA origami structures. A circular scaffold strand of 8634 nucleotides was used to allow for a maximal size, which was folded into its final configuration by a total of 211 staple strands. Each of the six struts in the tetrahedron is based on a bundle of six parallel double helices [14, 26], 227 paired bases in length,

with each double helix represented by a cylinder in the three-dimensional schematic (Figure 1(a)). The bundles are connected at each of the four hinged vertices to the two neighboring bundles by a four-base single-stranded section of the circular scaffold extending between their termini, as indicated in the inset in Figure 1(b). At each vertex, adjacent double helices within a single six-helix bundle were selected as connecting points to each of the two neighboring struts so as to minimize possible strains resulting from sterically induced stretching of the roughly 4 nm single-stranded connecting section. Additionally, connection points on opposite ends of a single strut extend from the same pair of double-stranded helical sections, which minimizes any possible unfavorable twist-strain within the bundle [21, 27]. We have adopted the nomenclature as indicated in Figure 1(a) whereby each strut is labeled 1 through 6. Due to circular continuity of the scaffold strand and the periodicity of scaffold crossovers between neighboring helices within a single six-helix bundle, struts 1, 5, and 6 contain points where three scaffold crossovers are contained within a seven-base section along the double helix. As highlighted in Figure 1(c) for strut 5, the three nearly aligned gaps within the strut are stabilized only by staple oligonucleotides hybridized to scaffold sections on opposing sides of each opening. Lacking a direct connection from the internal scaffold path running throughout the structure, these junctions, referred to as 1, 5, and 6 in coordination with the previous nomenclature, must be viewed as weak points susceptible to rupture; however, they provide the overall tetrahedron with its structural variability as will be discussed in later sections. A full schematic of both scaffold and staple arrangement within the overall structure can be seen in the Supplementary Materials in Figure S1.

Specific binding of tetrahedra to surfaces was facilitated by the addition of an 18-base sequence on the 3' end of six staples, each terminating at the end of a bundle lying on the plane formed by struts 1, 2, and 3, to which a complementary oligonucleotide containing a biotin molecule conjugated to its 3' end could be hybridized. This allowed stable attachment of structures to surfaces coated with biotin-binding proteins such as streptavidin. The positioning of the biotin on the 3' end of the modified strand directly abutting the structure imposes the closest possible binding between the object and surface. In a similar manner, one staple positioned along the length of each of struts 1, 2, and 3 with their 3' terminus on the outer surface of the bundle was selected as a handle for complimentary oligonucleotides with an ATTO655 dye conjugated to the 3' end of the strand in DNA PAINT experiments. In both cases, any combination of biotin or dye sites could be included within the structure by the replacement of normal staple strands with those extended by the complimentary "handle" or docking sequence.

3.2. Full Tetrahedron Structural Properties. The structures were annealed in a one-pot reaction in TE buffer in the presence of 14 mM MgCl₂. As analyzed by agarose gel electrophoresis after annealing, well-defined bands were observed indicating a population of uniformly annealed structures, along with signs of additional slower migrating

aggregate products, as can be seen in the Supplementary Materials in Figure S2. Little change in band structure was observed by varying the annealing time from 18 to 170 hours, although a lengthening of the single-stranded scaffold sections between struts caused a higher migration speed and a less-defined band structure (see Figure S2 in the Supplementary Materials). From analysis of relative band intensity in gels, the yield of primary annealed product was approximately 20%. The majority of scaffold-containing material remained in the gel pockets, where presumably aggregated structures are unable to effectively enter or migrate through the gel matrix.

Annealed objects were negatively stained with uranyl acetate and analyzed via transmission electron microscopy (TEM) for structural characteristics. Despite the defined structure of gel bands, TEM observations yielded an absence of intact tetrahedra, with a large portion of the structures displaying apparent breaks along one or more of the individual struts. Two such examples are shown in the left panel of Figure 2; the individual six-helix bundle struts appear to be well formed and connectivity within most vertices is maintained; however, the structures display a deformed or flattened configuration appearing to arise from a small number of ruptures along the length of one or two edges. Measured lengths of individual struts varied from 70 to 90 nm, close to the estimated value of 75 nm based on a 0.34 nm axial pitch between adjacent bases in the double helix.

3.3. Piecewise Verification of Proper Annealing. The pervasive existence of malformed structures under TEM observation points to one of two possible causes; either a systematic error in annealing occurs due to unexpected internal strains or kinetic traps, or properly annealed tetrahedra are denatured as a consequence of mechanical stresses endured in the process of purifying, fixing, and staining the objects. The lack of a clear predominance of any single "broken" tetrahedron configuration as viewed under TEM despite well-defined band structure in electrophoresis strongly indicates that the second consideration is the more likely explanation for the aforementioned observations. As previously emphasized, the three gap areas within each of struts 1, 5, and 6 formed by the close alignment of scaffold crossovers must be considered as weakened points along the bundles. A closer examination of the underlying staple connections across the gaps as pictured in Figure 1(c) for strut 5 shows that the hybridized sections stabilizing gaps along a single helical axis are in several cases as short as two nucleotides in overlap before the termination of the particular staple strand. While some degree of stabilization stemming from stacking interactions could occur for some abutting helices [28, 29], these points are nevertheless more susceptible to rupture under strong shear or compression forces than other points along continuous sections of a strut or at vertices. This can be understood through a simple comparison of the two different bond types responsible for stabilizing scaffolded DNA structures: hydrogen bonding of complimentary base pairing and the covalently connected polymer backbone comprising the main DNA scaffold through the structure.

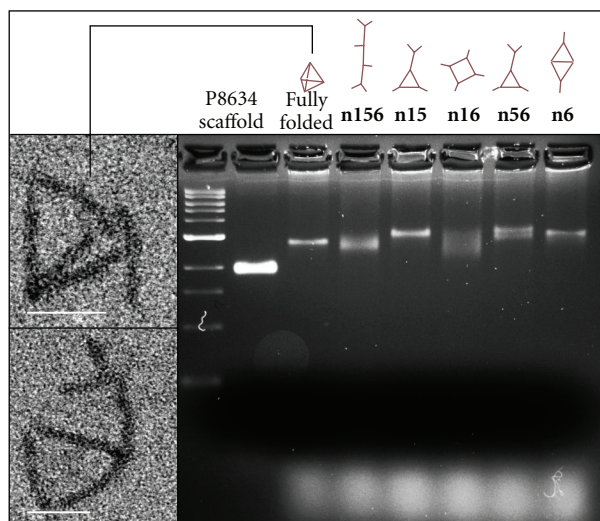


FIGURE 2: (Left) Transmission electron microscopy (TEM) imaging of tetrahedron structure containing all staple nucleotides. Typically, tetrahedrons displayed one or more ruptured struts, generating the widely observed flattened configuration. Scale bars: 60 nm. (Right) Agarose gel electrophoresis separation of the different configurations formed by targeted gap staple omission in struts 1, 5, and 6. Left to right: lanes 1-2 contain a 1 kb ladder and the circular p8634 scaffold, respectively. Lanes 3–8 contain the full tetrahedron, and the open configurations **n156**, **n15**, **n16**, **n56**, and **n6**, as indicated by the sketched representations above each lane.

In the case of the former, it has been demonstrated that forces on the order of 50 piconewtons are sufficient to induce shear-oriented rupture of hybridized DNA strands [30, 31]. Conversely, earlier work has shown that covalent bonds can generally withstand forces up to the nanonewton scale before experiencing rupture [32]. Concerning the overall stability of the tetrahedron presented in this work, the relatively weak hybridized staple oligonucleotides spanning the gap regions in struts 1, 5, and 6 would be far more susceptible to rupture under external stress than any of the other areas whose stabilities are in addition to base pairing supported by the continuous, covalently-linked scaffold backbone.

Standard techniques for examining DNA-based nanostructures such as TEM or AFM depend on a strong electrostatic binding of the negatively charged structures to layers such as mica or the carbon coating on grids used for TEM, and staining protocols include washing and drying steps with rapid, high-shear addition and removal of fluids. While this has proven to cause only nominal damage to more compactly rigid structures, the weakened struts are particularly susceptible to rupture due to electrostatic-driven compression or deforming forces containing a shear component and are likely candidates for the observed open configurations compressed on the surface.

With force-induced rupturing of weakened points formed by gaps within the struts identified as a likely candidate for the observed deformation of tetrahedra, we sought to investigate the various configurations resulting from the targeted opening of those gaps in different combinations. Due to their design and the local stapling paths around these junctions, these two-dimensional conformations could be generated by the omission of staple groups spanning each of the three gaps during annealing. For this purpose, an open configuration formed by a particular combination of

omitted gap staples is referred to by the number assigned to the gap or gaps presumably left open. By this nomenclature, the configuration generated by the omission of all gap staples is referred to as **n156**; that resulting from the opening of the gap along strut 6 is **n6**, and so on. While there are a total of seven possible combinations of gap staple groups which can be left out, structural redundancies mean that a total of only four possible flat configurations exist. These are roughly sketched above their corresponding lane in the gel shown in the right panel of Figure 2, with **n6** being the representative structure for the three identical configurations containing a single omission.

The various flat structures were annealed and analyzed as the full tetrahedron. As can be seen in the gel in Figure 2, differences in migration and band structure amongst the variants were evident after a three-hour separation at 70 V over 22 cm in 2% agarose. Bands of the different flat two-dimensional assemblies displayed a predictably lower resolution than their fully annealed counterpart, presumably due to their increased degree of configurational flexibility around open, flexible joints. Two of these structures, the linearized **n156** form and the rectangular **n16**, have bands with a significant population of products which migrate faster than the full tetrahedron structure containing all staples. This can be explained by the lack of structurally rigid triangular substructures within the two frames, which can lead to an elongated conformation able to effectively reptate through the gel pores. Furthermore, the geometrically redundant **n15** and **n56** as well as the **n6** configurations all have primary populations which display a slower migration character visibly absent from the fully annealed version. In both cases, this is a strong indication that none of those are preferentially occurring in any detectable amount during annealing of the full tetrahedron and that weakened

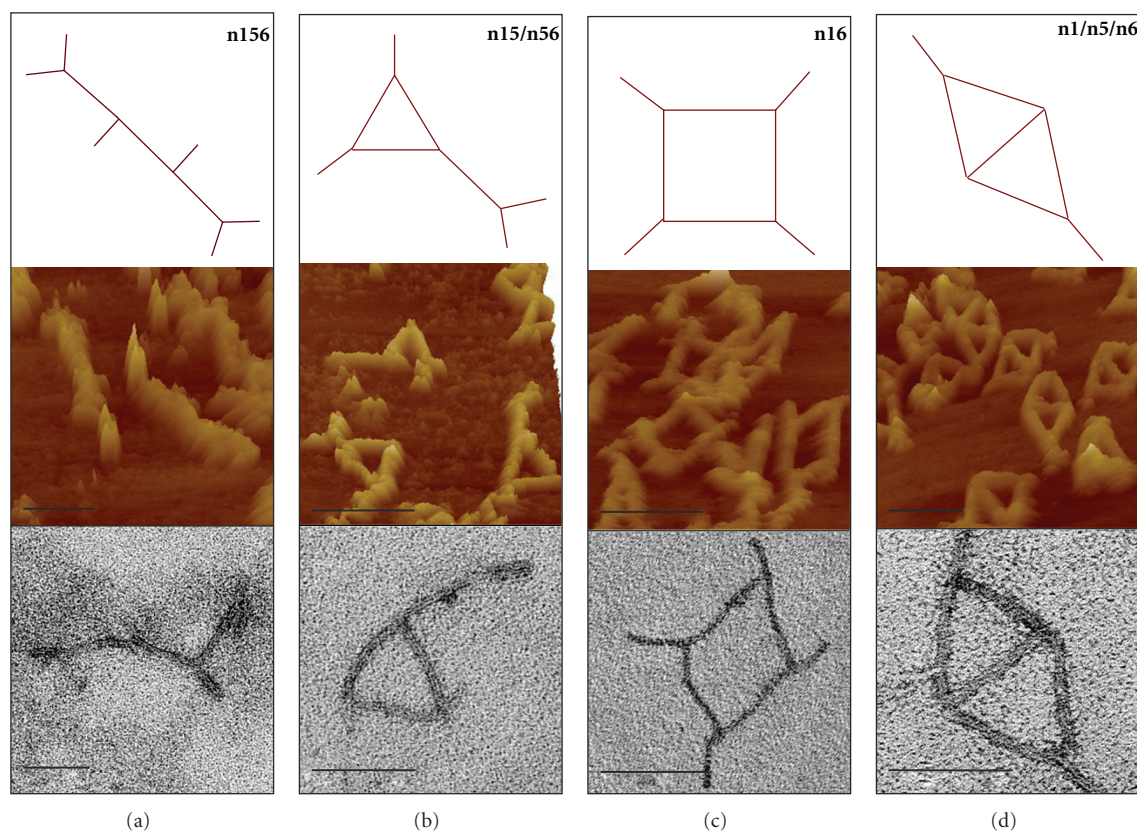


FIGURE 3: Schematic (upper row), atomic force microscopy (center), and TEM imaging (bottom) of flattened structures produced by targeted gap staple omission. (a) The chain-like **n156** configuration is formed when all gaps are left open. (b) Removal of staple groups connecting gaps in struts 1 and 5 or alternatively 5 and 6 form the geometrically redundant **n15** and **n56** projections. (c) Jointed square structures **n16** are formed by the opening of gaps in struts 1 and 6, displaying a degree of transverse flexibility due to possessing four flexible hinges. Omission of a single gap staple group as in (d) has a three-fold redundancy of structures with geometry indicated by the **n6** object shown. Scale bars: 150 nm (AFM) and 75 nm (TEM).

points in the struts are not ruptured within the gel. This absence of any primary product resulting from the variable open configurations which displays the same migration speed as the full tetrahedron as well as the narrow band structure of the closed tetrahedron indicate that it adopts its final, defined conformation unique from those resulting from some combination of ruptured struts. Approximate yields of primary annealed products were estimated through comparison of relative band intensities. For all opened variants, this was found to be approximately 20–25%, in a similar range as the fully annealed tetrahedron, although a lesser degree of band clarity does make any precise determination in this manner unreliable. Highest yields were found with the more flexible and elongated **n156** and **n16** variants, likely due to the greater amount of overall material able to enter the gel. Conversely, the most rigid of the variants containing only one gap opening (represented as **n6** in Figure 2) showed the smallest yields of all products, usually under 20%; however, with the greatest clarity in band structure and highest amount of aggregation near the gel pockets.

Prominent bands of each flattened conformation were excised from the gel, and structures were isolated via spin

filtration before being imaged by TEM and AFM, as shown in Figure 3. In each case, most structures were found in the configuration suggested by the pattern of openings along the struts. Vertices forming connections between three partial or complete struts appeared to be well formed, and the length of spanning segments was in the range of the ideally expected 75 nm. In some cases, partial bundles resulting from an intentionally opened gap were not clearly distinguishable, likely due to the small size of these parts and possible overlapping with other struts. Populations containing fewer deformed or aggregated objects were generally seen under observation via AFM, likely resulting from the lack of potentially harsh drying steps which are typical in uranyl acetate negative staining used for TEM observations.

Taken in concert, the different two-dimensional frames demonstrate, on an individual basis, the ability for each vertex and strut, whether continuous or containing a gap region, to correctly anneal as a part of a particular flat variant of the tetrahedron. This does not fully eliminate the possibility that unintended internal stresses resulting from closure of the full structure lead to some degree of deformation. However, the single primary band migrating with the speed different to those of all open conformations

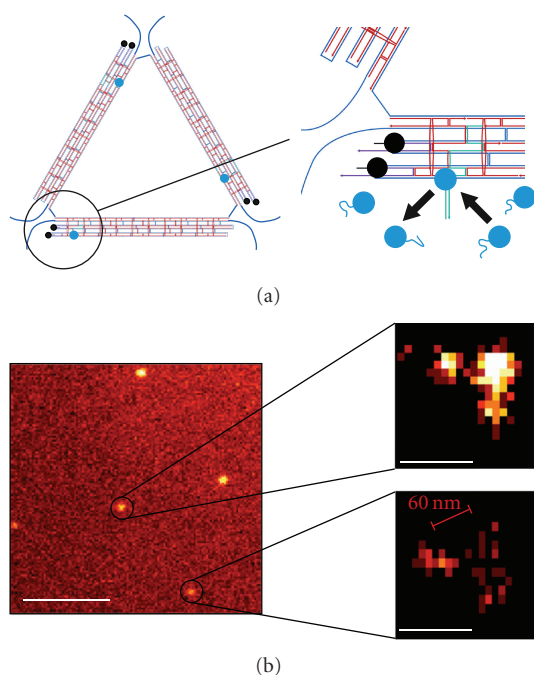


FIGURE 4: DNA PAINT measurements on the triangular base of the tetrahedron. (a) Design schematic of the base showing docking sites for complimentary biotin- and ATTO655-conjugated oligonucleotides. The scaffold path is shown in blue, and staples lacking extended docking sequences are in red. Only basal struts 1, 2, and 3 are shown in the full schematic (left), and local detail at docking sites on strut 1 is given (right). The six extended staples containing docking sites for complimentary biotin-nucleotides are shown in purple, with biotin and the affixed nucleotide strand in black. Likewise, the three docking staples for ATTO655 dye are shown in green, while the ATTO655 dye and attached 8-base nucleotide which transiently hybridize to the structures are in light blue. (b) Resolution of triangular structure via DNA PAINT. (Left) Sample frame and (right) superresolution 2D reconstruction of local binding events. In the color scheme on the reconstructions, lighter colors correspond to a higher number of binding events, showing the underlying triangular form matching the schematic arrangement of dyes. For a comparison, the approximate expected distance between docking sites of 60 nm is indicated in the image. Scale bars: $4\ \mu\text{m}$ (left) and 100 nm (right).

is strong evidence for the successful annealing of the full tetrahedron. From this, we can conclude that rupturing occurs during fixing and staining procedures onto carbon-coated TEM grids due to strong surface interactions from surface adsorption or transverse shear forces incurred in washing and drying steps.

3.4. Superresolution Analysis via DNA PAINT. Single-layer DNA origami structures have recently been shown to function as ideal substrates for superresolution microscopy techniques such as DNA PAINT [24] (points accumulation for imaging in nanoscale topography) or Blink microscopy [19] due to the ability to place fluorescent dyes at prescribed locations on the structure's surface with nanometer precision. The localization of fluorescent molecules beyond the

normal diffraction limit of visible light is predicated by the principle that only a single molecule within the detection area is active, that is, emitting fluorescent light, at any given time [22, 23]. Switching between ON and OFF states of fluorescent molecules is generally controlled by either chemical means or by utilizing intrinsic dark states [33]. In contrast, for systems involving interactions on surface-bound DNA-based nanostructures due to hybridization-based binding and unbinding between dye-oligonucleotide-conjugate detector strands and complimentary docking strands on the structures, switching occurs as a natural consequence of two factors: (i) freely diffusing strands within solution cause minimal background due to TIR excitement of only dyes near to the surface by the evanescent wave and (ii) a 70% increase of fluorescence is attained upon hybridization due to a significant reduction of intrastrand guanine quenching [24]. This results in the relatively straightforward detection of single hybridization events occurring between single, labeled detector oligonucleotides and complimentary docking strands extending outward from the surface of the origami object. Furthermore, control over rates of binding/unbinding events can be achieved by altering the length of the hybridized segment and concentration of the detector strand within the surrounding solution, respectively [24].

Binding of tetrahedra to a streptavidin-coated surface was accomplished by the inclusion of six handle sites for complimentary biotin-oligonucleotide hybridization, two each extending from the ends of struts 1, 2, and 3, as indicated in Figure 4(a) and in Figure S1 of the Supplementary materials. Passivation of the glass surface with a protein layer containing BSA and streptavidin has the additional advantage of shielding the negatively charged structures from the strong electrostatic binding which proves destructive to their three-dimensional morphology as seen with the carbon or mica surfaces described in the previous sections. In addition, one staple with an extended handle sequence extending from the 3' end for ATTO655-oligonucleotide docking was incorporated into each of struts 1, 2, and 3, as outlined in detail for strut 1 in Figure 4(a) and shown for all struts in the Supplementary materials in Figure S1. The positioning of each dye site along its respective strut is shown in Figure 4(a), which together form a triangular arrangement with approximately 60 nm dimension. An 8-base docking length for the detector oligonucleotide was selected to give sufficiently long binding times for accurate position determination, and a high detector concentration of 50 nM was chosen in order to have high enough association rates [24].

Binding/unbinding events were recorded over 100 s with a capture rate of 20 Hz during TIR excitation from a single-mode diode laser with wavelength of 650 nm. Recorded movies were analyzed in a custom software package programmed in LabVIEW [34]. Spots where binding events in each frame occurred were fitted with a 2D Gaussian, and the peak coordinates of each spot were entered into a 2D histogram with a binning of 10 nm. According to the color scheme used, brighter spots represent a greater frequency of binding events at that particular position.

The left frame in Figure 4(b) shows a single snapshot of the $11.5\ \mu\text{m} \times 11.5\ \mu\text{m}$ area monitored, and the two frames on the right show the superresolved 2D histograms of two different localized areas of binding/unbinding events. In contrast to raw data, the superresolved histograms of local spots indicate a localization of three peak event occurrences. The three apparent binding locations on the origami object display the correct distance scale and geometrical arrangement for spacing suggested by docking site placement along the base of the tetrahedron. Through the analysis of six docking site pairs, we found an average distance between localized histogram peaks of (68 ± 12) nm. For a comparison, the approximate expected distance of 60 nm is indicated in the image. Our data generally demonstrates the ability for DNA PAINT to resolve subdiffraction limit structures in two dimensions as well as the potential of such a DNA origami framework for superresolution techniques.

4. Conclusion

The construction of wire-frame, cage-like structures of nanometer size is an endeavor which not only holds great potential for studies requiring mechanically stable nanoscale spacers and scaffoldings but also could prove crucial for the development of containers suitable for targeted drug delivery. In this work, we have presented a DNA origami-based design for the simplest architecture of this kind; a four-faced tetrahedron consisting of six flexibly jointed struts. Analysis of annealed objects via gel electrophoresis strongly indicates the presence of a population of uniformly annealed tetrahedra comprising approximately 20% of the total number of scaffolded objects, although structures appear to suffer ruptures at select weakened points along the struts likely due to forces occurring during electrostatic adsorption to surfaces and staining procedures. Intentional, targeted opening of these weak “gaps” in the struts via selected staple oligonucleotide omission led to the formation of a set of four different open configurations, again at a yield of approximately 20%, which were analyzed by gel electrophoresis and visualized via atomic force microscopy and transmission electron microscopy. We found populations of structures that displayed the expected open morphologies when bound to surfaces, which demonstrated proper assembly of the individual vertices and full struts, further supporting the suggestion of rupture of full three-dimensional frameworks from external forces. By exploiting the nanometer-precise positioning of dyes on the tetrahedra, a key feature provided by the DNA origami technique, its triangular base was used as a stage for visualization in two dimensions with the superresolution DNA PAINT microscopy method. Analysis confirmed the triangular arrangement of attached dyes and similar spacing as predicted by the structural schematic. As a consequence, we expect such structures to be suitable test objects for 3D superresolution microscopy.

While the observed breakage of the tetrahedra at weakened points along the struts is proposed to arise from external stresses during fixation and staining, this apparent

structural instability under stress is nevertheless a concern for future implementation of such objects as stable load-bearing scaffolds or cargo-bearing containers. This can potentially be resolved by longer overlaps between the connecting staples spanning the individual helices or by the incorporation of a linear scaffold strand into future designs to reduce the weakened gap regions along the struts imposed by the necessity of maintaining circular scaffold continuity. Enzymatic ligation of abutting 3' and 5' ends of staples within origami structures has been posited as a potential means to increase the overall stability of single-layer architectures [35] and could serve to further strengthen three-dimensional frameworks as presented in this work. Additionally, recently developed techniques for metallization of DNA nanostructures could be applied as a potential means to mechanically stabilize and electrically functionalize the tetrahedron and its two-dimensional variants [36–38].

Acknowledgments

This work was financially supported by funding from NIM, CeNS, and DFG (LI1743/2-1, TI329/5-1). The authors would like to additionally acknowledge Dr. Susanne Kemper for assistance with transmission electron microscopy imaging and both Philipp Nickels and Dr. Ralf Jungmann for their help with atomic force microscopy visualization.

References

- [1] N. C. Seeman, “Nucleic acid junctions and lattices,” *Journal of Theoretical Biology*, vol. 99, no. 2, pp. 237–247, 1982.
- [2] E. Winfree, F. Liu, L. A. Wenzler, and N. C. Seeman, “Design and self-assembly of two-dimensional DNA crystals,” *Nature*, vol. 394, no. 6693, pp. 539–544, 1998.
- [3] J. Malo, J. C. Mitchell, C. Vénien-Bryan et al., “Engineering a 2D protein-DNA crystal,” *Angewandte Chemie—International Edition*, vol. 44, no. 20, pp. 3057–3061, 2005.
- [4] Y. He, Y. Chen, H. Liu, A. E. Ribbe, and C. Mao, “Self-assembly of hexagonal DNA two-dimensional (2D) arrays,” *Journal of the American Chemical Society*, vol. 127, no. 35, pp. 12202–12203, 2005.
- [5] J. Zheng, J. J. Birktoft, Y. Chen et al., “From molecular to macroscopic via the rational design of a self-assembled 3D DNA crystal,” *Nature*, vol. 461, no. 7260, pp. 74–77, 2009.
- [6] J. Chen and N. C. Seeman, “Synthesis from DNA of a molecule with the connectivity of a cube,” *Nature*, vol. 350, no. 6319, pp. 631–633, 1991.
- [7] Y. Zhang and N. C. Seeman, “Construction of a DNA-truncated octahedron,” *Journal of the American Chemical Society*, vol. 116, no. 5, pp. 1661–1669, 1994.
- [8] W. M. Shih, J. D. Quispe, and G. F. Joyce, “A 1.7-kilobase single-stranded DNA that folds into a nanoscale octahedron,” *Nature*, vol. 427, no. 6975, pp. 618–621, 2004.
- [9] J. Zimmermann, M. P. J. Cebulla, S. Mönninghoff, and G. von Kiedrowski, “Self-assembly of a DNA dodecahedron from 20 trisigonucleotides with C_{3h} linkers,” *Angewandte Chemie—International Edition*, vol. 47, no. 19, pp. 3626–3630, 2008.
- [10] R. P. Goodman, I. A. T. Schaap, C. F. Tardin et al., “Chemistry: rapid chiral assembly of rigid DNA building blocks for molecular nanofabrication,” *Science*, vol. 310, no. 5754, pp. 1661–1665, 2005.

- [11] Z. Li, B. Wei, J. Nangreave et al., "A replicable tetrahedral nanostructure self-assembled from a single DNA strand," *Journal of the American Chemical Society*, vol. 131, no. 36, pp. 13093–13098, 2009.
- [12] Y. He, T. Ye, M. Su et al., "Hierarchical self-assembly of DNA into symmetric supramolecular polyhedra," *Nature*, vol. 452, no. 7184, pp. 198–201, 2008.
- [13] P. W. K. Rothemund, "Folding DNA to create nanoscale shapes and patterns," *Nature*, vol. 440, no. 7082, pp. 297–302, 2006.
- [14] S. M. Douglas, H. Dietz, T. Liedl, B. Högberg, F. Graf, and W. M. Shih, "Self-assembly of DNA into nanoscale three-dimensional shapes," *Nature*, vol. 459, no. 7245, pp. 414–418, 2009.
- [15] B. Högberg, T. Liedl, and W. M. Shih, "Folding DNA origami from a double-stranded source of scaffold," *Journal of the American Chemical Society*, vol. 131, no. 26, pp. 9154–9155, 2009.
- [16] E. Pound, J. R. Ashton, H. A. Becerril, and A. T. Woolley, "Polymerase chain reaction based scaffold preparation for the production of thin, branched DNA origami nanostructures of arbitrary sizes," *Nano Letters*, vol. 9, no. 12, pp. 4302–4305, 2009.
- [17] S. M. Douglas, J. J. Chou, and W. M. Shih, "DNA-nanotube-induced alignment of membrane proteins for NMR structure determination," *Proceedings of the National Academy of Sciences of the United States of America*, vol. 104, no. 16, pp. 6644–6648, 2007.
- [18] I. H. Stein, V. Schüller, P. Böhm, P. Tinnefeld, and T. Liedl, "Single-molecule FRET ruler based on rigid DNA origami blocks," *ChemPhysChem*, vol. 12, no. 3, pp. 689–695, 2011.
- [19] C. Steinhauer, R. Jungmann, T. L. Sobey, F. C. Simmel, and P. Tinnefeld, "DNA origami as a nanoscopic ruler for super-resolution microscopy," *Angewandte Chemie—International Edition*, vol. 48, no. 47, pp. 8870–8873, 2009.
- [20] T. Liedl, B. Högberg, J. Tytell, D. E. Ingber, and W. M. Shih, "Self-assembly of three-dimensional prestressed tensegrity structures from DNA," *Nature Nanotechnology*, vol. 5, no. 7, pp. 520–524, 2010.
- [21] H. Dietz, S. M. Douglas, and W. M. Shih, "Folding DNA into twisted and curved nanoscale shapes," *Science*, vol. 325, no. 5941, pp. 725–730, 2009.
- [22] B. Huang, M. Bates, and X. Zhuang, "Super-resolution fluorescence microscopy," *Annual Review of Biochemistry*, vol. 78, pp. 993–1016, 2009.
- [23] S. W. Hell, "Microscopy and its focal switch," *Nature Methods*, vol. 6, no. 1, pp. 24–32, 2009.
- [24] R. Jungmann, C. Steinhauer, M. Scheible, A. Kuzyk, P. Tinnefeld, and F. C. Simmel, "Single-molecule kinetics and super-resolution microscopy by fluorescence imaging of transient binding on DNA origami," *Nano Letters*, vol. 10, no. 11, pp. 4756–4761, 2010.
- [25] S. M. Douglas, A. H. Marblestone, S. Teerapittayanon, A. Vazquez, G. M. Church, and W. M. Shih, "Rapid prototyping of 3D DNA-origami shapes with caDNAo," *Nucleic Acids Research*, vol. 37, no. 15, pp. 5001–5006, 2009.
- [26] R. Jungmann, T. Liedl, T. L. Sobey, W. Shih, and F. C. Simmel, "Isothermal assembly of DNA origami structures using denaturing agents," *Journal of the American Chemical Society*, vol. 130, no. 31, pp. 10062–10063, 2008.
- [27] C. E. Castro, F. Kilchherr, D.-N. Kim et al., "A primer to scaffolded DNA origami," *Nature Methods*, vol. 8, no. 3, pp. 221–229, 2011.
- [28] A. Rajendran, M. Endo, Y. Katsuda, K. Hidaka, and H. Sugiyama, "Programmed two-dimensional self-assembly of multiple DNA origami jigsaw pieces," *ACS Nano*, vol. 5, no. 1, pp. 665–671, 2011.
- [29] K. N. Kim, K. Sarveswaran, L. Mark, and M. Lieberman, "Comparison of methods for orienting and aligning DNA origami," *Soft Matter*, vol. 7, no. 10, pp. 4636–4643, 2011.
- [30] M. Rief, H. Clausen-Schaumann, and H. E. Gaub, "Sequence-dependent mechanics of single DNA molecules," *Nature Structural Biology*, vol. 6, no. 4, pp. 346–349, 1999.
- [31] T. Strunz, K. Oroszlan, R. Schäfer, and H. J. Güntherodt, "Dynamic force spectroscopy of single DNA molecules," *Proceedings of the National Academy of Sciences of the United States of America*, vol. 96, no. 20, pp. 11277–11282, 1999.
- [32] M. Grandbois, M. Beyer, M. Rief, H. Clausen-Schaumann, and H. E. Gaub, "How strong is a covalent bond?" *Science*, vol. 283, no. 5408, pp. 1727–1730, 1999.
- [33] C. Steinhauer, C. Forthmann, J. Vogelsang, and P. Tinnefeld, "Superresolution microscopy on the basis of engineered dark states," *Journal of the American Chemical Society*, vol. 130, no. 50, pp. 16840–16841, 2008.
- [34] Software for PAIN analysis, <http://www.e14.ph.tum.de>.
- [35] A.-P. Eskelinen, A. Kuzyk, T. K. Kaltiainenaho et al., "Assembly of single-walled carbon nanotubes on DNA-origami templates through streptavidin-biotin interaction," *Small*, vol. 7, no. 6, pp. 746–750, 2011.
- [36] R. Schreiber, S. Kempter, S. Holler et al., "DNA origami templated growth of arbitrarily shaped metal nanoparticles," *Small*, vol. 7, no. 13, pp. 1795–1799, 2011.
- [37] K. Keren, M. Krueger, R. Gilad, G. Ben-Yoseph, U. Sivan, and E. Braun, "Sequence-specific molecular lithography on single DNA molecules," *Science*, vol. 297, no. 5578, pp. 72–75, 2002.
- [38] J. Liu, Y. Geng, E. Pound et al., "Metallization of branched DNA origami for nanoelectronic circuit fabrication," *ACS Nano*, vol. 5, no. 3, pp. 2240–2247, 2011.

4.4 Associated Publication P4

M1.3 - a small scaffold for DNA origami

By

Hassan Said, Verena J Schüller, Fabian J Eber, Christina Wege, Tim Liedl, and Clemens Richert

published in

Nanoscale 2012, 4, 284–290

Ref. [159] - Reproduced by permission of The Royal Society of Chemistry.

M1.3 – a small scaffold for DNA origami †

Cite this: DOI: 10.1039/c2nr32393a

Hassan Said,^a Verena J. Schüller,^b Fabian J. Eber,^c Christina Wege,^c Tim Liedl^b and Clemens Richert^{*a}

The DNA origami method produces programmable nanoscale objects that form when one long scaffold strand hybridizes to numerous oligonucleotide staple strands. One scaffold strand is dominating the field: M13mp18, a bacteriophage-derived vector 7249 nucleotides in length. The full-length M13 is typically folded by using over 200 staple oligonucleotides. Here we report the convenient preparation of a 704 nt fragment dubbed "M1.3" as a linear or cyclic scaffold and the assembly of small origami structures with just 15–24 staple strands. A typical M1.3 origami is large enough to be visualized by TEM, but small enough to show a cooperativity in its assembly and thermal denaturation that is reminiscent of oligonucleotide duplexes. Due to its medium size, M1.3 origami with globally modified staples is affordable. As a proof of principle, two origami structures with globally 5'-capped staples were prepared and were shown to give higher UV-melting points than the corresponding assembly with unmodified DNA. M1.3 has the size of a gene, not a genome, and may function as a model for gene-based nanostructures. Small origami with M1.3 as a scaffold may serve as a workbench for chemical, physical, and biological experiments.

Received 21st August 2012
Accepted 26th October 2012

DOI: 10.1039/c2nr32393a

www.rsc.org/nanoscale

Introduction

Deoxyribonucleic acid (DNA) has become a versatile material for the construction of nanoscale objects.^{1–3} The introduction of the scaffold-based DNA origami method has been an important step in DNA nanostructuring towards larger and more complex assemblies.⁴ The use of a long single-stranded scaffold strand, folded into the desired geometries through shorter, synthetic 'staple strands' is a robust, high-yielding method for generating two- and three-dimensional shapes.⁵ DNA origami structures have been used to create patterns of proteins,⁶ or nanoparticles,^{7–9} and applications include origami-based alignment media for nuclear magnetic resonance structure elucidation,^{10,11} production of nanocarriers that deliver antibody fragments,¹² or immune-stimulating nucleic acid sequences to cells.¹³ Further, origami can act as a scaffold or a workbench for single molecule analyses or chemical reactions.^{14–18} Even nanoscale assembly lines have been

realized on DNA origami platforms.¹⁹ Despite these exciting opportunities to set up spatially controlled experiments at a length scale on the order of 1–100 nm, the DNA origami approach has not yet become a mainstream method for chemists.

Most current origami structures are large. Single-stranded, circular M13mp18, a commercial bacteriophage-derived vector of 7249 nucleotides in length,²⁰ is most frequently used as a scaffold. Several reports exist on scaled-up versions of DNA origami with an increased number of addressable positions.^{21–28} But, DNA origami based on M13mp18 also has drawbacks. This very long scaffold strand increases the likelihood of strand cleavage and makes analysis at a molecular level challenging. Furthermore, known hairpin-forming regions in the M13mp18 sequence can impede folding of parts of the structures. As a consequence of the scaffold length, a large number of staple sequences, typically 120–200 synthetic oligonucleotide sequences, has to be ordered to construct a full origami. If not, a long loop of the unpaired scaffold remains that might interfere with the desired functions of the DNA origami structure. Very recently, a method for assembling large nanoscale shapes without a template strand has been reported.^{29,30} The full set of strands used to construct the different shapes from the basic 'canvas' design includes 362 'internal' oligonucleotides and 1344 'edge protectors', again calling for a very substantial investment in synthetic oligonucleotides prior to generating the desired structures. A large number of staple strands leads to significant costs that can dampen the enthusiasm of experimentalist wishing to set up origami structures, *e.g.* as chemical work benches. Much smaller origami than established sheets

^aInstitute for Organic Chemistry, University of Stuttgart, Pfaffenwaldring 55, 70569 Stuttgart, Germany. E-mail: lehrstuhl-2@oc.uni-stuttgart.de; Fax: +49 711 685 64321; Tel: +49 711 685 64311

^bFakultät für Physik and Center for Nanoscience, Geschwister-Scholl-Platz 1, 80539 München, Germany. E-mail: Tim.Liedl@lmu.de; Fax: +49 89 2180 3182

^cDepartment of Molecular Biology and Plant Virology, Institute of Biology, University of Stuttgart, Pfaffenwaldring 57, 70569 Stuttgart, Germany. E-mail: christina.wege@bio.uni-stuttgart.de; Fax: +49 711 685-65096

† Electronic supplementary information (ESI) available: Materials, full sequence of M1.3, alternative restriction reactions, sequences and origami designs, ALEX data, estimated cost of producing M13, additional melting data for origami, and MALDI spectra of individual capped oligonucleotides. See DOI: 10.1039/c2nr32393a

should suffice for many chemical experiments, while still being easy to detect by TEM and/or AFM.

Successful attempts have been made to produce shorter scaffolds. Woolley and co-workers employed the polymerase chain reaction (PCR) with a biotinylated primer, followed by purification over streptavidin-coated magnetic beads³¹ to produce single-stranded linear scaffolds 756 to 4808 nucleotides in length.³¹ Högberg *et al.* used a double-stranded PCR product of 1.3 kb to generate an origami by fast temperature drop and gradual removal of formamide in the presence of staple strands.³² Compared to approaches based on biotechnologically generated M13mp18, PCR is very costly and difficult to scale up. Furthermore, the need for a biotinylated primer, combined with purification over streptavidin-coated magnetic beads,³¹ makes PCR-based processes more costly than a process using unmodified synthetic oligonucleotides, combined with inexpensive enzymes and conventional gel electrophoresis.

We sought a DNA origami construct as a nanoscale chemical workbench. This bench was to fulfil several criteria: (i) reliable in its folding properties, (ii) inexpensive, (iii) assembling with a small number of staple oligonucleotides and (iv) of sufficient size to be analyzed with the established methodologies for DNA origami structures. It was critical that no more than a small number of staple strands were required, because we were interested in employing custom-modified synthetic oligonucleotides that are costly. For many chemical applications, even unmodified oligonucleotides are costly, and we expected that a robust, small origami, using much fewer staple strands, would more readily open up the field to synthetic organic chemists. Hence, we sought a scaffold strand derived from M13 approx. one order of magnitude smaller than the full vector. Here we report the convenient preparation of a M13 fragment as a linear or cyclic scaffold and the assembly of small origami. Because we were aiming at reducing the size by approx. one order of

magnitude, our scaffold was dubbed “M1.3”, with the number “1.3” derived from dividing the number 13 by ten.

Results and discussion

We wished to use a fraction of the M13 sequence because the sequence is well behaved, without a strong propensity to fold intramolecularly or to form aggregates. Further, M13 is commercially available and can be easily produced, even in academic settings by straightforward biotechnological culture.¹⁰ A calculation of the material costs for 0.1–1 mg of this DNA is presented in the ESI.†

Fig. 1 shows the method developed to excise the desired sequence with the help of restriction endonucleases. The use of restriction enzymes in generating scaffolds is not without precedent.³³ In our case, short double-stranded regions were generated by hybridizing two cleavage-inducing oligonucleotides (CIOs) to complementary sites in the scaffold. Type II restriction enzymes were used. Different restriction endonucleases and CIO sequences and lengths (8, 12, 20 and 40 nucleotides) were tested, as well as a range of oligonucleotide concentrations (1 to 1000 equiv.), and the concentration of the enzymes and reaction times were varied. A combination of *EcoRI* and *BglII* was selected, together with two CIO 20mers (Fig. 1a), producing M1.3 with a length of 704 nucleotides. Enzyme combinations for other fragments of M13 can be found in Chapter 3 of the ESI.† Both of the selected enzymes are inexpensive, with current total costs below 10 € for a large scale run with both enzymes (250 units each), and both are active in the same restriction buffer. The cleavage fragments of the CIOs are short enough to dissociate from the termini of M1.3 upon mild heating. The remaining long fragments of M13 and M1.3 were easily separable by agarose gel electrophoresis (Fig. 1c). The desired band was excised, the DNA was extracted, and desalted to obtain linear, single-stranded M1.3.

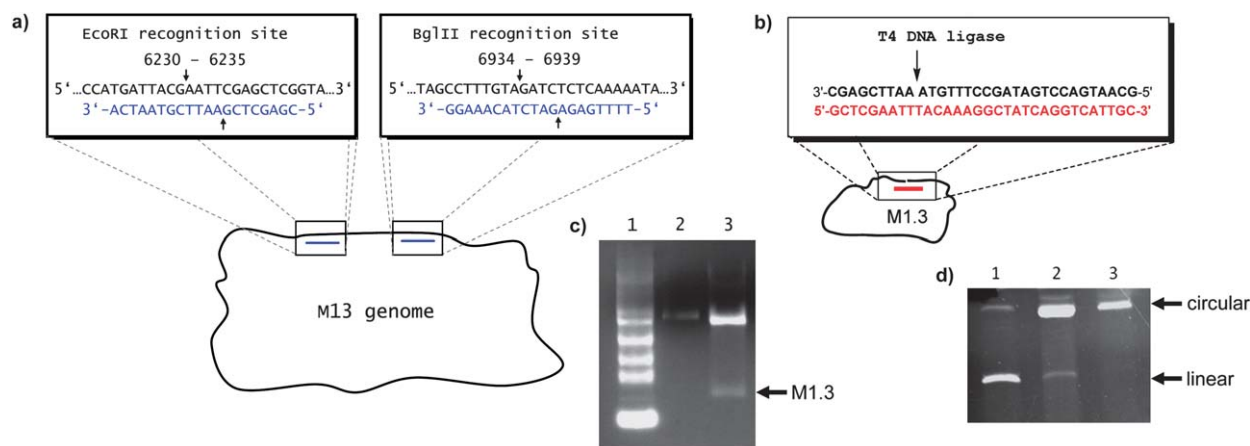


Fig. 1 Preparation of M1.3. (a) Excising M1.3 from the single-stranded M13mp18 vector DNA with the aid of two cleavage-inducing oligonucleotides (blue) and restriction endonucleases *EcoRI* and *BglII*. The cleavage sites are marked with arrows, and positions in the M13 sequence (GenBank accession no: X02513) are given numerically in the blow-up boxes. (b) Ligating linear M1.3 to cyclic M1.3 (cM1.3) with the aid of a template oligonucleotide of asymmetric coverage (red) and T4 DNA ligase. (c) Agarose electrophoresis gel showing the digestion of M13 to M1.3. Lane 1: 0.24–9.5 kb RNA ladder, lane 2: 0.2 pmol M13, lane 3: 0.8 pmol M13 after digestion, showing the fast-migrating band of M1.3. (d) PAGE (8% denaturing) of the products of the enzymatic cyclization of M1.3 with T4 DNA ligase, using a template strand with symmetric (lane 1) or asymmetric coverage of the termini of the linear scaffold (lane 2). Lane 3 shows purified circular M1.3.

Most origami structures can be readily produced with linear scaffold strands, but circular scaffolds offer an additional entropic benefit and fold more readily. Therefore, a protocol for cyclizing the 704mer linear M1.3 with the aid of a template strand and an inexpensive ligase (T4 DNA ligase) was developed. For efficient ligation, the template strand and linear scaffold need to be at an equimolar concentration. For very long DNA, stoichiometries are difficult to adjust accurately. Initial ligation attempts, using conventional template strands that cover the ligation site symmetrically, were unsatisfactory (Fig. 1d, lane 1). To overcome this problem, an asymmetric template strand was applied at a 5-fold excess. After annealing, the mixture was heated to 40 °C, a temperature at which the shorter double-stranded region at the 5'-terminus of the scaffold melts, and excess template strand was removed by ultrafiltration. The desired duplex with a template to scaffold ratio of 1 : 1 was cooled to 16 °C and ligation was induced through addition of ATP and T4 DNA ligase, leading to circular M1.3 (cM1.3) in >80% yield (Fig. 1d, lane 2).

Starting from linear or circular M1.3, a first small origami sheet was assembled, using 24 unique staple strands (see ESI† for sequences). The sheet was designed using caDNAno.³⁴ It is non-symmetrical, with one receding corner to facilitate the assignment of the two faces. It is of sufficient size (approx. 20 × 30 nm) to set up a 'chemical workbench' with both small molecules and small proteins and to detect its shape by AFM. Due to its remote resemblance to features of a human hand, it was dubbed 'four finger sheet' or '4F sheet'. Fig. 2 shows a cartoon of the sheet, a gel of assembly mixtures for linear and circular M1.3, and a TEM micrograph. Images of partly frayed structures, as in the blow-up in Fig. 2c, further confirmed the formation of the desired shape, but more compact forms were more abundant in the TEM images, as expected for the design. In addition, alternating laser excitation (ALEX)³⁵ measurements showed that two fluorescently labeled staple strands are efficiently integrated into the 4F sheet, confirming the successful formation of the full DNA origami structure (see Fig. S4, ESI†).

Encouraged by these results, an additional set of M1.3 origami was prepared, including a flat, 'two-dimensional'

triangle, a curved six helix bundle,³⁶ and a three-dimensional cube³⁷ (Fig. 3). The latter two are smaller versions of the known M13 origami. The small structures cover a range of different design features, such as deletions and insertions and three-dimensional packing arrangements. They required between 15 and 21 different staple oligonucleotides, demonstrating that the number of staple oligonucleotides can be scaled with the length of the scaffold.

As the long-term focus of our study is on synthetically enforced origami, we then devised a method for generating sets of staple strands consisting entirely of modified strands. We

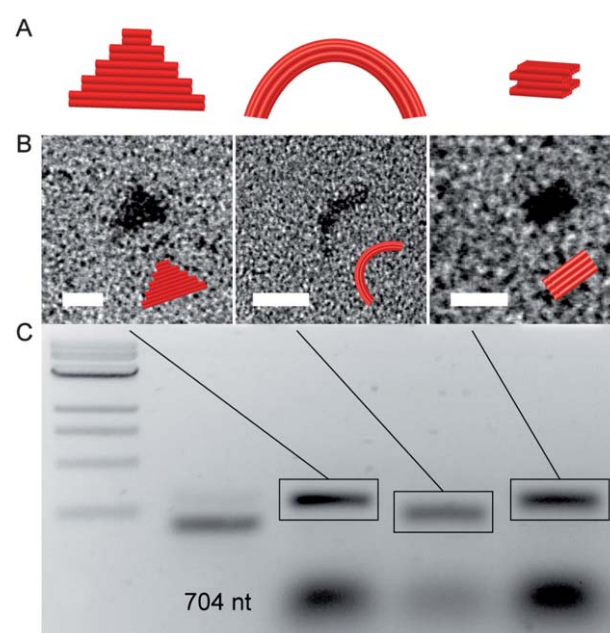


Fig. 3 DNA origami structures assembled by using the M1.3 scaffold. (A) Schemes of DNA origami structures: 2D triangle, curved six-helix bundle (6HB), and 3D cube. (B) Electron micrographs of DNA origami structures. (C) Agarose gel of assembled structures. Left to right: 2-log 1 kb DNA ladder, M1.3 704 nt scaffold, 2D triangle, curved six-helix bundle (6HB), and 3D cube (0.2 pmol each). Scale bars: 20 nm. Different granularities are due to different sample settings.

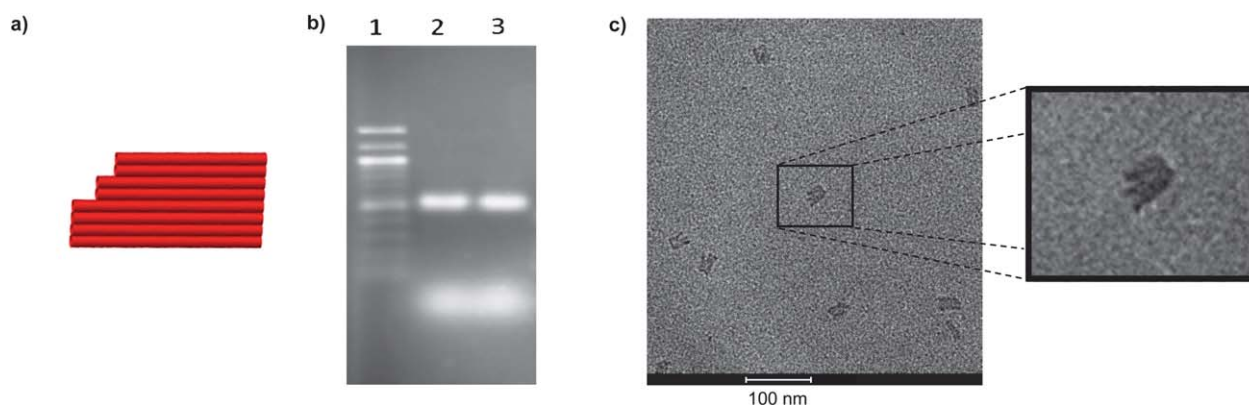


Fig. 2 Folding of M1.3 with 24 staple strands into a four finger sheet (4F sheet). (a) Design of 4F sheet, (b) fluorescence image of agarose gel with ethidium bromide staining, lane 1: 100 bp ladder; lane 2: 0.5 pmol linear M1.3, assembled with 10 equivalents of staple strands; lane 3: 0.5 pmol circular M1.3, assembled with 10 equivalents of staple strands, diffuse bands at the bottom are from excess staple strands, (c) transmission electron micrograph. Note the characteristic finger-like substructure of the sheet when viewed perpendicular to the sheet plane.

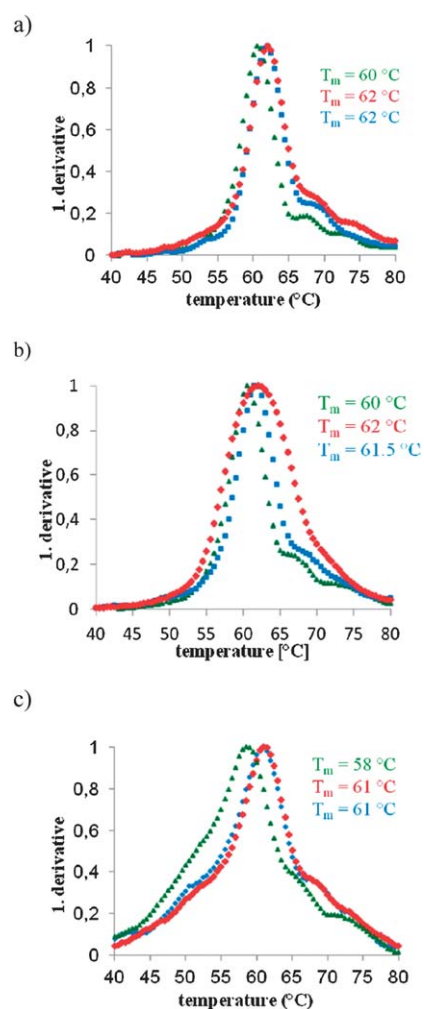
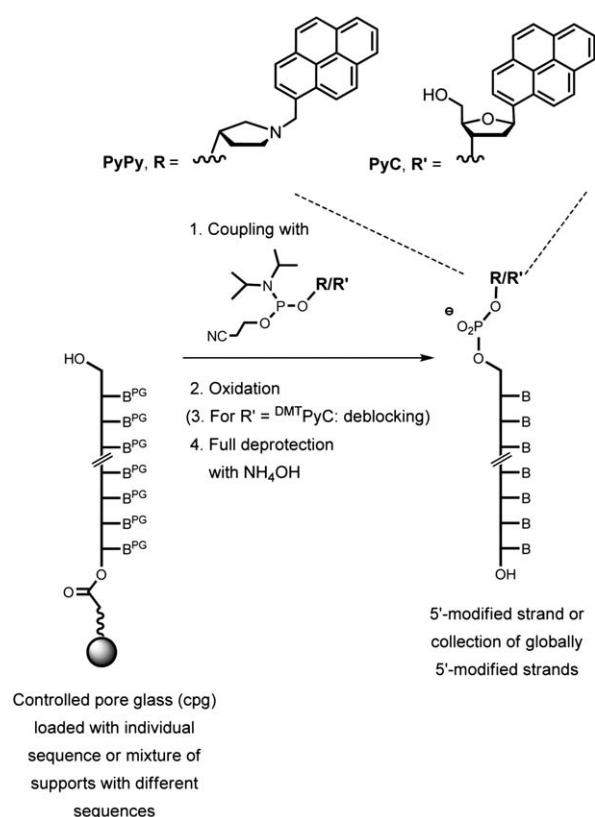
chase staples that each bear a molecular cap at their 5'-terminus. Caps can enhance duplex stability and base-pairing fidelity at the termini of linear duplexes by bridging helices with correctly paired terminal base pairs more strongly than helices with mispaired termini.³⁸ Scheme 1 shows the synthesis of modified strands with a pyrenyl-*C*-nucleoside³⁹ (**PyC**) or a pyrenylmethyl-pyrrolidinol residue (**PyPy**) as the 5'-cap.⁴⁰ Pyrenes can intercalate,⁴¹ show weak fluorescence, and can give excimer bands when in close proximity.⁴² The phosphoramidite of the **PyPy** cap is commercially available.⁴³

The two sets of globally 5'-modified staple strands for the 4F sheet were prepared by pooling 2 mg each of the controlled pore glass supports (cpg's) bearing the individual protected staple strand sequences. After thorough mixing, the pooled supports were subjected to one cycle of DNA chain extension using the pyrenyl building blocks. Conventional deprotection procedures then gave the mixture of strands required to assemble the modified origami with a pyrenyl moiety at every 5'-terminus of a staple strand. A control synthesis with a single sequence was also performed to confirm high coupling yields for the reagents used. When annealed to the M1.3 scaffold, either set of staple strands gave high yields of 4F origami. The

origami bands showed slightly decreased mobility in agarose gels compared to unmodified 4F origami (Fig. S5, ESI†), as expected for structures with a modest increase in rigidity and size.

The 4F origami sheets were freed of excess staple strands by membrane filtration over 100 kDa cut-off spin filters. To study the effect of the caps on the stability of the sheets, UV-melting curves of the origami assemblies, monitored at 260 nm, were measured for the unmodified 4F origami and either of its counterparts with 5'-capped staple strands. All three gave a sharp transition and a T_m typical for M13 origami⁴⁴ (Fig. 4 and S6 in the ESI†).

Both pyrenyl caps induced an increase in the UV-melting point, as defined by the maximum of the first derivative, by approximately 2 °C (Table S1, ESI†). Perhaps more importantly, 4F origami with the capped staples shows slower kinetics of melting, meaning that a fraction of the duplex regions survives



longer under thermal stress, resulting in a broader transition. This effect is most pronounced with the **PyC** cap at a heating rate of $1\text{ }^{\circ}\text{C min}^{-1}$ (Fig. 4b). We hypothesize that a bridging effect of the pyrenyl residues that stabilize selected duplex regions causes this effect. The global assembly kinetics appear to be similar for sheets with and without capped staples, though, as judged by similar shapes of transitions observed in cooling curves measured at a cooling rate of $0.2\text{ }^{\circ}\text{C per minute}$ (Fig. 4c). Here, the main peaks observed for the pyrenyl-modified origami are slightly sharper, suggesting that the polycyclic aromatic substituents aid in the cooperative process of origami formation. At the faster cooling rate of $1\text{ }^{\circ}\text{C min}^{-1}$, only the sheet with **PyPy** caps shows this sharpening effect (Fig. S7 and Table S2, ESI†).

We note that the current design of the 4F sheet is not optimized for accommodating tetracyclic aromatic hydrocarbons, such as pyrenes. We expect that optimization of caps and their binding sites will lead to stronger effects than what the current, strictly exploratory results show. For example, larger ligands that can bridge two duplexes at a time, placed at strategic positions, are expected to have stronger effects. Both thermal stability and rapid assembly can be favorable for practical applications. Perhaps more importantly, catalytically active moieties,⁴⁵ recognition motifs,⁴⁶ or reporter groups,⁴⁷ properly positioned in space with the aid of modified staple strands, can be expected to lead to new, functional origami. The small M1.3 platform may help to rapidly prototype such origami.

Conclusions

The transition from the molecular scale, where structures at or below the 1 nm limit can readily be produced by organic synthesis to the 100 nm scale of full size origami sheets, is quite dramatic. Most chemical experiments that cross the boundaries of traditional synthetic assemblies require spatial control on the 10–30 nm scale, rather than the 100 nm scale. Small scaffolds, such as M1.3, give access to this scale. We are currently starting a spectroscopic study on chromophore arrays on an M1.3 sheet that offers the functionality of larger arrays, based on M13 platforms,¹⁸ with a fraction of the number of staple strands. But, the advantage of the reduction in oligonucleotide staples is greatest when many or all of them are chemically modified. Globally capping or derivatizing oligonucleotides requires accurately weighing out individual cpg samples, and completely reacting the mixture batch in a solid-phase apparatus, a task that is difficult to do with conventional synthesizer cartridges for sets of 100 or more different cpg supports. We note that properly derivatized staples allow for covalently locking individual staple strands. We are actively pursuing locking methodologies.⁴⁸

Routine access to both small and large origami broadens the range of functional constructs that can be formed through inter-origami hybridization. But, smaller origami structures have hydrodynamic properties that make it easier to study them spectroscopically with bulk methods in solution, using conventional chemical analysis methods. Our data show how

inexpensive ensemble experiments can yield data on the stability of origami structures and the global kinetics of their formation. Together, our data suggest a role for small origami structures that complements that of genome-sized ones, both for asking scientific questions and for developing devices that require a defined three-dimensional structure at the low nanometer scale.

Experimental

Excision of M1.3 from M13mp18 ssDNA

A solution of 20 pmol (50 μg) circular single-stranded M13mp18 DNA and ten equivalents of each of the two cleavage-inducing oligonucleotides (20mers) in 450 μL of restriction buffer (50 mM Tris-HCl, pH 7.5, 10 mM MgCl_2 , 100 mM NaCl, 0.1 mg mL^{-1} BSA) was heated to $85\text{ }^{\circ}\text{C}$ for 5 min and allowed to cool to $20\text{ }^{\circ}\text{C}$ in 2 h. To the solution were added 25 μL each of stock solutions of *EcoRI* and *BglIII* ($10\text{ U } \mu\text{L}^{-1}$) to give a final volume of 500 μL and final concentrations of 40 nM M13mp18 DNA, 400 nM oligonucleotides and 5 units of each enzyme per μg of DNA. The solution was incubated at $40\text{ }^{\circ}\text{C}$ for 6 h. The digestion was stopped by adding 25 μL of 0.5 M EDTA (pH 8.0) to give a final concentration of EDTA of 24 mM. The volume of the solution was reduced to 200 μL by lyophilisation, followed by loading into several wells of a 1% agarose gel in $1\times$ TAE buffer (40 mM Tris, 1 mM EDTA, 40 mM acetic acid). After running the gel for 90 min at 60 V and staining with ethidium bromide ($0.5\text{ } \mu\text{g mL}^{-1}$), the desired band was excised with an extraction kit (NucleoSpin gel and PCR clean-up, Macherey-Nagel, Düren, Germany). Then, the DNA was desalted using an Amicon Ultra 0.5 mL centrifugal filter with a molecular weight cut-off of 30 000 Da (Millipore, Billerica, MA, USA). The yield of M1.3, as determined by UV absorption at 260 nm, was 62% (12.4 pmol).

Cyclization with asymmetric template strand

A sample of linear M1.3 (2 pmol) and 10 pmol of the asymmetric template strand in ligase buffer (30 μL , 40 mM Tris-HCl, pH 7.8, 10 mM MgCl_2 , 10 mM DTT, 5 mM ATP) were heated to $85\text{ }^{\circ}\text{C}$ for 5 min and allowed to cool to $4\text{ }^{\circ}\text{C}$ for 2 h, followed by incubation at $4\text{ }^{\circ}\text{C}$ for 16 h. The solution was diluted with ligase buffer to 500 μL and warmed to $40\text{ }^{\circ}\text{C}$ for 20 min. The excess template strand was removed by filtration at $40\text{ }^{\circ}\text{C}$, using an Amicon Ultra 0.5 mL centrifugal filter with a molecular weight cut-off of 30 000 Da. The filter was washed twice with ligase buffer. The DNA was recovered (20 μL), and the solution was allowed to cool slowly from $40\text{ }^{\circ}\text{C}$ to $16\text{ }^{\circ}\text{C}$, followed by incubation at $16\text{ }^{\circ}\text{C}$ for 2 h. Then, solutions of ATP (1.5 μL of 10 mM) and T4 DNA ligase (3 μL , 1 Weiss unit per μL), 50% PEG 4000 (3 μL) and $1\times$ ligase buffer were added to a final volume of 30 μL . After 3 h, the ligation was stopped by heating to $70\text{ }^{\circ}\text{C}$ for 10 min. The solution was lyophilized, and the residue was dissolved in sample buffer (20 μL , 50% formamide, 1 mM EDTA, pH 8.0), heated to $90\text{ }^{\circ}\text{C}$ for 2 min, and immediately placed on ice. Successful cyclization was confirmed by 8% denaturing PAGE (7 M urea).

Assembly of origami

For the 4F sheet, a solution of 0.5 pmol M1.3 and 5 pmol staple strands in 20 μL of folding buffer (pH 8.0) containing 5 mM Tris-HCl, 1 mM EDTA, and 12 mM MgCl_2 was heated to 85 $^\circ\text{C}$ for 5 min, and then cooled to 4 $^\circ\text{C}$ over the course of 2.5 h, followed by incubation at 4 $^\circ\text{C}$ for 12 h. For gel electrophoresis, 0.75 g of agarose in 50 mL of TBE buffer (45 mM Tris borate, 1 mM EDTA, pH 8.3) was boiled, cooled to 60 $^\circ\text{C}$, and treated with MgCl_2 solution (2 M, 300 μL) to give a 12 mM MgCl_2 concentration, and cast as gel. A loading dye (0.025% xylene cyanol in 30% aqueous glycerol) was added to origami samples, followed by electrophoresis in the gel for 4 h at 50 V, followed by staining with ethidium bromide (0.5 mg mL^{-1}) for 20 min. A similar procedure was employed for the assembly of the other M1.3 origami (Fig. 3), by annealing 10 nM scaffolds and 100 nM staple strands, in 1 \times TE with 10 mM MgCl_2 for 1 h, and purification using a 2% agarose gel, 0.5 \times TBE, 11 mM MgCl_2 running buffer for 2 h at 70 V. Isolation involved the 'freeze and squeeze' procedure with 10 min in a freezer and centrifugation for 10 min at 13 000 rpm.

Synthesis of globally 5'-capped sets of staple strands

For the global modification of 24 staple strands, 2 mg of each cpg loaded with a given sequence (approx. 0.06 μmol loading) and the dimethoxytriyl (DMT)-protected 3'-phosphoramidite of the **PyC** C-nucleoside (23.6 mg, 28.8 μmol , 20 eq.) or the phosphoramidite of the **PyPy** nucleoside analog (14.5 mg, 28.8 μmol , 20 eq.) were dried at 0.1 mbar in a polypropylene reaction vessel for 2 h. Then, activator solution (200 μL , 4,5-dicyanoimidazole, 0.25 M in CH_3CN) was added under a N_2 stream. After 1 h, the cpg was washed with CH_3CN and then treated with oxidizer solution (200 μL of 0.02 M iodine in water-pyridine-THF, 2 : 21 : 77 v/v/v) for 10 min, followed by washing with CH_3CN . In the case of the **PyC**-capped oligonucleotide, deblock solution (200 μL , trichloroacetic acid in CH_2Cl_2 , 3 : 97, 200 μL) was added to the cpg, and the mixture was incubated for 20 min, followed by washing with CH_3CN . After drying at 0.1 mbar, the cpg was treated with ammonium hydroxide (25% aqueous NH_3 , 500 μL) for 5 h at 55 $^\circ\text{C}$. (**Caution:** pressure builds up when heating ammonia solution.) After cooling, excess ammonia was removed by gently blowing a stream of nitrogen onto the surface until the solution was odorless, and the solution was filtered (0.2 μm pore size, Whatman Inc., Chilton, NJ). Solutions were lyophilized and the modified staple strand mixtures were dissolved in water (100 μL) to produce a stock solution.

UV-melting curve experiments

After assembly of the 4F origami from 4 pmol M1.3 and 80 pmol (modified) staple strands in 50 μL of folding buffer (pH 8.0) containing 5 mM Tris-HCl, 1 mM EDTA, and 12 mM MgCl_2 via heating to 85 $^\circ\text{C}$ for 5 min, and cooling to 4 $^\circ\text{C}$ for 2.5 h, followed by incubation at 4 $^\circ\text{C}$ for 12 h, the solution was diluted with folding buffer to 500 μL , and excess staple strands were removed by filtration at 10 $^\circ\text{C}$, using an Amicon Ultra 0.5 mL centrifugal filter with a molecular weight cut-off of 100 000 Da.

The filter was washed three times with 500 μL of folding buffer. The origami was recovered (30 μL), the solution was diluted with folding buffer to 80 μL , and transferred to a UV/Vis microcuvette (10 mm path length). To prevent evaporation during the melting experiment, the sample was covered with 100 μL of mineral oil. The first derivatives were calculated using the spectrometer software (UV Winlab 3.0, Perkin Elmer).

Acknowledgements

The authors are grateful to Dominik Kauert and Dr Ralf Seidel (TU Dresden) for joint exploratory experiments on the folding of the M1.3 sheet, Dr Ingo Stein and Prof. Philip Tinnefeld (L.M.U. Munich) for access to a single molecule laser set-up, and Dr M. Schweikert (U. Stuttgart) for assistance with TEM imaging. This work was supported by DFG (grant no. RI 1063/9-1 to C.R.; LI 1743/2-1 to T.L.), and the University of Stuttgart.

Notes and references

- 1 N. C. Seeman, *Nature*, 2003, **421**, 427–431.
- 2 U. Feldkamp and C. M. Niemeyer, *Angew. Chem., Int. Ed.*, 2006, **45**, 1856–1876.
- 3 F. A. Aldaye, A. L. Palmer and H. F. Sleiman, *Science*, 2008, **321**, 1795–1799.
- 4 P. W. K. Rothmund, *Nature*, 2006, **440**, 297–302.
- 5 B. Sacca and C. M. Niemeyer, *Angew. Chem., Int. Ed.*, 2012, **51**, 58–66.
- 6 R. Chhabra, J. Sharma, Y. Ke, Y. Liu, S. Rinker, S. Lindsay and H. Yan, *J. Am. Chem. Soc.*, 2007, **129**, 10304–10305.
- 7 S. Pal, Z. Deng, B. Ding, H. Yan and Y. Liu, *Angew. Chem., Int. Ed.*, 2010, **49**, 2700–2704.
- 8 B. Ding, Z. Deng, H. Yan, S. Cabrini, R. N. Zuckermann and J. Bokor, *J. Am. Chem. Soc.*, 2010, **132**, 3248–3249.
- 9 A. Kuzyk, R. Schreiber, Z. Fan, G. Pardatscher, E.-M. Roller, A. Högele, F. C. Simmel, A. O. Govorov and T. Liedl, *Nature*, 2012, **483**, 311–314.
- 10 S. M. Douglas, J. J. Chou and W. M. Shih, *Proc. Natl. Acad. Sci. U. S. A.*, 2007, **104**, 6644–6648.
- 11 M. J. Berardi, W. M. Shih, S. C. Harrison and J. J. Chou, *Nature*, 2011, **476**, 109–113.
- 12 S. M. Douglas, I. Bachelet and G. M. Church, *Science*, 2012, **335**, 831–834.
- 13 V. J. Schüller, S. Heidegger, N. Sandholzer, P. C. Nickels, N. A. Suhartha, S. Endres, C. Bourquin and T. Liedl, *ACS Nano*, 2011, **12**, 9696–9702.
- 14 For a recent review, see: A. Rajendran, M. Endo and H. Sugiyama, *Angew. Chem., Int. Ed.*, 2012, **51**, 874–890.
- 15 M. Endo, Y. Katsuda, K. Hidaka and H. Sugiyama, *J. Am. Chem. Soc.*, 2010, **132**, 1592–1597.
- 16 N. V. Voigt, T. Topping, A. Rotaru, M. F. Jacobsen, J. B. Ravensbaek, R. Subramani, W. Mamdouh, J. Kjems, A. Mokhir, F. Besenbacher and K. V. Gothelf, *Nat. Nanotechnol.*, 2010, **5**, 200–203.
- 17 I. H. Stein, C. Steinhauer and P. Tinnefeld, *J. Am. Chem. Soc.*, 2011, **133**, 4193–4195.

- 18 I. H. Stein, V. Schüller, P. Böhm, P. Tinnefeld and T. Liedl, *ChemPhysChem*, 2011, **12**, 689–695.
- 19 H. Gu, J. Chao, S.-J. Xiao and N. C. Seeman, *Nature*, 2010, **465**, 202–205.
- 20 C. Yanisch-Perron, J. Vieira and J. Messing, *Gene*, 1985, **33**, 103–119.
- 21 M. Endo, T. Sugita, Y. Katsuda, K. Hidaka and H. Sugiyama, *Chem.–Eur. J.*, 2010, **16**, 5362–5368.
- 22 A. Rajendran, M. Endo, Y. Katsuda, K. Hidaka and H. Sugiyama, *ACS Nano*, 2011, **5**, 665–671.
- 23 M. Endo, T. Sugita, A. Rajendran, Y. Katsuda, T. Emura, K. Hidaka and H. Sugiyama, *Chem. Commun.*, 2011, **47**, 3213–3215.
- 24 A. Rajendran, M. Endo and H. Sugiyama, *Curr. Protoc. Nucleic Acid Chem.*, 2012, **48**, 12.9.1–12.9.18.
- 25 Z. Zhao, H. Yan and Y. Liu, *Angew. Chem., Int. Ed.*, 2010, **49**, 1414–1417.
- 26 Z. Zhao, Y. Liu and H. Yan, *Nano Lett.*, 2011, **11**, 2997–3002.
- 27 W. Liu, H. Zhong, R. Wang and N. C. Seeman, *Angew. Chem., Int. Ed.*, 2011, **50**, 264–267.
- 28 H. Zhang, J. Chao, D. Pun, H. Liu, Q. Huang and C. Fan, *Chem. Commun.*, 2012, **48**, 6405–6407.
- 29 B. Wei, M. Dai and P. Yin, *Nature*, 2012, **485**, 623–626.
- 30 P. Rothmund and E. Sloth-Andersen, *Nature*, 2012, **485**, 584–585.
- 31 E. Pound, J. R. Ashton, H. A. Becerril and A. T. Woolley, *Nano Lett.*, 2009, **9**, 4302–4305.
- 32 B. Högberg, T. Liedl and W. M. Shih, *J. Am. Chem. Soc.*, 2009, **131**, 9154–9155.
- 33 S. M. Douglas, H. Dietz, T. Liedl, B. Hogberg, F. Graf and W. M. Shih, *Nature*, 2009, **459**, 414–418.
- 34 S. M. Douglas, A. H. Marblestone, S. Teerapittayanon, A. Vazquez, G. M. Church and W. M. Shih, *Nucleic Acids Res.*, 2009, **37**, 5001–5006.
- 35 A. N. Kapanidis, N. K. Lee, T. A. Laurence, S. Doose, E. Margeat and S. Weiss, *Proc. Natl. Acad. Sci. U. S. A.*, 2004, **101**, 8936–8941.
- 36 H. Dietz, S. M. Douglas and W. M. Shih, *Science*, 2009, **325**, 725–730.
- 37 Y. Ke, S. M. Douglas, M. Liu, J. Sharma, A. Cheng, A. Leung, Y. Liu, W. M. Shih and H. Yan, *J. Am. Chem. Soc.*, 2009, **131**, 15903–15908.
- 38 (a) C. F. Bleczinski and C. Richert, *J. Am. Chem. Soc.*, 1999, **121**, 10889–10894; (b) Z. Dogan, R. Paulini, J. A. Rojas Stütz, S. Narayanan and C. Richert, *J. Am. Chem. Soc.*, 2004, **126**, 4762–4763; (c) J. Tuma, W. H. Connors, D. H. Stitelman and C. Richert, *J. Am. Chem. Soc.*, 2002, **124**, 4236–4246; (d) S. Egetenmeyer and C. Richert, *Chem.–Eur. J.*, 2011, **17**, 11813–11827.
- 39 (a) K. M. Guckian, B. A. Schweitzer, R. X.-F. Ren, C. J. Sheils, P. L. Paris, D. C. Tahmassebi and E. T. Kool, *J. Am. Chem. Soc.*, 1996, **118**, 8182–8183; (b) S. Hainke, S. Arndt and O. Seitz, *Org. Biomol. Chem.*, 2005, **3**, 4233–4238.
- 40 S. Narayanan, J. Gall and C. Richert, *Nucleic Acids Res.*, 2004, **32**, 2901–2911.
- 41 S. Smirnov, T. J. Matray, E. T. Kool and C. de los Santos, *Nucleic Acids Res.*, 2002, **30**, 5561–5569.
- 42 M. E. Østergaard and P. J. Hrdlicka, *Chem. Soc. Rev.*, 2011, **40**, 5771–5788.
- 43 *Catalog no. 10-1987*, Glen Research Inc., Sterling, VA 20164, USA.
- 44 For earlier reports on UV-melting curves of origami, see: (a) A. Rajendran, M. Endo, Y. Katsuda, K. Hidaka and H. Sugiyama, *J. Am. Chem. Soc.*, 2011, **133**, 14488–14491; (b) J. Song, J.-M. Arbona, Z. Zhang, L. Liu, E. Xie, J. Elezgaray, J.-P. Aime, K. V. Gothelf, F. Besenbacher and M. Dong, *J. Am. Chem. Soc.*, 2012, **134**, 9844–9847.
- 45 (a) G. Roelfes and B. L. Feringa, *Angew. Chem., Int. Ed.*, 2005, **44**, 3230–3232; (b) A. J. Boersma, B. de Bruin, B. L. Feringa and G. Roelfes, *Chem. Commun.*, 2012, **48**, 2394–2396.
- 46 See e.g.: C. Kröner, M. Röthlingshoefer and C. Richert, *J. Org. Chem.*, 2011, **76**, 2933–2936.
- 47 See e.g.: (a) C. Holzhauser and H. A. Wagenknecht, *ChemBioChem*, 2012, **13**, 1136–1138; (b) S. M. Biner and R. Häner, *ChemBioChem*, 2011, **12**, 2733–2736.
- 48 C. Prestinari and C. Richert, *Chem. Commun.*, 2011, **47**, 10824–10826.

A Appendix

Supporting Information for Associated Publication P1

Supporting Information

Single-Molecule FRET Ruler Based on Rigid DNA Origami Blocks

By

Ingo H. Stein, Verena Schüller, Philip Böhm, Philip Tinnefeld and Tim Liedl

published in

ChemPhysChem 2011, 12, 689–695

Reprinted with permission from ref. [73]. Copyright 2011 WILEY-VCH.

CHEMPHYSICHEM

Supporting Information

© Copyright Wiley-VCH Verlag GmbH & Co. KGaA, 69451 Weinheim, 2011

Single-Molecule FRET Ruler Based on Rigid DNA Origami Blocks

Ingo H. Stein,^[a] Verena Schüller,^[b] Philip Böhm,^[b] Philip Tinnefeld,^{*,[a, c, d]} and Tim Liedl^{*,[b, c]}

cphc_201000781_sm_miscellaneous_information.pdf

Figure S1: Influence of the linker lengths on donor-acceptor separation

Both images are a front view of the DNA helices with the helical axis perpendicular to the image plane.

Left: For the dsDNA the donor-acceptor separation is strongly dependent on the length of the linkers and additionally varies for different basepair separations. For a donor-acceptor separation of e.g. 7 bps on opposite strands, the linkers should be almost parallel and on the same side of the cylindrically shaped DNA helix and their lengths (but not their dynamics) should cancel out. On the other hand, for one or twelve base pairs separation, corresponding roughly to a full turn, the dyes are on the opposite side of the DNA cylinder and the relatively undefined lengths of the linkers have to be added together and largely contribute to the donor-acceptor distance

Right: On the DNA origami block, the linkers of all acceptors are almost parallel to the donor and on the same side of the origami block. The linker length itself has negligible influence on the static (averaged) donor-acceptor distance.

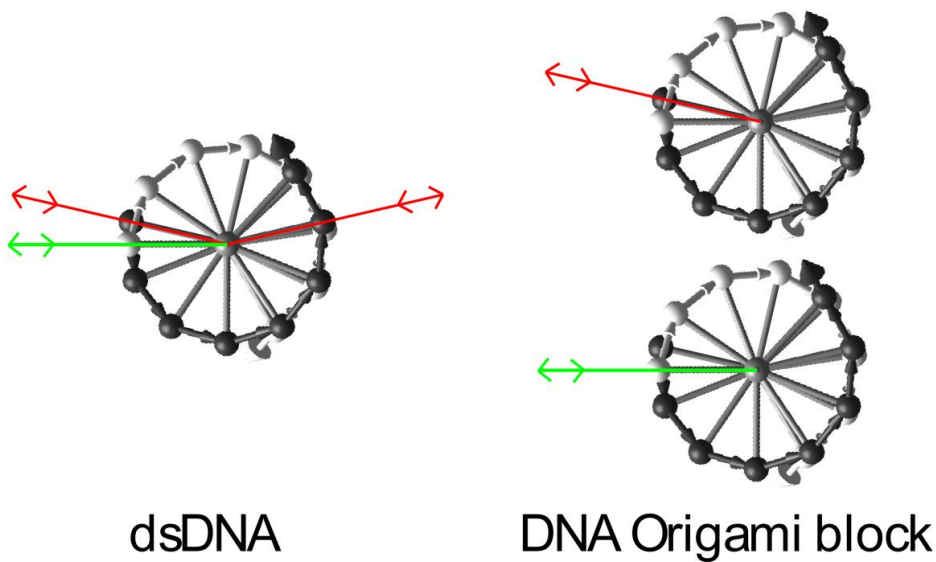


Figure S2: Design schematic of DNA origami block

Scaffold routing and staple design in two-dimensional representation. Graphics and sequences created with caDNAo.

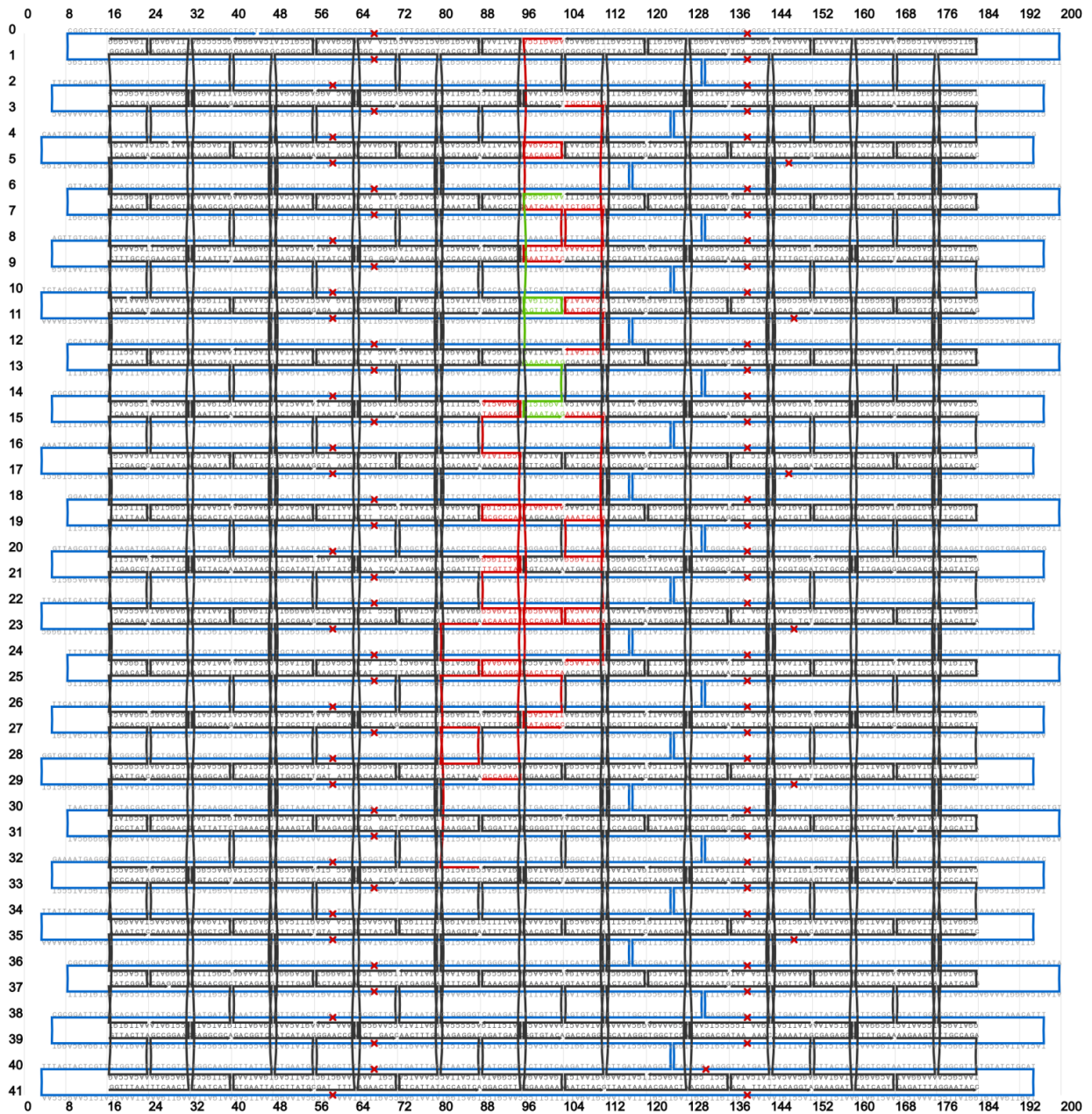


Figure S3:

Top: E-S histogram of doubly labeled dsDNA (8 bp separation)

Bottom: E-S histogram of doubly labeled DNA origami block (position of acceptor (0,10) as defined in Scheme 1A, 3.5 nm separation)

The two-dimensional histograms were obtained by 2D-binning of the E- and S-values with 40 bins each in the range of -0.1 to 1.1. Additionally one-dimensional histograms for the E- as well as the S-values are shown.

The slightly broader distribution of E- and S-histograms for the dsDNA samples is most likely due to increased shot noise. Due to longer diffusion times of the origami samples a higher number of photons could be collected per burst.

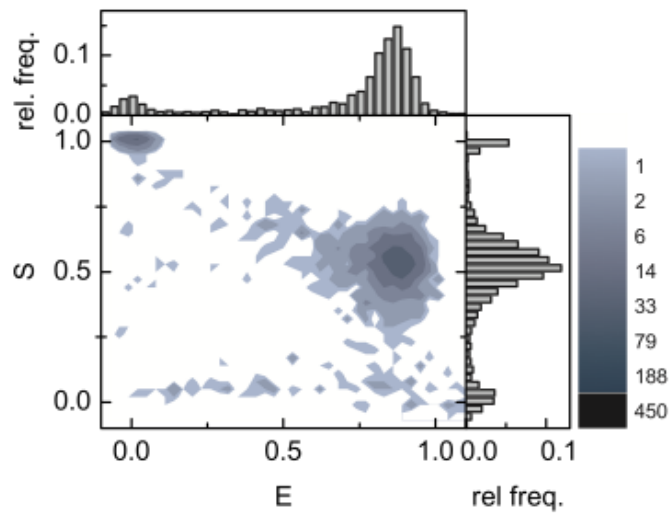
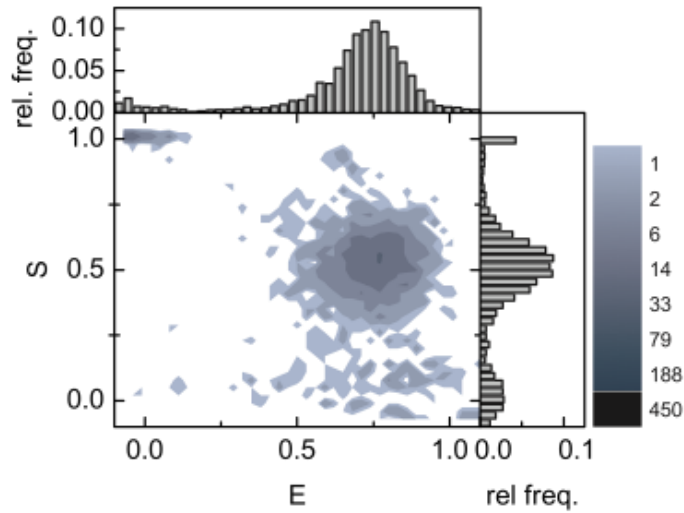


Table S4: Distance calculation between donor and acceptor dyes on DNA origami blocks

The values given in table S4 correspond to the following:

1st column: Relative positions of the fluorophores in the DNA origami block. The first value is the position of the donor, which is defined as helix 0 and base 0.

2nd column: Calculated with the simplified assumption of an average center-to-center distance of 2.6 nm between the helices.

3rd column: Differences to the original positions if the tilt of the bases to which the acceptor molecules are attached in respect to the donor molecule is taken into account.

4th column: Differences to the original positions if the model incorporates the bowing of neighboring double strands due to electrostatic repulsion.

5th column: Positions and distances between the dye molecules if all corrections are applied.

Position (helix, nucleotide)	(x, y, distance to donor) uncorrected / nm	(Δx , Δy , distance to donor) correction i) / nm	(Δx , Δy , distance to donor) correction ii) / nm	(x, y, distance to donor) corrected / nm
(0, 0)	(0.0, 0.0, 0.0)	(0.0, 0.0, 0.0)	(0.1, 0.0, 0.0)	(0.1, 0.0, 0.0)
(-1, -3)	(-2.6, -1.0, 2.8)	(0.6, 0.0, 2.3)	(-0.0, 0.0, 3.0)	(-2.0, -1.0, 2.4)
(0, 10)	(0.0, 3.4, 3.4)	(-0.6, 0.0, 3.5)	(0.0, 0.0, 3.4)	(-0.6, 3.4, 3.5)
(-2, 0)	(-5.2, 0.0, 5.2)	(0.0, 0.0, 5.2)	(0.1, 0.0, 5.2)	(-5.1, 0.0, 5.2)
(2, -10)	(5.2, -3.4, 6.2)	(0.6, 0.0, 6.7)	(-0.1, 0.0, 6.0)	(5.7, -3.4, 6.5)
(-2, -11)	(-5.2, -3.7, 6.4)	(-0.6, 0.0, 6.9)	(-0.1, 0.0, 6.6)	(-5.9, -3.7, 7.1)
(3, 8)	(7.8, 2.7, 8.3)	(1.1, 0.0, 9.3)	(-0.1, 0.0, 8.1)	(8.8, 2.7, 9.2)
(4, -1)	(10.4, -0.3, 10.4)	(-1.1, 0.0, 9.3)	(0.1, 0.0, 10.4)	(9.4, -0.3, 9.3)
(5, 17)	(13.0, 5.8, 14.2)	(0.0, 0.0, 14.2)	(0.1, 0.0, 14.2)	(13.1, 5.8, 14.2)

Figure S5: Measurements of dsDNA and FRET blocks with Magnesium

Top: FRET efficiencies of dsDNA samples in absence and presence of 18 mM magnesium as a function of donor-acceptor separation in basepairs. The solid line is a fit to the data according to a geometric model as described in the main text. The fitting parameters of both measurements agree within measurement uncertainty:

without magnesium: $a = 17.8 \pm 0.9 \text{ \AA}$, $L = 9.4 \pm 1.0 \text{ \AA}$, $\theta_0 = 243.3^\circ \pm 9^\circ$;

18mM magnesium: $a = 17.8 \pm 1.3 \text{ \AA}$, $L = 7.2 \pm 1.4 \text{ \AA}$, $\theta_0 = 232^\circ \pm 11^\circ$

Bottom: FRET efficiencies of FRET blocks in absence and presence of 18 mM magnesium as a function of distance. The pair of data points for each origami sample was marked according to the nomenclature given in Scheme 1A of the main text (i.e. (Δ helix, Δ nucleotide)). To illustrate the shift of E-values with and without magnesium the same distances for identical acceptor positions on the origami block were used as in Figure 3 of the main text. The increased energy transfer values in the presence of magnesium are explained by the reduced DNA repulsion in the presence of divalent cations, which leads to shorter inter-helix distances.

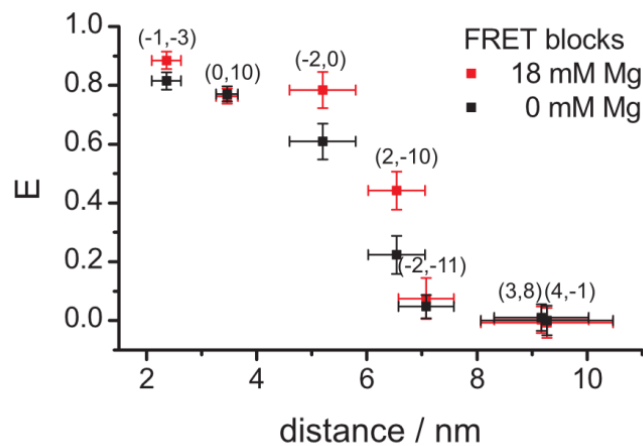
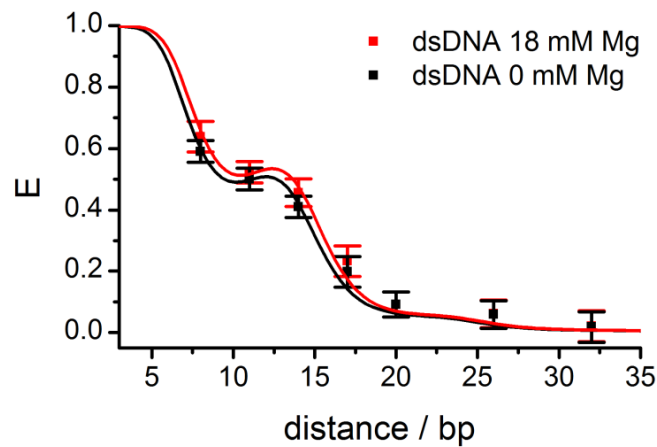


Table S2: Staple sequences with optional dye modification

Each fully assembled structure contains the donor sequence with the donor attached to designated base (Thymine) and all of the following oligonucleotides except for one. This particular sequence is replaced by an oligonucleotide labelled with the acceptor at a given position (cf. Experimental Section).

Donor	AATGCGCGAGTTACAAATCCTGATAAACATAGTAGGT _{Cy3} CTGTAATAAG
Acc 2.5 nm	AGAGTCCACACAGACAATCCAGAAAATCAATATATCTTTAGAAATTAT _{Cy5} C
Acc 3.5 nm	ACAAAGTTAGTCTGAGCGCCCAAGCGTTATATAAGCGGTAGAGACT _{Cy5} A
Acc 5.2 nm	AGAGTCCACACAGACAATCCAGAAAATCAATATATCTTTAGAAAT _{Cy5} TATC
Acc 6.4 nm	AATAAACATTT _{Cy5} TAGCGAAATCAGAAAAACAGGAAACCGATAATAACG
Acc 7.3 nm	TGCCTGAGAT _{Cy5} CTAAATCTGGTCATCAATATAAATCGCGCTATTCATT
Acc 9.0 nm	GCCAGAATAAAAGAACAAAAGGGCATTAGACGTTGT _{Cy5} TTAAGACTTGCG
Acc 9.2 nm	AATAGATAACCAGAAGGAAGCGCGACATTCTATTAT _{Cy5} CACCCATAGCCC
Acc 14.3 nm	CGTACTCACAT _{Cy5} CGGCAGGAACCGCCCAAGACTGGCATGAATAGCCGA

Table S3: Unmodified staple sequences of DNA origami blocks

GCCCCGAAAAAGGGATTGACGCTAGAGCCAGTAGAAGTATTAATTTT
GTCAAAGCCCTTCTGCAGGAAAACACCTTGAGCCGTTGCGGA
AGCCCGAGATAGGGTATCATGGTGCCTTGCCTTGAGTGT
AAATCCCTTGTATCCTGCCTAATGGTGTGCCGGTGCCGCATCCCTT
TCACCGCATTAAATTCATAGCTGCAGTTGA
AGGCCGATTAAGGGGAGAAAGGAGCCTACATTCATTCTGGCAGCAGAA
CTCGTTAGAATCAGAGGTAGCGGTCAATTGCAAACCTGAAAACATCGCC
GACGAGCACGCCGCGCCTGGTAATATATTTTTGAATGTGC
GAGACGGGCAACAGCTGATTGCGGCCCGCTT
AGTCTGTCTGAGGATTACAGCAAATTCAAAATTTACCTTTTTTACATTT
GCAATACTATAGATTACTGAACCTCTGAATAATTCGCCTGGATGAAAC
TCCAGTCACGATCCAGCGCAAAAATGGGTA
TTAATGAAGCAGCCAGGGCCAGAATCCGCCGGAGGTGTCCCGGACTTG
CGGCCTTGTTAATGCGGTTCCAGTTTGGAACA
CCAGTAATTTTAGAGCAGGAAGGGAAGAAAGCTTTTAGACAGTAAAAG
GATAGAAGGCGAAAAAGGGCGCTGGCAAGTCGGGAGCTCGTTGTA
ATACGTGGCTATTAAGCGTAACCACCACACCCGTATAACACATCACT
AATTCGTATGAGTGTTCGCTACAGGGGCCCT
TGTGAAATTATAAATCGAGAGAGTTGCAGCAATTTTCTTTAGCTGCA
GATAAACAGTAACAGATTTGCACTGAGTGAAGCTGATGCTAATTTCA
ATTAATAAATACGGATGGAAGGGCTATTAACCTTAGGTTTGAATA
GGATCCCCCGTCCGGTGGCCCTGCGGAAGATGC
TCTTCGCGACGGCTGGGCGCGGTTGTCCGTTTACAGGCGGTCATTTGC
CACTGCGCACTGTTGTGCCATCTGGTCAG
AATACATTCATCAGCTGGAATACGGGCGCTACCGTCTATCAAGGGA
AACAACATCTTTGATCCGCCAGCCAGCTGCGAACGTGGAAGTCCAAC
GGAAGGTTTGAAGAAGTCAAAGTGTACTATGGTTGCTTT
TGCATCAGGGGAAACCTAACTCACCTGGCCCTAAAAGAAT
AAAAGTTTATGTAATTAACCTTGGCTTAATTAAGTACCAGAAACCA
ACAAAGAAACCTCCGGTTAATTTTACCAGTACCAGACGAAATAATAT
ATCATATTCAAAATCAGATAGCTCTGTTTAGAATGCAGATTATCAAC
AAGGTTTGTAAGTTAAACGAGCAGAAACA
ACACTGGTAAAGCCGCTTTCTGTCTGAGAGATAAATCGGCGAAGTTGGG
GCAATTCAGTTGGCAAAGCGCTATTAGTCTTT
GAATATACAGAGGTGACCACGCTGCAAT
AGAAACAATACCGAATAAAGCATACGCTCAAATTAACAAACAGG
GAATACCAAACCTGATAAAACCTCCAATATTATAGTAATAGTCTTTC
GGCAGCACGGGTACCGATCAACAGCTCACTAT
ACCAGCTTTCCGTGAGCACTCTGTGAGTGAGCTGTCTGTGCTCACCAGT
AACAATTTGAGAATATGAGAATCGCGCACTCAGCTACAAATAGTTACAA
AAACATCAATCTGTTAAAGCCATTTTCATTAATCAACAATCCA
CAGCAACCGGTGGAGCCGGAAAAAGGTTTCAG
TAGAACGTCCGGAACGACTTTCTGATCGGTGTCTGGTGTCTTGAGGG

TGATTGCGCTCTCACGCCACGGGACGTTG
ATAACTATGAGTAACACTACCATAGAAAAATCCGAACCACCCAACAGA
CCTTTTTAACCACCAGTTATACTTCAAATATCGCCCTAAAGCGTAAGA
ATTTATCCTGATTATCAGAGGTGGAATTGA
GATGAAGGCTTTGCTCAGCCGGGTCGCCTGTGCCTCCTCATTTCTG
TCTTCTGATGCACCCATCGAGAACATTGAGCGAGCTATCTAACGTAGA
CCGACCGTTGAAGCCTCGTAGGAAAACTGAACGTAAGCAGTTAAGACT
GCGGATCCGCCATTCGCCAATTGATGGGCG
CGCCAGCAGCACCGCTCGGGCCTCTCCGTGGGGCTTTCATACGTTAAT
GAAAAAGCTAGATTAAGCCCGAATAGAGGAAC
AGTAATAACATTTGAAAATATATGGTAAAACAGAACGTTATTAGACTT
GTAAGTAAGAAAAACAATCGTCGTTAGAACTTATCATTAAATAGAT
AACAACATCTGAGCAAATCCTTGATGTTTGGAAAGGAGCGGGAGCACT
CTTTCAGAGCAAGAATGACGCTGAGCTTGATG
TAACCTCACAGCGTGGCAAACGCGCGGTATGGTCATAAAGTGCCCC
ATCAATAAATAGCAATCTAATATCAGTTTATTTTACCATTAGCGACAG
CCCATCCTAAGAAAAACCTGATATGGTTATTAGAGCACTGTAG
TAAAACGAGCCATCAAGTCACGTTTATTAATA
TAACGCCATGTAGCCAAACAACGCGGTTGATCTGGAGCATTAAATGC
GCTGCGCGGGATAGAAATAATTTTTTGT
TGCTATTTCTAAATTACAGTAGGCTTCTGTAAAAATTAACATCGGG
GGAGGTTTGTGATAAACAAATCTCCCTTAGAAAAGAGATATTGCTTT
AGGCAAAGAACTTAAAAGGGATACGTTCCGGTGTGGTCCCACGCA
AATAACATAGCACCATTTGTCACAACCTCAGTCAGACGAGGGTCAGT
AATAAGAAATTTGGGATACCAGCGTCCCTCAATAAATCTACAGGAG
ATGAAAATAAGGTGAAACCGATTGATCACCGGCAGTCTCTTCCAGTA
CATCGTAGAACGGTAATCGTGACAATATGA
GACGACGACCTGAGAGTAATCAGATGTAGGTAAATTTTAAATTAAGC
AATAACATTATAGAAGGCCCTGTACGCGAAG
ACAATGAATCGGCTGTCCAAGTACCCATATTTATTTAGTAAATCCAA
CCCTTTTTAATTTACCGTTTTTAACGCTCATAATGGTTGGGTTAT
ATAGGAACCGGCCAGTGCTTATCCGAGTACTA
GGCCTTCCGGTTTTTCGGAAGGGCCCGTGGTGATTTCTGCCCTTTAGT
AAATACATGAGGCAGGAGCCACCATATTTCGAACCGCCTGTACCGT
CCTTATTACAAACAAGAGCCGCCTGAGACTAGTACCGCAAACACTAC
GAATACCCGAAAGCGAACCCAGAGCGGGTTTTGGAATAGGGCCCTCAT
AAATCAGCCTTTTGGGAGTCAAATCCGTGGGG
ATTTTGTAGGATAAAAAGATTCAATTTCTACTCAAATGGTCCATATA
CTAGCATCGGAGACGGAGAAGCAAATCGG
ATCACCAGCCATATTAGAGGGTAAAGCAAGCGAGCATGTGACAAAAG
CTTGAGCCACGATTTTGGAGAATTTTATTACCACAAGAAACGACAATA
ATTCATTAAGCAGCCTTTACAGTACTAAGAAC
GAATCGATACCGTGCAACCGTAATAACTGTTGCCAGTCACGAACGGA
AATCAAGTCACCCTCATGAAACATGGAGTGAGAAAGGAGCGTTAAAGG
CGCGTTTTGGAGTTTTCTCAAGAATTTTGTCTTGTCTTCGATATAT
CCTTATTATATAGCCCTGCTCAGTCCAGACGTGATACCGAGACAATGA
TATTCATATATTTTTCATTTTCGCAACTAAA
CGGAGAGGACATTTCAATA
AGGAGGTTACATAAAGACGGAATAAGAGAGATAATTTGCCTTTATCCT
GATATTCACGCAGTAAAAATCAACAAAGTCATTTATCCGATTAGT
CTGTAATATCATTTTTAAGGTAAAGGTGAGAG
TCAACGCAAAAATTCGTATGTACCGCGGATTGTCTGCCAGCGGAAACC
GCCTTGAGAGGCTCCAATAGAAAAGCAACGGCGTATCATCGAGGCGCA
TGTAAGTTTATCAGAAACAACCTTTTTTCCCAAGCGCACTGACC
AGCGTCATAACAGCTTTAGTAAATTAATAACAAAACACTGGTGTACA
TTGTACCACCAGACCGATGTTTTACCTAAATG
AATAAAGCATTAGAGATTAATTGCAATGACCATGCGGAATTTTTGCAA
CGCGAGCGCTCAACGAAGCAAATTCAAAT
AGAACCGCTTGCTTTGAACCGCCATCAATAGTGTAGCATACCGAAG
GATATAAGGCGTTTTGCCATCTCATCGGAAATT

TGTTTAGCCCGTTCTAAGAAAGGCGTCAATCACATTAATCGCGTCT
AACACTGAGGAGATTTTACAGAGGTGAATAAGGTGAATTACCTTATGC
AACGCCTGCGATTATAATGAGGAACCAAACTACTCATTATAACCAGTCA
AGTTAGCGAATACACTGTAATGCCAGTAATCTAATCTACG
GTACGGTTGAATCCCCCTCAAAGACGACGATAAAAAAC
TCGTCTTTACCAGGGGATGTACCGGAATTACC
CAAAAAATAACAGTGTGCGAACCCCTCAGATAATCAGTAGCAAGGC
GTATCGGGTAATAAGTAAGAGGCACCCCTCAAGCGTCAGCAGCAA
AAAGCGAAAAAACATTGATAAGTGCACTTTCA
AGGTCAGGCTCAGAGCTGGCATCAAAAGGGTGGCTGATAAAAAACAAGA
CCGCTTTTTAATCATTGCTTGCCCTGACGAGAGCCGGAACGCCTGATA
TCGGTCGAGAACTGGACGTAACAAGCTGCGGAACCGAGAAACAA
CAACAACCGGAAGAAATGACAAGAACCGGATAAGATGAACCATCTTTG
ATCGCGTTACGGAACCCCTCGTTTAGACCT
AGATTAAGCATCAGTTTACGAGGCATAGTAAGCGAGAGGCCGTCATAA
GGTAGGAACAACGGAACCCAACCCTCAG
CTTTAAATATCATAAACATTATTACAGGTA
AGTACAACGTTTCGTGTTTTACGCGAAAGTATTTTTAACGTTGGCCTT
ACCCCCAGTAGCATTCTGTATGGGGAAGGATTTTTGATGATCATTAAA
GGCAAAAGTAACGATCTAAAGATGAGAGGGTT
ATATTCATGTCTGAAATGCTGTATGAAAAGGATAAAGCTCTTTATT
GACGGTCAATCATAAGTCATTACGCTTTGAGGTGCAGGGACTTTAATT
AACTTTGAAAGAGGACTTCATTACGTTTCCATCGCATAACCGAGGTGA
GACCAGGCGCATAGGCTGGCTCCAACGAAAGA
CAAAATAGAGCAACACCAGTTCAGCGAAAGACCTCCAAC
TCATCAAGACTACGAAAGCGCGCTAGTTTTTC
GATTTTACTGAGGCTACTAAAGATTCAACAACCAGTACCACCCTC
GGACGTTGATCGCCATAAACGGGGAATTTCCACAGACATGTATCAC
TTAATAAAACGAACTATTAATTCGGGCACCAAATTTTTG
GAAAGATTAGGAAGCCAAAACGAGTGAATATAGTTTCATTCAATAACC
TGGGCGCCAGGGTGGTGCCTGAGCCTGGGGGCTCACAAGTGCCTGT
CGTCGGCCACCGAGGAACGGTACGCCAG
TACAAACAATCAGTGATGAAATGGGGCGAGAATTGACGGG
GGTTACCTTCGGCCAAAGTGTAACGCTGGTTGGTTCCGAAATCGGCA
TCGCAAGACTTTGCCCGAAA
CCGTAAAAGTGTTACGGCACTCAATGCGGCGGCAGCAGCTTCCACAC
GAATCTTATCAATATAACAACGCCATAAATCTTACCTTTCGTAGAT
GCTTTCGGTGGGCGGAATTTGTCGTGCTGGAACGTGCAGCATCAG
CGGAAACGCAGAGCCTAACCCACAGTATTAACCTTTCCTTTTCGAGCC
GGTCATTGCAGTATCGTCGGATTCTTCGCTATAGGCGATTAAACGTAC
AGCCACCACAGCACCAGCCGCCACAAGACACCGTGGCAACAGCAAGAA
CATTAGATGTAGCTATGAGTAATGAAAGCCCAATTGTAACAACATTA
CAGTTGATTCCAATACTAAATCAAAAAGGAATGAGATTTAGGAATACC
AATTGTGTGCCCAATATAAAGGAATGCCTATTCCTGATAGCATTGAC
GGATAGCGTCCCAATTGCGGATGGTAGCATTAAATAGCAAGAACCCTC
GTTACTTAAACACCAGCATCGGAAGTACCCTAAAATCTC
AAGAAGTTTTGCCAGATAACGCCAAAATCAGGGCGGATTGAATTGCTC
GGTTAATTTCAACTTGCGGGATCCGAG
ATTTCTTAACATGGCTAGGATTAGCCACCACCTTTTCGGTGTACCCGA
TCAATTACGTTTACGCTTATCATATTAGCAAGCAACCTCCCCGTCAAAA
GCGAGGCGCCGGAATCATAATACGTCAATAGTGA
TAAACAACAGTGGGCGGTATCACACGA
TAATCAAAAGGGAGGGTAACGCAAGGAAACCA
GTAGCTTAGAGCGTACCTTTTCATCAAAA

Supporting Information for Associated Publication P2

Supporting Information

**Cellular Immunostimulation by
CpG-Sequence-Coated DNA Origami Structures.**

By

Verena J. Schüller, Simon Heidegger, Nadja Sandholzer, Philipp C. Nickels, Nina A.
Suhartha, Stefan Endres, Carole Bourquin and Tim Liedl

published in

ACS Nano 2011, 5, 9696–9702

Reprinted with permission from ref. [80]. Copyright 2011 American Chemical Society.

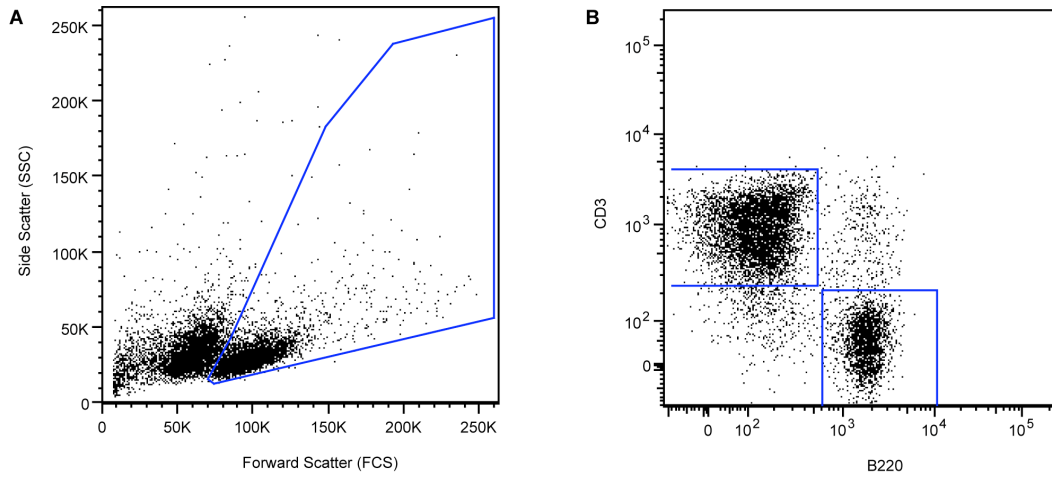
Supporting Information

Cellular Immunostimulation by CpG-Sequence-Coated DNA Origami Structures

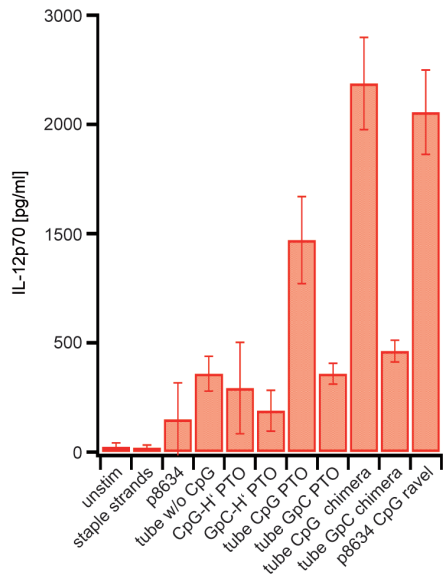
Email: carole.bourquin@unifr.ch.de; tim.liedl@lmu.de

Table of Contents

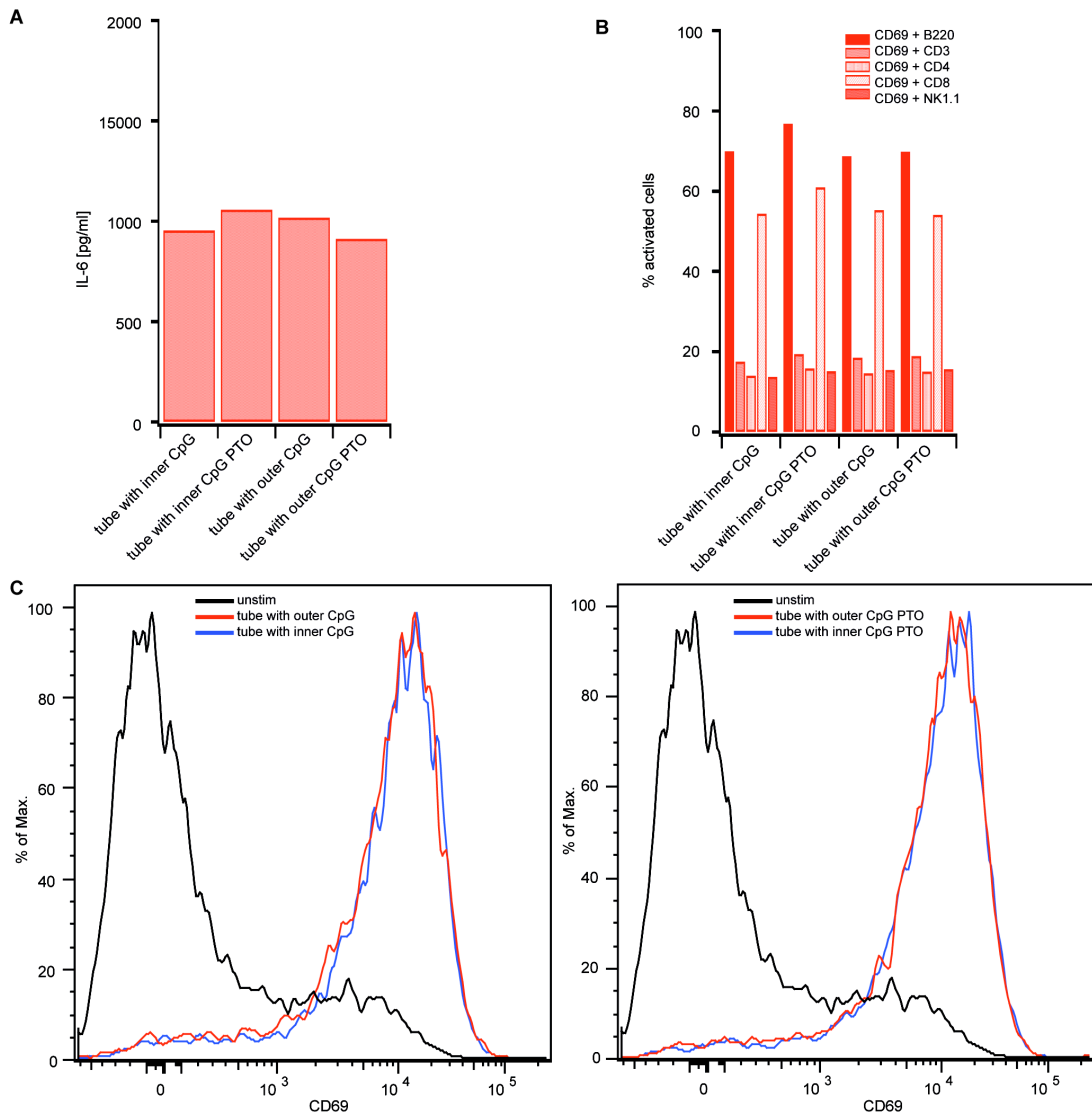
Supporting Figure 1	Representative flow cytometry plots and gates for B-cells and T-cells.
Supporting Figure 2	ELISA analysis of IL-12p70 levels of splenocytes 18 h after transfection with DNA origami tubes.
Supporting Figure 3	ELISA and flow cytometry analysis of immune stimulation caused by CpG-H's on inner versus outer surface of DNA origami tube and representative histograms of CD69.
Supporting Figure 4	ELISA and flow cytometry analysis of IL-6 levels and CD69 expression 18 h after transfection with lipofectamine used as transfection reagent.
Supporting Figure 5	FACS analysis of splenocyte viability after incubation with CpG-H'-decorated DNA origami tubes.
Supporting Figure 6	Gel, TEM and flow cytometry analysis of stability of p8634 CpG ravel and DNA origami tube after pre-incubation in FBS.
Supporting Figure 7	Design schematic of DNA origami tube used in transfection experiments.
Supporting Table 1	Sequences of unextended staple strands of DNA origami tube.
Supporting Table 2	Sequences of staple strands, that are optionally extended by handle sequences for CpG-H's.



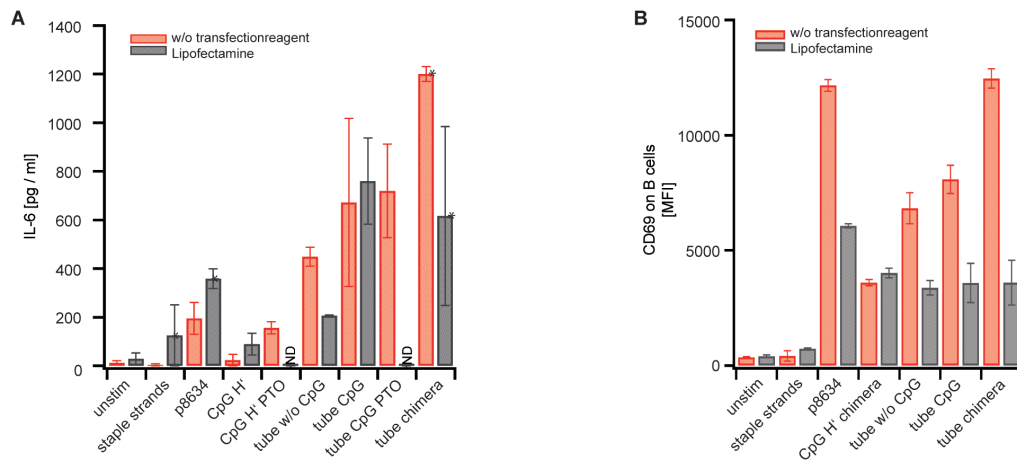
Supporting Figure 1. Representative flow cytometry plots (A) 2D forward versus side scatter dot plot: gates are set for lymphocytes. (B) Two color dot plot of fluorescence intensity of B220+ for B cells versus CD3 for T cells: gate is set for B cells against T cells.



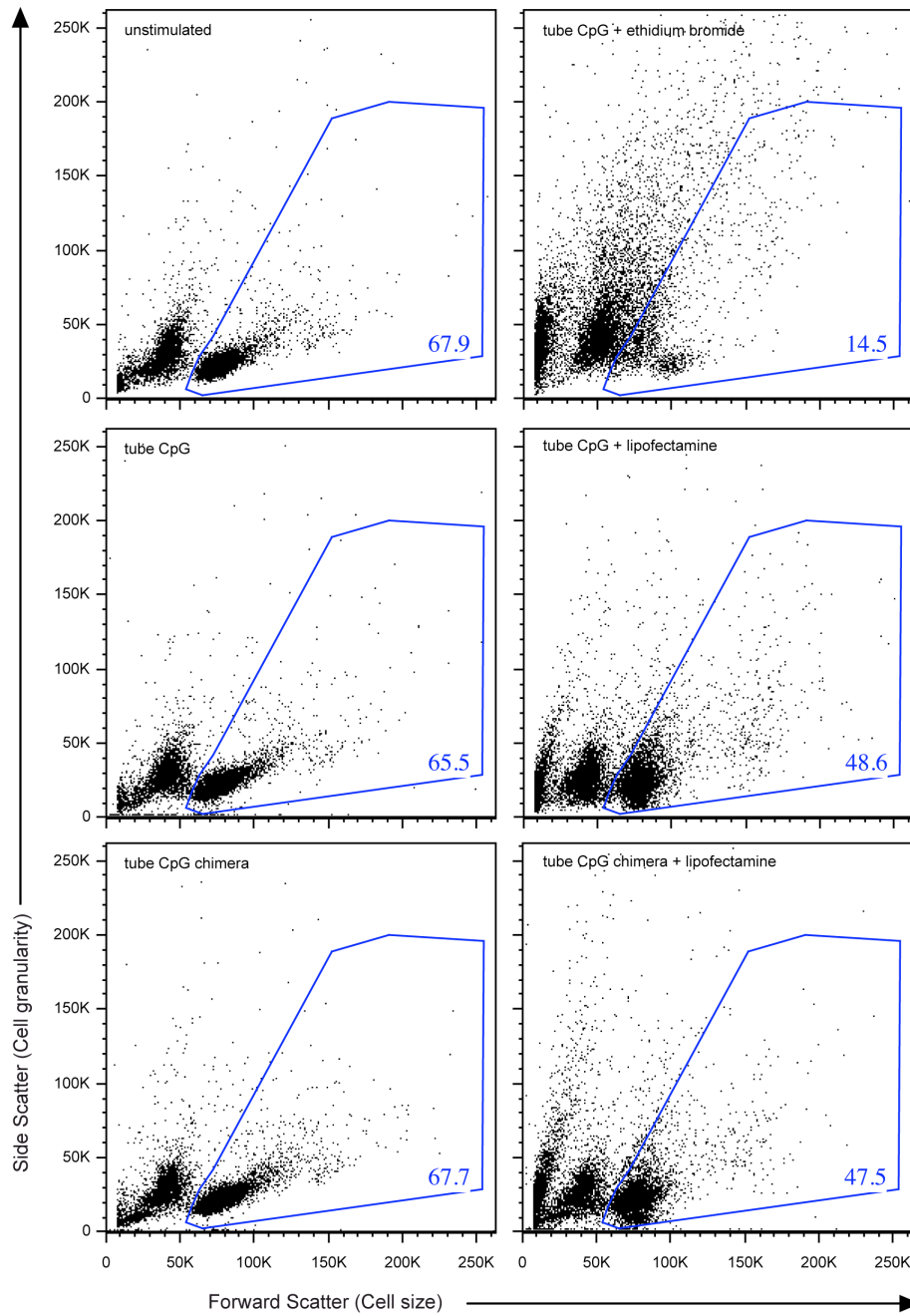
Supporting Figure 2. ELISA analysis of IL-12p70 levels after splenocytes were cultured in the presence of different DNA origami structures for 18 h. 50 μ l of 2.4 nM (DNA origami tubes, p8634, staple strands) or 50 μ l of 62 x 2.4 nM (CpG-H' PTO, CpG-H' chimera) of sample were added per 400,000 cells in a well. In all experiments, the net CpG weight was 50 ng. Data show the mean value of triplicate samples \pm SE and are representative of two independent experiments.



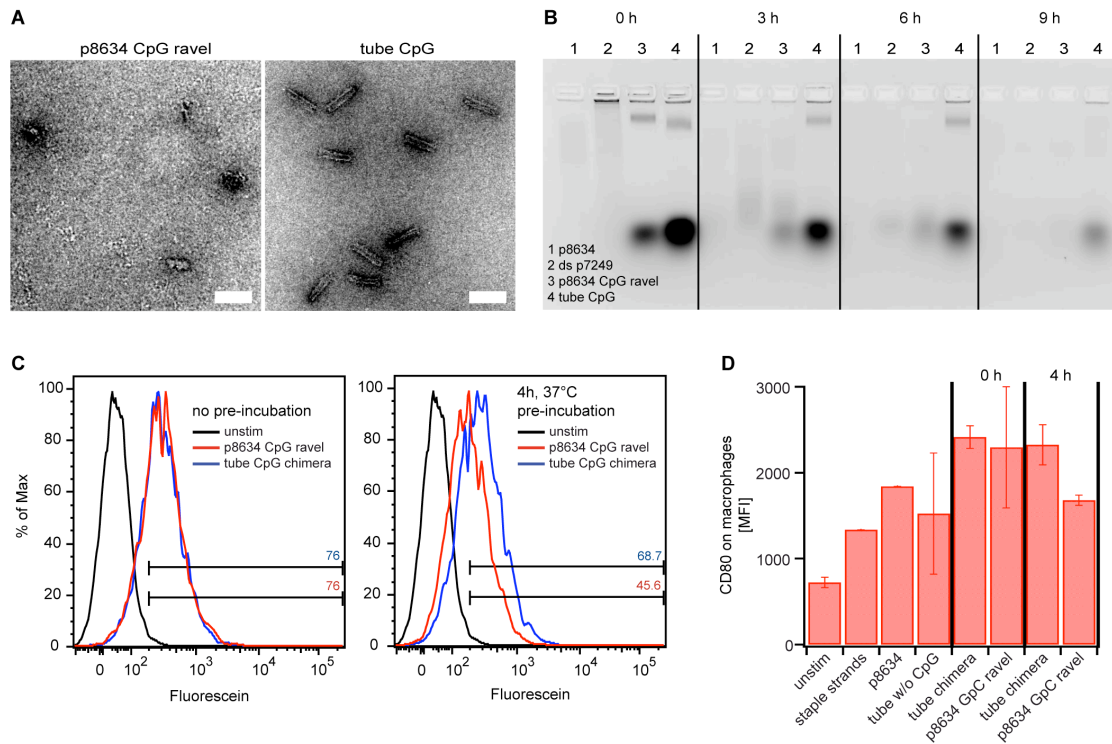
Supporting Figure 3. (A) ELISA and (B) flow cytometry analysis of immune stimulation caused by CpG-H's attached to the inner surface of the tube compared to CpG-H's positioned on the outer surface of the DNA origami tube. (B) Representative histograms show CD69 expression on B cells stimulated with the indicated CpG-decorated origami tubes.



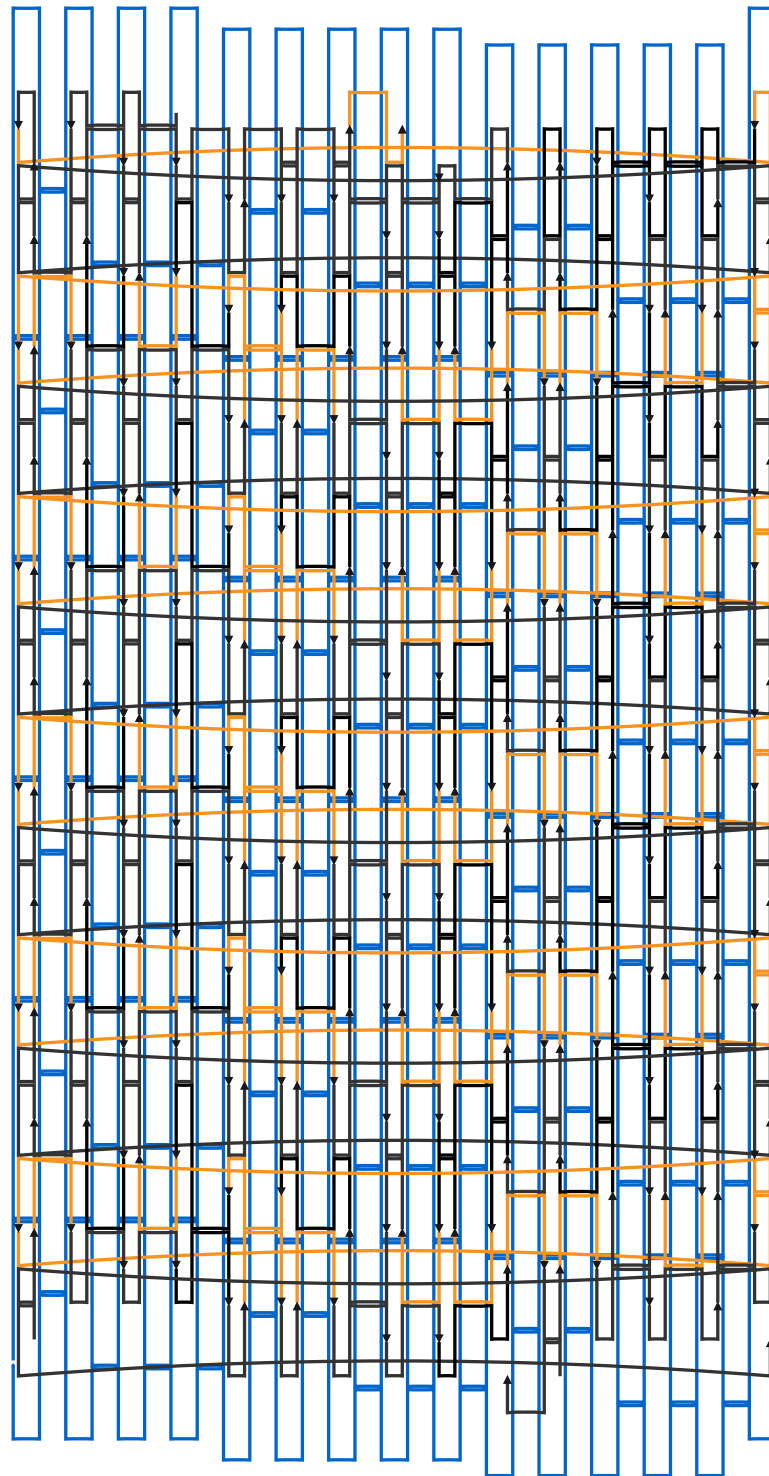
Supporting Figure 4. (A) ELISA analysis of IL-6 levels 18 h after transfection with lipofectamine used as transfection reagent and without transfectionreagent. 50 μ l of 2.4 nM (DNA origami tubes, p8634, staple strands) or 50 μ l of 62 x 2.4 nM (CpG-H', CpG-H' PTO) of sample and were added to 400,000 cells per well. In all experiments, the net CpG weight was 50 ng. Lipofectamine was applied as suggested by the supplier. Mean values are derived from independent cell experiments on different days. Error bars indicate the absolute minimum and maximum error values. Values denoted with * originate from a single experiment with two replicates. Error bars indicate the absolute minimum and maximum error. (B) Flow cytometry analysis of immune cell activation after incubation with DNA origami tubes. Freshly isolated splenocytes from wild-type and TLR9-deficient mice were incubated with 50 μ l of 2.4 nM (DNA origami tubes, p8634, staple strands) or 50 μ l of 62 x 2.4 nM (CpG-H' PTO, CpG-H' chimera) for 18 h. Surface expression of the activation marker CD69 was analyzed on B cells.



Supporting Figure 5. FACS analysis of splenocyte viability after incubation with CpG-H' and CpG-H' chimera decorated DNA origami tubes. Freshly isolated splenocytes were incubated without DNA, with 50 μ l of 2.4 nM CpG-H' and with CpG-H' chimera-decorated DNA origami tubes for 18 h. In some conditions, lipofectamine or ethidium bromide was added to the culture. Dot blots from a representative experiment show the morphology of unstained splenocytes. The number indicates the frequency of viable cells within in the sample.



Supporting Figure 6. (A) Electron micrographs of p8634 CpG ravel and DNA origami tubes chimera. Scale bars: 100 nm. (B) Gel analysis of p8634, ds7249, p8634 CpG ravel and DNA origami tubes chimera 0h, 3h, 6h and 9h after pre-incubation in serum-containing medium. Without incubation, a prominent band is visible for both DNA ravel and origami structure. After 6 hrs of incubation the band of the ravel disappeared while the preserved band of the DNA origami tube indicates still intact structures. (C) Representative histograms show fluorescence shift indicating decreased uptake of p8634 CpG ravel compared to DNA origami tubes chimera after 4h of pre-incubation in FBS. (D) Flow cytometry analysis of immune cell activation after addition of DNA origami tubes and p8634 CpG ravel 0h and 4h after pre-incubation in FBS. Freshly isolated splenocytes were incubated with 50 μ l of 2.4 nM (DNA origami tubes, p8634, staple strands, p8634 CpG ravel) for 18 h. Surface expression of the activation marker CD80 was analyzed on macrophages.



Supporting Figure 7. Design schematic of DNA origami tube used in transfection experiments. blue: scaffold path, black: unextended staple strands, orange: staple strands, optionally extended by handle sequence for CpG-H's.

Supporting Table 1. Sequences of unextended staple strands of DNA origami tube.

AAAAAGATTGGGCTCTGAGTTAGAGTCT	AACTCAACGAGCAACAGAGTCTGTAGTG
AGGCAAAGCGCAATGTCTGGTGCCGGA	ATTCAACCGTTCCGAACGGCGGATTGGA
CCCTGACTATTAAGTGAAAAATCAGGTC	TCATTACCAAAGAAAAAGAAGTTTGA
AACAGTTTCAGCGCAGTTGCTAAACAAC	CCGTTCCAGTAATTTACCGTAACACTAA
CTGGCATGATTATGATGGAATACCCAAA	AGAAAAATAATATAAGAATTGAGTTAGA
CATGCAGTCTCAGGCACGTTATCAATGT	GGAGTAATAAAAAGGGACCTGAAAGCGTG
GATCGGTAAATTAAGCATTGCGCCATTCA	CGTGTCAGATGATGACTGTTCTTTAT
AGAGGAAGCGAAACAATAGTCAAGAAGCA	GAACCGTAATGGGAACCGTGCATCTGAA
GAATAATGGAACCCAGAGGAGTGAGAATA	AAGCCAGAGGGGTATACTGCGGAATGG
AAATACATGTAATGCAGACTCCTTATT	AGGAGTTTCGTCACAGACGCCCTCACA
GACGGCCAGTGCTGCGCACGACGTTGTA	ATGAATCACTGCCCCGTTTCCATTAATT
CCTTTTGATAAGGCAGAGTACCTTTAAT	AACGGGATCCATGAATTGGTAGATTGGA
GATACCGATAGTTCAATTTCTTAAACA	TTTTAGAATACTTTTGCGGGAAAAACATT
ACAAAAGGGCGAGCAGTTTACCAGCGCC	GAACCGACCATGTTACTTAGCCGAAATC
GCATTGCGATCATAGAATGATGCTGACGCGAAGA	CCAGCATCCACCACCCTCAGAGAACC GC
AATAATTCGCGTACCTTAGGAACGCCATCATAAAA	ATGAGTATCAATTTAATGCAAGGAGTTT
AGGAATTACGAGAACC GATACATAACGCCAATTAC	TCCGGCACCGCTTAACGCACTCCAGCCA
CCACCCTCAGAAGGGCAGGAGTTTAGTACGGAAC	TGACCATAAATCCTACGTTCCAGAAAACG
GGGAAGCGCATTAGTGAATAACATAAAAACGCGA	CTGTATGGGATTAGTGTAGTAAATGAA
GCGAAAAGGTCCACGCTGGTTTCCCTTACCGCCT	CGCAATAATAACTCAAGGAAACCGAG
CTTGCAAGTTTCTCGTTCAGGGTTGTGAGTGT	GAAATTGTTATCCCTCTAGCTGTTCTCT
GGCATCAATTCTAGGGCGGAGCTGAAAAAATGGT	ACTTATCAGTAAATATGCCAGGAGGATC
AACCTAAAACGAAGTGCCACTACGAAGGTCATGAG	TTAACATCCAATGGTAACTAATAGTAGT
CGTTTTCATCGGTCTAGCGTCAGACTGTAGCACCG	CACTAAAACACTCCGAAAGAGGCAAAAAG
CGTCGCTATTAATGTTTAAATGGAACAAAATTAA	CCCTTATTAGCTTTACATTTTCGGTCA
TCGAAGACGCTGGCATGAAGGTTTATAGTCGGCA	TAAAGCAGCCTGCAACAGTGC GCGGTCA
AAATTTTCATTTGGTTGGGTAAACGCCAGTGCTGCA	TACAAATCACGAAGGTGTTTATTGTCTC
TGTAANAATACGTAACAAACTCCAACAGGAGCGAAC	AGGCGATGCCTCTTCGCTATTGAAGGGC
GCCAAGTTTGCCTTGTTTATCAGCTTGGGAGCCT	CAGACCGGAAAGACTTCAAATAAGATTA
AATTGAATTACCTTTCAATCAATAGACGGAATA	TTAATTGTTTTACGTTGAAAGAATTGC
GCGTTGCTGTAAGCCTGGGGCGAGCCGACGCTCACAAATC	CGCCACCAGGCTATCGATAGATGAACTG
CGCAGACGCGTGAAGCGGCAGAAATTAACACACAGAGAGTTTC	TTGATTAGTTTGACTGTTTAGCTATAC
ATGACCCTAAAGCCTCAGAGCATTAGCAGCAAATCATAACAGG	CGCTACAGAGGCTTCCATTAACCGGGCT
CGCGACCTACAACGGAGATTTACCAAGGCCATCTTTGACCC	GAGGAAACGTCACCTAGCGACAGAATTT
CACCCTCCACCACCGGAACCGAATCACC AAGTTTGCCATCTT	TGTCGCGCAGAGGCTAACAAATTCATAG
GTTTGAAATGCAATCCAATCAACTATATAGAATTTATCAAA	GGGCATCAGAAATAGCGCCGCTGAATG
TAGAATCGCTGAGAAGAGTCAATAGTCATTTAATTTCCCT	AAGGTGCTGGAAGTGC GAACGAGTACG
GGCGATCATCTGCCACTATTACAGCAATAAAAATGAAGAAT	ATTGCGGGATCGTCGGGTAGCAACGGGA
CAATAACCCATTAGATACATTTTGATTTCCCAATCTTTCATT	ATATTTGGGAATTAATTAGCAAGGCCCA
GAAGTTTTGAGGACTAAAGACCAGCATCGGAACGAACCTCA	AACAGGTTTAACGTC AAGTTACAAAAAG
TAATCAGAATGAAACCATCGAGTAGCACCATTACCGAGCCAG	TTATCCTGAATCTTATTGGC
TTACATTGAATTATTCATTTTCATTGCTTTGAATACCAGATGA	TTGCCCTCACACGAGTACGGT
TTTCGCGTGATAACGCTTGTGAAAGCGTGAGTATTATTGCTAAACTGCG	GATTAATCATGCGTATTAAAC
ACCCGCTCACATTAATGTGAGTAGCTGATAAATCTACAAAGGCTGC	GCTCAACACTAATTGCTGAAT
AACCAAAGTCTCGTTTACCAGACTCAACGTAACAAACGAGAAACCCAC	CGCTGAGAACACGCATAACCG
ATAGCAATGAGCCACCACCTCAGCGTCATACATGAGTTTAAACGGGAC	AAAGGTGACAATATTGACGGA
GCTAATAAGACAAAGTCAGAGGGTCCCATCTAATACCGCACTCATCAC	GACTTTAGGCAGACATCTTG
AACGACATACATGACTGATACCGTTTAGGTTGAGTATTATCTACCGTAC	CGAACGTAATATGCAACTAA
CTCAGGAAGATCCCAGCAGCAGCAGTATATGGGCGCATCGTATAGGTCA	TGCGGAAGGGAGTTAAAGGCC
ATGCTTTAAACATGTCATTGAATCCCCCTGGATAGCGTCCAAATAGTA	TATTCTACCGTCACCGACTT
TCTTCCAGACGACCGATCTAAAGTTTTCTGTAGCATTCCACCAGTACA	TGATTGTAAGAAATTGCGTAG
CAAAGTTACCAGTTAGTAAAGCAGATAGCATAGCAATAGCTATAGAGCAA	ATGAAAGCAACGAATCGCCATCTGGTG
GTAANAACGTAACAGTGCCTGAATTACCGAAAACAGTACATATGTAAT	TAATCAGGTCATTGGAACGGTAATCGAA
TTATCCGGCCGTTTTATTTTGTATTAA	CAAGAACGAGTAGTTAATCATTGTGAAA
ATTGTCGTGCCAGCGCGGTTTGGCTGA	GAGTCAGTGCCTTGCTGCCTATTTCGG

GCGTGCTGGAAGTCAAAACGCCGCGAGC	TAGAGAACAAGCAAGTATTCTAAGAACA
AGTCAACGCAAGGATGCAATGCCGTGAAA	GGCCCTGAGAGATCAGTCACACGACCCA
TTCAGACGGTCAATAGGACAGATGAACG	AGAACTCACCGTCTATCATTTTAGATTA
GAACCACCACCAGAGGTCAGACGATTA	AGGTCAAGTTAGTAACTATCGAGATTA
TACAAATCGACCGTGTGATAATTTAATG	ATTAAATAGCAAATATTTAAACTTTGCC
AGTTTATTAAGGTGGCAACAACGTAGA	CAGTTGAAAAACGAACTAACGATCATT
CAATGTGCGAGAGATTACAATCCCAT	TATAAGTGGTTTTGCTCAGTAATCATCA
CGGCATCGTACAGATATACTTGCGGTATTT	TTAACGTCAGCCATATTATTATAATCC
ATCATAGAGGTTGGGTTATATGCAAGACACC	CTCCTGTTTCAGGATGCAGGTGGGTTGG
TAAATAAGGCTATCATAAACGCTCTTAGGCA	CTAGCATGTTAAATCAGCTCAAATTCGC
CCACTATTAAGACCCAGTTTGGAAACAAATCAA	CTTATGCTAGGAATACCACATGATTCAT
TGACCTGGAAGAGGTATCAAGCACTGCACAGTTTC	CTATTATCCCGAATAGGTGTGGGTTGA
GGTTGATAATCATTGTCAATCATATGTAACAAGAG	GGCGTTTAAATGAAAATAGCAGTTTTTGT
ATTATACCAGTCTTGATTTTAAGAACTGTTAATT	AGAATAGTCGGCAAATCCCTCCAGCAG
TAAGAGGCTGAGAGTCTGAAACATGAAAAACAGTT	TTGTTGTGTCCGTGAAGACGGATGGGAG
TGCACCCAGCTAAATAGCGAACCTCCCGAGAAGGC	AATCGATCCTGAGAGTCTGGACTATTTT
TAAGCGTACGAAGGTGTTATCGGCAGCAAATCAA	TCAACTTAAATGGGCTTGAGTAAGGCT
TGAGAGATAATGCCGGAGAGATCATCAATATGAT	AATGCCAGTAACAGTGCCCGGTGACT
TGCCCTGAGCTGCTCATTCAGGCAGAACCGGATAT	TACCAGTTTGAGGGTCATATATTTAAATAAAAAT
GGTAATAGCTTTTGATGATACTCTCTGAATTTA	CACGTCATAAATATACCAACTTTGAAAGCATAAGG
ACCAAGTTTACGAGCATGTAGATAAGTCTGAACA	CATAGTTAGCGTAAAGGAGGTTGAGGCAGCCGCCG
GGTAAGAATACGTGAACGCGCGGGGAGATGCATTA	GACTTTTTAAGAAAACAGTATAAAGCCTGCCTTA
GGACATAAACATTGAACCGCAATACATCTGGATG	TAATCATGGTCAACGTACCGAGCTCGAATAAATGC
CAATAAACAAACATGATTCTGTGAGCCAGATGTAATAACAGTA	ATATACAAGAAATATTGGATTAAATAAACACAATT
ACAGCCCAATAATACTTACCGAAGCCGGCATTTCAGACG	
ACTTCCGTTTGTATGGAGCGCGGGGATTATTATAACA	
ATCCTCGCTCTGTACAATAGAGCGAAAAAACGTTGGACTCC	
TACAGCGGAAAGATCAAACAAAAGACCTGTTTCTGCGGCA	
CCATATAATGTTTTTATTAATTTGTATATTGAAAAGCCCAA	
GCAGCGAGCTTGACAAAAGACGTTAATGAAGGACGTTGGGA	
CAAATCAATTATCGATTATCTTAGCGGATACTCCTCAAGAG	

Supporting Table 2. Sequences of staple strands, that are optionally extended by handle sequences for CpG-H's.: (A) staple sequences without handles for undecorated DNA origami tubes. (B) staple sequences with handles for DpG-H's.

(A)

TCAAAGGTAATACATTTGAGGACGATAC	AACAAATAAATCAACGGCCTTGATATT
ATCGAAGTTCGACAACCTCGTAGTTCAGG	GGGCTTAAAAAGCCTGTTTAGGTTAAAT
AGGAAGATTTAAAAGTTTGTAGTGTGTA	GAGAGCTAACTCACAGTCGGGAAACCAA
AAATCTAACCACAGAAGGAGATTCGGT	AAATGACGACTGGGACACCATCGATTTT
ATTAGGAAGATGATGGCAATTATTCATT	TTCGGTTGTACCAAGAAGCCTTTATTAA
AGTTACAATACTTCTGAATAATTTGCAC	TTGATAAATTGTGTCGGAACGAGGCGTT
AAATCGCTATTACGGAGTATCTGCATGT	AGCCGCCACCCTCAGCCGCCACCAGAAA
GTATATTTGTTAATTTTTAACCAAGG	TGTGCCACAACATATGCCTAATGAGTGC
AATACAGGTAGAAATCAACTAATGCACC	GGCTGAGTGAGCGAAGCAGGCAATGCC
AGGTGCCGTGAGAATCACCCTACTCTC	AAGCGAGGCAAAGAATAAAGCTAAATTA
AAATAAGAAACGATCCTTTACAGAGAAT	GAAAGAGCGATTATGTATCATCGCCTTC
GTTTTGTAAGGCTAAAGGAGAGTGAG	ACGCACATAATCAACCTCCCTCAGAGAA
CAGCTTTCATCAGGAACCTGCTTCTCTG	CAAGATCCGGTGTCTGTAGATGAAGGGT
ACTATCATAACCAGGCGCATAGTAAGAG	GACGCAACTGTTGGACGCCAGCTGGCGA
CGCCACCCTCAGAAATCCGCCACCCTCA	CAGATTGCATCAAATCGCGTTTAAACA
TGAACACCTGAGATAAGACGGGAGAAT	CCGAACAATAAAGATCTCCAAAAAATA
ACAGCTGATTGCGTTCACCAAGTGAAGCG	TTGTATGTTAGCAATATAAAGAAACGC
TTGAGCTTGAAAATGTGTAGGGAAACTG	GTTATAGATATAGAAGTCTAATGAAGCG

CAGTCAAATCACAGTATGAGAAAGGCCG	TGGAAAGGGGGATGGGTTTTCCAGTGA
GTAATCTTGACACCACCTGACCTTCATC	AGTTTCGAGCTTCAATCAGGATTAGAGGT
TGGAAAGCGCAGAGTGCTCATTAAAGCC	AAAAGGCTCCAAAACCTTCGAGGTGACC
TCAAACACTTCACAGCGATGCTGCTGAA	TAGCAAAGACACCAAATTCATATGGCG
CGTTGGTTCTCCGTGGGAACAAGTAACA	CAAAATTATTATCTATAATGACTGATAC
AAATGTTTCGAGAGGCTTTTGCCGATAAA	CATTCACCCTCAACGTCAGCTTTATTA
AACTACAAATAGGAACCCATGTTCAAGGG	TGGCTTAGAGCTAGTCAGGTCATTTTTG
GAAACAAAGAGATAACCCACAATTGAGC	ACAACCATCGCCGATTTGCGCCGACAAT
GTTTTTCTTTTCGGCTATTGGGCGCCAG	GGAGGGAAGGTACATACATTCAACCGAT
ATTGCGCTAACAAAGCGCCAGGAGAACGA	ATTCAAAATTTAGAACATCATTACGCCG
GATTCAAAAGGGGATCGTAATGTGTAGG	CGCATAGGCTGGGCGTCGGGTACAGAC

(B)

TCAAAGGTAATACATTTGAGGACGATACTCTTCCACCGTAATCTT	AAATGACGACTGGGACACCATCGATTTTTCTCTTCCACCGTAATCTT
ATCGAACTTCGACAACCTCGTAGTTCAGGTCTTCCACCGTAATCTT	TTCCGGTTGTACCAAGAAGCCTTTATTAATCTCTTCCACCGTAATCTT
AGGAAGATTTAAAAGTTGAGTGCTGTATCTTCCACCGTAATCTT	TTGATAAATTTGTGTCGGAACGAGGCGTTTCTCTTCCACCGTAATCTT
AAATCTAACCCAGAAAGGAGATTTCGGTTCTTCCACCGTAATCTT	AGCCGCCACCCTCAGCCGCCACCAGAAATCTTCCACCGTAATCTT
ATTAGGAAGATGATGGCAATATTCAATTTCTTCCACCGTAATCTT	TGTGCCACAACATATGCCTAATGAGTGCTCTTCCACCGTAATCTT
AGTTACAATACTTCTGAATAATTTGCACTCTTCCACCGTAATCTT	GGTGAGTGAGCGAAGCAGGCAATGCCCTCTTCCACCGTAATCTT
AAATCGCTATTACGGAGTATCTGCATGTTCTTCCACCGTAATCTT	AAGCGAGGCAAGAATAAAGCTAAATTATCTTCCACCGTAATCTT
GTATATTTTGTAATTTTAAACCAAGGCTCTTCCACCGTAATCTT	GAAAGAGCGATTATGTATCATCGCCTTCTCTTCCACCGTAATCTT
AATACAGGTAGAAATCAACTAATGCACCTCTTCCACCGTAATCTT	ACGCACATAATCAACCTCCCTCAGAGAATCTTCCACCGTAATCTT
AGGTGCCGTCGAGAATCACCCTACTCTCTTCCACCGTAATCTT	CAAGATCCGGTGTCTGTAGATGAAGGGTTCTTCCACCGTAATCTT
AAATAAGAAACGATCTTTACAGAGAATTCTTCCACCGTAATCTT	GACGCAACTGTTGGACGCCAGCTGGCGATCTTCCACCGTAATCTT
GTTTTGTAAAAGCCTAAAGGAGAGTGAGTCTTCCACCGTAATCTT	CAGATTGCATCAAAATCGCGTTTAAACATCTTCCACCGTAATCTT
CAGCTTTCATCAGGAACTGGCCTTCTGTCTTCCACCGTAATCTT	CCGAACAATAAAGATCTCCAAAAAATATCTTCCACCGTAATCTT
ACTATCATAACCAGGCGCATAGTAAGAGTCTTCCACCGTAATCTT	TTGTATGTTAGCAATATAAAGAAGCCTCTTCCACCGTAATCTT
CGCCACCCTCAGAAATCCGCCACCCTCATCTTCCACCGTAATCTT	GTTATAGATATAGAAGTCTAATGAAGCGTCTTCCACCGTAATCTT
TGAACACCCTGAGATAAGACGGGAGAATTCTTCCACCGTAATCTT	TGGAAAGGGGGATGGGTTTTCCAGTGATCTTCCACCGTAATCTT
ACAGCTGATTGCGTTCACCACTGAGACGTCTTCCACCGTAATCTT	AGTTCGAGCTTCAATCAGGATTAGAGGTTCTTCCACCGTAATCTT
TTGAGCTTGAAATGTGTAGGGAACTGTCTTCCACCGTAATCTT	AAAAGGCTCCAAAACCTTCGAGGTGACCTCTTCCACCGTAATCTT
CAGTCAAATCACAGTATGAGAAAGGCCGTCTTCCACCGTAATCTT	TAGCAAAGACACCAAATTCATATGGCGTCTTCCACCGTAATCTT
GTAATCTTGACACCACCTGACCTTCATCTCTTCCACCGTAATCTT	CAAAATTATTATCTATAATGACTGATACTCTTCCACCGTAATCTT
TGGAAAGCGCAGAGTGCTCATTAAAGCCTCTTCCACCGTAATCTT	CATTCACCCTCAACGTCAGCTTTATATCTTCCACCGTAATCTT
TCAAACACTTCACAGCGATGCTGCTGAATCTTCCACCGTAATCTT	TGGCTTAGAGCTAGTCAGGTCATTTTTGTCTTCCACCGTAATCTT
CGTTGGTTCTCCGTGGGAACAAGTAACATCTTCCACCGTAATCTT	ACAACCATCGCCGATTTGCGCCGACAATTCTTCCACCGTAATCTT
AAATGTTTCGAGAGGCTTTTGCCGATAAATCTTCCACCGTAATCTT	GGAGGGAAGGTACATACATTCAACCGATTCTTCCACCGTAATCTT
AACTACAAATAGGAACCCATGTTCAAGGCTCTTCCACCGTAATCTT	ATTCAAAATTTAGAACATCATTACGCCGTCTTCCACCGTAATCTT
GAAACAAAGAGATAACCCACAATTGAGCTCTTCCACCGTAATCTT	AGTACCATTAAATCTTGTAACCGTTATATCTTCCACCGTAATCTT
GTTTTTCTTTTCGGCTATTGGGCGCCAGTCTTCCACCGTAATCTT	GCTTTAATAACATTGAACAACATTATACTCTTCCACCGTAATCTT
ATTGCGCTAACAAAGCGCCAGGAGAACGATCTTCCACCGTAATCTT	GAGCCATCGGAATTCAGGCGGATAAAAATCTTCCACCGTAATCTT
GATTCAAAAGGGGATCGTAATGTGTAGGCTCTTCCACCGTAATCTT	ATTTTTTCATCAATATCCCAATCCAAGGTCTTCCACCGTAATCTT
CGCATAGGCTGGGCGTCGGGTACAGACTCTTCCACCGTAATCTT	GGGCTTAAAAGCCTGTTTAGGTTAAATCTTCCACCGTAATCTT
AACAAATAAATCAACGGCCTTGATATTTCTTCCACCGTAATCTT	GAGAGCTAACTCACAGTCGGGAAACCAATCTTCCACCGTAATCTT

Supporting Information for Associated Publication P3

Supporting Information

**A Structurally Variable Hinged Tetrahedron
Framework from DNA Origami.**

By

David M. Smith, Verena Schüller, Carsten Forthmann, Robert Schreiber, Philip Tinnefeld,
and Tim Liedl

published in

Journal of Nucleic Acids 2011, vol. 2011, Article ID 360954, 9 pages, 2011.

doi:10.4061/2011/360954

Reprinted with permission from ref.[158]. Copyright 2011 David M. Smith et al.

Supporting information for the manuscript:

A structurally variable hinged tetrahedron framework from DNA origami

David M. Smith,¹ Verena Schüller,¹ Carsten Forthmann,^{2,3} Robert Schreiber,¹ Philip Tinnefeld,^{2,3,4} and Tim Liedl^{1,4}

¹*Physik weicher Materie und Biophysik, Ludwig-Maximilians-Universität, 80539 Munich*

²*Angewandte Physik-Biophysik, Ludwig-Maximilians-Universität, 80539 Munich*

³*Physikalische und Theoretische Chemie-NanoBioScience, Technische Universität Braunschweig, 38106 Braunschweig*

⁴*Center for NanoScience, Ludwig-Maximilians-Universität, 80799 Munich*

david.smith@physik.uni-muenchen.de; tim.liedl@physik.lmu.de

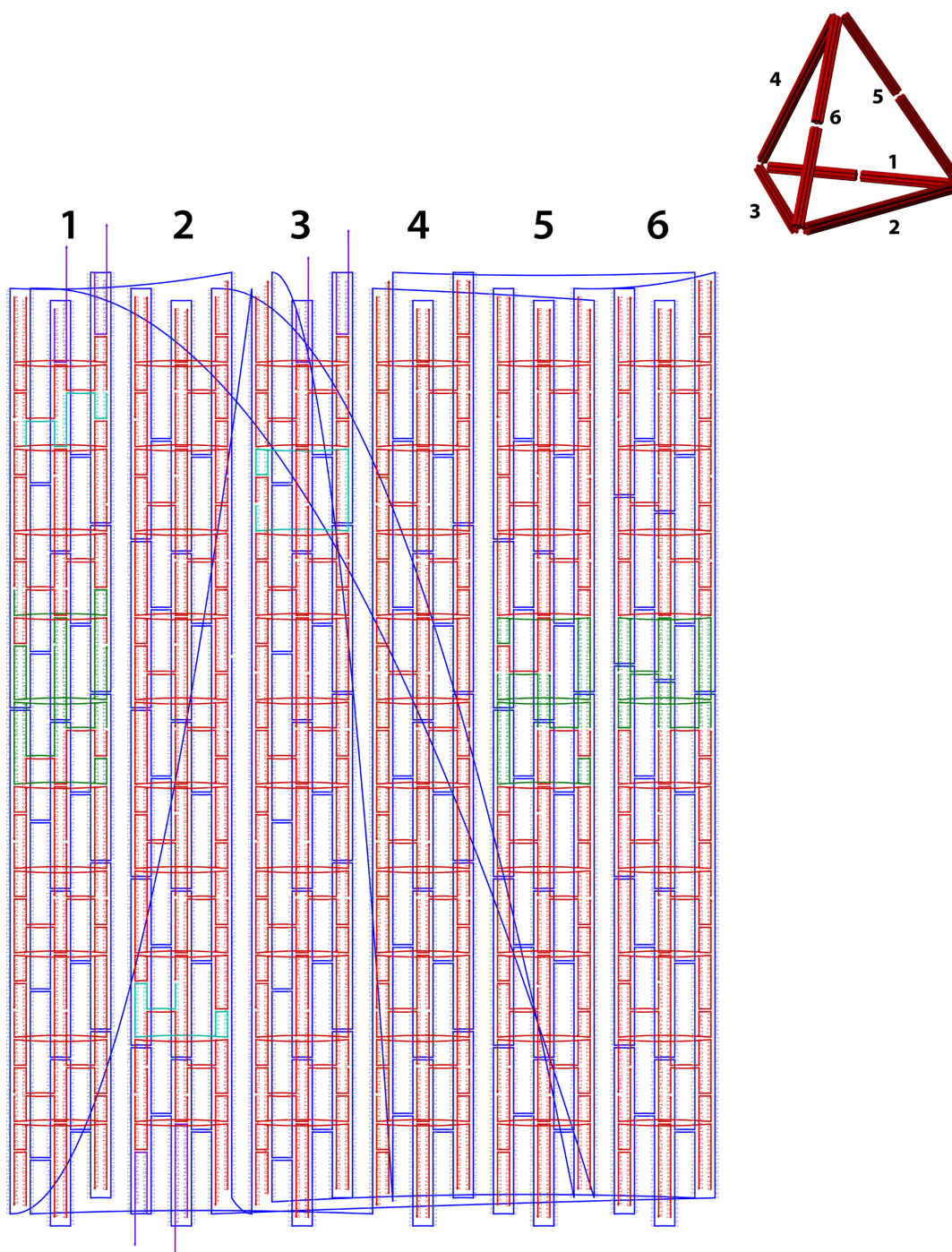


Figure S1: DNA origami tetrahedron design. Strand diagram with scaffold path (blue) and sequence of staple oligos for DNA origami tetrahedron is shown. Green-labeled strands span gap regions on struts 1, 5 and 6, and are selectively omitted to generate the varied open configurations. Strands in purple have been selected for 3' extension with handle sequences for biotin attachment. Light-blue labeled strands are extended at the 3' end with short sequences for transient hybridization of oligos attached to ATTO655 molecules for PAINT measurements.

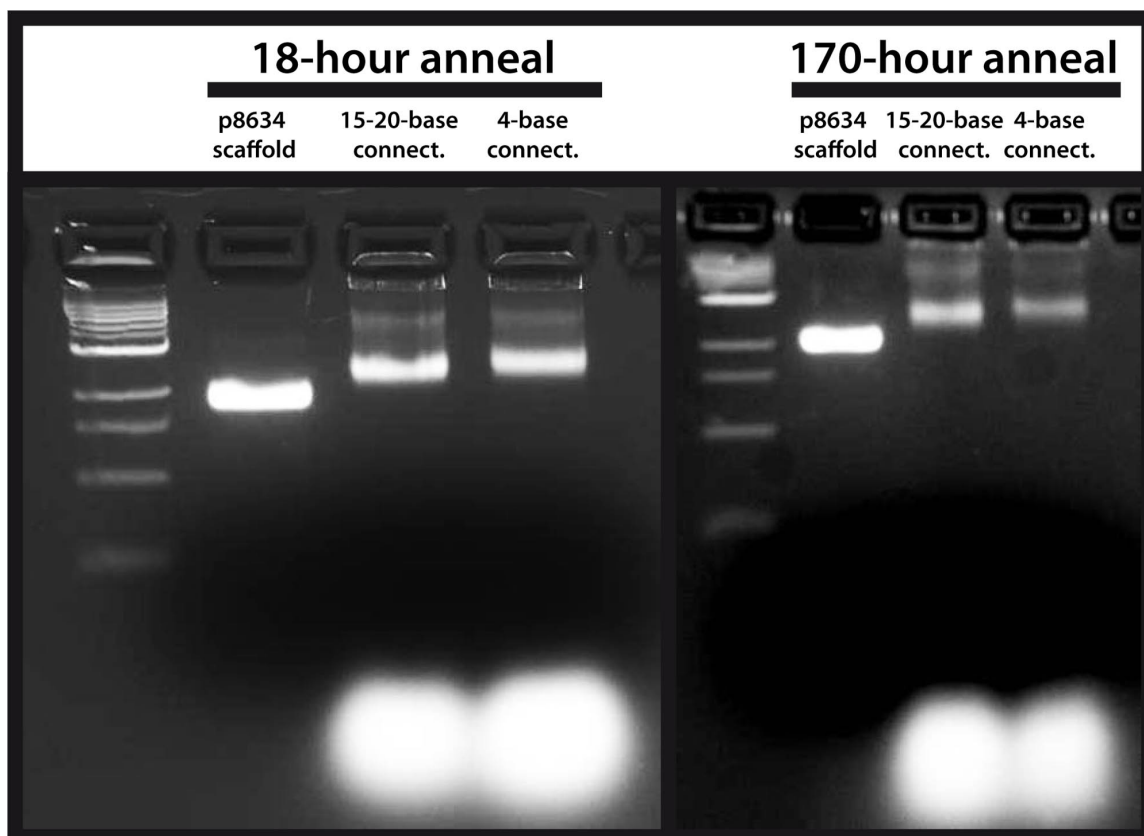


Figure S2: Agarose gel separation of full tetrahedral folded for (left) 18 hours and (right) 170 hours. In each, lanes 1-2 contain 1kb ladder and the circular p8634 scaffold, respectively. Lane 3 contains tetrahedra with a four-base single-stranded connection between adjacent struts, while lane 4 contains tetrahedral with longer single-stranded connections ranging from 15-20 bases. Gels are 2% agarose and run at constant 70V over 22 cm for approximately 3 hours.

Oligonucleotide sequence. Staples spanning gap regions in the struts are marked. Extended staples for biotin attachment, transient hybridization of ATTO655-conjugated oligos along with ATTO655- and biotin-modified oligos are given at the bottom.

Oligo1	CTAATGATGTCAGATATCTTACTTTCGCGTCTGCTTCA	Oligo89	AACGAGTAGATTCAGTTTCATTCATATAAAGTAGAAGAGT
Oligo2	ACCGTTGTAGCAATACTCTGAGAGTTGTCTGA	Oligo90	CAAAAACATATGCGCAATAAGCCTCAGAGAATACCTGGGA
Oligo3	AAAGGAGAGTGACAAACTACATTAATT	Oligo91	AATGCTTTACGCATGCAAAAGCGGATTGCTCAAATACGCGCT
Oligo4	AACGCTTGTGAAAATGCTGAATGCTGAAACGAGATCGGTTTGTAAA	Oligo92	TGCTCCTGCAGTATTAATATGCAACTAACAGTTGATTA
Oligo5	GATGCCAGAGTCTGATAGCTGAGCTTACATTG	Oligo93	TCTGCCAATCTCGGCCAAGCTTCAGTAAACAGAGATACGA
Oligo6	TGCGACGCTTTGTACATTTGAGGATTTAGAAGTATT	Oligo94	CAGTACATTTGAAAAAATAATACATCCGAACGATTAAT
Oligo7	CCGAGGACCTTATAAATAGCTATACATATAAAAGAAACGCAA	Oligo95	CGTCAGAAAATGCAATTTGCACGTAATAATTCGCGGATTCGCT
Oligo8	CGCTCAACAGTAGGCTAAGAGTCTTCTGAC	Oligo96	TGTTGGATATCACATCAATATAATCCTATCAGACGGGAAT
Oligo9	GGAAATCATAATTACTAATAAGAATAAA	Oligo97	GCAGGCAATGCAAACTCGTGAAGCGGCGAAATTAECTCAA
Oligo10	TAATTTCACTGTCATACACGCAA	Oligo98	GTGTGCGAACGAATGTGAGTGTGGCGCGTGTAGTGGTTCG
Oligo11	CCGAAATCGGAAAATCAACGCAATTAAGACTCGATAGCCGAACA	Oligo99	ACATCATGATTTCTATTCGCATTCACCGCACTGATGGGAG
Oligo12	CGAGTATAATTAAGATCAAAATCTTACCAGTATAAAG	Oligo100-G5	AGACAGTAGGAAACTTGCATTCTGATTGTCAGGAGAACGAG
Oligo13	CCAGCAGCACCTCAGCCACCCTAGGTGTATCACCGT	Oligo101	TATCATTCAGATGATGAAACAACTCAAGTTTGACCAAGTT
Oligo14	TGCGCTCACTGCCCGCTACAGACCTAATCTT	Oligo102-G5	TATCATCGCGGTTTGAACCTACCATATAGAAGGATGATGGC
Oligo15	ACAGGCGGGTTCCTGTTTGTAGGT	Oligo103	CGAGCAGATACGACAGCTTTCCATGAAAATCAAACTCTC
Oligo16	TTGATATAAGTATAGCCCGGAACCCCTGTACCATAAGTCCGTCGAG	Oligo104	TTACCATTAGCAAGCAGCAGCCTGATCAGTAAATACCCGTC
Oligo17	AGGAGGTTTAGTACCAGCGGAAAAACAAGT	Oligo105	CCTCGTAACTGCGGCTCAGGAAGATATCGTGTGCGTGGGA
Oligo18	ACGGTGTTCAGGTTCTATTGTAATTAACCTTATGCGATTTA	Oligo106	TGATATTTGAGGCGAGCCGCGCAGCAATTCATATGAATTT
Oligo19	TGTCATATGAATACCAAGAAATACATACAGGTAGAAA	Oligo107	GAAACCCAGCCGATCAGAGCCGCAACCCCGGAAAGGG
Oligo20	AACGAAGTCCGTGAAGATAGAACCCTGTAGG	Oligo108	TTTTCGGAGACTGTCAGAAATCAAGTTTGCACCCGAGCAACC
Oligo21	CTGGCTCATTAGACGCTGGCATTCG	Oligo109	AGTAGCCCAATTCACCTTGAGCCATTTGGAATTTATGACGG
Oligo22	GTTCATAGCTGATAATCAATATGATATTC	Oligo110	TAGATGGGCGCAGCAGCGCGGATTGACCGATTCTCCGGGCT
Oligo23	AAACGAACTAACGGAACCACTGAACGTTGGGAGAAAATCTACGTT	Oligo111	GTATAAGCAAAATGAGCATGTCAATCAACCGTAGCTGCAA
Oligo24	AATGCTGAGTATCTCATATATTTAA	Oligo112	CGACATTCAGAGCCGCAACCCAGCAACCAAGCAACCCGCT
Oligo25	CTCAGTTGAGATTAGGATGTCTTACCAGT	Oligo113	CGAAAGGGAACGCCATCAAGGACGACGAATACCGCTAACAA
Oligo26	AAATTTTCGGAACAGATCTCAAAAGGCTATCAGGTCAATTCG	Oligo114	TACCGAGAGTCAATATGGAGATGATAACTACGCGCGGGAT
Oligo27	ATAGGTCAACTGTAATCTTGATTTTCAAAATATTT	Oligo115	CGAACTGATAGCAGTGTAGTAGAAGAAGTGTAGG
Oligo28	AAAAATGCGCCGCTGAATTTGCTAAACTGGA	Oligo116	ATGTTGTCAGAAATCATTCTGCAAGTCTGAGCAAA
Oligo29	GCTTAGGTTGGGTTTACTCTTTTAAACC	Oligo117	ACCTCAAGCAATAAAATATCTTAGGTAGATAATTAGTAA
Oligo30	GGGATTAATGAAAGTATTAACCAACAG	Oligo118	ATTCACCAATATCTTTTGAATGGCTATACGTTGGCCCTCTG
Oligo31	AGCAAAAGAACGCGAGAAAACATAATGTAATGCTGATGCAAACTCAAT	Oligo119	CAAAAATGAAAAGCGATTTTGTGTTTACCCTATCTTTGGAA
Oligo32	CAGTCAGCAGCTGTAAAACGACGCTCATGCATGGCAG	Oligo120	GCCCTTTAAATAGCAATCAAAAGAATAGTTACCAGGAAGAAA
Oligo33	TTTACAAACAATTCGACTGAGAGAAATAAATAGAAAGTCAATA	Oligo121	AAACAAAATAAACATAAAGAACGTTGACCTTAAAATTTTAA
Oligo34	TAAGGTAACCACTAGAGAAATTAACAGCGCAACACAG	Oligo122	CTAAATTAAGCGCTTAGAAAA
Oligo35	AACAGTGTTTTGTCCGTCATACATAGCGGGTTTGTCT	Oligo123	AGTTTCGTAGGAACCTCAITTCAGGGATCCCTCAGAGAACC
Oligo36	TAAATTTTGTAAATCAAGTTGGCAAGAGA	Oligo124	AATTTATAGTAAAAATCAACGTAACACCCGATCAGATGA
Oligo37	GCCTATTTGGAACAAACAGTTAATGCC	Oligo125	CGTAAAGCATGTAGATAAATTTAGCATCCACAG
Oligo38	AGCCCAAAACAGAGCTGTGATAATCA	Oligo126	CGAGGCGCAGACCTTGGGCTTGGCGACCTGCTCCATGTTTA
Oligo39	TCCTCAAGAGAAAGGATAGGATTTGAAACATGAAAGTATTAAGAGGCTG	Oligo127	GACAAGAAAGCTGCAACACCA
Oligo40	GAGTCTGGAGCAAAAGTACGCCAGGGTT	Oligo128	CATCGTTTACCAGAGAGTATC
Oligo41	AACCGGAATAAGTTTACCCTGATCTATTAATCTAAGTTTTAACG	Oligo129	CCGGAGAGGGTAAGCCGGAGCAGTCAATCAAAAGAGGATAA
Oligo42	GGCGATTAGCTCATAACGTTAATATTTGTTAAAAATTC	Oligo130	TAAAGATATCAACATTAATG
Oligo43	GAGGAAGGTTATCTCAACAGTTGAAAGG	Oligo131	ACTAATGTGAGGTCGACGATAAAAACCTGCCAGAGGGGCA
Oligo44	TCTAAAGCATCACCCAGCAGCAAAATGA	Oligo132	ATATTTTGTATCTACAGCAAGGCAAGCATAAAGCTATA
Oligo45	AAATACATACATAAAGGTTGGCATTATTACGCGATGTTAGCAAACG	Oligo133	GTGAAAACAATTTCAATAATCAATGATTAAGACGTAATACATAGC
Oligo46	ACCTTCATCAAGAGAGCGGCATAGGCTG	Oligo134	TATTCATTTCAATTAATCGCGCAGAGGCTTGAATGTAATAT
Oligo47	AAGAACTGGCATGATAATAACGGAATAC	Oligo135	GATTGCTGAAACAGTACCTTTTACATCGGGAGATGGTTTAA
Oligo48	TTGCCCTGACGAGATCATTCAGTGAATA	Oligo136	GGGTCGACAGGAGGCAACAAATAGAGTGTACTGGTAATGGCTTTG
Oligo49	AAAGTGTAAATGACAGATCAACGAAAGGTCGAGCCGGTGGCAG	Oligo137	ACCGTTGAGAAATCCTTAAAGCGGAAATGGACCTTGGCT
Oligo50	TTATCCGGAATATTACATAACAATCTCCCTGTGTCGCCGGG	Oligo138-G6	ACTTCGCCATTCAGGCTGCAATTAAGTGTGAATTAGAGCCCA
Oligo51-G1	GCCATTGCAACAATAAGCAATTTACATTTACATTGGCAG	Oligo139	ATCGATGATGATCCGAAGATT
Oligo52	CGCTCAAAGCACATAATCTTGGTCAAGTATATACGCAACAG	Oligo140-G6	GAAACCATCGCAACTGTGGGAAAGGCGCGCATCCAGCCAT
Oligo53	AAGATTGCTGATACATTTATAAGGGGTG	Oligo141	ACTCAGAGCCACCCTCTTTAGCTGCTCATAGCCCTTCA
Oligo54-G1	ATGGAAAAACGCTCTGAGCACTTCCGCTCGAATTCGTACA	Oligo142	TGTAGCCGGAATAATTCGCGTCAITTTAAATTTGATTTTAA
Oligo55	ATCCTAAAACATCGCCATTCTGTAAGAATTAGTCTTTCGGCT	Oligo143	ATGATACCAGTAAGCAATCAATAGAATTAGTGCCTTGAGT
Oligo56	ACCTGAAGGCCAACCCAGTAAATAAACAACATAATAGG	Oligo144-G6	GGCAAGCGCCAAATTTCTGTGTCGGGAACAGCTTTCCGGCA
Oligo57	CGTACTCAAAGGCTATGAGTATCAATGAGTTAGATGAAGCAT	Oligo145-G1	TGCTGGTAGTCAACAAGAGATAGACGCTTGAATGGATATCT
Oligo58	AGGTACTCACAAAGTGAATAATTTATACGATGAAATTTG	Oligo146	TAACTACCCGCTACCTCAATAGAAGATAAAACAGAGGGG
Oligo59	CGGTGATTAACACTTGCATTAGAG	Oligo147	CAAGGAGCGTTTAGTCTTTACATAAAGTGTAGTATGATGAC
Oligo60	CATATTTATCAGTGTGAAATACCAATAAACAACAGAAGTGT	Oligo148	AAATGACAAATCCGAAAGGTTTATAAGTGGCATACTAGATGA
Oligo61	GAGCGCTCCCTGAAATTAGACGGGAGAACCCGAGAAGCAAGA	Oligo149	TGAAGACTGATACCTCCACCAACATAGTTTATGAAATATT
Oligo62	ACCAACGACGCTACTCAAGATAGTTGCCACTATGCCATAT	Oligo150	TGTACAAAACATTTGGAGAAATGGAGTCCGTTGAAACGATAA
Oligo63	AACCGGAGGCGTCTTATCCGGTATTCCAAATCATCAAAGG	Oligo151	CCTCCGGTGTCTTGTCTCCACATCGGGATTTGGCGTTATCA
Oligo64	GCATCAAAAGAAGCATCGGCTGCTTTACCGTCTCGCCCAA	Oligo152	GTATAGATGATTAACCCATATAGAGTCTACTTGCCTCTC
Oligo65	AACAAGAAAAATCCAAACAATAGATAAGTGAACGCAACGGTA	Oligo153G1	GAACTCGATAATACCTACATTTTACGCTCAATACACAGACA
Oligo66	TAAAGTATTTTCGACCAACATGTAATTTATCCTGATGTTGAG	Oligo154	ACATTTAGAAAAATCCGAACGCAACCCAGCCAAACAATA
Oligo67	AGCTGTTTGTAGTAAACCGTGTGATAAATTAATGTTAGGCCAC	Oligo155G1	TTATTTGCAATCATGGTCAAGCTGTGTCACCTCGGGGTTTT
Oligo68	CAAGAGTTAAGAATAACATAAACAACAGGGTTCAGCAAAATAA	Oligo156	AAGTTAACTGAACAATAATCAGAGAGAAAGAAAGTAAAGCATCCGGA
Oligo69	GGCAAAACTCTTCCGGGAGGTTTGAAGTCCAACGGATATAG	Oligo157	AGTAGACGCTTTACAGAGTTTTCACCTTACGAGCGTCTGT
Oligo70	CGCCAGAAGTACGAGCATGTAGAAACCAAGACAGGGCCTGTT	Oligo158	TCCTTAGCCAACTCCCGATATCTTCGAGAACAGCAGC
Oligo71	ACGGTTCACAGACGTTAGTAAATGAATAGAGAGTTTACGTT	Oligo159	AAAATATCCATCTTAATTCGACAGGACCCGCAAAAAGGTTG
Oligo72	GCTGATTAACCGATAGTTGCGCGGACATGAGACGGCAGGCA	Oligo160	AACAATGTTATAACCCCAAGAAATGAGTTAAGAAGGTAAT
Oligo73	GGCCAGGCTACGTAATGCCACTACGAAGGTTTCCGGAGATT	Oligo161	GACCAATAAAGTAGGGTTGAGTGTGTAAGCGCCAAAGTC
Oligo74	ATGAATCAGCCGAAGTACCAACTTTGATGCCAGCATGGTTT	Oligo162	TATTTATACTTCCAGAGCTAATTTGCCAGTTGGGAATCTT
Oligo75	ACAGCCAAGCCCAATCACCAGGTTTGGC	Oligo163	TAGCAAGTAAAGCCGTTTTTATTTTCACTGTAGTCAAGTACC
Oligo76	TTTCAGGTTGAATCCGCTCACCTCTTTAATTTGATCGGTTCT	Oligo164	TAGAATCATTACCGATCAAAAGGATTTTATCAATAGGATTA
Oligo77	ATGAGGAGTTTTCAAAAGTACACAGAGGCTTTGAGGACTGC	Oligo165	CTAATGCCCAAAGTAAATCTCTCCAGACGACCCAGGAGATAA
Oligo78	CCACCTCAGCTGTACAACACTACAACGCTGTTTTCGAGCA	Oligo166	TTTATAAACAACGCGCAGTAAATCATATGCGTTGAATTCG
Oligo79	TTTCTAGCCGCTTCAAAAGGCTTCAAAAGGAGCCAGGCAACA	Oligo167	GAAAATCTTCGGAAGAATAAGAAAGCAACAGCAATTTGGGAT
Oligo80	CGCCACGCTGGTTACGAGGGTAGCAACGGCTAACGATTTGG	Oligo168	AAGACAGCGGGGATTTGCAGGGAGTTAAATTTTCGCAACCAT

Oligo81	ACGAAAGGGCCAACATAAATGTGTGCGAAATCCAGTGCATTA	Oligo169	TGTATCACGCGAAATTTGACCCCGAGCGTACACTAACCTAAA
Oligo82	TTCAGGACAGAATCGTCATAAATTCATGGAGGTCGAGAGG	Oligo170	AAAGGAATCCAAAACCGCCTGGCCCTGTTTCTGTCAGCGGA
Oligo83	ACATCATATCCCAACAGGTCAGGATTAGGTAGTAAGATTA	Oligo171	CGCTTTTCATCGGATTCCTTTCCACAGATGACAAGTCGCTG
Oligo84	TCTGCGTTACATTTCGCAAATGGTCAATGACCTGCGGTGTC	Oligo172	TACCAAGTCGCTGGCGGGGAGAGGGCGGCCACCAAAACACT
Oligo85	AGACTCCAGCGGGGAGAAGCCTTTATTTTCGCCATGCAAAAT	Oligo173	GAACGAGACTTTAACGGGAAACCTGTGGAAGAGGAATTCATT
Oligo86	CTATCATAACCCGGGCATAGTAAGAGCCGCCAAAACATTCA	Oligo174	GTAAGTTTTGTCGTCTTTCGAACCGCCAAGCCTCATAGTTAG
Oligo87	GTTTAGACTGGAAATGCAAAAAGAGTTTAAAATAGCAATGGG	Oligo175	AGTCTTAAACAGCTTGATCAACTTCAAATATCAGCTTGCT
Oligo88	CTTCAAAGCGAAGCAAGCCGAAAGACTATCAAAAACATATCG	Oligo176	CACCATTAACGGGTAAAAATAACCGATAGAAAGACTTTTTTC
Oligo177	ACGGTCAATCATAAGGGAAGCAAAAAGAATACTTAGCCGGAA	Oligo195	TAATTTTAAATGTGAGTGAATAACCTTGCTTCAAATGGAAA
Oligo178	CTTTATAGTCAGAACGCTTATACGGGGTTTGAATCAGAATGA	Oligo196	ACGTAATCGTCGCTTATTAATTTAAAGAAAACCTTACCTT
Oligo179	GAAGCTCAACATGTATCGAAACAGACCCAGAGTACTTGCGGA	Oligo197	AAAACAATAACGGAACAAGAAACCCCAAAATGTAGATT
Oligo180	TGTCCAATAAATCAAAGCACTGCCTGTAACCTGAAAAGGT	Oligo198	AAGTGAGCATTGCCAGGAGGATCGAACTTATATGTTACAGG
Oligo181	TAGCTATTTTGTAGCAGTTTCTTGTGTCAACGCAGGTGAGA	Oligo199	AGGTGTTCTCATTGGACGCTGGCAGCATCAGAAAGGCTATA
Oligo182	TTACCCTGACTATAAATCAAAAATCAGGAAAACGCCCTCA	Oligo200	GAAACCATCGCAACTGTTGGGAAGGGCGCGCACTCCAGCCAT
Oligo183	ATATAATGCTGTGGTTAGAGCTTAATTTGGTCAATTTCTTAAT	Oligo201	ACTCAGAGCCACCCTCTTTAGCGTCTCATAGCCCTCA
Oligo184	GTAGCATTAACAGATCAATCTACTAATCGAGCTGTTTAGCT	Oligo202	TGTAGCCGGAAATAATTCGCGTCAATTAATTTGATTTTTAA
Oligo185	CCTAGCGTCCAATACTGCGGATACATAAAATAATAGTAAAT	Oligo203	ATGATACCAGTAAAGACAATCAATAGAAATTAGTCCTTGAGT
Oligo186	TGCCAGACCGGAAGCAAAACAGTTCAAGTTTAAATTCGAG	Oligo204	GGCAAAGCGCAAATCTGTTGCGCGGAACAAGCTTTCGGGA
Oligo187	GGTAGTTTGACCATTAGATTGATAAGAGCTCCCAATTCGCG	Oligo205	TCAAGCGCAGTCTGTTTACCAGCGCCACCAGAGGTCAG
Oligo188	AAGACCCTGTAATCTTTTGGGGCGAGAAATCGTTGATC	Oligo206	ACAATCAAATCACTTGAGGGAGGGAAGGTAGCGAAGCGCGT
Oligo189- G5	CGATTGTATGTTGAGCTTGAACAGCAATTGTAACGGGAA	Oligo207	CCCGTCGGTAATGGATAGCTTTCATCAACACTTGCCTTCC
Oligo190	TTTTACCTGAGCAAAAGAAGAATAAAGTGAATATACAGTAT	Oligo208- Gap6	AAATTATCGATAGGCCGGAAACGTCACACAGCAAATCACC
Oligo191- G5	TTACTTCTGAATAATGGAATGGAACCTGCAACCGCCGACAT	Oligo209	CTTCGCTCAGTATCATCTGCCAGTTTGAAGGTCACGTTGGTG
Oligo192	CCTAGCGTCCAATACTGCGGATACATAAAATAATAGTAAAT	Oligo210	AGAGCCACTTATAGCGTTTGCCATCTTTTCATCGATCGGCA
Oligo193	GATAGCTCCCTTAGATTAATCCTTTGCTTTTATCAAAATC		
Oligo194	GATATTGCGCTAGCACCAAGCAATACATCTGGATGAACCCAT		
Oligo43- biotin	GAGGAAGGTTATCTCAACAGTTGAAAGGCATCTCCTATTACTACC		
Oligo44- biotin	TCTAAAGCATCACCCAGCAGCAATGACATTCTCCTATTACTACC		
Oligo45- biotin	AAATACATACATAAAGGTGGCÁCTTATACGCAGTATGTAGCATTCTCCTATTACTACC		
Oligo46- biotin	ACCTTCATCAAGAGAGGGCGCATAGGCTGCATTCTCCTATTACTACC		
Oligo47- biotin	AAGAACTGGCATGATAATAACGGAATACCATTCTCCTATTACTACC		
Oligo48- biotin	TTGCCCTGACGAGATCATCAGTGAATACATTCTCCTATTACTACC		
Oligo52- PAINT	CCGTCAAAGCACTAATCTGGTCAGTTATATCAAGCAACAGTCTTCAAC		
Oligo61- PAINT	GAGCGCTCCCTGAAATTAGACGGGAGAACCCGAGAAGCAAGATCTCAAC		
Oligo74- PAINT	ATGAATCAGCCGAACCTGACCAACTTTGATGCCAGCATGGTTTCTTCAAC		
ATTO655- PAINT	GGTGAAGA _{ATTO655}		
BIOTIN	GGTAGTAATAGGAGAATG _{bt}		

Supporting Information for Associated Publication P4

Supporting Information

M1.3 - a small scaffold for DNA origami.

By

Hassan Said, Verena J Schüller, Fabian J Eber, Christina Wege, Tim Liedl, and Clemens
Richert

published in

Nanoscale 2012, 4, 284–290

Ref. [159] - Reproduced by permission of The Royal Society of Chemistry.

Electronic Supplementary Information

for

manuscript entitled

M1.3 - A Small Scaffold for DNA Origami

by

Hassan Said, Verena Schüller, Fabian J. Eber, Christina Wege, Tim Liedl, and Clemens Richert

Contents	Page
1. Materials and Methods	S2
2. Full sequence of M1.3	S3
3. Alternative restriction reactions	S4
4. Origami designs	S6
5. ALEX data, stoichiometry histogram for fluorescently labeled pair of staples	S11
6. Estimated cost of producing 1 mg of M13 single-stranded DNA scaffold	S13
7. Gel of 4F M1.3 origami with 5'-capped staples	S14
8. Melting curves of 4F M1.3 Origami with and without 5'-capped staple strands	S15
9. Melting points and corresponding transition breadths	S17
10. MALDI spectra of individual 5'-capped oligonucleotides	S18
11. Reference for Supporting Information	S20

1. Materials and Methods

Materials

Single-stranded M13mp18 was purchased from *Bayou Biolabs* (Materie, LA, USA), from which M1.3 scaffold was excised as described in the Experimental Part of the main paper. For the 4F origami sheet, cartridge-purified staple oligonucleotides were purchased from *Biomers* (Ulm, Germany) and were used without modification. ATTO-labeled Oligonucleotides were obtained from Eurofins MWG/Operon in HPLC-purified form and were used further purification. Concentrations of M1.3 scaffold and oligonucleotide solutions were determined by measuring the UV absorbance with a *Nanodrop ND-100* spectrophotometer (*NanoDrop Technologies*, Willmington, DE, USA). Restriction enzymes were purchased from *Fermentas* (St. Leon Rot, Germany). For DNA extraction from agarose gels, a *NucleoSpin gel and PCR clean-up* kit (*Macherey-Nagel*, Düren, Germany) was used. Buffer salts and agarose were obtained from *Carl Roth* (Karlsruhe, Germany). Amicon Ultra filter devices (MWCO 30,000 Da) were purchased from *Millipore* (Billerica, MA, USA). TEM grids were from Plano (Wetzlar, Germany). The 0.24-9.49 kb RNA ladder for gels was purchased from *Life Technologies* (Darmstadt, Germany). The 100 bp ladder was received from *New England Biolabs* (Ipswich, MA, USA).

TEM Imaging

For analysis of the four finger sheet (4F sheet), 0.5 pmol of linear M1.3 was allowed to assemble using 10 eq of the staple strands, as described in the Experimental Part of the main paper. The sample was diluted with folding buffer (5 mM Tris-HCl pH 8.0, 1 mM EDTA pH 8.0, 12 mM MgCl₂) to give a 1 nM solution of the scaffold. Transmission electron microscopy employed a sample of the solution (3 µL) that was applied to a carbon-coated glow-discharged TEM grid. After 1 min, excess liquid was soaked up with filter paper, and the sample was stained with 1% uranyl acetate for 30 s. The grid was dried in air, and the sample was visualized at 68000-fold magnification with a *FEI Tecnai G²* transmission electron microscope.

For electron microscopy of the other origamis, a similar procedure was employed, using argon plasma-cleaned grid, placing 1.5 µL of gel purified sample for 1 min on the grids, washing with 7 µL uranyl acetate (1%), and staining with 7 µL uranyl acetate (1%) for 8 s.

2. Full Sequence of M1.3 scaffold (704 nt, linear version)

5'-

AATTCGAGCTCGGTACCCGGGATCCTCTAGAGTCGACCTGCAGGCATGCAAGCTTGGCACTGGCCGTCGTTTTA
CAACGTCGTGACTGGGAAAACCCTGGCGTTACCCAACCTAATCGCCTTGCAGCACATCCCCCTTCGCCAGCTGGC
GTAATAGCGAAGAGGCCCGCACCGATCGCCCTTCCCAACAGTTGCGCAGCCTGAATGGCGAATGGCGCTTTGCCT
GGTTCCGGCACCAGAAGCGGTGCCGAAAGCTGGCTGGAGTGCATCTTCCTGAGGCCGATACTGTCGTCGTCC
CCTCAAACCTGGCAGATGCACGGTTACGATGCGCCATCTACACCAACGTGACCTATCCATTACGGTCAATCCGCC
GTTTGTTCCACGGAGAATCCGACGGGTTGTTACTCGCTCACATTTAATGTTGATGAAAGCTGGCTACAGGAAGGC
CAGACGCGAATTATTTTTGATGGCGTTCCTATTGGTTAAAAAATGAGCTGATTTAACAAAAATTTAATGCGAATTTT
AACAAAAATTAACGTTTACAATTTAAATATTTGCTTATACAATCTTCCTGTTTTTGGGGCTTTTCTGATTATCAACC
GGGGTACATATGATTGACATGCTAGTTTTACGATTACCGTTCATCGATTCTCTTGTTTGCTCCAGACTCTCAGGCAA
TGACCTGATAGCCTTTGTA

-3'

3. Other restriction enzyme combinations for excising fragments from single-stranded M13mp18 DNA

3.1 Overview of other successful excision reactions

a HindIII + BsrBI: restriction fragment size of 708 nucleotides

b HindIII + BglII: restriction fragment size of 653 nucleotides

c EcoRI + BglII: restriction fragment size of 704 nucleotides

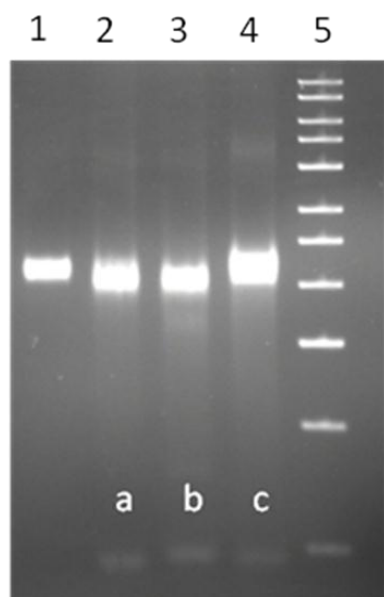


Fig. S1. Excising M1.3 with other enzyme combinations.

Lane 1: 0.2 pmol M13; *Lane 2:* 0.4 pmol M13 after digestion with HindIII and BsrBI; *Lane 3:* 0.4 pmol M13 after digestion with HindIII and BglII; *Lane 4:* 0.4 pmol M13 after digestion with EcoRI and BglII; *Lane 5:* Lambda DNA/PstI digest ladder.

3.2 The special case of excision with NaeI + Eco53kI: restriction fragment size of 624 nucleotides

- NaeI recognition site: 5'...GCCGGC...3'
- Eco53kI recognition site: 5'...GAGCTC...3'

Initially, with these two enzymes, no restriction fragment was detected in agarose gels. NaeI is a type II restriction enzyme, for which both cleavable and resistant NaeI recognition sequences were found.¹ In fact, NaeI is a type IIe subclass restriction enzyme, requiring the recognition of a second DNA site to induce cleavage. Hence, some DNA sequences, including M13mp18, with a single recognition site, cannot be readily cleaved by NaeI. Topal and coworkers found that the cleavage of resistant sites can be induced by adding appropriate external DNA duplexes.¹ By adding a DNA duplex that contains a NaeI recognition site, a successful cleavage of single-stranded M13mp18 DNA was achieved. The sequence of this duplex is:

5'-TGG TGG GCG CCG GCG GTG TGG GCA-3'
3'-ACC ACC CGC GGC CGC CAC ACC CGT-5'

Shown below is the gel after the cleavage reaction.

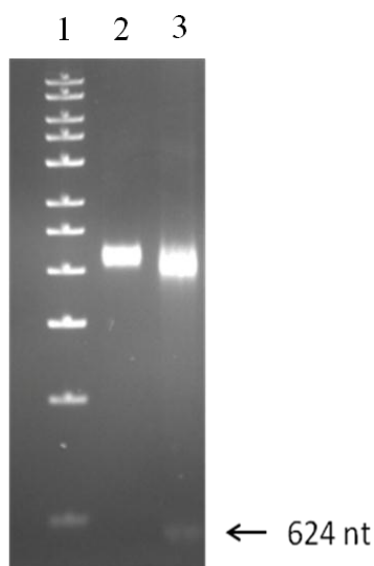


Fig. S2. Excising M1.3 with restriction enzymes NaeI and Eco53kI.

Lane 1: 0.5 µg Lambda DNA/PstI digest ladder; *Lane 2:* 0.2 pmol M13; *Lane 3:* 0.4 pmol M13 after digestion with Eco53kI and NaeI.

5[5]	6[5]	TTGGGTAACGCGGATCCCCGGG	22
6[23]	4[24]	ACTCTAGACAGGGTTTTCCAGTCAGGGGGAT	32
7[5]	6[24]	TACCGAGCTCGAATTTACAAAGGCTATGCAGGTCG	35
0[44]	1[51]	CCGTGCATCTGCCTTTCCGGCACCTTCTCCGTG	33
1[52]	0[45]	GGAACAAACGGCGTAGATGGGGCGCATCGTAA	31
2[51]	3[43]	CCCGTCGGAGCTTCTGGTGCGCGATCGGTGCG	32
3[44]	2[52]	GGCCTTTCACGCCATCAAAGCGAGTAACAA	32
4[43]	5[46]	CCAGCTGGCGAAACGACGTTGTAAAAC	27
5[47]	4[44]	GACGGCGATTGTATAAGAACCAATAGGAGCTATTACG	37
6[42]	7[50]	CTTGATGCCTCAGGTCATTGCCTGAGAGT	30
7[51]	6[43]	CTGGAGCAAACAAAAAACAGGAACAGTGCCAAG	34

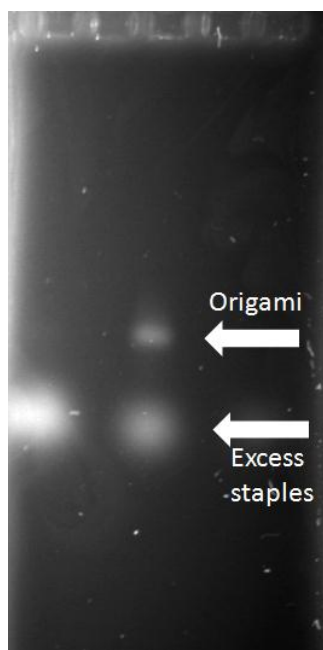
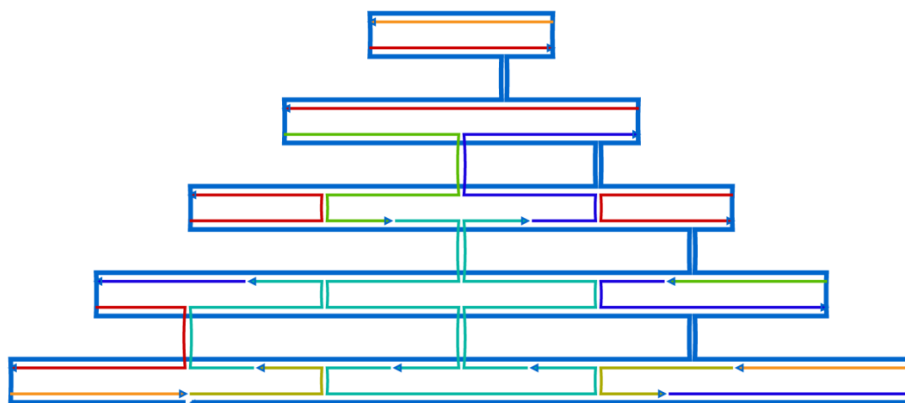


Fig. S3. Additional Agarose gel of four finger M1.3 sheet with ethidium bromide staining. For a different gel of the same assembly, see Figure 2 of the main paper. Left-most lane: M1.3 at high concentration, without staples; center lane: four finger origami sheet assembled with 10 equivalents of staple strands.

Other M1.3 Origami Designs (compare Figure 3)

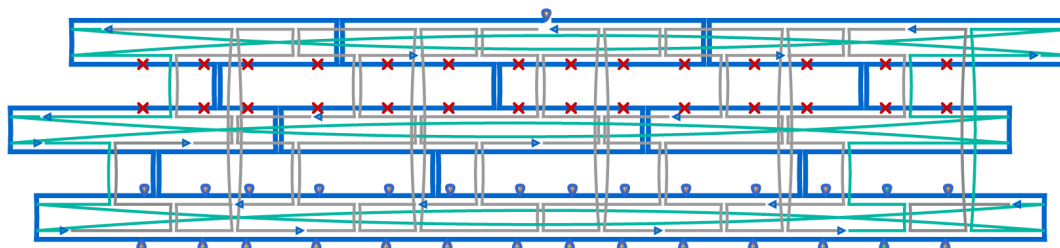
2D Triangle (square lattice)



2D Triangle

```
GCATGCCTCGCTATTACGCCAGCTGCGCAACTG
AAGATCGCATTTCGCCATTCAGGCTGGCGAAAGGGGATGTAAAACGAC
GGCCAGTGCAATCATATGTACCCCGTTGATAATCAGAAACCAGTCAC
GACGTTGTGCTGCAAGGCGATTAACCAGGCAAAGCGCCACTCCAGC
TGTTACCAGGGTTTTTCAGCCCCAA
CGTAAAACACTAGCATGTCCAAGCTT
TTGGGAAGGGCGATCGGTTTTT
AAACAGGAAGATTGTATAAGCAAATATTTTTTTT
GTGCCGGAGTTGGGTAACGAAATTCGCATTAAATTTTTT
CAGCTTTCGTTGGTGTAGATGGGCTAATGGGATAGGTCACCCATCTTTT
TTTTTTTGTTAAATCAGCTCCTG
TTTTGAACAAACGGCGGATTGACCGGCATCGTAACCGTGCAGCCTCAGG
TTTTCATTAATGTGAGCGATGGCCTTTTT
TTTTTTAACCAATAGGAACGCGGCACCGCTTATTTTTTTT
TTTTGACGACGACAGTATCGTCTGCCAGTTTGAGGGTTTT
TTTTGCGGGCCTCTTGCAAGTCTGACTCTAGAGGATCTTTT
TTTTAAAATAATTCGCGTCGTAACAACCCGTCGGATTCTCCGTGGTTTT
TCCTGTAGCTCCTCTTTTGAGGAACAAGTTTTCTTGTCAGCTTTCATCAA
AAATTGTATCCTCTTTTGAGGAACAAGTTTTCTTGTAACGTTAATATTT
CCCGGGTTCCTCTTTTGAGGAACAAGTTTTCTTGTAACGAGCTCGAATT
```

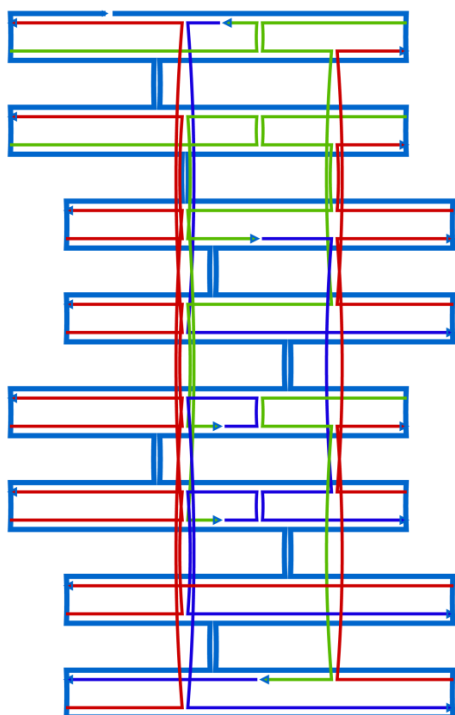
Curved 6 helix bundle with deletions (red crosses) and insertions (blue loops) (honeycomb lattice)



curved 6 helix bundle

```
AGGTCATCGGTCCGGCAGATGAACGGTAGTAAAGACGTTCC  
AGGCTGCCCCTTACCCTCTTCGCTTGCCTCATATCGGCAAG  
GAGAATTGCCTGATTCTCCGTGGGAACAACCAGTCACACGACGG  
TGCGGGGCAACTGTTGGTGT  
ACTAAATAAAGCAGCAAAGCCCC  
TGTTGCCAAGCCGTAACGCCAGGGTTTTACGGCGGACGAATT  
TGTATTTTATTAGCTTAAATTGTTATTTTGGTGAGCGAG  
CCAGTGCATGCCTACTCTAGAGGATCCGAGCTTTGACCGT  
AAAAACAGCATTAAATTTAAAATTTCGCATTA  
CCGGTTGACCGTCGGAGAGTCTGGAGTTAAAAACGCTAAA  
GCGATTAGGTCACGTTGGGAAGGGGTACCCGCCCAGC  
TAACAATAATCAGAATGTCAATCATATGTAATCGAAACAA  
AATGGGATAAGTTGGGAAAGGGGATGTGCATTACGGATCGG  
AGTTTGAGGGGACCATCGTAAGCCATTC  
CAGCTTTCATCAAGACGTCTGATTTCGAGAT
```

3D Cube (square lattice)



3D Cube

```
ATGGGGAGCGAGTAACAACCCTTTT
CGCTATTA ACTCCAGCGGTATCGGCCTCAGGTTTT
CGAGTATTTAAATTGCCATTCAGGCTGCGCAACTTTT
TCTGACGTTAATTGGAACAAACGGCGGATTGACCGTAATGTTTT
ATTCCAGCTTTCTGTGCGCATCGTAACCGTGCATCTGCCAGTTTTT
TTTTAGCAAACAAGAGAATCGCCAAGCTTGCGTAC
TTTTAAAGCGCCATTCGTAAGTGCCGGATGGTGTAG
TTTTAAA ACTAGCATGTCAATCATGGGTAACCGACGGCCAGCCTCTT
TTTTTCTAGAGGATCCCCGGATGCCTGCGATCGGTGCGGGCCCCCGCT
TTTTTACGACGTTGTA AAAAGCCAGGGTTGCAAGGCGATTAAGTAATA
TTTTAAGGGGGATGTGCTTTCCAGTTTT
TTTTTGTTGGAAGGGCAGGTGACTTTT
TTTTAAGATCGCCGCCAGCTGGCGATTTT
TTTTGGATAGGTCACGTAACCAGGCTTTT
TTTTTGATAATCAGAAAAGTGATGAACGGTAATCGTTTTT
TTTTTTGTATAAGCAA ACTCGAATTTGAGAGTCTGGTTTT
TTTTTAAATTTTTGTTAAATCACAAAAACAGGAAGATTTT
TTTTCAATAGGAACGCCATCAAATATGTACCCCGGTTTTT
TTTTCATCAACATTA AACGGCAGCTCATTTTTTA ACTTTT
TTTTGTCGGATTCTCCGATTTTGTTAAAATTCGCATTTTT
TTTTTTGAGGGGACGACGACAGTCTGGCCTTCCTGTAGCCAGCTTTTTTT
```

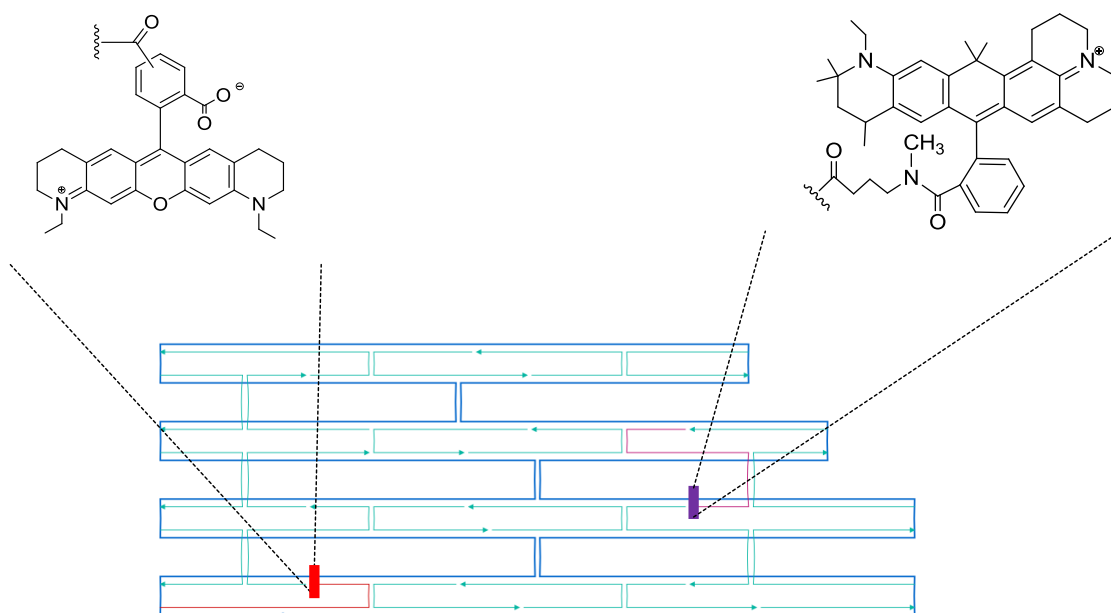
5. ALEX data, stoichiometry histogram for fluorescently labeled pair of staples

5.1 Design of 4F M1.3 sheet with two fluorophore-labeled oligonucleotides

Sequences of labeled oligonucleotides

Start	End	Sequence 5' → 3'-Terminus	Length
7[5]	6[24]	TACCGAGCTCGAATTTACAAAGGCTATGCAGGTCGTTT – Atto565	35
2[71]	4[72]	TAAATGTGAATAATTCGCGTCTGGAATCAGCTTTT– Atto647N	32

Structure of doubly labeled 4F Sheet and position of fluorophores (Atto565 is shown in red and Atto647N is shown in purple, all other staple sequences unchanged)



5.2 Sample Preparation, Data Acquisition and Data Evaluation.

Annealed 4F sheets were purified using Amicon Ultra-0.5mL centrifugal filters (100,000 MW cut-off) 4 × at 14'000g for 5 min. Between each centrifugal step, 500 μL of buffer (TE with 12

mM MgCl₂) were added. After the last step, the filter was turned and spun at 1000 g for 1 min to recover the sample. The single-molecule fluorescence measurements were carried out at 21°C in standard phosphate buffer saline (PBS) with Trolox to reduce blinking and bleaching.³ To prevent DNA accumulation at the surface, the sample chambers were incubated with BSA (1 mg/ml BSA in PBS) prior to the measurements. The ALEX measurements were performed on a custom-built confocal microscope that is described in detail in reference 4. The light intensities were 20 μW at 533 nm for Atto565 and 20 μW at 640 nm for Atto647N. Data evaluation was performed as described in reference 4. The parameters of the Seidel burst search algorithm for the 4F sheet were T=0.5 ms, M=30, L=50. The dye molecules are alternately excited and the fluorescence of Atto565 and Atto647N is detected separately. The stoichiometry value *S* is defined by the Atto565 emission induced by excitation at 533 nm $F^{Atto565}$ and the Atto647N emission induced by excitation at 640 nm $F^{Atto647N}$ (reference 5).

$$S = F^{Atto565} / (F^{Atto565} + F^{Atto647N})$$

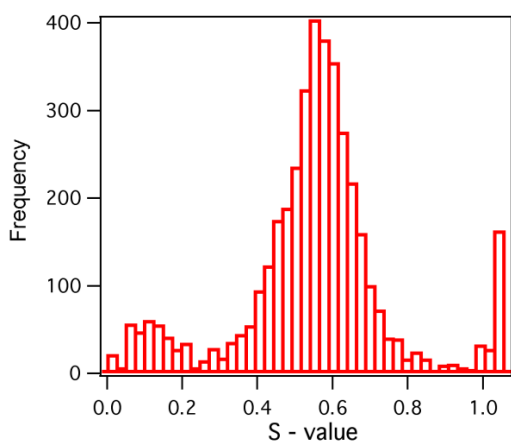


Fig. S4. Stoichiometry histogram of fluorescently labeled 4F sheet that describes the ratio between the dyes Atto565 and Atto647N. A large fraction of 4F sheets has integrated both fluorescently labeled staple strands ($S = 0.5$). Due to the burst search algorithm that identifies doubly labeled structures preferentially over singly labeled molecules, the absolute ratio between doubly labeled and singly labeled 4F sheets cannot be determined.

6. Estimated cost of producing 1 mg of M13 single-stranded DNA scaffold by conventional molecular biology methodology

Estimated cost of materials required for mid-scale production of M13 circular single-stranded DNA in a German university molecular biology setting (excluding costs for equipment, energy, and labor). Similar costs will arise when using one-way purification cartridges for single-stranded DNA, which may speed up the procedure by one to two days.

Bio/Chemicals for the preparation of 1 l phage-multiplying E. coli culture (expected yield of M13 single-stranded DNA: 0.1-1 mg/l)

	€ prices
<u>LB broth medium (1 l)</u>	
Trypton 10 g	1.20 €
NaCl 10 g	0.02
Yeast Extract 5 g	1.20
<u>Reagents (biology quality)</u>	
MgCl ₂	0.05
PEG-6000 or similar	0.80
NaCl	0.12
Tris buffer, pH adjusted	0.08
Phenol, buffer-saturated	12.00
Chloroform	1.70
Na-acetate pH 4.8	0.40
Ethanol (Rotisol)	1.20
Ultrapure water, buffer, etc	0.20
antibiotics, agar etc.	
<u>Consumables approx.</u>	<u>1.00</u>
<u>Quality control approx.</u>	<u>2.00</u>
(agarose, ethidium bromide, loading/electrophoresis buffer, documentation)	
<u>Total</u>	<u>22.00</u> (not including VAT)

Time effort: approx. 3-4 days during a full week, as specified below
(1 person working, including preparation, sterilization, clean-up etc.):

Day 1: Preparation of media and equipment, plating of starter culture: ca. 5 h

Day 2: Set-up of liquid pre-cultures and transfer into cold room: ca. 1 h

Day 3: Set-up of 10 production cultures à 100 ml (works better than one large culture) and infection by M13: approx. 2 h (including pre-treatment of shaker etc.), plus harvest: 2 h

Day 4: Isolation, including DNA precipitation

Day 5: DNA resuspension and quality control *via* gel electrophoresis; documentation.

7. Gel of 4F M1.3 Origami with 5'-Capped Staples

The formation of M1.3 with the 5'-pyrenyl capped staple strands was analyzed by using agarose gel electrophoresis. In both cases, with the **PyC** and the **PyPy** cap, a clear band was detected. As shown below, the bands of the modified M1.3 origami gave a modest shift in the gel in comparison with the unmodified 4F M1.3 origami.

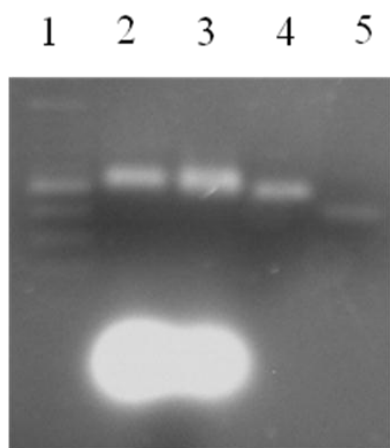


Fig. S5. Fluorescence image of an agarose gel with ethidium bromide staining. *Lane 1:* 100 bp ladder; *Lane 2:* 0.5 pmol linear M1.3, assembled with 50 equivalents of staple strands with **PyC** 5'-caps; *Lane 3:* 0.5 pmol linear M1.3, assembled with 50 equivalents staple strands with **PyPy** 5'-caps; *Lane 4:* 0.5 pmol linear M1.3, assembled with 10 equivalents of *unmodified* staple strands; *Lane 5:* 0.5 pmol linear M1.3 scaffold alone.

8. Melting curves of 4F M1.3 Origami with and without 5'-capped staple strands

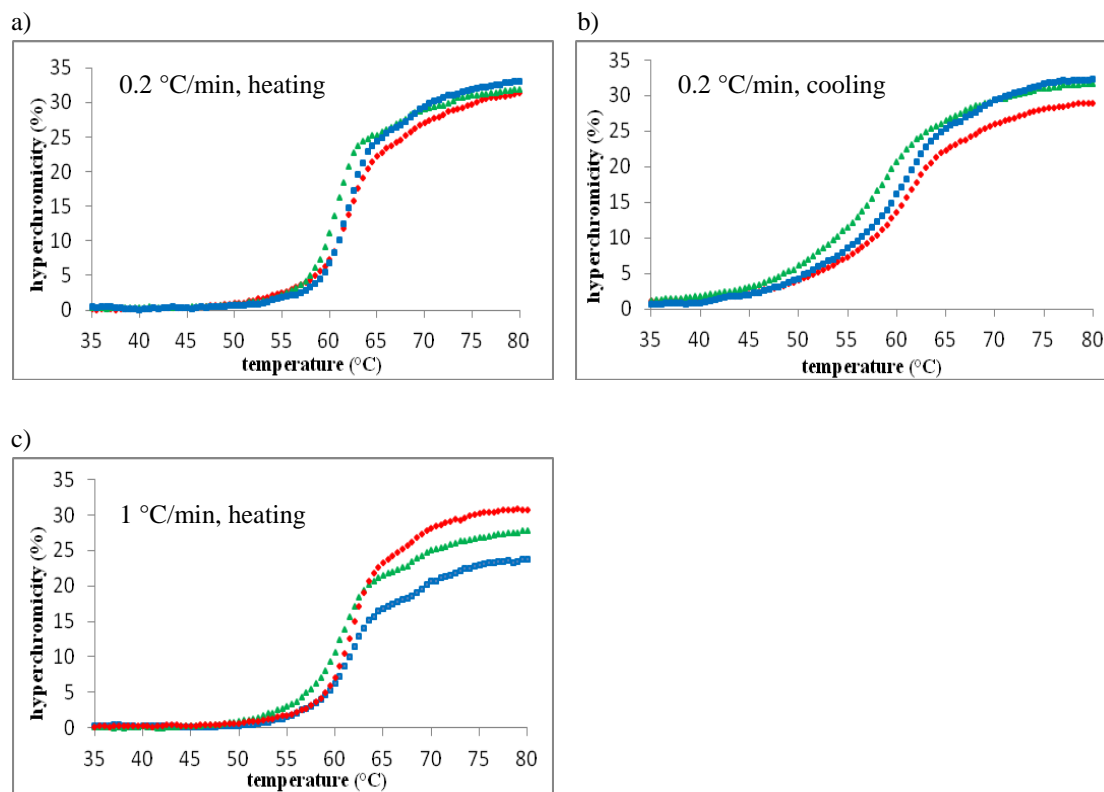


Fig. S6. UV-melting curves for unmodified 4F M1.3 origami (*green*), 4F M1.3 with globally 5'-PyPy capped staples (*blue*), and 4F M1.3 with globally 5'-PyC capped staples (*red*), measured at 260 nm at 50 nM concentration of M1.3 in each experiment.. a) Heating curves at a rate of 0.2 °C/min, (b) cooling curves at a rate of 0.2 °C/min, (c) heating curves at a rate of 1 °C/min.

The curves shown in a), b), and c) are the primary data for the first derivatives shown in Fig. 4 of the main paper. For an additional set of curves and their first derivative (fast cooling), see Figure S7, below.

Additional melting curves

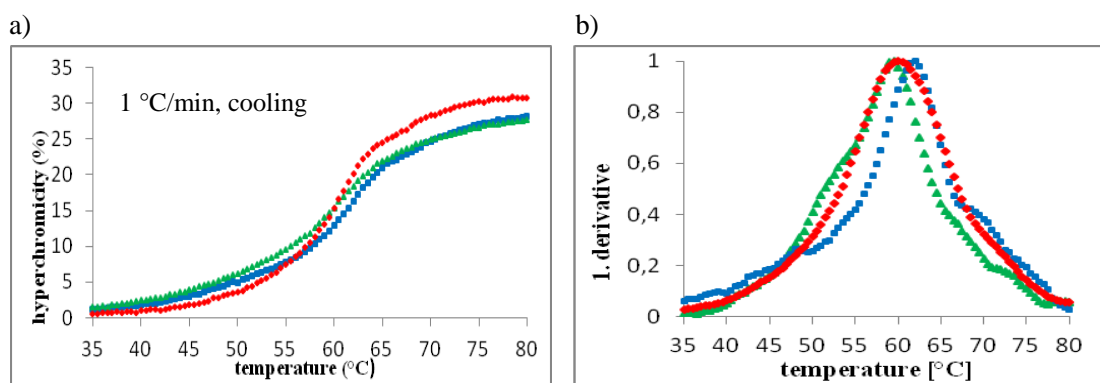


Fig. S7. UV-melting curves for unmodified 4F M1.3 origami (*green*), 4F M1.3 with globally 5'-PyPy capped staples (*blue*), and 4F M1.3 with globally 5'-PyC capped staples (*red*), measured at 260 nm at 50 nM concentration of M1.3 in each experiment.

(a) Cooling curves at 1 °C/min. (b) First derivative of the melting curve shown in a).

This is the set of cooling curves that corresponds to the melting curves shown in Fig. 4b (main paper) and Fig. S6c (above).

9. UV-Melting points and melting transition breadths of 4F sheets

Table S1. UV melting points (T_m) of unmodified 4F M1.3 origami (4F) and 4F M1.3 origami with globally 5'-**PyPy** capped staples (4F PyC) or globally 5'-**PyC** capped staples (4F PyPy) at a heating and cooling rate of 0.2 °C/min or 1 °C/min. Data are the average of two measurements.

Sample	T_m^{melting} (°C)	T_m^{melting} (°C)	T_m^{cooling} (°C)	T_m^{cooling} (°C)
	at 1 °C/min	at 0.2 °C/min	at 1 °C/min	at 0.2 °C/min
4F	60	60	59.5	58
4F PyC	62	62	61	61
4F PyPy	61.5	62	62	61

Table S2. Cooperativity of melting transition, as determined by the breadth of UV-melting transitions ("transition breadths", T_b) of unmodified 4F M1.3 origami (4F) and 4F M1.3 origami with globally 5'-**PyPy** capped staples (4F PyC) or globally 5'-**PyC** capped staples (4F PyPy). Data are based on the curves shown in Fig. 4 of the main paper and Fig. S7b, above). For an early example of analyzing the melting transition breadths of DNA duplex-mediated nanostructures, see ref. 6.

Sample	T_b^{melting} (°C)	T_b^{melting} (°C)	T_b^{cooling} (°C)	T_b^{cooling} (°C)
	at 1 °C/min	at 0.2 °C/min	at 1 °C/min	at 0.2 °C/min
4F	5.9	5.5	12.7	11.2
4F PyC	11.2	6.5	13.4	9.5
4F PyPy	7.7	6.1	9.8	10.1

10. MALDI spectra of individual 5'-capped oligonucleotides

Shown below are mass spectra of oligonucleotide sequences that were 5'-capped in parallel to the global capping of mixtures of support-bound staple strands. The latter are very difficult to analyze by MALDI-TOF mass spectrometry due to the large number of signals and the large differences in desorption/ionization yield for the different sequences involved. The MALDI-mass spectra were recorded on a Bruker REFLEX IV spectrometer in linear negative mode using 2,4,6-trihydroxyacetophenon monohydrate (THAP, 0.3 M in ethanol) and diammonium citrate (0.1 M in water) in ratio (2:1 v/v) as matrix/comatrix, with an accuracy of $\pm 0.1\%$ of the mass.

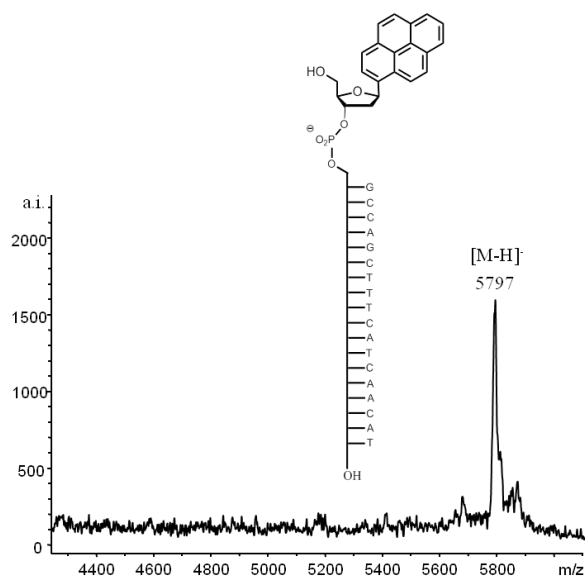


Fig. S8. MALDI-TOF mass spectrum of 5'-PyC-GCCAGCTTTCATCAACAT-3'. For the pseudomolecular ion [M-H]⁻: calcd 5798, found 5797

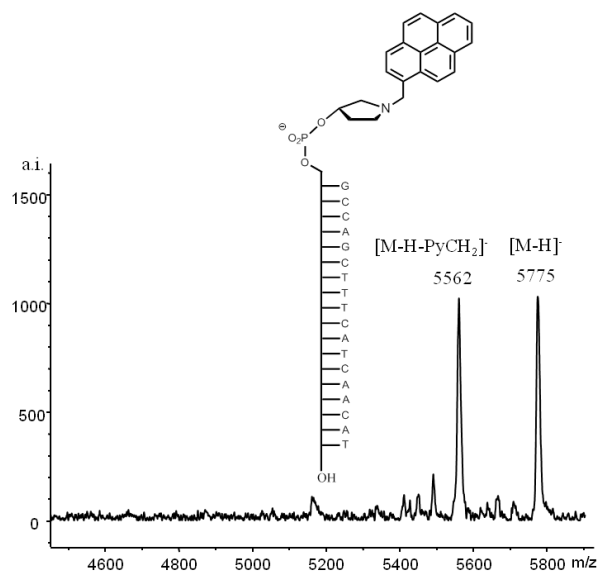


Fig. S9. MALDI-TOF mass spectrum of 5'-PyPy-GCCAGCTTTCATCAACAT-3'. Note that the pyrenyl cap fragments, as described in the literature.² For the unfragmented pseudomolecular ion [M-H]⁻: calcd 5778.7, found 5775.

11. Reference for Supporting Information

1. A. R. Oller, W. Vanden Broek, M. Conrad and M. D. Topal, *Biochemistry*, 1991, **30**, 2543-2549.
2. S. Narayanan, J. Gall and C. Richert, *Nucleic Acids Res.*, 2004, **32**, 2901-2911.
3. T. Cordes, J. Vogelsang and P. Tinnefeld, *J. Am. Chem. Soc.*, 2009, **131**, 5018-5019.
4. I. Stein, V. Schüller, P. Böhm, P. Tinnefeld and T. Liedl, *ChemPhysChem.*, 2011, **12**, 689-695.
5. A. N. Kapanidis, N. K. Lee, T. A. Laurence, S. Doose, E. Margeat and S. Weiss, *Proc. Natl. Acad. Sci. USA*, 2004, **101**, 8936-8941.
6. T. A. Tanton, C. A. Mirkin, and R. L. Letsinger, *Science*, 2000, **289**, 1757-1760.

Bibliography

- [1] N C Seeman. Nanomaterials Based on DNA. *Annual Review of Biochemistry*, 79:65–87, 2010.
- [2] V A Bloomfield, D M Crothers, and I Tinoco. *Nucleic Acids: Structure, Function and Properties*. University Science Books Sausalitos, California, 2000.
- [3] O T Avery, C M Macleod, and M M McCarty. Studies on the Chemical Nature of the Substance Inducing Transformation of Pneumococcal Types: Induction of Transformation by a Deoxyribonucleic Acid Fraction Isolated From Pneumococcus Type III. *Journal of Experimental Medicine*, 79(2):137–158, January 1944.
- [4] A D Hershey and M Chase. Independent Functions of Viral Protein and Nucleic Acid in Growth of Bacteriophage. *Journal of General Physiology*, 36(1):39–56, September 1952.
- [5] J D Watson and F H Crick. Molecular Structure of Nucleic Acids. *Nature*, 171(4356):737–738, April 1953.
- [6] R E Franklin and R G Gosling. Molecular configuration in sodium thymonucleate. *Nature*, 171(4356):740–741, April 1953.
- [7] E E CHARGAFF. Chemical specificity of nucleic acids and mechanism of their enzymatic degradation. *Experientia. Basel*, 6(6):201–209, June 1950.
- [8] J D WATSON and F H CRICK. The structure of DNA. *Cold Spring Harbor Symposia on Quantitative Biology*, 18:123–131, November 1953.
- [9] M M Meselson and F W Stahl. The Replication of DNA in Escherichia Coli. *Proceedings of the National Academy of Sciences of the United States of America*, 44(7):671–682, July 1958.
- [10] N C Seeman. Nucleic acid junctions and lattices. *Journal of theoretical biology*, 99:237–247, January 1982.
- [11] M M Levitt. How many base-pairs per turn does DNA have in solution and in chromatin? Some theoretical calculations. *Proceedings of the National Academy of Sciences of the United States of America*, 75(2):640–644, January 1978.
- [12] An Ghosh and M Bansal. A glossary of DNA structures from A to Z. *Acta Crystallographica Section D Biological Crystallography*, 59(4):620–626, March 2003.

- [13] B Alberts, D Bray, J Lewis, M Raff, and K Roberts. *Molekularbiologie der Zelle*. 1989.
- [14] P Yakovchuk, E Protozanova, and M D Frank-Kamenetskii. Base-stacking and base-pairing contributions into thermal stability of the DNA double helix. *Nucleic acids research*, 34(2):564–574, December 2005.
- [15] J Sponer, J Leszczynski, and P Hobza. Nature of Nucleic Acid Base Stacking: Nonempirical ab Initio and Empirical Potential Characterization of 10 Stacked Base Dimers. Comparison of Stacked and H-Bonded Base Pairs. *The Journal of Physical Chemistry*, 100(13):5590–5596, December 1996.
- [16] C G Baumann, S B Smith, V A Bloomfield, and C Bustamante. Ionic effects on the elasticity of single DNA molecules. *Proceedings of the National Academy of Sciences of the United States of America*, 94(12):6185–6190, June 1997.
- [17] T V Chalikian, J Völker, G E Plum, and K J Breslauer. A more unified picture for the thermodynamics of nucleic acid duplex melting: a characterization by calorimetric and volumetric techniques. *Proceedings of the National Academy of Sciences of the United States of America*, 96(14):7853–7858, July 1999.
- [18] J SantaLucia and D Hicks. The Thermodynamics of DNA Structural Motifs, 33(1):415. *Annu Rev Biophys Biomol Struct*, 33(1):415–440, September 2004.
- [19] M Rubinstein and R Colby. *Polymer Physics (Chemistry)*. 2003.
- [20] C Bustamante, J F Marko, E D Siggia, and S Smith. Entropic elasticity of lambda-phage DNA. *Science*, 265(5178):1599–1600, September 1994.
- [21] S B Smith, Y Cui, and C Bustamante. Overstretching B-DNA: the elastic response of individual double-stranded and single-stranded DNA molecules. *Science*, 1996.
- [22] N C Seeman. DNA in a material world. *Nature*, 421:427–431, January 2003.
- [23] D Smith, V Schüller, C Engst, J Rädler, and T Liedl. Nucleic acid nanostructures for biomedical applications. *Nanomedicine*, 8(1):105–121, January 2013.
- [24] S M Douglas, T Dietz, Hand Liedl, B Högberg, F Graf, and W M Shih. Self-assembly of DNA into nanoscale three-dimensional shapes. *Nature*, 459(7245):414–418, May 2009.
- [25] Z Zhao, H Yan, and Y Liu. A Route to Scale Up DNA Origami Using DNA Tiles as Folding Staples. *Angewandte Chemie International Edition*, 49:1414–1417, January 2010.
- [26] A Rajendran, M Endo, Y Katsuda, K Hidaka, and H Sugiyama. Programmed two-dimensional self-assembly of multiple DNA origami jigsaw pieces. *ACS nano*, 5(1):665–671, December 2011.
- [27] Y Yang, D Han, J Nangreave, Y Liu, and H Yan. DNA Origami with Double Stranded DNA as a Unified Scaffold. *ACS Nano*, 6(9):8209–8215, July 2012.
- [28] H Zhang, J Chao, D Pan, H Liu, Q Huang, and C Fan. Folding super-sized DNA origami with scaffold strands from long-range PCR. *Chemical communications*, 48:6405–6407, May 2012.

- [29] Z Zhao, Y Liu, and H Yan. Organizing DNA origami tiles into larger structures using preformed scaffold frames. *Nano Letters*, 11(7):2997–3002, July 2011.
- [30] A Rajendran, M Endo, K Hidaka, and H Sugiyama. Control of the two-dimensional crystallization of DNA origami with various loop arrangements. *Chemical communications*, 49:686–688, January 2013.
- [31] D A Jackson, R H Symons, and P Berg. Biochemical method for inserting new genetic information into DNA of Simian Virus 40: circular SV40 DNA molecules containing lambda phage genes and the galactose operon of Escherichia coli. *Proceedings of the National Academy of Sciences of the United States of America*, 69(10):2904–2909, October 1972.
- [32] S N Cohen, A C Chang, H W Boyer, and R B Helling. Construction of biologically functional bacterial plasmids in vitro. *Proceedings of the National Academy of Sciences of the United States of America*, 70(11):3240–3244, November 1973.
- [33] R Holliday. A mechanism for gene conversion in fungi. *Genetical Research*, 5(02):282–304, April 1964.
- [34] I G Panyutin and P Hsieh. The kinetics of spontaneous DNA branch migration. *Proceedings of the National Academy of Sciences of the United States of America*, 91:2021–2025, March 1994.
- [35] X Wang and N C Seeman. Assembly and Characterization of 8-Arm and 12-Arm DNA Branched Junctions. *Journal of the American Chemical Society*, 129(26):8169–8176, July 2007.
- [36] C Mao, W Sun, and N C Seeman. Designed Two-Dimensional DNA Holliday Junction Arrays Visualized by Atomic Force Microscopy. *Journal of the American Chemical Society*, 121:5437–5443, May 1999.
- [37] M H Caruthers. Gene synthesis machines: DNA chemistry and its uses. *Science*, 230:281–2851, October 1985.
- [38] S Ko, H Liu, Y Chen, and C Mao. DNA nanotubes as combinatorial vehicles for cellular delivery. *Biomacromolecules*, 9(11):3039–3043, October 2008.
- [39] E S Andersen, M Dong, M M Nielsen, K Jahn, R Subramani, W Mamdouh, M M Golas, B Sander, H Stark, C L P Oliveira, J S Pedersen, V Birkedal, F Besenbacher, K V Gothelf, and J Kjems. Self-assembly of a nanoscale DNA box with a controllable lid. *Nature*, 459(7243):73–76, April 2009.
- [40] R Jungmann, C Steinhauer, M Scheible, A Kuzyk, P Tinnefeld, and F C Simmel. Single-Molecule Kinetics and Super-Resolution Microscopy by Fluorescence Imaging of Transient Binding on DNA Origami. *Nano Letters*, 10(11):4756–4761, 2010.
- [41] N C Seeman. Synthesis from DNA of a molecule with the connectivity of a cube. *Nature*, 30:631–633, April 1991.
- [42] Y Zhang and N C Seeman. Construction of a DNA-truncated octahedron. *Journal American Chemical Society*, 116(5):1661–1669, February 1994.

- [43] Y He, T Ye, M Su, C Zhang, A E Ribbe, W Jiang, and C Mao. Hierarchical self-assembly of DNA into symmetric supramolecular polyhedra. *Nature*, 452(7184):198–201, March 2008.
- [44] R P Goodman. Rapid Chiral Assembly of Rigid DNA Building Blocks for Molecular Nanofabrication. *Science*, 310(5754):1661–1665, December 2005.
- [45] W M Shih, Joel D Quispe, and Gerald F Joyce. A 1.7-kilobase single-stranded DNA that folds into a nanoscale octahedron. *Nature*, 427(6975):618–621, February 2004.
- [46] C Mao, W Sun, and N C Seeman. Assembly of Borromean rings from DNA. *Nature*, 386(6621):137–138, March 1997.
- [47] X Li, X Yang, J Qi, and N C Seeman. Antiparallel DNA Double Crossover Molecules As Components for Nanoconstruction. *Journal of the American Chemical Society*, 118(26):6131–6140, January 1996.
- [48] T J Fu and N C Seeman. DNA double-crossover molecules. *Biochemistry*, 32(13):3211–3220, April 1993.
- [49] P Sa-Ardyen, N C Seeman, and A V Vologodskii. The Flexibility of DNA Double Crossover Molecules. *Biophysical Journal*, 84(6):3829, June 2003.
- [50] T H LaBean, H Yan, J Kopatsch, and F Liu. Construction, Analysis, Ligation, and Self-Assembly of DNA Triple Crossover Complexes). *Journal of the American Chemical Society*, 122(9):1848–1860, March 2000.
- [51] E Winfree, F Liu, LA Wenzler, and N C Seeman. Design and self-assembly of two-dimensional DNA crystals. *Nature*, 394:539–544, August 1998.
- [52] D Liu, M Wang, Z Deng, and R Walulu. Tensegrity: construction of rigid DNA triangles with flexible four-arm DNA junctions. *Journal American Chemical Society*, 126(8):2324–2325, August 2004.
- [53] J Zheng, J J Birktoft, Y Chen, T Wang, R Sha, P E Constantinou, S L Ginell, C Mao, and N C Seeman. From molecular to macroscopic via the rational design of a self-assembled 3D DNA crystal. *Nature*, 461(7260):74–77, March 2009.
- [54] P W K Rothmund. Folding DNA to create nanoscale shapes and patterns. *Nature*, 440(7082):297–302, March 2006.
- [55] P Yin, R F Hariadi, S Sahu, H M T Choi, S H Park, T H LaBean, and J H Reif. Programming DNA Tube Circumferences. *Science*, 321(5890):824–826, August 2008.
- [56] B Wei, M Dai, and P Yin. Complex shapes self-assembled from single-stranded DNA tiles. *Nature*, 485(7400):623–626, May 2012.
- [57] Y Ke, L L Ong, W M Shih, and P Yin. Three-dimensional structures self-assembled from DNA bricks. *Science*, 338(6111):1177–1183, November 2012.
- [58] H Yan, S H Park, G Finkelstein, J H Reif, and T H LaBean. DNA-templated self-assembly of protein arrays and highly conductive nanowires. *Science*, 301(5641):1882–1884, September 2003.

- [59] S H Park, P Yin, Y Liu, Jn H Reif, T H LaBean, and H Yan. Programmable DNA self-assemblies for nanoscale organization of ligands and proteins. *Nano Letters*, 5(4):729–733, March 2005.
- [60] Y Liu, C Lin, Hg Li, and H Yan. Aptamer-Directed Self-Assembly of Protein Arrays on a DNA Nanostructure. *Angewandte Chemie*, 117(28):4407–4412, July 2005.
- [61] S Rinker, Y Ke, Y Liu, R Chhabra, and H Yan. Self-assembled DNA nanostructures for distance-dependent multivalent ligand-protein binding. *Nature Nanotechnology*, 3(7):418–422, June 2008.
- [62] D N Selmi, R J Adamson, H Attrill, A D Goddard, R J C Gilbert, A Watts, and A J Turberfield. DNA-templated protein arrays for single-molecule imaging. *Nano Letters*, 11(2):657–660, February 2011.
- [63] C Zhang, C Tian, F Guo, Z Liu, W Jiang, and C Mao. DNA-Directed Three-Dimensional Protein Organization. *Angewandte Chemie*, 51:3382–3385, February 2012.
- [64] E Nakata, F F Liew, C Uwatoko, S Kiyonaka, Y Mori, Y Katsuda, M Endo, H Sugiyama, and T Morii. Zinc-Finger Proteins for Site-Specific Protein Positioning on DNA-Origami Structures. *Angewandte Chemie*, 124(10):2471–2474, January 2012.
- [65] J Sharma, R Chhabra, C S Andersen, K V Gothelf, H Yan, and Y Liu. Toward reliable gold nanoparticle patterning on self-assembled DNA nanoscaffold. *Journal of the American Chemical Society*, 130(25):7820–7821, June 2008.
- [66] S Pal, Z Deng, B Ding, H Yan, and Y Liu. DNA-Origami-Directed Self-Assembly of Discrete Silver-Nanoparticle Architectures. *Angewandte Chemie*, 122(15):2760–2764, March 2010.
- [67] B Ding, Z Deng, H Yan, S Cabrini, R N Zuckermann, and J Bokor. Gold Nanoparticle Self-Similar Chain Structure Organized by DNA Origami. *Journal of the American Chemical Society*, 132(10):3248–3249, March 2010.
- [68] X Shen, C Song, J Wang, D Shi, Z Wang, N Liu, and B Ding. Rolling up gold nanoparticle-dressed DNA origami into three-dimensional plasmonic chiral nanostructures. *Journal of the American Chemical Society*, December 2011.
- [69] Z Zhao, E L Jacovetty, Y Liu, and H Yan. Encapsulation of Gold Nanoparticles in a DNA Origami Cage. *Angewandte Chemie International Edition*, 50(9):2041–2044, January 2011.
- [70] R Schreiber, S Kempter, S Holler, V Schüller, D Schiffels, S S Simmel, P C Nickels, and T Liedl. DNA Origami-Templated Growth of Arbitrarily Shaped Metal Nanoparticles. *Small*, 7(13):1795–1799, May 2011.
- [71] A Kuzyk, R Schreiber, Z Fan, G Pardatscher, E-M Roller, A Högele, F C Simmel, A O Govorov, and T Liedl. DNA-based self-assembly of chiral plasmonic nanostructures with tailored optical response. *Nature*, 483(7389):311–314, March 2012.

- [72] C Steinhauer, T L Jungmann, Rand Sobey, F C Simmel, and P Tinnefeld. DNA origami as a nanoscopic ruler for super-resolution microscopy. *Angewandte Chemie International Edition*, 48(47):8870–8873, December 2008.
- [73] I H Stein, V Schüller, P Böhm, P Tinnefeld, and T Liedl. Single-Molecule FRET Ruler Based on Rigid DNA Origami Blocks. *ChemPhysChem*, 12(3):689–695, February 2011.
- [74] I H Stein, C Steinhauer, and P Tinnefeld. Single-Molecule Four-Color FRET Visualizes Energy-Transfer Paths on DNA Origami. *Journal of the American Chemical Society*, 133:4193–4195, January 2011.
- [75] A Gietl, P Holzmeister, D Grohmann, and P Tinnefeld. DNA origami as biocompatible surface to match single-molecule and ensemble experiments. *Nucleic acids research*, 40(14):e110–e110, July 2012.
- [76] C Lin, R Jungmann, A M Leifer, C Li, D Levner, G M Church, W M Shih, and P Yin. Submicrometre geometrically encoded fluorescent barcodes self-assembled from DNA. *Nature chemistry*, 4(10):832–839, September 2012.
- [77] M Nishikawa, M Matono, S Rattanakiat, Nao M, and Y Takakura. Enhanced immunostimulatory activity of oligodeoxynucleotides by Y-shape formation. *Immunology*, 124(2):247–255, June 2008.
- [78] S Rattanakiat, M Nishikawa, He Funabashi, D Luo, and Y Takakura. The assembly of a short linear natural cytosine-phosphate-guanine DNA into dendritic structures and its effect on immunostimulatory activity. *Biomaterials*, 30(29):5701–5706, October 2009.
- [79] J Li, H Pei, B Zhu, Le L, M Wei, Y He, N Chen, D Li, Q Huang, and C Fan. Self-Assembled Multivalent DNA Nanostructures for Noninvasive Intracellular Delivery of Immunostimulatory CpG Oligonucleotides. *ACS Nano*, 5(11):8783–8789, November 2011.
- [80] V J Schüller, S Heidegger, N Sandholzer, P C Nickels, Na A Suhartha, S Endres, C Bourquin, and T Liedl. Cellular Immunostimulation by CpG-Sequence-Coated DNA Origami Structures. *ACS Nano*, 5(12):9696–9702, December 2011.
- [81] J Fu, M Liu, and Y Liu. Spatially-Interactive Biomolecular Networks Organized by Nucleic Acid Nanostructures. *Accounts of Chemical Research*, 45(8):1215–1226, May 2012.
- [82] S M Douglas, I Bachelet, and G M Church. A logic-gated nanorobot for targeted transport of molecular payloads. *Science*, 335(6070):831–834, February 2012.
- [83] K Mohri, M Nishikawa, N Takahashi, T Shiomi, N Matsuoka, K Ogawa, M Endo, K Hidaka, H Sugiyama, Y Takahashi, and Y Takakura. Design and Development of Nanosized DNA Assemblies in Polypod-like Structures as Efficient Vehicles for Immunostimulatory CpG Motifs to Immune Cells. *ACS Nano*, 6(7):5931–5940, June 2012.
- [84] X Liu, Y Xu, T Yu, C Clifford, Y Liu, H Yan, and Y Chang. A DNA Nanostructure Platform for Directed Assembly of Synthetic Vaccines. *Nano Letters*, 12(8):4254–4259, July 2012.

- [85] Y-X Zhao, A Shaw, X Zeng, E Benson, A M Nyström, and B Högberg. A DNA Origami Delivery System for Cancer Therapy with Tunable Release Properties. *ACS Nano*, 6(10):8684–8691, September 2012.
- [86] B Yurke, AJ Turberfield, AP Mills Jr, and FC Simmel. A DNA-fuelled molecular machine made of DNA. *Nature*, 406:605–608, August 2000.
- [87] J-S Shin and N A Pierce. A Synthetic DNA Walker for Molecular Transport. *Journal of the American Chemical Society*, 126(35):10834–10835, September 2004.
- [88] P Yin, H M T Choi, C R Calvert, and N A Pierce. Programming biomolecular self-assembly pathways. *Nature*, 451(7176):318–322, January 2008.
- [89] D Y Zhang, A J Turberfield, B Yurke, and E Winfree. Engineering Entropy-Driven Reactions and Networks Catalyzed by DNA. *Science*, 318(5853):1121–1125, November 2007.
- [90] H Yan, T H LaBean, L Feng, and J H Reif. Directed nucleation assembly of DNA tile complexes for barcode-patterned lattices. *Proceedings of the National Academy of Sciences of the United States of America*, 100(14):8103–8108, July 2003.
- [91] H Dietz, S M Douglas, and W M Shih. Folding DNA into Twisted and Curved Nanoscale Shapes. *Science*, 325(5941):725–730, August 2009.
- [92] T Liedl, B Högberg, J Tytell, D E Ingber, and W M Shih. Self-assembly of three-dimensional prestressed tensegrity structures from DNA. *Nature Nanotechnology*, 5(7):520–524, June 2010.
- [93] D Han, S Pal, J Nangreave, Z Deng, Y Liu, and H Yan. DNA Origami with Complex Curvatures in Three-Dimensional Space. *Science*, 332(6027):342–346, April 2011.
- [94] E S Andersen, M Dong, M M Nielsen, K Jahn, A Lind-Thomsen, W Mamdouh, K V Gothelf, F Besenbacher, and J Kjems. DNA origami design of dolphin-shaped structures with flexible tails. *ACS Nano*, 2(6):1213–1218, 2008.
- [95] S M Douglas, A H Marblestone, S Teerapittayanon, A Vazquez, Ge M Church, and W M Shih. Rapid prototyping of 3D DNA-origami shapes with caDNAno. *Nucleic acids research*, 37(15):5001–5006, August 2009.
- [96] Y Ke, S M Douglas, M Liu, J Sharma, A Cheng, A Leung, Y Liu, W M Shih, and H Yan. Multilayer DNA Origami Packed on a Square Lattice. *Journal of the American Chemical Society*, 131(43):15903–15908, November 2009.
- [97] B Högberg, T Liedl, and W M Shih. Folding DNA Origami from a Double-Stranded Source of Scaffold. *Journal of the American Chemical Society*, 131(26):9154–9155, July 2009.
- [98] W W Liu, H H Zhong, R R Wang, and N C Seeman. Crystalline two-dimensional DNA-origami arrays. *Angewandte Chemie International Edition*, 50(1):264–267, January 2011.

- [99] Y Ke, S Lindsay, Y Chang, Y Liu, and H Yan. Self-Assembled Water-Soluble Nucleic Acid Probe Tiles for Label-Free RNA Hybridization Assays. *Science*, 319(5860):180–183, January 2008.
- [100] H T Maune, S Han, R D Barish, M Bockrath, W A Goddard, P W K Rothmund, and E Winfree. Self-assembly of carbon nanotubes into two-dimensional geometries using DNA origami templates. *Nature Nanotechnology*, 5(1):61–66, 2010.
- [101] L A Stearns, R Chhabra, J Sharma, Y Liu, W T Petuskey, H Yan, and J C Chaput. Template-Directed Nucleation and Growth of Inorganic Nanoparticles on DNA Scaffolds. *Angewandte Chemie*, 121(45):8646–8648, October 2009.
- [102] J Liu, Y Geng, E Pound, S Gyawali, and J R Ashton. Metallization of Branched DNA Origami for Nanoelectronic Circuit Fabrication. *ACS Nano*, 5(3):2240–2247, July 2011.
- [103] Y Sannohe, M Endo, Y Katsuda, K Hidaka, and H Sugiyama. Visualization of dynamic conformational switching of the G-quadruplex in a DNA nanostructure. *Journal of the American Chemical Society*, 132(46):16311–16313, November 2010.
- [104] M Endo, Y Yang, Y Suzuki, K Hidaka, and H Sugiyama. Single-Molecule Visualization of the Hybridization and Dissociation of Photoresponsive Oligonucleotides and Their Reversible Switching Behavior in a DNA Nanostructure. *Angewandte Chemie*, 51(42):10518–10522, October 2012.
- [105] H Gu, J Chao, S-J Xiao, and N C Seeman. A proximity-based programmable DNA nanoscale assembly line. *Nature*, 465(7295):202–205, May 2010.
- [106] K Lund, A J Manzo, N Dabby, N Michelotti, A Johnson-Buck, J Nangreave, S Taylor, R Pei, M N Stojanovic, N G Walter, E Winfree, and H Yan. Molecular robots guided by prescriptive landscapes. *Nature*, 465(7295):206–210, May 2010.
- [107] S F J Wickham, M Endo, Y Katsuda, K Hidaka, J Bath, H Sugiyama, and A J Turberfield. Direct observation of stepwise movement of a synthetic molecular transporter. *Nature Nanotechnology*, 6(3):166–169, February 2011.
- [108] C E Castro, F Kilchherr, D-N Kim, E L Shiao, T Wauer, P Wortmann, M Bathe, and H Dietz. A primer to scaffolded DNA origami. *Nature Methods*, 8(3):221–229, March 2011.
- [109] Y Ke, N V Voigt, K V Gothelf, and W M Shih. Multilayer DNA Origami Packed on Hexagonal and Hybrid Lattices. *Journal of the American Chemical Society*, 134(3):1770–1774, December 2011.
- [110] T G Martin and H Dietz. Magnesium-free self-assembly of multi-layer DNA objects. *Nature communications*, 3:1103–1110, October 2012.
- [111] R Jungmann, T Liedl, T L Sobey, W Shih, and F C Simmel. Isothermal assembly of DNA origami structures using denaturing agents. *Journal of the American Chemical Society*, 130(31):10062–10063, August 2008.

- [112] J-P J Sobczak, T G Martin, T Gerling, and H Dietz. Rapid folding of DNA into nanoscale shapes at constant temperature. *Science*, 338(6113):1458–1461, December 2012.
- [113] G Bellot, M A McClintock, C Lin, and W M Shih. Recovery of intact DNA nanostructures after agarose gel-based separation. *Nature Methods*, 8(3):192–194, March 2011.
- [114] C Lin, S D Perrault, M Kwak, F Graf, and W M Shih. Purification of DNA-origami nanostructures by rate-zonal centrifugation. *Nucleic acids research*, 41(2):e40, January 2013.
- [115] R Erni, M D Rossell, C Kisielowski, and U Dahmen. Atomic-resolution imaging with a sub-50-pm electron probe. *Physical Review Letters*, 102(9):096101–096101, March 2009.
- [116] X Bai, T G Martin, S H W Scheres, and H Dietz. Cryo-EM structure of a 3D DNA-origami object. *Proceedings of the National Academy of Sciences of the United States of America*, 109(49):20012–20017, September 2012.
- [117] G Binnig, C F Quate, and C Gerber. Atomic Force Microscope. *Physical Review Letters*, 1986.
- [118] A A Deniz, M Dahan, J R Grunwell, T Ha, A E Faulhaber, D S Chemla, S Weiss, and P G Schultz. Single-pair fluorescence resonance energy transfer on freely diffusing molecules: observation of Förster distance dependence and subpopulations. *Proceedings of the National Academy of Sciences of the United States of America*, 96(7):3670–3675, March 1999.
- [119] T Förster. Zwischenmolekulare Energiewanderung und Fluoreszenz. *Annalen der Physik*, 437(1-2):55–75, 1948.
- [120] R M Clegg. Observing the Helical Geometry of Double-Stranded DNA in Solution by Fluorescence Resonance Energy Transfer. *Proceedings of the National Academy of Sciences*, 90(7):2994–2998, April 1993.
- [121] P R. Selvin and T Ha, editors. *Single-Molecule Techniques: A Laboratory Manual*. Cold Spring Harbor Laboratory Press, 2008.
- [122] R E Benesch and R R Benesch. Enzymatic removal of oxygen for polarography and related methods. *Science*, 118(3068):447–448, October 1953.
- [123] I I Rasnik, S A McKinney, and T Ha. Nonblinking and long-lasting single-molecule fluorescence imaging. *Nature Methods*, 3(11):891–893, October 2006.
- [124] J Vogelsang, R Kasper, C Steinhauer, B Person, M Heilemann, M Sauer, and P Tinnefeld. A Reducing and Oxidizing System Minimizes Photobleaching and Blinking of Fluorescent Dyes. *Angewandte Chemie International Edition*, 47(29):5465–5469, July 2008.
- [125] M Dahan, A A Deniz, T Ha, D S Chemla, P G Schultz, and S Weiss. Ratiometric measurement and identification of single diffusing molecules. *Chemical Physics*, 247(1):22–22, July 1999.

- [126] N K Lee, A N Kapanidis, Y Wang, X Michalet, Ja Mukhopadhyay, R H Ebright, and S Weiss. Accurate FRET measurements within single diffusing biomolecules using alternating-laser excitation. *Biophysical Journal*, 88(4):2939–2953, April 2005.
- [127] A N Kapanidis, N K Lee, T A Laurence, S Doose, E Margeat, and S Weiss. Fluorescence-aided molecule sorting: analysis of structure and interactions by alternating-laser excitation of single molecules. *Proceedings of the National Academy of Sciences of the United States of America*, 101(24):8936–8941, June 2004.
- [128] L Stryer and R P Haugland. Energy transfer: a spectroscopic ruler. *Proceedings of the National Academy of Sciences of the United States of America*, 58(2):719–726, July 1967.
- [129] P R Schimmel and P J Flory. Conformational energy and configurational statistics of poly-L-proline. *Proceedings of the National Academy of Sciences of the United States of America*, 58(1):52–59, June 1967.
- [130] B Schuler, E A Lipman, P J Steinbach, M Kumpke, and W A Eaton. Polyproline and the "spectroscopic ruler" revisited with single-molecule fluorescence. *Proceedings of the National Academy of Sciences*, 102(8):2754–2759, February 2005.
- [131] R B Best, K A Merchant, I V Gopich, B Schuler, A Bax, and W A Eaton. Effect of flexibility and cis residues in single-molecule FRET studies of polyproline. *Proceedings of the National Academy of Sciences*, 104(48):18964–18969, November 2007.
- [132] S Doose, H Neuweiler, H Barsch, and M Sauer. Probing polyproline structure and dynamics by photoinduced electron transfer provides evidence for deviations from a regular polyproline type II helix. *Proceedings of the National Academy of Sciences of the United States of America*, 104(44):17400–17405, October 2007.
- [133] A I Murchie, R M Clegg, E von Kitzing, D R Duckett, S Diekmann, and D M Lilley. Fluorescence energy transfer shows that the four-way DNA junction is a right-handed cross of antiparallel molecules. *Nature*, 341(6244):763–766, October 1989.
- [134] P J Hagerman. Flexibility of DNA. *Annual Review of Biophysics and Biophysical Chemistry*, 17(1):265–286, June 1988.
- [135] A Dietrich, V Buschmann, C Müller, and M Sauer. Fluorescence resonance energy transfer (FRET) and competing processes in donor-acceptor substituted DNA strands: a comparative study of ensemble and single-molecule data. *Journal of biotechnology*, 82(3):211–231, January 2002.
- [136] N Di Fiori and A Meller. The Effect of Dye-Dye Interactions on the Spatial Resolution of Single-Molecule FRET Measurements in Nucleic Acids. *Biophysical Journal*, 98(10):2265–2272, May 2010.
- [137] J-M Arbona, J-P Aimé, and J Elezgaray. Modeling the mechanical properties of DNA nanostructures. *Physical review. E, Statistical, nonlinear, and soft matter physics*, 86(5 Pt 1):051912–051912, October 2012.
- [138] R S Yalow and S A Berson. Immunoassay of endogenous plasma insulin in man. *The Journal of clinical investigation*, 39:1157–1175, July 1960.

- [139] E Engvall and P Perlmann. Enzyme-linked immunosorbent assay (ELISA). Quantitative assay of immunoglobulin G. *Immunochemistry*, 8(9):871–874, September 1971.
- [140] B K Van Weeman and A Schuurs. Immunoassay using antigen-enzyme conjugates. *FEBS Letter*, 15(3):232–236, June 1971.
- [141] M J Fulwyler. Electronic separation of biological cells by volume. *Science*, 150(3698):910–911, November 1965.
- [142] W M Dittrich and W H Goehde. Flow-through Chamber for Photometers to Measure and Count Particles in a Dispersion medium. *Patent US 3761187*, 1973.
- [143] K Strebhardt and A Ullrich. Paul Ehrlich’s magic bullet concept: 100 years of progress. *Nature Reviews Cancer*, 8:473–480, May 2008.
- [144] F C Simmel. Towards biomedical applications for nucleic acid nanodevices. *Nanomedicine*, 2(6):817–830, December 2007.
- [145] J-W Keum and H Bermudez. Enhanced resistance of DNA nanostructures to enzymatic digestion. *Chemical Communications*, 49:7036–7038, 2009.
- [146] Q Mei, X Wei, F Su, Y Liu, C Youngbull, R Johnson, S Lindsay, H Yan, and D Meldrum. Stability of DNA Origami Nanoarrays in Cell Lysate. *Nano Letters*, 11(4):1477–1482, April 2011.
- [147] S Rudolf and J O Rädler. Self-Assembly of Stable Monomolecular Nucleic Acid Lipid Particles with a Size of 30 nm. *Journal of the American Chemical Society*, 134(28):11652–11658, October 2012.
- [148] Y Ke, G Bellot, N V Voigt, E Fradkov, and W M Shih. Two design strategies for enhancement of multilayer–DNA-origami folding: underwinding for specific intercalator rescue and staple-break positioning. *Chemical Science*, 3(8):2587–2597, 2012.
- [149] Q Jiang, C Song, J Nangreave, X Liu, L Lin, D Qiu, Z-G Wang, G Zou, X Liang, H Yan, and B Ding. DNA Origami as a Carrier for Circumvention of Drug Resistance. *Journal of the American Chemical Society*, 134(32):13396–13403, July 2012.
- [150] H Lee, A K R Lytton-Jean, Y Chen, K T Love, A I Park, E D Karagiannis, A Sehgal, W Querbes, C S Zurenko, M Jayaraman, C G Peng, K Charisse, A Borodovsky, M Manoharan, J S Donahoe, J Truelove, M Nahrendorf, R Langer, and D G Anderson. Molecularly self-assembled nucleic acid nanoparticles for targeted in vivo siRNA delivery. *Nature Nanotechnology*, 7(6):389–393, 2012.
- [151] J Vollmer and A M Krieg. Immunotherapeutic applications of CpG oligodeoxynucleotide TLR9 agonists. *Advanced drug delivery reviews*, 61(3):195–204, February 2009.
- [152] D M Klinman. Immunotherapeutic uses of CpG oligodeoxynucleotides. *Nature Reviews Immunology*, 4(4):249–259, April 2004.
- [153] A M Krieg, A K Yi, S Matson, T J Waldschmidt, G A Bishop, R Teasdale, G A Koretzky, and D M Klinman. CpG motifs in bacterial DNA trigger direct B-cell activation. *Nature*, 374(6522):546–549, April 1995.

- [154] V Hornung and E Latz. Intracellular DNA recognition. *Nature Reviews Immunology*, 10(2):123–130, February 2010.
- [155] H Hemmi, O Takeuchi, T Kawai, T Kaisho, S Sato, H Sanjo, M Matsumoto, K Hoshino, H Wagner, K Takeda, and S AKIRA. A Toll-like receptor recognizes bacterial DNA. *Nature*, 408(6813):740–745, December 2000.
- [156] F Takeshita, C A Leifer, I Gursel, K J Ishii, S Takeshita, M Gursel, and D M Klinman. Cutting edge: Role of Toll-like receptor 9 in CpG DNA-induced activation of human cells. *Journal of immunology*, 167(7):3555–3558, September 2001.
- [157] A M Krieg. CpG Motifs in bacterial DNA and their Immune Effects- Annual Review of Immunology. *Annual review of immunology*, 20(1):709–760, 2002.
- [158] D M Smith, V Schüller, C Forthmann, R Schreiber, P Tinnefeld, and T Liedl. A Structurally Variable Hinged Tetrahedron Framework from DNA Origami. *Journal of Nucleic Acids*, 2011:1–9, 2011.
- [159] H Said, V J Schüller, F J Eber, C Wege, T Liedl, and C Richert. M1.3 - a small scaffold for DNA origami . *Nanoscale*, 5(1):284–290, November 2012.

Full list of publications

- I. H. Stein*, **V. Schüller***, P. Böhm, P. Tinnefeld, and T. Liedl. Single-molecule FRET ruler based on rigid DNA origami blocks. *ChemPhysChem*, 12, 689-695 (2011). *equal contribution
- R. Schreiber, S. Kempter, S. Holler, **V. Schüller**, D. Schiffels, S. S. Simmel, P. C. Nickels and T. Liedl. DNA Origami-Templated Growth of Arbitrarily Shaped Metal Nanoparticles. *Small*, 7, 1795-1799 (2011).
- D. M. Smith, **V. Schüller**, C. Forthmann, R. Schreiber, P. Tinnefeld, and T. Liedl. A Structurally Variable Hinged Tetrahedron Framework from DNA Origami. *Journal of Nucleic Acids* doi:10.4061/2011/360954 (2011).
- **V. Schüller***, S. Heidegger*, N. Sandholzer, P. C. Nickels, N. A. Suhartha, S. Endres, C. Bourquin, and T. Liedl. Cellular Immunostimulation by CpG-Sequence-Coated DNA Origami Structures. *ACS Nano*, 5, 9696-9702 (2011). *equal contribution.
- H. Said, **V. J. Schüller**, F. J. Eber, C. Wege, T. Liedl, and C. Richert. M1.3 - a small scaffold for DNA origami. *Nanoscale*, 5, 284-290 (2013).
- D. Smith, **V. Schüller**, C. Engst, J. Rädler, and T. Liedl. Nucleic acid nanostructures for biomedical applications. *Nanomedicine*, 8, 105-121 (2013).
- R. Schreiber, J. Do, E. Roller, T. Zhang, **V. J. Schüller**, P. C. Nickels, J. Feldmann, T. Liedl. Hybrid Planet-Satellite Metal Nanoclusters based on DNA Origami. *submitted to Nature Nanotechnology*.

Vielen Dank an

- **Prof. Tim Liedl**, für eine hervorragende und strukturierte Betreuung sowie interessante Diskussionen, die in einem idealen Maß sowohl fördernd als auch fordernd waren, für die motivierende Arbeit in einem jungen Forschungsbereich und für die Möglichkeit, hier in München, auf weltweiten Konferenzen und bei einem unvergesslichen Aufenthalt in Boston auf spannende Leute und deren Forschung treffen zu können.
- **Prof. Joachim Rädler**, für die idealen Forschungsbedingungen an seinem Lehrstuhl, sein Interesse an meiner Arbeit und seine kontinuierliche Unterstützung.
- **die Kollaborationspartner**: Prof. Philip Tinnefeld und seine Gruppe für die wunderbare Zusammenarbeit im DNA Origami FRET Ruler-MgCl₂-Projekt und die Einführung in die Einzelmolekülspektroskopie. Prof. Peng Yin und Prof. William Shih für eine faszinierende und lehrreiche Zeit in ihren motivierten Gruppen. Prof. Carole Bourquin für die spannende Zusammenarbeit mit ihrer Gruppe im CpG-Projekt und Einblicke in die Immunologie. Prof. Clemens Richert und seine Gruppe für die interessante Kollaboration im Small-Origami-Projekt. Prof. Hendrik Dietz und seine Gruppe für die class averages der TEM Aufnahmen der DNA Origami-Struktur.
- **Dr. Susanne Kempter, Susanne Rappl und Gerlinde Schwake**, ohne die im Labor nichts laufen würde.
- **die Mitglieder der Arbeitsgruppe Liedl**: Philipp Nickels, Robert Schreiber, David Smith, Daniel Schiffels, Tao Zhang, Stephanie Simmel, Alex Maier, Samet Kocabey, Yongzheng Xing, Eva-Maria Roller, Philip Böhm, Johanna Schappert und das Biomod-Team für die große Hilfsbereitschaft im Labor sowie auch außerhalb z.B. bei head plants.
- **die Mitglieder des Lehrstuhls Rädler** für eine einmalig freundschaftliche und entspannte Atmosphäre. Besonders Susanne Rappl, Carolin Leonhardt und Svenja Lippok haben die Zeit zu etwas ganz Besonderem werden lassen: Danke, dass Ihr immer für mich da seid! Dank auch an Samira Hertrich für die lustige Zeit in unserem Kabuff.
- **die Korrekturleser** der Arbeit, deren konstruktive Kritik unerlässlich war: Philipp Nickels, Carolin Leonhardt, Svenja Lippok, Dr. Lawrence Parnell, Regina Träger und Felix Schüller.
- **die Weggefährten** während des Studiums und der Doktorarbeit: Ingo Stein für die perfekte Zusammenarbeit bei unserem ersten Paper und beim MgCl₂-Projekt. Christof Mast, Stefan Schlögl und Hubert Krammer für unermüdliche freundschaftliche Unterstützung nicht nur beim Schnitzelwirt.
- **meine Familie**: meine Eltern, die mir diese Ausbildung erst ermöglicht haben und mir den Rücken freihalten. Meine Schwester, die in jeder (Prüfungs)-Situation für mich da ist.
- **Felix** für Alles!

Danke

